Republic of Iraq
Ministry of Higher Education
And Scientific Research
University of Anbar
College of Engineering
Mechanical Engineering Department

Investigation of Heat Transfer and Flow Characteristics of Jet Impingement on a Heated Surface with Ribs

A Thesis
Submitted to the Council of the College of Engineering - University of Anbar in Partial Fulfillment for the Requirements of the Master Degree of Science in Mechanical Engineering

By

Saad Mutlag Hatem
(B.Sc. in Mechanical Engineering - 2017)

Supervised by

Asst. Prof. Dr. Mohammed Abed Ahmed

1442 **2021**

SUPERVISOR'S CERTIFICATION

I certify that this thesis entitled "***Investigation of Heat Transfer and Flow Characteristics of Jet Impingement on a Heated Surface with Ribs"*** was prepared by "Saad Mutlag Hatem" under my supervision in the Mechanical Engineering Department / College of Engineering / University of Anbar as a partial fulfillment of the requirements for degree of Master in Mechanical Engineering.

Signature
Name: Asst. Prof. Dr. Mohammed Abed Ahmed
Date: / / 2021

In view of the available recommendation, I forward this thesis for debate by the examining committee.

Signature
Name: Asst. Prof. Dr. Mazin Yaseen Abbood
Head of Mechanical Engineering Department
Date: / / 2021

LINGUIST CERTIFICATION

This is to certify that I have read the thesis titled "***Investigation of Heat Transfer and Flow Characteristics of Jet Impingement on a Heated Surface with Ribs***" and corrected any grammatical mistake I found. The thesis is therefore qualified for debate as far as language is concerned.

Signature

Name: Dr. Ghalib R. Ibrahim

Date: / / 2021

EXAMINATION COMMITTEE CERTIFICATION

We certify that we have read the thesis titled "***Investigation of Heat Transfer and Flow Characteristics of Jet Impingement on a Heated Surface with Ribs***" and as examining committee examined the student "***Saad Mutlag Hatem***" in relation to all aspects of this thesis. In our opinion, it meets the standards of a thesis for the degree of Master (M.Sc.) in Mechanical Engineering.

Signature:
Prof. Dr. Qasim Saleh Mahdi
Date: / / 2021
(Chairman)

Signature:
Asst. Prof. Dr. Hamdi E. Ahmed
Date: / / 2021
(Member)

Signature:
Dr. Ahmed Ali Najeeb
Date: / / 2021
(Member)

Signature:
Asst. Prof. Dr. Mohammed Abed Ahmed
Date: / / 2021
(Member and supervisor)

Approval of The College of Engineering

Signature
Asst. Prof. Dr. Mazin Yaseen Abbood
(Head of Mechanical Engineering Department)
Date: / / 2021

Signature
Asst. Prof. Dr. Ameer Abdulrahman Hilal
(Dean of Engineering College)
Date: / / 2021

DECLARATION

I hereby declare that this thesis, submitted to mechanical engineering department at University of Anbar as a requirement for master degree has not been submitted as an exercise for similar degree at any other universities. I also support this work that is qualified here is entirely my own except for excerpts and summaries whose sources are congruently cited in the references.

Saad Mutlag Hatem

2021

ACKNOWLEDGMENTS

Firstly, all praise and thank to ALLAH who gave me plentiful science and helped me to accomplish this work.

I would like to express my sincere thanks and great gratitude to my supervisor (***Asst. Prof. Dr. Mohammed Abed Ahmed***) for his useful knowledge, outstanding giving and continuous guidance and for his continuous effort, advice and guidance from the beginning of the research stage until the completion of this thesis, ALLAH rewarded him for me the best reward.

I extend the highest expressions of thanks and appreciation to my dear parents, who instilled in the love of knowledge from a young age, and gave me all the most precious and precious, and they had the merit after ALLAH for what I reached now, so I can only pray for them for long life and good work.

I am also pleased to extend my sincere thanks to all the teaching staff in the Mechanical Engineering Department, and to everyone who helped me, gave me a favor, or gave me advice, or had a small or large contribution to the completion of this work.

ABSTRACT

Jet impingement cooling is considered to be one of the better techniques of achieving an especially high heat transfer improvement and hence is employed in several engineering applications. Various ribs shapes mounted on the target surfaces can be used to achieve high thermal performance.

In the present investigation, the fluid flow, heat transfer, and entropy generation for the confined slot-jet impinging have been numerically and experimentally investigated. Three various shapes of the ribs, namely; wing, oval, and flat ribs, which installed on the impinging target plate are used. The effects of different parameters such as rib shape, heights of rib, the spacing between the stagnation point and the rib, jet Reynolds number on the heat transfer and flow fields have been presented and discussed. Validations of the numerical results with previous investigations available in the literature have been conducted and a good agreement between the results is noted. On the other hand, the numerical results have been compared with the experimental data, and good concords are achieved.

Results indicated that the average Nusselt number, pressure drop, and average total entropy generation increases when jet Reynolds number increases, rib height increases, and the spacing between the stagnation point and the rib location decreases. While the performance evaluation criteria increased with increasing rib height. It was found that the peak values of the average Nusselt number enhancement around 90.01, 74.16, and 65.34% for the wing, oval and flat ribs at rib height of 2 mm, rib location 10 mm and jet Reynolds number of 4000, 4000, and 3000, respectively. While the best performance evaluation criteria up to 1.682 which provided by the wing ribs at the rib location of 10 mm, rib height of 2 mm, and jet Reynolds number of 3000.

LIST OF CONTENTS

ACKNOWLEDGMENTS ..... **i**

ABSTRACT ..... **ii**

LIST OF CONTENTS ..... **iii**

LIST OF TABLES ..... **vi**

LIST OF FIGURES ..... **vii**

NOMENCLATURES ..... **xii**

1 CHAPTER ONE: INTRODUCTION **1**

1.1 Background 1

1.1.1 Impinging Jet 3

1.1.2 Impinging jet regions 4

1.2 Problem Statement 6

1.3 Objectives of the Study 7

1.4 Thesis Outlines 7

2 CHAPTER TWO: LITERATURE REVIEW **9**

2.1 Overview 9

2.2 Effect of Jet Impingement on the Convection Heat Transfer 9

2.3 Effect of Jet Impinging and Ribs on Convection Heat Transfer 19

2.4 Effect of Jet Impingement on the Entropy Generation 27

2.5 Summary 28

2.6 Scope of investigation 28

3 CHAPTER THREE: NUMERICAL SOLUTION **29**

3.1 Overview 29

3.2 Problem Description and Assumptions 29

3.3 Governing Equations 32

3.4 Transport Equations of Turbulence Model 33

3.5 Body Fitted Coordinates System 35
3.6 Computational Grid 35
3.7 Transformation of the Governing Equations in the Body-Fitted Coordinates Systems 37
3.8 Discretization of Governing Equations 40
3.9 SIMPLE Algorithms 43
3.10 Convergence Criteria 45
3.11 Entropy Generation 47
3.12 Thermo-physical Properties of Working Fluid 49
3.13 Boundary Conditions 50
3.14 Numerical Calculations 52
3.14.1 Local and Average Nusselt Numbers 52
3.14.2 Thermal-Hydraulic Performance Factor 53

4 CHAPTER FOUR: EXPERIMENTAL SET-UP 54

4.1 Overview 54
4.2 Experimental Set-up 54
4.2.1 Test Sections 56
4.2.2 Inlet Slot and Exit Sections 58
4.2.3 Thermocouples 59
4.2.4 Electrical Heater and Power Regulator 61
4.2.5 Water Pump, PPR Pipes, and Water Tank 62
4.2.6 Heat Exchanger 63
4.3 Measurement Devices 63
4.3.1 Flowmeter and Flow Sensor 63
4.3.2 Manometer and Pressure Sensor 64
4.3.3 Data Logger 64
4.3.4 Thermostat 64
4.3.5 Multimeter 64
4.4 Experimental Procedure 65
4.5 Data Reduction 66
4.6 Uncertainty Analysis 68

5 CHAPTER FIVE: RESULTS AND DISCUSSION 69

5.1 Overview 69

5.2 Grid Independence Test 69

5.3 Code Validation 71

5.4 Comparison Between Numerical and Experimental Results 75

5.5 Numerical Results 79

5.5.1 Effect of Jet Reynolds Number 79

5.5.2 Effect of Ribs Heights 86

5.5.3 Effect of Ribs Locations 100

5.5.4 Effect of Ribs Shapes 111

6 CHAPTER SIX: CONCLUSIONS AND RECOMMENDATIONS 118

6.1 Conclusions 118

6.2 Suggestions for Future Work 120

REFERENCES 121

APPENDIX A: NUMERICAL SOLUTION 131

APPENDIX B: EXPERIMENTAL SET-UP 157

APPENDIX C: CALCULATION OF MEASUREMENTS UNCERTAINTY 163

LIST OF TABLES

Table 3.1: The parameters of general transport equation (Equation 3.39) 41
Table 3.2: Thermo-physical Properties of water at 25 ºC..... 49

LIST OF FIGURES

Figure 1.1: Application of jet impingement in the cooling of electronic components [5]. 2
Figure 1.2: Types of impinging jet (a) Free impinging jet, (b) Submerged impinging jet [6]. 3
Figure 1.3: (a) Unconfined impinging jet, (b) Confined impinging jet. ... 4
Figure 1.4: Schematic diagram of impinging jet regions [8]. 5
Figure 3.1: Physical domain of the current study: (a) Wing ribs, (b) Flat ribs, (c) Oval ribs, (d) Smooth impinging target surface, (e) Dimensions of ribs..... 31
Figure 3.2: Transformation from Physical domain (left) to computational domain (right)..... 35
Figure 3.3: Computational grid of the current study: (a) Wing ribs, (b) Flat ribs, (c) Oval ribs, (d) Smooth impinging target surface. 37
Figure 3.4: Contra-variant velocities components. 39
Figure 3.5: Control volume employed for the discretization of the governing equations. 41
Figure 3.6: Solution procedure for CFD program in the present study. . 46
Figure 3.7: The boundary conditions of the present study. 52
Figure 4.1: photograph of the experimental set-up. 55
Figure 4.2: Schematic diagram of the experimental set-up. 56
Figure 4.3: Different shapes of ribs for test section, (a) wing ribs (b) flat ribs, (c) oval ribs, and (d) smooth target surface. 57
Figure 4.4: Front view of test section after installation. 58
Figure 4.5: Front and top views for test section that connected with exit sections. 59
Figure 4.6: Bottom view for test section showing holes of thermocouples. 60

Figure 4.7: Calibration of thermocouple. 61
Figure 4.8: Installation of test section. 62
Figure 5.1: Average Nusselt number with jet Reynolds number for various mesh sizes at a=2 mm and d=20 mm. 70
Figure 5.2: Friction factor with jet Reynolds number for various mesh sizes at a=2 mm and d=20 mm. 70
Figure 5.3: The comparison of the average Nusselt number for present study with numerical investigation of Manca et al. [15]. 71
Figure 5.4: The comparison of the local Nusselt number for present study with the numerical investigation of Sharif and Banerjee [20]. 72
Figure 5.5: The comparison of the friction factor for present study with the numerical investigation of Buonomo et al. [23]. 73
Figure 5.6: The comparison of the average Nusselt number for present study with the numerical investigation of Buonomo et al. [23]. 73
Figure 5.7: The comparison of the average total entropy generation for present study with the numerical investigation of Rashidi et al. [57]. ... 74
Figure 5.8: The comparison of the local Nusselt number for present study with the numerical investigation of Cadek [67], and Gardon and Akfirat [68]. 75
Figure 5.9: Average Nusselt number versus jet Reynolds number for various shapes of ribs at a=2 mm and d=10 mm. 76
Figure 5.10: Pressure drop versus jet Reynolds number for various shapes of ribs at a=2 mm and d=10 mm. 77
Figure 5.11: Average Nusselt number enhancement vs. jet Reynolds number for various shapes of ribs at a=2 mm and d=10 mm. 78
Figure 5.12: Performance evaluation criteria versus jet Reynolds number for various shapes of ribs at a=2 mm and d=10 mm. 79

Figure 5.13: Streamwise velocity contours for various jet Reynolds number at a=2 mm and d=10 mm for (a) Wing rib, (b) Oval rib, (c) Flat rib. 82
Figure 5.14: Velocity vector for various jet Reynolds number at a=2 mm and d=10 mm for (a) Wing rib, (b) Oval rib, (c) Flat rib. 83
Figure 5.15: Temperature contours for various jet Reynolds number at a=2 mm and d=10 mm for (a) Wing rib, (b) Oval rib, (c) Flat rib. 84
Figure 5.16: Total entropy generation contours for various jet Reynolds number at a=2 mm and d=10 mm for (a) Wing rib, (b) Oval rib, (c) Flat rib. 85
Figure 5.17: Streamwise velocity contours for various rib height at jet Re=5000 and d=10 mm for (a) Wing rib, (b) Oval rib, (c) Flat rib. 87
Figure 5.18: Temperature contours for various rib height at jet Re=5000 and d=10 mm for (a) Wing rib, (b) Oval rib, (c) Flat rib. 90
Figure 5.19: Total entropy generation contours for various rib heights at jet Re=5000 and d=10 mm for (a) Wing rib, (b) Oval rib, (c) Flat rib. .. 91
Figure 5.20: Local Nusselt number along the impinging target surface for various rib heights at jet Re=5000 and d=10 mm for (a) Wing rib, (b) Oval rib, (c) Flat rib. 92
Figure 5.21: Average Nusselt number vs. jet Reynolds number for various rib heights at d=10 mm for (a) Wing rib, (b) Oval rib, (c) Flat rib. 93
Figure 5.22: Pressure drop versus jet Reynolds number for various rib heights at d=10 mm for (a) Wing rib, (b) Oval rib, (c) Flat rib. 95
Figure 5.23: Average total entropy generation versus jet Reynolds number for various rib heights at d=10 mm for (a) Wing rib, (b) Oval rib, (c) Flat rib. 96
Figure 5.24: Average Nusselt number enhancement with jet Reynolds number for various rib heights at d=10 mm for (a) Wing rib, (b) Oval rib, (c) Flat rib. 97

Figure 5.25: Performance evaluation criteria versus jet Reynolds number for various rib heights at d=10 mm for (a) Wing rib, (b) Oval rib, (c) Flat rib. 99
Figure 5.26: Velocity contours for various rib locations at jet Re=7000 and a=2 mm for (a) Wing rib, (b) Oval rib, (c) Flat rib, (d) smooth surface. 101
Figure 5.27: Temperature contours for various rib locations at jet Re=7000 and a=2 mm for (a) Wing rib, (b) Oval rib, (c) Flat rib, (d) smooth target. 102
Figure 5.28: Total entropy generation contours for various rib locations at jet Re=7000 and a=2 mm for (a) Wing rib, (b) Oval rib, (c) Flat rib, (d) smooth target. 104
Figure 5.29: Average Nusselt number with jet Reynolds number for various rib locations at a=2 mm for (a) Wing rib, (b) Oval rib, (c) Flat rib. 105
Figure 5.30: Pressure drop with jet Reynolds number for various rib locations at a=2 mm for (a) Wing rib, (b) Oval rib, (c) Flat rib. 108
Figure 5.31: Average total entropy generation versus jet Reynolds number for various rib locations at a=2 mm for (a) Wing rib, (b) Oval rib, (c) Flat rib. 109
Figure 5.32: Performance evaluation criteria versus jet Reynolds number for various rib locations at a=2 mm for (a) Wing rib, (b) Oval rib, (c) Flat rib. 110
Figure 5.33: Average Nusselt number versus jet Reynolds number for various rib shapes at d=10 mm for (a) a=0.5 mm, (b) a=1 mm, (c) a=1.5 mm, (d) a=2 mm..... 112
Figure 5.34: Pressure drop versus jet Reynolds number for various rib shapes at d=10 mm for (a) a=0.5 mm, (b) a=1 mm, (c) a=1.5 mm, (d) a=2 mm..... 113

Figure 5.35: Average total entropy generation with jet Reynolds number for various rib shapes at d=10 mm for (a) a=0.5 mm, (b) a=1 mm, (c) a=1.5 mm, (d) a=2 mm..... 114
Figure 5.36: Average Nusselt number enhancement with jet Reynolds number for various rib shapes at d=10 mm for (a) a=0.5 mm, (b) a=1 mm, (c) a=1.5 mm, (d) a=2 mm. 116
Figure 5.37: Performance evaluation criteria versus jet Reynolds number for various rib shapes at d=10 mm for (a) a=0.5 mm, (b) a=1 mm, (c) a=1.5 mm, (d) a=2 mm..... 117

NOMENCLATURES

Symbol	*Description*	*Units*
a	Rib height	mm
A_S	Surface area	mm^2
A_C	Cross-section area	mm^2
a_1, a_2	Constants in Eqs. A.25 & A.26	----
$A_P, A_E, A_W,$ A_N, A_S	Coefficients in Eq. 3.40	----
b	Rib length	mm
B	Coefficient in Eq. A.130	----
b_ϕ	Non-pressure term in equation 3.39	----
b_p^ϕ	Pressure term in Eq. 3.39	----
B_E, B_W, B_N, B_S $B_{NE}, B_{NW}, B_{SE}, B_{SW}$	Coefficients in Eq. A.76	----
B_P^u, B_P^v	Coefficients in Eqs. 3.48 & 3.49	----
C	Coefficient in Eq. A.131	----
C_μ, C_1, C_2	Empirical constants in Eq. 3.15	----
C_p	Specific heat	(J/*kg. K*)
C_P^u, C_P^v	Coefficients in Eqs. 3.48 & 3.49	----
d	Rib location	mm
D_h	Hydraulic diameter, $D_h = W$	mm
D_E, D_W, D_N, D_S	Diffusion conductance	----
f	Friction factor	----
f_e^+	Linear interpolation factor	----
f_μ, f_1, f_2	Turbulence model functions	----
F_e, F_w, F_n, F_s	Mass flow rates a cross cell faces	----
$G_{u11}, G_{u12}, G_{u22}$ $G_{v11}, G_{v12}, G_{v22}$	Terms in Eq. A.109	----
h	Convection heat transfer coefficient	$W.m^2.K^{-1}$
H	Channel height	mm
I	Current	A
k	Turbulent kinetic energy	$m.s^{-2}$
k_f	Thermal conductivity of fluid	$W.m^{-1}.K^{-1}$

L	Length of impingement target surface	mm
$\dot{m}$	Mass flow rate	$kg.s^{-1}$
Nu	Nusselt number	----
p	Pressure	Pa
P_k	Production rate of turbulent kinetic energy	----
$P(\xi,\eta)$, $Q(\xi,\eta)$	Control functions in Poisson equation	----
$P(\xi)$, $q(\xi)$, $r(\xi)$, $s(\xi)$	Control functions at the boundaries	----
Pr	Prandtl number, $Pr = \nu/\alpha$	----
Pr_t	Turbulent Prandtl number	----
Q_f	Heat received by the fluid	W
Q_{heater}	Heat subjected to the electrical heater	W
Q_{loss}	Heat loss	W
q_{11} , q_{12} , q_{22}	Geometry factors	----
R_ϕ	Relative convergence criteria presented in Eq. 3.58	----
Re	Reynolds number	----
Re_T	Turbulent Reynolds number	----
S_m	Mass imbalance over control volume	----
S_d^ϕ	Source term defined in Eq. A.63	----
S_ϕ^r	Source term defined in Eq. 3.56	----
$\dot{S}'''_{gen,th.}$	Entropy generation rare due to thermal	$W.m^{-3}.K^{-1}$
$\dot{S}'''_{gen,vi.}$	Entropy generation rate due to viscous	$W.m^{-3}.K^{-1}$
T	temperature	K
u , v	Velocity components	$m.s^{-1}$
V	Voltage	V
W	Width of slot jet	mm
x , y	2-D Cartesian coordinates	mm
x_ξ , x_η , y_ξ , y_η	Geometry factors	----
Z	Channel depth	mm

Greek symbols		
ξ , η	Body-fitted coordinates system	----
α	Thermal diffusivity	$m^2.s^{-1}$
α_ϕ , α_P	Under-relaxation factors	----
$\beta_{11}, \beta_{12}, \beta_{21}, \beta_{12}$	Transforming coefficients	----
σ_k , σ_ε	Empirical constants of turbulence model	----
ϕ	General variable	----
ϕ_ε	Function used in the ε transport equation	----
ε	Dissipation rate of turbulent kinetic energy	$m^2.s^{-3}$
ε_w	Dissipation rate at the wall	$m^2.s^{-3}$
υ	Kinematic viscosity	$m^2.s^{-1}$
μ	Dynamic viscosity	$N.s.m^{-2}$
μ_t	Turbulent dynamic viscosity	$N.s.m^{-2}$
ρ	Density	$kg\ m^{-3}$
Γ	Diffusion coefficient	----
Δp	Pressure drop	Pa
$\Delta\xi$, $\Delta\eta$	Distance between two adjacent interfaces in ξ and η directions	----
Subscripts		
b	Bulk fluid	
eff	Effective	
e, w, n, s ne, nw, se, sw	Face values of the control volume	
P, E, W, N, S NE, NW, SE, SW	Node values of the control volume	
f	Fluid	
in	Inlet	
av	Average value	
o	Outlet	
r	Rib	
s	Smooth target surface	
th	Thermal	
vi	Viscous	
w	Wall	

x	Local value
enh	Enhancement
Superscripts	
C	Contra-variant velocity
*	Guessed values
′	Correction values
·	Rate
Abbreviations	
CFD	Computational Fluid Dynamic
FS	Full scale
FVM	Finite Volume Method
SIMPLE	Semi-Implicit Method for Pressure-Linked Equations
TDMA	Tri-Diagonal Matrix Algorithm
PEC	Performance Evaluation Criteria

CHAPTER ONE
INTRODUCTION

1.1 Background

Jet impingement is widely utilized to cool or heat solid surfaces. Generally, the heat transfer by jets impinging is better than that obtained with conventional convective transport methods. The technique of jet impinging cooling has higher rates of heat transfer compared with the technique of horizontal flow cooling. Therefore, certain practical impinging jet applications occur in industries where the requirements of the heat transfer have exceeded the ordinary capacity cooling and heating techniques. The range of applications of industrial jet impinging include cooling of electronic components, cooling of gas turbine blades, the cooling of the outer of combustors wall, drying of textiles and paper, annealing of metals as well as the tempering of glass [1, 2], as shown Figure 1.1. In various applications, the concept of heat transfer improvement has attracted significant attention by investigators in order to provide the increasing need for greater efficiencies in these applications. The improvement of heat transfer in jet impingement can be carried out utilizing different methods, which are categorized into three categories [3, 4]: active, passive, and compound methods. The active method includes external power input to improve heat transfer such as electrodynamics, spray, mechanical aids, and fluid and surface vibrations. Due to the costs, and the concerns connected with acoustic noise or vibration, this method has attracted little financial interest. While the passive heat transfer improvement methods do not need the external power

source such as using; extended surfaces, Inserts (for example; ribs, plates, and baffles), surface modification, additives used, and treated surfaces. This method often consists of growing the area of the transfer surface. When two or more of these methods are utilized simultaneously to improve heat transfer, this term is known compound method. In general, due to the acoustic of vibration and noise in the active methods, researchers choose the passive methods for enhancement in heat transfer.

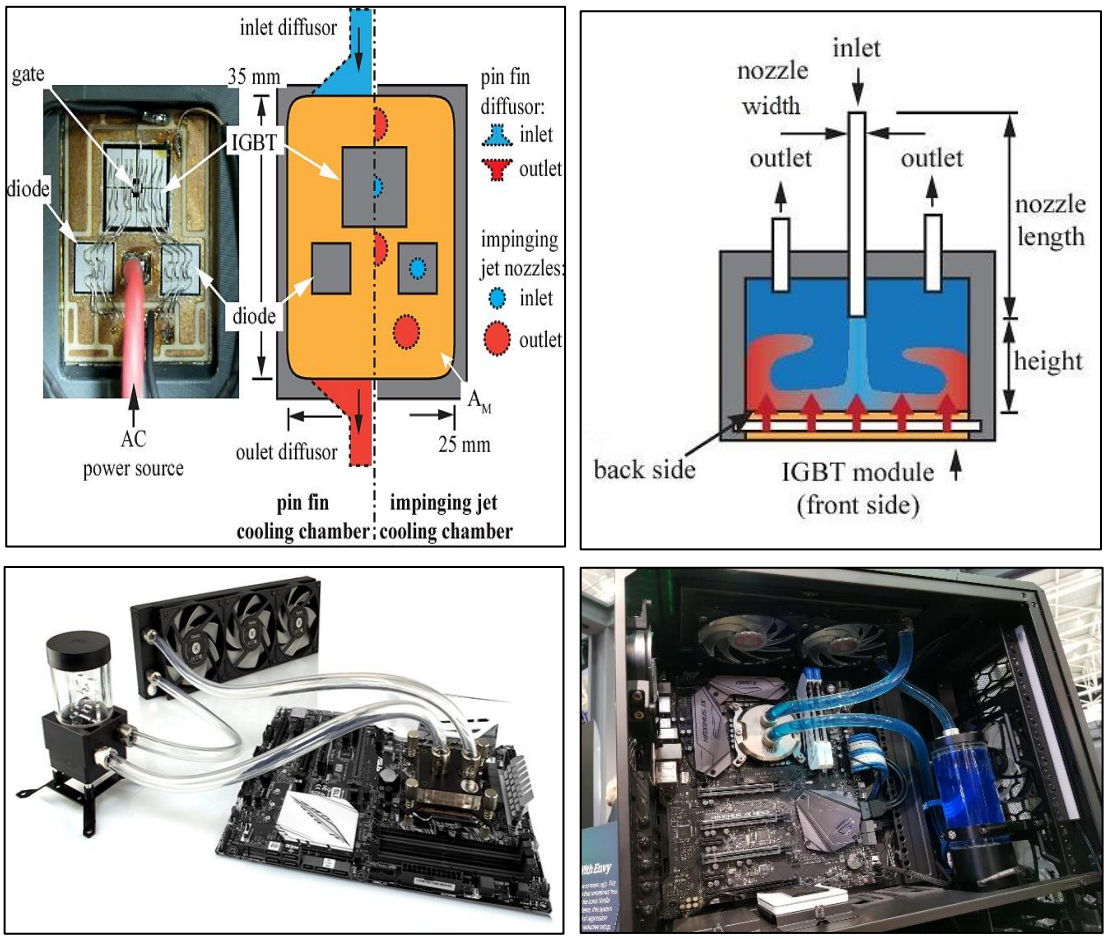

Figure 1.1: Application of jet impingement in the cooling of electronic components [5].

1.1.1 Impinging Jet

The impinging jet can be categorized into two types: free jet impinging and submerged jet impinging [6]. In the first case, the fluid released by the jet impinging has a various density and nature than of surrounding fluid. While the other case, the fluid released by the jet impinging is the same density and nature of the surrounding fluid. In the free jet case, this type of unstable is usually not significant and turbulent movement in the shear layer is not being an essential influence on the flow. In the submerged jet case, the shear layer is formed at the interface between the surrounding fluid and the jet impinging fluid. This layer is unsteady and generates turbulence. Figure 1.2 displays these two cases.

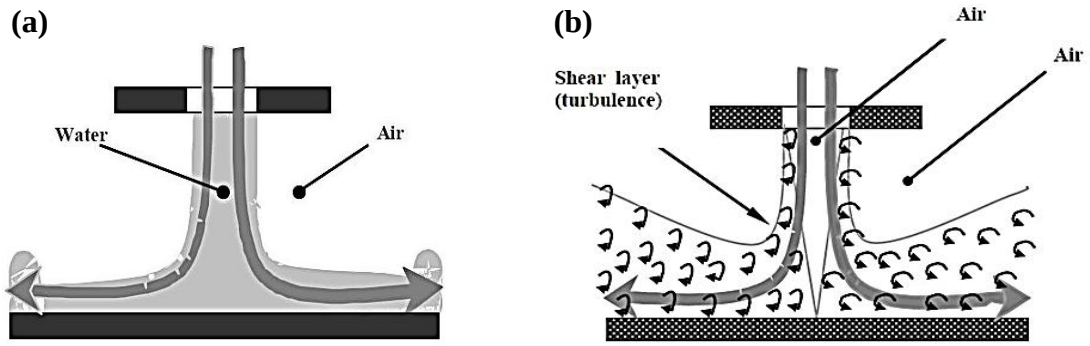

Figure 1.2: Types of impinging jet (a) Free impinging jet, (b) Submerged impinging jet [6].

Moreover, there is a distinction between the types of impinging jets such as unconfined and confined impinging jets. In the unconfined impinging jet, there is no upper surface or confinement, so after it impinges on an impinging target plate, the impinging jet flow is free to expand. The air atmosphere has a significant influence. In the case of a confined impinging jet, the fluid stays surrounded between two surfaces (orifice surface and target surface) during its flow. The air atmosphere has a very low influence. In this case, in order to influence the re-circulation zone, flow configuration, and improve heat transfer, the target plate is appropriately

close to the jet flow [7]. Thus, it is vastly employed in the cooling of electronic components. Figure 1.3 illustrates the different between the unconfined and confined impinging jets.

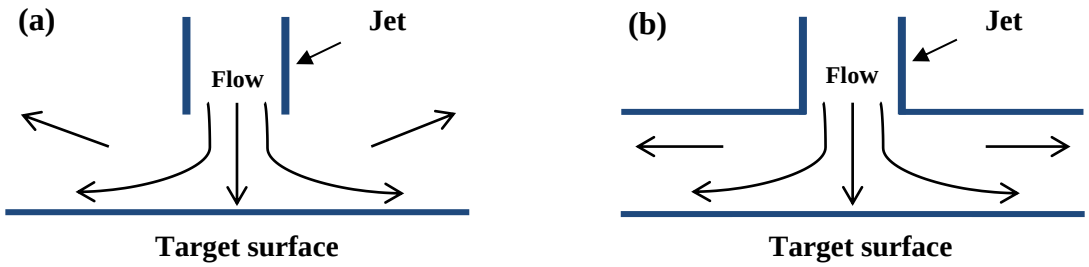

Figure 1.3: (a) Unconfined impinging jet, (b) Confined impinging jet.

1.1.2 Impinging jet regions

When the fluid jet has been impinged on the target surface, three major regions are specified according to previous investigations [2, 6 and 8]. These zones are known as wall jet zone, stagnation zone (impingement zone), and free jet zone which can be described as below (as shown in Figure 1.4):

- ❖ The wall jet zone: due to the viscous influences in this zone, the fluid flow velocity near the wall jet is low.
- ❖ The stagnation zone: the ambient fluid impinges upon the target surface in this zone, and develops a sudden change of direction. The local stagnation point is generated when the flow strokes on the target surface.
- ❖ Free jet zone: There is no significant influence of the wall in this zone on the flow field.

Generally, the free jet zone can be divided into three regions:

- ❖ The potential core region: the velocity stays fixed and equal to the velocity of jet exit. The potential core length depends on the intensity of turbulence in the jet exit and the profile of initial velocity.
- ❖ The developing region: this region is characterized by the degeneration of the profile of axial velocity due to significant shear stresses at the boundary of the jet. These significant shear stresses enhance additional fluid entrainment and generate turbulence.
- ❖ The fully developed region: The velocity profile is fully developed after the developing region; the jet expands linearly in the fully developed region and the axial velocity decay is also linear.

In addition, the flow experiences a sudden change of direction and slows after the impinging between the target surface and flow in the wall jet zone.

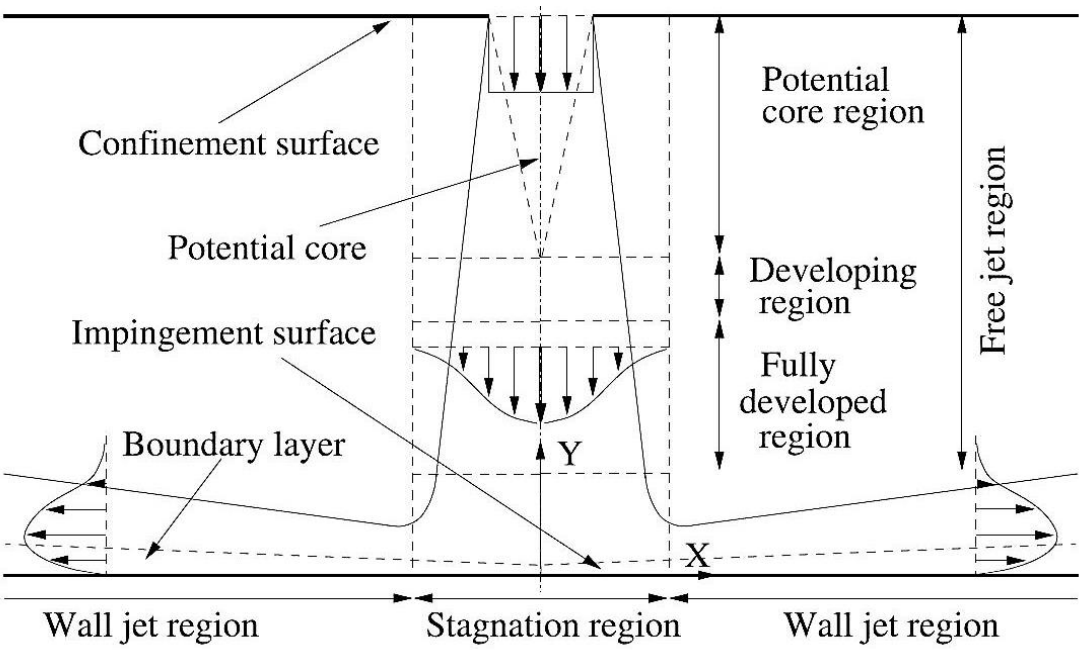

Figure 1.4: Schematic diagram of impinging jet regions [8].

1.2 Problem Statement

Due to the miniaturization of the electronics components or devices along with the faster operational speed, the enhancement of thermal performance of such components or devices became very important to meet all the practical applications. In addition, the electronic devices should be operated in the ranges of a specific temperature. The exceeding allowable temperature, the devices will be under serious problem. Therefore, in order to keep the operating temperature constant, the cooling system must dissipate the generated heat. Generally, the temperature of fluid near the wall (impinging target surface) is always higher than the fluid temperature in the core region of the channel. Using combined techniques of heat transfer enhancement such as ribs and jet impingement can be enhancing the heat transfer significantly. Furthermore, the rate of heat transfer enhances if the cold fluid at the core region is mixed with the hot fluid near the wall. The use of various shapes of ribs on the impinging target surface can enhance the mixing of fluids, leading to improve the rates of heat transfer. It is hypothesized that by using impinging jets on the heated impinging target surfaces with ribs, the mixing of fluid in channels can be enhanced and, hence, improve the performance of the electronic components.

Moreover, the current investigation attempts to answer the following questions:

- ✓ What is the effect of the jet impingement alone?
- ✓ What is the effect of the jet impingement and ribs together?

1.3 Objectives of the Study

The study objectives can be formulated as:

1) To study the effect of different shapes of ribs such as (Wing ribs, Flat ribs, and Oval ribs) as well as smooth target surface (without ribs) on the heat transfer, pressure drop, and entropy generation.
2) To investigate the effect of the rib locations on the heat transfer and flow characteristics.
3) To study the effect of the rib heights on the flow and thermal fields.

1.4 Thesis Outlines

This dissertation consists of six chapters, and it is briefly offered as follows:

- **Chapter One:** Presents the background, types, and zones of an impinging jet, problem statement, and the objectives of the present investigation. As well as the outlines of this dissertation have been introduced in this chapter.
- **Chapter Two:** Explains the literature review of experimental and numerical studies for the conventional fluid by using jet impingement on the smooth target surface, various shapes of the target surface and entropy generation.
- **Chapter Three:** Deals with the numerical solution employed in the present investigation. The problem description and assumptions, the governing equations of the turbulent flow in Cartesian coordinates, (k-ε) turbulence model, the computational grid, the governing equations transformation from Cartesian coordinates into body-fitted coordinates, and entropy generation equations are described. Finally,

the thermo-physical properties for the working fluid (water) used in this investigation will be presented.

- **Chapter Four:** The experimental setup is presented in this chapter, followed by the operational procedure. As well as the description of the test sections and experimental apparatus used in the present investigation. Therefore, the procedure of data reduction is introduced. This is followed by uncertainties calculation in the experimental measurement.
- **Chapter Five:** Presents the results of the numerical and experimental obtained in the present investigation. The first section of this chapter focuses on the grid independence test of the current CFD code and the code validation. Then the comparison between the experimental data and the numerical results are presented. Furthermore, the effects of various parameters such as jet Reynolds number, the heights and locations of the ribs, and various ribs shapes on the heat transfer and flow characteristics as well as entropy generation are introduced in this chapter.
- **Chapter Six:** Summarizes the main conclusions are obtained from the current investigation. Then some recommendations are proposed for future works.

CHAPTER TWO
LITERATURE REVIEW

2.1 Overview

This chapter shows some reviews of previous studies that concern with the flow field and heat transfer characteristics of impinging jet on the target surface. The first section introduces the effect of jet impingement on the heat transfer. The second section presents the effect of jet impingement and ribs on the convection heat transfer. The third section displays the effect of jet impingement on the entropy generation.

2.2 Effect of Jet Impingement on the Convection Heat Transfer

Park et al. [9] carried out a numerical investigation on fluid flow and heat transfer characteristics of air slot jet impingement. The (k-ω) turbulence model was adopted. The two-dimensional governing equations have been solved using the finite element method based on SIMPLE and upwind techniques. The effects of various parameters such as the jet Reynolds number range of (220 – 25,100) and the jet-to-target plate spacing range of (0.5 - 4) on the skin friction coefficient of laminar and turbulent systems and the flow field. They observed that the maximum skin friction coefficient occurred nearby the stagnation zone. It was also found that the highest heat transfer rate was at the stagnation point whereas decreases gradually toward downstream. The highest local heat transfer coefficient occurred at the maximum Reynolds number and the jet-to-target plate spacing of 0.5.

Nirmalkumar et al. [10] presented an experimental study to investigate of local heat transfer distribution by the normal slot air jet impingement on a smooth surface. The data showed that the target surface was manufactured from stainless steel foil with (length of 202 mm, a width of 91 mm, and a thickness of 0.06 mm). They studied the effects of the jet-to- target surface distances of (0.5-12) and the jet Reynolds number ranged from 4200 to 12,000 on a heat transfer distribution. They observed that the heat transfer coefficient increased with increasing Reynolds number and decreasing jet-to-plate spacing. Furthermore, they found the highest Nusselt number happened at the distance of the jet to the target surface of 0.5 and maximum Reynolds number of 12,000.

Caggese et al. [11] have conducted an experimental and numerical study to investigate the heat transfer and flow characteristics of the fully confined impinging air jet. The momentum, energy, and pressure terms were solved by applying the second-order upwind scheme. The local heat transfer coefficient distributions were provided a bottom wall (smooth target surface) and the top wall (jet surface). The effects of jet Reynolds numbers range of (16,500 - 41,800) and the jet-to-plate distances (0.5-1.5) jet diameters. They noted that the average Nusselt number of an impinging plate increases as the nozzle Reynolds number increases. Low dependence on the level of the local and average heat transfer with the jet-to-plate distances was observed for the smooth target surface, although the results for jet-to-plate distance of 1 appeared to provide the best performance of heat transfer. Therefore, the heat transfer rate of the impinging target surface was approximately 40% lower compared with the target surface which experiences impinging (stagnation) regions.

Culun et al. [12] investigated heat transfer characteristics of the air confined multi-jet arrangement impingement on the flat impinging plate.

The Shear-Stress Transport (SST) turbulence model was utilized. The jet impinging flows were included inline and staggered arrays and two types of jets were used circular jets and square jets. The impingement target surface under a constant heat flux of 9000 $^{W}/_{m^2}$. Different jet-to-plate spacing of (2, 3, and 4) jet hydraulic diameter and various Reynolds numbers of 5000, 10,000, and 15000. The outlet fluid domains consisted of three cases of one exit and (two and three) exits. Numerical results showed that an increasing jet Reynolds number, the Nusselt number increased. It was the highest heat transfer occurred by using square jets compared to circular jets for one exit case. Also, it was noticed that the enhancement of heat transfer was 73% when increasing Reynolds number from (5000 to 10,000).

Zhou et al. [13] conducted an experiment to improve the heat transfer and flow field using air jet impingement at narrow spacings. They used two types of jets which were sweeping and circular jets, and the length of the jet was 40 mm. The circular tube was 200 mm long, with outer and inner diameters of 13 mm and 10 mm, respectively. The influences of various coolant air nozzle Reynolds numbers varying of (Re = 5000, 10000, and 15,000) for both jets and nozzle-to-plate spacing of (0.5, 1.0, 2.0, and 3.0) nozzle diameters on the heat transfer. The results were presented that the Nusselt number increased with increasing nozzle Reynolds number and decreasing narrow spacings. The heat transfer improvement for a sweeping nozzle was better than a circular nozzle in the stagnation zones. Furthermore, it was reported that the maximum heat transfer performance up to 40% compared with a circular nozzle around the stagnation zone.

Fechter et al. [14] carried out a numerical and experimental study of heat transfer characteristics by employing the single-row of five impinging air jets cooling on a heated flat surface. The numerical part was used that the

Shear-Stress Transport (SST) turbulence model. In this investigation, the distribution of the jet was from inline and staggered pattern configurations. Various Reynolds numbers between (10,000 and 40,000) and jet-to-target spacing of 1 and 3 jet diameters. Results indicated that with the increasing Reynolds number, the average Nusselt number increase. Also, the discharge coefficient increased with increasing jet-to-surface spacing. It was reported for the inline pattern configuration, the maximum heat transfer rate occurred at jet-to-target spacing of 1 jet diameter. Also, it was found that the discharge coefficient was approximately 20% higher for jet-to-target spacing of 3 jet diameters over Reynolds number range.

Manca et al. [15] performed a numerical investigation to study the heat transfer performance using a confined slot jet impingement on the flat impinging surface. The (k-ε) turbulence model was employed. The two-dimensional governing equations of momentum, continuity, and energy were solved utilizing the finite volume method (FVM). The length of the flat impinging plate, slot jet width, and height (between the impinging plate and orifice jet) were 310 mm, 6.2 mm, and (24.8-124 mm), respectively. The jet-to-target surface spacing of (4-20), and jet Reynolds numbers range of (5000-20,000). They observed that the highest local Nusselt number was at a stagnation point while the lowest value at end of a target surface. The average Nusselt number increased with increasing jet Reynolds number. The maximum heat transfer enhancement was up to 18% at the jet-to-target surface distance of 10. The required pumping power was increased with jet Reynolds numbers.

Lv et al. [16] carried out an experimental study to enhance the heat transfer using a free single impinging jet on the cylinder surface The test area included the copper cylinder (diameter of 100 mm, and height of 50 mm).

The effects were at jet Reynolds number between 4000 and 12,000, the jet angles of (50º, 70º, and 90º), and the jet-to-surface spacing of (2-5) jet diameters on the heat transfer coefficient. The results indicated that the heat transfer coefficients increased with increasing the jet angle, jet Reynolds number, and before the jet-to-surface distance of 4. They observed the better heat transfer performance occurred at the impinging point. It was shown that the maximum heat transfer coefficient was 61.4% at jet-to-surface spacing of 4, the nozzle angle of 90º.

Chougule et al. [17] investigated the fluid flow and heat transfer characteristics of multiple impinging jets on the target smooth surface experimentally and numerically. The aluminum impinging flat surface with dimensions 60 mm of length, width of 60 mm, and thickness of 6 mm and all nozzles with diameter of 5 mm. The measurement indicated that the different of air jet Reynolds umbers of (Re = 7000 to 11,000), nozzle-to- target plate spacing (6, 8, and 10) nozzle diameter, and the constant heat flux of (8333 $^{w}/_{m^2}$) applied on the bottom smooth plate. At the surface spacing-to-jet diameter ratio of 6 and increase Reynolds number, the temperature of the flat surface became colder. It was observed that the minimum temperature occurred at the stagnation point. The average heat transfer coefficient increased with increasing nozzle Reynolds number at jet-to-target spacing of 6, where the percentage of average heat transfer coefficient was up to 24%. The higher heat transfer enhancement occurred at a lower target spacing-to-jet diameter ratio of 6 due to a reduction in the impinging surface area. The deviation between the numerical and experimental results was (±5%).

Afroz and Sharif [18] presented a numerical investigation to study heat transfer under two-dimensional oblique twin turbulent confined impinging slot-jet on an isothermal smooth target surface. They used two types of

numerical turbulence models; the Re-Normalization Group (k-ε) and Shear-Stress Transport (k-ω) turbulence models. The geometric parameters included the various air jet Reynolds numbers ranged between (23,000 and 50,000), jet-to-plate distance ratio of (2.6, 4, and 6), and jet impingement angle of (45º-90º). They reported that the Reynolds number and jet impingement angle played the major role for impinging the target surface on the heat transfer. With an increasing Reynolds number, the average Nusselt number increased. The average Nusselt number decreased about (25-50%) with decreasing jet impinging angle from (90º- 45º) for various jet Reynolds numbers.

A numerical and experimental study of the heat transfer on the circular heated cylinder surface using impinging circular air jet was performed by Singh et al. [19]. The model of three dimensional of axial and circumferential directions. The mass, momentum, and energy conservation equations were solved by using the Finite Volume Method to discretize governing equations. The length and overall diameter of the target circular cylinder were 600 mm and 50.5 mm, respectively. The cylinder surface was subjected to the fixed heat flux. Also, the circular pipe of the jet was made of aluminum and contained three different inner diameters of (6, 10.5, and 12.5 mm). The influence of air nozzle Reynolds numbers varied from 10,000 to 25,000, nozzle-to-target cylinder spacing of (4-16) nozzle diameters, and the ratio of jet diameter to target cylinder diameter ranged of (0.11-0.25) on the local Nusselt number. An increasing Reynolds number of the nozzle leads to the heat transfer rate increased. The stagnation point Nusselt number increased with decreasing the ratio of nozzle diameter to target cylinder diameter. At higher jet Reynolds number, as the ratio of jet diameter to the diameter of target cylinder decreased, the local Nusselt number was less than that of a higher ratio of

nozzle diameter to the diameter of the circular cylinder after some axial distance. Moreover, it was observed that the local Nusselt number was significant up to the axial direction of cylinder-to-cylinder diameter ratio of 1 and nozzle angle of 90º in axial and circumferential directions, respectively.

Sharif and Banerjee [20] studied numerically the flow and heat transfer characteristics on an isothermal flat plate due to confined impinging-air slot jet. The two-dimensional (k-ε) turbulence model was used. The width of slot-jet of 6.2 mm and the target impinging length of 100 mm. They showed that the different nozzle exit Reynolds numbers of (5000, 10,000, 15,000, and 20,000), nozzle-to-impinging surface spacing of (6 and 8), and dimensionless surface velocity (normalized plate velocity) varied from (0 - 2). The constant temperature of impingement plate of 338 K and the inlet temperature of the jet was 373 K. The results were, at the fixed location, the local Nusselt number increased with Reynolds number and at low normalized surface velocity for all jet to target spacing. It also noted at the fixed surface velocity, the average skin friction coefficient decreased while the average Nusselt number increased with increasing nozzle exit Reynolds number for all normalized nozzle to plate spacing.

Amjadian et al. [21] carried out an experimental investigation to study the heat transfer performance of unconfined circular jet impingement on the heated smooth circular surface (disk). The aluminum disk diameter was 300 mm and its thickness was 4 mm. The jet diameter size of 12 mm as well as a constant jet-to-disk surface spacing. The influence of various Reynolds numbers between 7330 and 11,082 on the characteristics of heat transfer and fluid flow. The smooth disk surface applied under the constant heat flux of (1414.71 $^{W}/_{m^2}$). The experimental results presented that the highest Nusselt number appeared at a stagnation region (surface center).

The cooling nozzle impinging system heat transfer efficiency increased approximately 45% at Reynolds number of 7330. The minimum temperature of the disk surface occurred at the stagnation zone, and increased thereafter with a radial location.

Huang et al. [22] have presented a numerical investigation on an isothermal smooth impinging surface to study the performance of the turbulence models heat transfer using a confined impinging slot-air nozzle. They used two types of turbulence models; the developed and standard Shear Stress Transport (k-ω) turbulences models. The nozzle Reynolds number of (11,000, 11,400, and 20,000), nozzle-to-target surface spacing of (2 to 9.2), and the nozzle width of (40 mm). The impinging surface was under a constant temperature of 310 K. The results obtained that the highest static pressure happened at the stagnation point. The velocity was increased away from a stagnation point and also, it was reported that the highest velocity at position-to-slot width ratio of 2 was higher than a position-to-slot width ratio of 1. For the higher value of nozzle-to-surface spacing, skin friction monotonously decreased after the first maximum value along a smooth impingement surface. The standard (k-ω) model provided higher values of skin friction at jet-to-surface spacing of 9.2. In addition, it was observed that the maximum Nusselt number value occurred at a stagnation point. For all jet-to-surface spacing, the developed Shear Stress Transport (k-ω) turbulence model performed better than standard Shear Stress Transport (k-ω) turbulence model.

Buonomo et al. [23] numerically investigated the convective heat transfer on the isothermal heated smooth target plate of a confined slot-jet impingement. The two-dimensional (k-ε) turbulence model. As well as the governing equations were solved utilizing the Finite Volume Method. The momentum and energy equations were chosen by using a second

order-upwind scheme. They presented that the length of the computational domain of 620 mm, slot jet width of 6.2 mm, and the distance between the upper surface and target surface, ranged from (24.8 to 120 mm). The inlet temperature of the jet was 293 K and the bottom plate of the target with a constant temperature of 343 K. They studied the jet Reynolds numbers range from (5000 to 20,000), nozzle-to-wall target spacing varied from (6-10), and the plate-jet velocity ratio (dimensionless surface velocity) between (0 and 2). Results showed that the average Nusselt number increased with increasing nozzle Reynolds number, and plate-jet velocity ratio. The local Nusselt number at the impingement point started from the highest value for the stationary surface at the value of quasi-uniform in a downstream zone for the velocity surface of 2. In addition, the enhancement of heat transfer was not depending significantly on the nozzle-to-target moving surface spacing. It noted that the average skin friction coefficient increased with increasing dimensionless surface velocity and decreased with increasing Reynolds number for all jet-to-target spacing. However, it found that both moving and stationary conditions, the maximum local Nusselt number increased about 20% for a heated plate.

Adimurthy and Katti [24] performed an experimental investigation of local distribution of heat transfer and wall static pressure of impinging air unconfined slot-single jet cooling on the smooth target surface. The impinging surface made of stainless-steel foil with thickness of (0.06 mm) and the dimensions of the slot-jet geometry were high of 4.5 mm, width of 4 mm, and length of 90 mm. The effects of the exit jet Reynolds number ranging from (2500 to 20,000) and jet-to-target surface spacing (jet-to-plate distance to hydraulic diameter of jet) on heat transfer distribution and fluid flow characteristics. The results of the experiments showed that the

coefficient of wall static pressure was independent of jet Reynolds number in a range from (5000-15,000) for all nozzle-to-surface spacing. At Reynolds number of 5000, the wall static pressure at a stagnation point decreased with an increase in the jet to plate spacing. Furthermore, the Nusselt number values were the maximum at a stagnation point for all Reynolds number and jet-to-target spacing. An increase in Reynolds number, the average Nusselt number increases. It was also observed that the average Nusselt number decreased gradually with further increases in nozzle-to-plate spacing. At jet-to-target spacing of 4 and any Reynolds number, the heat transfer rate was higher at the potential core zone end.

A numerical investigation of heat transfer using a confined axis-symmetric impinging circular jet on the heated surface was presented by Huang [25]. The Shear Stress Transport (k-ω) turbulence model was employed. The governing equations of continuity, momentum, and energy were solved utilizing the Finite Volume Method. Furthermore, the diameter of the jet orifice and the radius geometrical configuration of 2 mm and 16 mm, respectively. The various circular jet Reynolds numbers, and jet-to-plate spacing were presented. The results presented at various Reynolds numbers from 5000 to 30,000, nozzle-to-target surface spacing of (1-5) nozzle diameters, and constant heat flux of (500000 $^{W}/_{m^2}$). They found that the highest local Nusselt number occurred at the stagnation point zone and the average Nusselt number increased with increasing Reynolds number. It was also observed that the peak average Nusselt number was up to 15% at Reynolds number of 30,000, and jet-to-plate spacing of 2.

2.3 Effect of Jet Impinging and Ribs on Convection Heat Transfer

Xu et al. [26] carried out a numerical investigation of the behavior of heat transfer and flow under twin impingement air slot-jets on flat and rough plates. The governing equations were solved utilizing the Finite Volume Method. The Re-Normalization Group (k-ε) turbulence model was performed. The nozzle Reynolds number varied from (2000 to 14,000), nozzle-to-target spacing of (2-7), nozzle separation-to-slot width of (1-6), roughness amplitude of (0 - 40%), and roughness frequency of (100 to 400 HZ) as well as constant impinging target temperature of 300 K. Results illustrated that the local Nusselt number for twin-slot impinging jets on the rough plate was significantly higher compared with the flat plate. Also, they found that the Nusselt number can be improved with surface roughness increase in the wall jet region.

Attalla et al. [27] investigated an experimentally heat transfer on the rough impinging target plate employing an impinging air circular jet. The target plate by a micro-cubic pin size was (0.4 × 0.4 mm) with various depths of (0.1, 0.2, and 0.3 mm). They studied several parameters such as roughened degree (rough plate area to flat plate area ratio) varied between 1 (for flat plate case), 1.64, 2.28, and 2.91, jet to impinging plate spacing range of (1-9), and Reynolds number ranged from 3150 to 10,150. Results illustrated that the local Nusselt number for a rough impinging surface was enhanced ranging of (9.9 to 32.17%) compared to flat plate. This enhancement depended on Reynolds number, roughened degree, and jet-to-impinging plate. Moreover, it reported that the enhancement factor was enhanced by (8.9, 16, and 24%) for the roughened degrees of (1.64, 2.28, and 2.94), respectively.

Mondal and Singh [28] numerically investigated the influence of convex protrusion on target surface using a single air slot-jet impingement. The

numerical model simulation was carried out using Shear Stress Transport (k-ω) turbulence model. They conducted that the performance of heat transfer over heated surface and a staggered nine by nine hemispherical (protrusion) convex dimple array. They used that the Reynolds numbers between 2750 and 11,000, fixed jet-to-plate spacing of 4, ratio of dimple depth to dimple diameter of (0.2), and ratio of the width of slot to the diameter of dimple of (0.5). It was noticed that when increased jet Reynolds number increased the Nusselt number over the flat plate as well as on a dimple plate at constant nozzle-to-surface spacing. Moreover, negligible Reynolds number influence was seen on a back and front locations of protrusions. The results were indicated that the heat transfer rate up to 50% in the case of the dimple presence (protrusion surface) when compared with the smooth plate.

Sagot et al. [29] conducted an experimental investigation of heat transfer enhancement with the axis-symmetric grooves on a circular plate using air jet impingement. The impingement surface was an aluminum circular surface with thickness and radius of 3 mm and 24 mm, respectively. Two grooves were triangular or square cross-section with width, depth, and pitch of (1, 1, and 2 mm), respectively. The experimental results showed at a constant jet-to-target spacing of 2 jet diameters and Reynolds numbers between 15,000 and 30,000. They found that the average Nusselt number increased up to 80% for a square groove when compared with a smooth surface reference case. This heat transfer performance was attributed to secondary flows generated inside grooves. The vortex was more shedding and vigorous frequently in the case a square groove. This is due to a greater heat removal from a surface with compared to smooth and triangular cases.

The flow and heat transfer characteristics in an impinging multi-jet cooling system were evaluated numerically and experimentally by Wan et al. [30]. The Shear Stress Transport (k-ω) turbulence model was presented. Different types of the target plates were used: flat surface, and (inline and staggered) square-pin-fin roughened surfaces. The model dimensions were included that the impingement surface length of 300 mm, jet diameter of 10 mm, and the distance between jets to target plate of 30 mm. The cooling air Reynolds number ranged from 15,000 to 35,000. The results were obtained that when Reynolds number increased, all the average Nusselt numbers increased. It was observed that the overall rate of heat transfer on the inline-pin-fin surface leads to an increase up to 34.5% as compared with the flat surface. The performance of heat transfer on the inline-pin-fin surface was better than that a staggered-pin-fin surface.

Ahmadi et al. [31] conducted a numerical study of heat transfer and flow field characteristics on a circular concave surface using a turbulent confined-slot impinging jet. Using Control Volume Method, momentum, mass, and energy conservation equations have been discretized. The pressure and velocity coupling were developed employing the SIMPLE algorithm. The circular concave with a diameter of 150 mm, and a width of the inlet jet equal to 5 mm. The data were obtained at Reynolds number of (Re = 4740, 7100, and 9000), the nozzle-to-plate distances of (3-10, and constant heat flux on the concave surface of (5000 $^{W}/_{m^2}$). They found that the local and average Nusselt numbers, pumping power, and pressure drop increased with increasing Reynolds numbers. Also, the highest heat transfer occurred in an impinging zone. The maximum improvement of the heat transfer rate occurred at the nozzle-to-plate spacing of 5.

Beitelmal et al. [32] presented an experimental investigation of the surface roughness influences on the heated surface using a single impinging air circular jet to increase the average Nusselt number. Two different circular target plates were made of the aluminum with a thickness of 2.0 mm and a diameter of 70 mm, one of the plates with a smooth surface and the other plate with some roughness added to a target surface. The roughness shape was the circular array of the protrusions (dimples) of 1.8 mm spacing, 0.5 mm base, and 0.5 mm height. As well as the jet diameter of 6.85 mm. The jet exit Reynolds numbers ranged from 9600 to 38,500. The temperatures were measured at the nozzle-to-target surface distance between 1 to 10 jet diameters. Results indicated that the average Nusselt number for both surfaces increased with increasing Reynolds number. The surface roughness protrusions disrupted the thermal boundary layer causing an increase in the average Nusselt number up to 6.0% when compared to the smooth surface. The highest heat transfer enhancement was at the jet-to-plate spacing between (4 and 8) jet diameters. The maximum deviation between experimental values and correlations was less than 10%.

Öztekin et al. [33] studied an experimentally and numerically the heat transfer characteristics of a turbulent slot air jet impinging on the concave plates. The convection terms in a momentum equation were obtained by applying the second-order upwind scheme. Also, the pressure-velocity coupling was solved by using a SIMPLE algorithm in the numerical simulation. The impinging aluminum flat surface was the dimensions of length, width, and thickness of (90, 63, and 0.2 mm), respectively. As well as the radiuses of a concave plate of (45, 65.25, and 117 mm). They showed that the effects of jet Reynolds numbers (Re = 3423-9485), nozzle-to-impinging surface spacing (1-14), and the curvature radius ratio of (0.5, 0.725, and 1.3) on the average Nusselt number were studied. They

noted that the average Nusselt number increased with increasing Reynolds number, curvature radius, and decreasing jet-to-impinging surface spacing. The highest Nusselt number happened at jet-to-impinging plate spacing of 1 and the curvature radius ratio of 1.3.

Zhou et al. [34] conducted an experimental investigation on the concave surfaces to study the heat transfer characteristics using air circular jet impinging. The impingement aluminum surfaces were at a constant length of 150 mm, thickness of 2 mm, and different diameters of (100 and 200 mm). The steel pipe with 16 mm inner and 20 mm outer diameters. The jet also was located inside of the steel pipe with diameters of (1, 2, and 3 mm). The experimental results were indicated that the jet Reynolds numbers (Re = 27,000 to 130,000), nozzle-to-plate distances ranged from (3.3 and 30) jet diameters, and surface curvature ratio of (1-2.6). They reported that the average Nusselt number increased with increasing jet Reynolds number, surface curvature ratio, and decreasing nozzle-to-plate distance. Furthermore, they found that the better heat transfer performance was at the surface curvature ratio of 2.6.

Xing et al. [35] carried out a numerical and experimental investigation of heat transfer of multiple air flow jet impinging on the flat surface and the micro rib-roughened surface. The impingement target surface was made of Perspex and with length of 450 mm. The micro-rib roughened surface dimensions were height, width, and pitch ribs of (1, 1, and 5 mm), respectively. The effects of jet Reynolds number range of 15,000, 25,000, and 35,000, crossflow of (maximum, medium, and minimum) schemes, and jet-to-target surface spacing range of (3, 4, and 5) jet diameters on heat transfer and pressure loss. For both smooth surface and rib roughened surface, the highest heat transfer coefficient occurred at the jet-to-surface spacing of 3 jet diameter and for different crossflow schemes. In a

downstream part, the heat transfer performance was better than that of an upstream part. The maximum improvement of heat transfer of the rib roughened surface area was up to 40% compared to the flat plate at Reynolds number of 35,000, the distance of jet-to-plate of 3, and a maximum crossflow case.

Shukla et al. [36] presented a numerical study of the slot-jet impingement to investigate the influence of the ribbed-rough impinging surface on the characteristics of flow and heat transfer. The standard (k-ε) turbulence model and Shear Stress Transport (k-ω) turbulence model were introduced. The convective and diffusive terms of governing equations have been discretized employing the second-order upwind and second-order central difference schemes, respectively. The SIMPLE method was utilized for a pressure and velocity coupling. The jet-to-impinging surface spacing (4, 8, and 9.2) and jet Reynolds number ranging from (5500 to 20,000). The results showed that the highest values of Nusselt number occurred at the stagnation zone vicinity for jet-to-surface spacing of 8 and Reynolds number of 5500 on the ribbed surface. It was also observed that the local Nusselt number prediction was more with a ribbed surface compared to flat surface. In addition, it found that the prediction of Nusselt number from (k-ε) turbulence model was more accurate than (k-ω) turbulence model.

El-Gabry and Kaminski [37] conducted an experimental study to investigate the influence of the plate roughness on the heat transfer using air jet impinging arrays. The diameter of the jet was 1.27 mm, and the distance between jets was 6.35 mm. The angles of jet were ranged between (30º, 60º, and 90º) which measured an impinging target plate, which was either a flat plate or a randomly roughened plate. In this work, the measurements were presented that the Reynolds numbers varied from

(15,000 to 35,000), and the jet-to-target spacing of (1 and 2) jet diameters. The results showed that, when jet Reynolds number increased and jet angle increased, the average Nusselt number increases. As compared with a smooth plate, the average Nusselt numbers increased with the use of the roughness plate and produced the distribution of uniform heat transfer. In addition, the influences of the jets impinging angle of 90º (normal jets impinging) on both plates have the highest average Nusselt number occurred at jet-to-target spacing of 2 jet diameters compared to the other cases.

Zhang et al. [38] introduced an experimental and numerical study of heat transfer and flow characteristics of impinging a single jet on a dimpled target plate. They used that the dimpled target surface was the thickness of 15 mm and with a (660 × 660 mm) square surface and the protrusion diameter was as large as 44 mm. In this paper, the various effects of air nozzle Reynolds number of (5000, 10,000, and 23,000), protrusion relative depth of (0.1, 0.2, and 0.3), and constant distance of jet-to-target surface of 2 jet diameter on the local, stagnation, and average Nusselt numbers were studied. The local Nusselt number increased with increasing nozzle Reynolds number. Furthermore, when a wall nozzle passes into dimple (protrusion) edge zone, the local Nusselt number decreased with increasing protrusion relative depth. The stagnation Nusselt number increased with increasing jet Reynolds number The stagnation Nusselt number on dimpled target plat was large than of smooth target plate. The overall heat transfer improvement was obtained by the performance of heat transfer in the stagnation zone and an increase of dimple sphere area.

Lafmajani et al. [39] presented an experimental study of heat transfer characteristics on the convex heated surface using impinging jet. They

used that the aluminum convex surface with dimensions were; length of 130 mm, width of 40 mm, radius of 200 mm, and the slot jet with length of 40 mm and width of 1.6 mm. The results presented that the effect of various Reynolds numbers varying between 1803 and 2782 on the heat transfer coefficient. They reported that the local and average heat transfer coefficients increased with increasing Reynolds numbers. Also, they found that the maximum performance of the average heat transfer coefficient up to 32.78% happened at Reynolds number of 2037.

Tan et al. [40] studied enhancement of heat transfer on the rib-roughened plate for closed-one side of a semi-confined channel using air jet impinging. The impinging target was made from the copper plate with ribs of 60 mm length, with width of 35 mm, and thickness of 1.5 mm. The height and width of the ribs were all constant as 1 mm, and the rib-pitch was constant as 8 mm. Three types of rib configurations were included V-shaped ribs, inverted V-shaped ribs, and orthogonal ribs. They presented that the jet-to- surface spacing range of (1-3) jet diameters, different air jet Reynolds number from 6000 to 30000, and constant heat flux of (8000 $^{W}/_{m^2}$). The results showed that the convective heat transfer was stronger at the lower jet-to-surface spacing because of the higher flow velocity in the channel, and it was observed that the convective heat transfer performance up to 30% in a ribbed region when compared with a smooth channel. Also, the convective heat transfer enhancement by using inverted V-shaped rib appeared to be advantageous. They reported that the flow coefficient inside a smooth channel was higher than a rib-roughened channel. However, they found that the flow coefficient of a rib-roughened was decreased (5-10%) compared with the smooth channel.

The effects of the plate roughness on an impinging target plate using an impingement cooling jet array were presented experimentally by Buzzard et al. [41]. The plate roughness shape was the rectangle in a combination with the larger rectangular-pin. The small rectangle roughness combinations and large-pins were studied together with a small rectangular roughness array only. The experimental tests were presented with air cooling at nozzle Reynolds numbers of (900-11,000). It showed that the higher local Nusselt numbers occurred with a small rectangle roughness, as compared with the surfaces including a large combination and small rectangle roughness at the low jet Reynolds number. The surfaces with the small combination and large rectangle roughness, presented higher local Nusselt numbers than other surfaces at the high jet Reynolds number. Also, for the all-jet Reynolds number, an increase in the height of small roughness led to the higher value of local Nusselt numbers.

2.4 Effect of Jet Impingement on the Entropy Generation

Xu et al. [42] carried out a numerical study of heat transfer and entropy generation of slot air impinging jet on the rough target surface. The numerical simulation was two-dimensional a (sinusoidal wave) model on the target surface with a length of the target surface of 100 mm. Results were at a different jet-to-plate distance (4-8) and Reynolds numbers of (2738-10,952). They noted that the heat transfer performance for a rough surface was significantly increased compared with that for a smooth surface. It was also conducted that the entropy generation which due to (viscous and heat transfer) as well as the average Nusselt number were increased with increasing Reynolds number. In addition, they found that the average Nusselt number for a rough target plate increased up to 40% when compared with that for a smooth surface.

2.5 Summary

This chapter displayed that the previous extensive review of experimental and numerical investigations related to the characteristics of the heat transfer and flow field using the single impinging jet. It was noticed that many experimental and numerical investigations have been conducted on the convective heat transfer of the impinging jet on the smooth impingement target plate using traditional fluids based on the above reviews. There are only a few experimental and numerical studies have been performed on the influence of the impinging jet on the impinging target surfaces (severe turbulators such as; roughness and dimples surfaces) by using traditional fluids. Furthermore, there is no numerical and experimental study focused on the turbulent confined impinging slot-jet on the impingement target surface with the various shapes of ribs. In addition, the influence of the various shapes of the ribs on heat transfer enhancement as well as the entropy generation of slot-jet impingement has never been investigated.

2.6 Scope of investigation

The scopes of the present investigation which utilized to obtain these objectives are:

1) The jet Reynolds number is from 3000 to 8000 as well as the water is used as the working fluid.
2) Three shapes of the ribs such as (Wing ribs, Flat ribs, and Oval ribs) as well as smooth target surface (without ribs).
3) Four different ribs heights; 0.5, 1, 1.5, and 2 mm for all ribs shapes.
4) Three different ribs locations (i.e., three different distances from the stagnation point to the rib) which are 10, 20, and 30 mm for all ribs shapes.

CHAPTER THREE
NUMERICAL SOLUTION

3.1 Overview

This chapter introduces the numerical solution employed in the present investigation. The first part of this chapter explains the problem description and assumptions employed to solve the governing equations. Moreover, the governing equations of the turbulent flow in Cartesian coordinates are displayed. The low Reynolds number (k-ε) turbulence model of Launder and Sharma is adopted in the present investigation [43]. The CFD code is developed using the FORTRAN programming language to simulate turbulent flows. Furthermore, the body-fitted coordinate, the computational grid, and the governing equations transformation from Cartesian coordinates into body-fitted coordinates are presented. The discretization of governing equations is described in this chapter, employing the Finite Volume Method. Also, the entropy generation equations and the thermo-physical properties of the working fluid are introduced. Finally, the numerical calculations of (local and average Nusselt numbers and the performance evaluation criteria) are included.

3.2 Problem Description and Assumptions

In the current study, the basic geometries of confined single slot-jet impingement with different ribs shapes, which are wing, flat, and oval ribs, attached to the impinging target surface, are shown in Figure 3.1. The length of the impinging target surface (L) equals 110 mm, the distance between the slot-jet and impinging target surface (H) equals 10 mm, the

width of the confined slot-jet (W) equals 10 mm, and the ribs length (b) equals 10 mm. Two identical ribs with a height of (a =0.0, 0.5, 1, 1.5, and 2 mm) attached to the impinging target surface, where the (a=0.0) is a smooth impinging target surface. The first rib was located left the stagnation point while the second rib located at right the stagnation point. The spacing between the stagnation point and the rib (d) is (d=10, 20, and 30 mm). In addition, the flow is two-dimensional, steady state, turbulent, and incompressible. The constant physical properties of working fluid (water) are taken into consideration. No-slip condition is assumed on the adiabatic and heated walls.

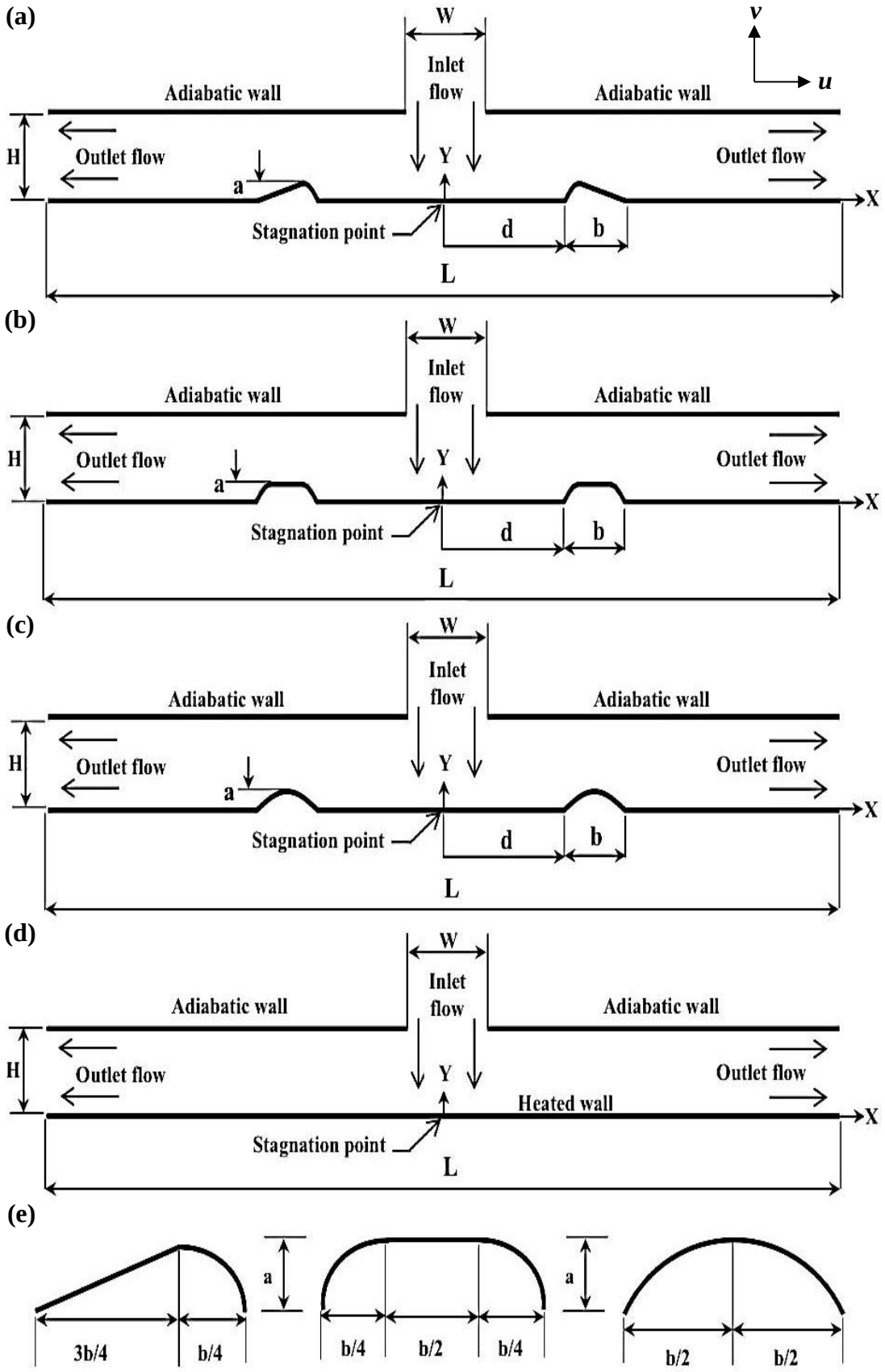

Figure 3.1: Physical domain of the current study: (a) Wing ribs, (b) Flat ribs, (c) Oval ribs, (d) Smooth impinging target surface, (e) Dimensions of ribs.

3.3 Governing Equations

Two dimensional governing equations of continuity, momentum, and energy in Cartesian coordinates can be defined as follows [44]:

Continuity equation:

$$\frac{\partial}{\partial x}(u) + \frac{\partial}{\partial y}(v) = 0 \tag{3.1}$$

u-momentum equation:

$$\frac{\partial}{\partial x}(\rho uu) + \frac{\partial}{\partial y}(\rho uv) = -\frac{\partial p}{\partial x} + \frac{\partial}{\partial x}\left[\mu_{eff}\frac{\partial u}{\partial x}\right] + \frac{\partial}{\partial y}\left[\mu_{eff}\frac{\partial u}{\partial y}\right] + \frac{\partial}{\partial y}\left[\mu_{eff}\frac{\partial v}{\partial x}\right] + \frac{\partial}{\partial x}\left[\mu_{eff}\frac{\partial u}{\partial x} - \frac{2}{3}\rho k_{\mathrm{f}}\right] \tag{3.2}$$

where,

$$\mu_{eff} = \mu + \mu_t \tag{3.3}$$

v-momentum equation:

$$\frac{\partial}{\partial x}(\rho uv) + \frac{\partial}{\partial y}(\rho vv) = -\frac{\partial p}{\partial y} + \frac{\partial}{\partial x}\left[\mu_{eff}\frac{\partial v}{\partial x}\right] + \frac{\partial}{\partial y}\left[\mu_{eff}\frac{\partial v}{\partial y}\right] + \frac{\partial}{\partial x}\left[\mu_{eff}\frac{\partial u}{\partial y}\right] + \frac{\partial}{\partial y}\left[\mu_{eff}\frac{\partial v}{\partial y} - \frac{2}{3}\rho k_{\mathrm{f}}\right] \tag{3.4}$$

Energy equation:

$$\frac{\partial}{\partial x}(\rho uT) + \frac{\partial}{\partial y}(\rho vT) = \frac{\partial}{\partial x}\left[\Gamma_T\frac{\partial T}{\partial x}\right] + \frac{\partial}{\partial y}\left[\Gamma_T\frac{\partial T}{\partial y}\right] \tag{3.5}$$

Where:

$$\Gamma_T = \frac{\mu}{Pr} + \frac{\mu_t}{Pr_t} \tag{3.6}$$

3.4 Transport Equations of Turbulence Model

In general, there are two equations of (k-ε) turbulence model considered the most utilized to calculate the turbulent dynamic viscosity (μ_t) based on a solution of turbulent kinetic energy (k) and dissipation rate (ε). The (k-ε) turbulence model proposed by Launder-Sharma is one of the most common turbulence models [43].This model is referred to as a low-Reynolds number *(*k-ε*)* model in the present study. Furthermore, it can be defined as follows:

Turbulent kinetic energy equation:

$$\frac{\partial}{\partial x}(\rho u k) + \frac{\partial}{\partial x}(\rho v k) = \frac{\partial}{\partial x}\left[\Gamma_k \frac{\partial k}{\partial x}\right] + \frac{\partial}{\partial y}\left[\Gamma_k \frac{\partial k}{\partial y}\right] + P_k - \rho(\varepsilon + \varepsilon_w) \quad (3.7)$$

Where:

$$\Gamma_k = \mu + \frac{\mu_t}{\sigma_k} \quad (3.8)$$

The term P_k is the turbulent kinetic energy production rate. It can be expressed as:

$$P_k = \mu_t \left\{2\left[\left(\frac{\partial u}{\partial y}\right)^2 + \left(\frac{\partial v}{\partial x}\right)^2\right] + \left(\frac{\partial u}{\partial y} + \frac{\partial v}{\partial x}\right)^2\right\} - \frac{2}{3}\rho k\left(\frac{\partial u}{\partial x} + \frac{\partial v}{\partial y}\right) \quad (3.9)$$

Dissipation rate at wall (ε_w):

$$\varepsilon_w = 2\frac{\mu}{\rho}\left[\left(\frac{\partial \sqrt{k}}{\partial x}\right)^2 + \left(\frac{\partial \sqrt{k}}{\partial y}\right)^2\right] \quad (3.10)$$

Turbulent kinetic energy dissipation equation:

$$\frac{\partial}{\partial x}(\rho u \varepsilon) + \frac{\partial}{\partial y}(\rho v \varepsilon) = \frac{\partial}{\partial x}\left[\Gamma_\varepsilon \frac{\partial \varepsilon}{\partial x}\right] + \frac{\partial}{\partial y}\left[\frac{\partial \varepsilon}{\partial y}\right]$$

$$+(C_1 f_1 P_k - \rho C_2 f_2 \varepsilon)\frac{\varepsilon}{k} + \emptyset_\varepsilon \quad (3.11)$$

where,

$$\Gamma_{\varepsilon} = \mu + \frac{\mu_t}{\sigma_{\varepsilon}} \tag{3.12}$$

$$\emptyset_{\varepsilon} = 2\mu_t \frac{\mu}{\rho}\left[\left[\left(\frac{\partial^2 u}{\partial x^2}\right)^2 + \left(\frac{\partial^2 v}{\partial x^2}\right)^2\right] + 2\left(\frac{\partial^2 u}{\partial x \partial y}\right)^2 + 2\left(\frac{\partial^2 v}{\partial x \partial y}\right)^2 + \left(\frac{\partial^2 v}{\partial y^2}\right)^2\right] \tag{3.13}$$

The turbulent eddy viscosity in the above equation is indicated by [45]:

$$\mu_t = C_{\mu}\, f_{\mu}\, \rho\, \frac{k^2}{\varepsilon} \tag{3.14}$$

In the above equations, the empirical constants and the turbulent Prandtl number are defined as [45]:

$$C_{\mu} = 0.09,\ \ C_1 = 1.44,\ \ C_2 = 1.92 \tag{3.15}$$

$$\sigma_k = 1.0,\ \ \sigma_{\varepsilon} = 1.3,\ \ Pr_t = 0.9 \tag{3.16}$$

In addition, the wall damping functions are expressed as [46]:

$$f_1 = 1.0 \tag{3.17}$$

$$f_2 = 1 - 0.3\, exp(-Re_T^2) \tag{3.18}$$

$$f_{\mu} = \exp\left[\frac{-3.4}{(1+0.02Re_T)^2}\right] \tag{3.19}$$

The turbulent Reynolds number is expressed by:

$$Re_T = \frac{\rho}{\varepsilon}\frac{k^2}{\mu} \tag{3.20}$$

3.5 Body Fitted Coordinates System

The body-fitted coordinate system is utilized due to the irregular geometry of the present study. The irregular physical domain is converted into a rectangular (regular) computational domain as shown in Figure 3.2. The governing equations are transformed from the Cartesian coordinate system (x,y) to a body-fitted coordinate system (ζ,η) [47]; as shown in Appendix A.

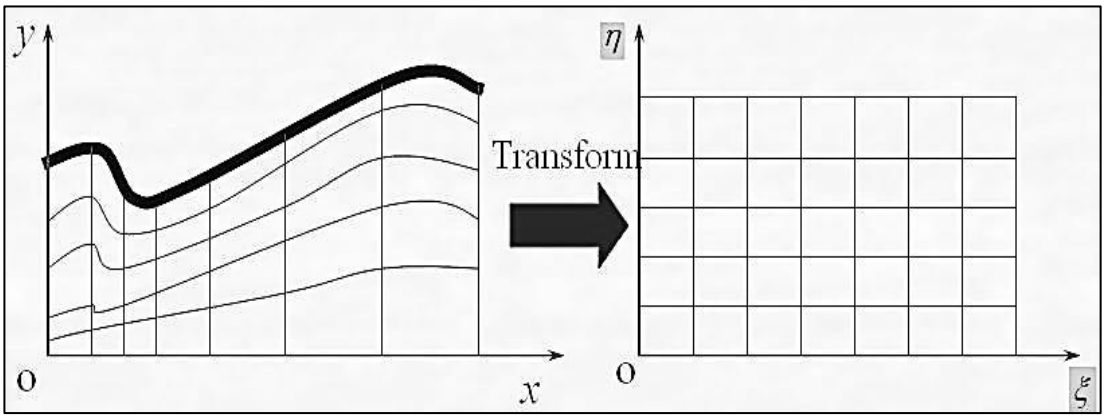

Figure 3.2: Transformation from Physical domain (left) to computational domain (right).

3.6 Computational Grid

In general, the computational grid used for CFD problems can be obtained through different methods, such as algebraic and differential equation methods. Due to the irregular geometries employed in the present study, the method of the differential equation (which is suggested by Thompson) can be employed to develop the computational mesh. Thus, this method is employed to evolve the computational mesh of the present geometry depends on Poisson equations. Therefore, the two-dimensional Poisson equations can be defined as follows [48]:

$$\frac{\partial^2 \xi}{\partial x^2} + \frac{\partial^2 \xi}{\partial y^2} = P(\xi, \eta) \tag{3.21}$$

$$\frac{\partial^2 \eta}{\partial x^2} + \frac{\partial^2 \eta}{\partial y^2} = Q(\xi, \eta) \tag{3.22}$$

Where $P(\xi, \eta)$ and $Q(\xi, \eta)$ are the control functions employed for the clustering of points near the boundaries given. The procedures employed for calculating the values of these functions are depicted in Appendix A in detail. The above equations are turned to the computational field by an interchange of dependent and independent variables, and thereafter calculated the unknowns (x,y) from the bellow equations.

$$q_{11} \frac{\partial^2 x}{\partial \xi^2} - 2q_{12} \frac{\partial^2 x}{\partial \xi \eta} + q_{22} \frac{\partial^2 x}{\partial \eta^2} + J^2 \left(P \frac{\partial x}{\partial \xi} + Q \frac{\partial x}{\partial \eta} \right) = 0 \tag{3.23}$$

$$q_{11} \frac{\partial^2 y}{\partial \xi^2} - 2q_{12} \frac{\partial^2 y}{\partial \xi \eta} + q_{22} \frac{\partial^2 y}{\partial \eta^2} + J^2 \left(P \frac{\partial y}{\partial \xi} + Q \frac{\partial y}{\partial \eta} \right) = 0 \tag{3.24}$$

The q_{11}, q_{12}, and q_{22} in equation 3.23 and 3.24 are the geometry factors can be expressed as:

$$q_{11} = \beta_{11}^2 + \beta_{21}^2 \tag{3.25}$$

$$q_{12} = -(\beta_{11}\beta_{12} + \beta_{21}\beta_{22}) \tag{3.26}$$

$$q_{22} = \beta_{12}^2 + \beta_{22}^2 \tag{3.27}$$

Equations 3.23 and 3.24 are solved numerically employing the Successive Line Over-Relaxation algorithm to calculate the values of (x,y) during each node of computational mesh [49]. Figure 3.3 displays the computational mesh utilized in the current study. From this figure, the grid shaped near the top and bottom walls can be noticed to be intense than that of the channel center. In addition, the mesh can also be shown to be orthogonal on the surfaces of all ribs.

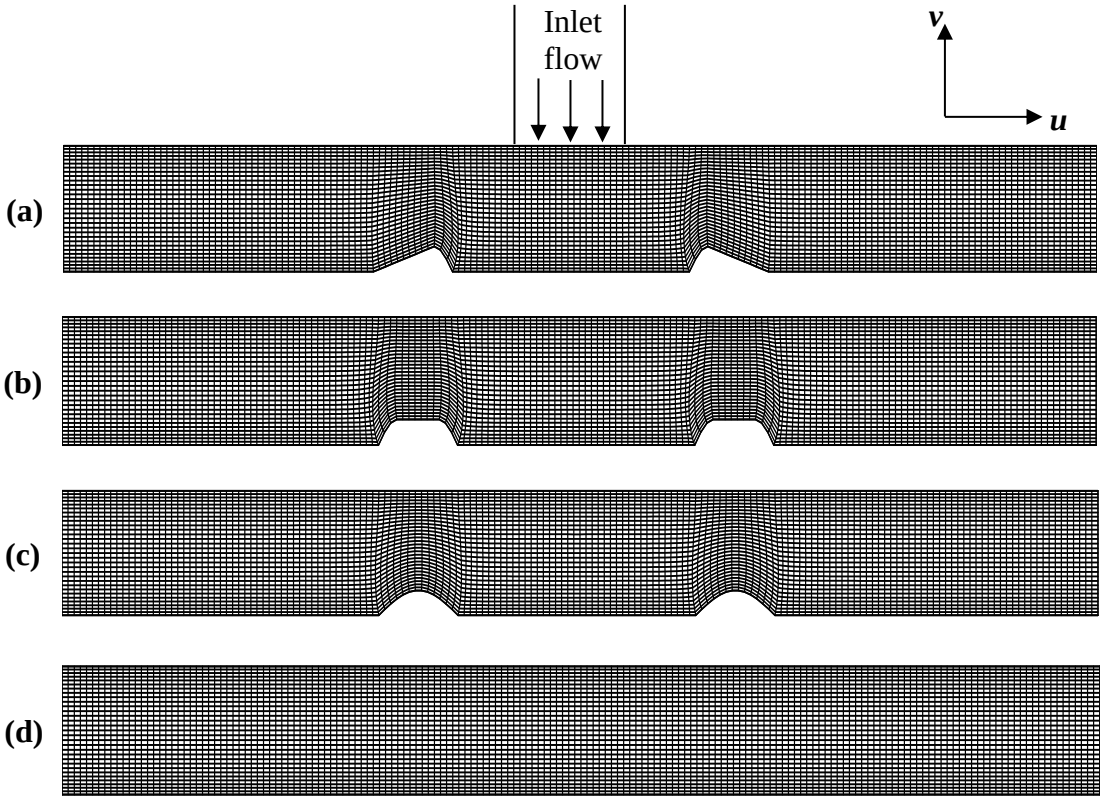

Figure 3.3: Computational grid of the current study: (a) Wing ribs, (b) Flat ribs, (c) Oval ribs, (d) Smooth impinging target surface.

3.7 Transformation of the Governing Equations in the Body-Fitted Coordinates Systems

The governing equations are converted from Cartesian coordinates to the body-fitted coordinates as follows [44]:

Continuity equation:

$$\frac{1}{J}\left[\frac{\partial}{\partial\xi}(\rho u U^c) + \frac{\partial}{\partial\eta}(\rho v V^c)\right] = 0 \qquad (3.28)$$

u-momentum equation:

$$\frac{1}{J}\left[\frac{\partial}{\partial\xi}(\rho u U^c) + \frac{\partial}{\partial\eta}(\rho u V^c)\right] = \frac{1}{J}\frac{\partial}{\partial\xi}\left[\frac{\Gamma_u}{J}\left(q_{11}\frac{\partial u}{\partial\xi} - q_{12}\frac{\partial u}{\partial\eta}\right)\right]$$

$$+\frac{1}{J}\frac{\partial}{\partial\eta}\left[\frac{\Gamma_u}{J}\left(q_{22}\frac{\partial u}{\partial\eta}-q_{12}\frac{\partial u}{\partial\xi}\right)\right]+\frac{\Gamma_u}{J}\frac{\partial}{\partial\xi}\left[\frac{1}{J}\left(\beta_{11}^2\frac{\partial u}{\partial\xi}+\beta_{11}\beta_{12}\frac{\partial u}{\partial\eta}\right)\right]$$

$$+\frac{\Gamma_u}{J}\frac{\partial}{\partial\eta}\left[\frac{1}{J}\left(\beta_{12}\beta_{11}\frac{\partial u}{\partial\xi}+\beta_{12}^2\frac{\partial u}{\partial\eta}\right)\right]+\frac{\Gamma_u}{J}\frac{\partial}{\partial\xi}\left[\frac{1}{J}\left(\beta_{21}\beta_{11}\frac{\partial v}{\partial\xi}+\beta_{21}\beta_{12}\frac{\partial v}{\partial\eta}\right)\right]$$

$$+\frac{\Gamma_u}{J}\frac{\partial}{\partial\eta}\left[\frac{1}{J}\left(\beta_{22}\beta_{11}\frac{\partial v}{\partial\xi}+\beta_{22}\beta_{12}\frac{\partial v}{\partial\eta}\right)\right]-\frac{2}{3}\rho\frac{1}{J}\left[\frac{\partial}{\partial\xi}\left(\beta_{11}k_{\mathrm{f}}\right)+\frac{\partial}{\partial\eta}\left(\beta_{12}k_{\mathrm{f}}\right)\right]$$

$$-\frac{1}{J}\left[\frac{\partial}{\partial\xi}\left(\beta_{11}p\right)+\frac{\partial}{\partial\eta}\left(\beta_{12}p\right)\right] \tag{3.29}$$

v-momentum equation:

$$\frac{1}{J}\left[\frac{\partial}{\partial\xi}\left(\rho vU^c\right)+\frac{\partial}{\partial\eta}\left(\rho vV^c\right)\right]=\frac{1}{J}\frac{\partial}{\partial\xi}\left[\frac{\Gamma_v}{J}\left(q_{11}\frac{\partial v}{\partial\xi}-q_{12}\frac{\partial v}{\partial\eta}\right)\right]$$

$$+\frac{1}{J}\frac{\partial}{\partial\eta}\left[\frac{\Gamma_v}{J}\left(q_{22}\frac{\partial v}{\partial\eta}-q_{12}\frac{\partial v}{\partial\xi}\right)\right]+\frac{\Gamma_v}{J}\frac{\partial}{\partial\xi}\left[\frac{1}{J}\left(\beta_{21}^2\frac{\partial v}{\partial\xi}+\beta_{21}\beta_{22}\frac{\partial v}{\partial\eta}\right)\right]$$

$$+\frac{\Gamma_v}{J}\frac{\partial}{\partial\eta}\left[\frac{1}{J}\left(\beta_{22}\beta_{21}\frac{\partial v}{\partial\xi}+\beta_{22}^2\frac{\partial v}{\partial\eta}\right)\right]+\frac{\Gamma_v}{J}\frac{\partial}{\partial\xi}\left[\frac{1}{J}\left(\beta_{11}\beta_{21}\frac{\partial u}{\partial\xi}+\beta_{11}\beta_{22}\frac{\partial u}{\partial\eta}\right)\right]$$

$$+\frac{\Gamma_v}{J}\frac{\partial}{\partial\eta}\left[\frac{1}{J}\left(\beta_{12}\beta_{21}\frac{\partial u}{\partial\xi}+\beta_{12}\beta_{22}\frac{\partial u}{\partial\eta}\right)\right]-\frac{2}{3}\rho\frac{1}{J}\left[\frac{\partial}{\partial\xi}\left(\beta_{21}k_{\mathrm{f}}\right)+\frac{\partial}{\partial\eta}\left(\beta_{22}k_{\mathrm{f}}\right)\right]$$

$$-\frac{1}{J}\left[\frac{\partial}{\partial\xi}\left(\beta_{21}p\right)+\frac{\partial}{\partial\eta}\left(\beta_{22}p\right)\right] \tag{3.30}$$

Energy equation:

$$\frac{1}{J}\left[\frac{\partial}{\partial\xi}\left(\rho U^cT\right)+\frac{\partial}{\partial\eta}\left(\rho V^cT\right)\right]=\frac{1}{J}\frac{\partial}{\partial\xi}\left[\frac{\Gamma_T}{J}\left(q_{11}\frac{\partial T}{\partial\xi}-q_{12}\frac{\partial T}{\partial\eta}\right)\right]$$

$$+\frac{1}{J}\frac{\partial}{\partial\eta}\left[\frac{\Gamma_T}{J}\left(q_{22}\frac{\partial T}{\partial\eta}-q_{12}\frac{\partial T}{\partial\xi}\right)\right] \tag{3.31}$$

U^c and V^c in above equations are referred to the Contra-variant velocity components of *x* and *y* direction as shown in Figure 3.4, these velocities can be expressed as [50]:

$$U^c = uy_\eta - vx_\eta \tag{3.32}$$

$$V^c = vx_\xi - uy_\xi \tag{3.33}$$

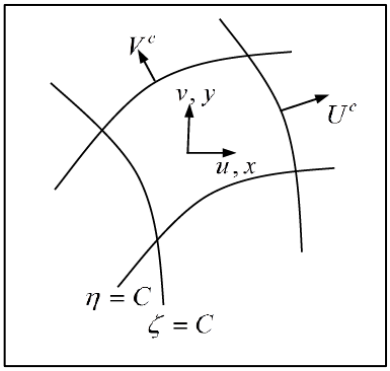

Figure 3.4: Contra-variant velocities components.

Turbulent kinetic energy equation is:

$$\frac{1}{J}\left[\frac{\partial}{\partial\xi}(\rho U^c k) + \frac{\partial}{\partial\eta}(\rho V^c k)\right] = \frac{1}{J}\frac{\partial}{\partial\xi}\left[\frac{\Gamma_K}{J}\left(q_{11}\frac{\partial k}{\partial\xi} - q_{12}\frac{\partial k}{\partial\eta}\right)\right]$$

$$+\frac{1}{J}\frac{\partial}{\partial\eta}\left[\frac{\Gamma_K}{J}\left(q_{22}\frac{\partial k}{\partial\eta} - q_{12}\frac{\partial k}{\partial\xi}\right)\right] + P_k(\xi,\eta) - \rho\left(\varepsilon + \varepsilon_w(\xi,\eta)\right) \tag{3.34}$$

where,

$$P_k(\xi,\eta) = 2\mu_t\left\{\frac{1}{J^2}\left[\frac{\partial}{\partial\xi}(\beta_{11}u) + \frac{\partial}{\partial\eta}(\beta_{12}u)\right]^2 + \left[\frac{1}{J^2}\frac{\partial}{\partial\xi}(\beta_{11}u) + \right.\right.$$

$$\left.\left.\frac{\partial}{\partial\eta}(\beta_{22}v)\right]^2 + \frac{1}{2}\frac{1}{J^2}\left[\frac{\partial}{\partial\xi}(\beta_{21}u) + \frac{\partial}{\partial\eta}(\beta_{22}u) + \frac{\partial}{\partial\xi}(\beta_{11}v) + \frac{\partial}{\partial\eta}(\beta_{12}v)\right]^2\right\}$$

$$-\frac{2}{3}\rho k\frac{1}{J}\left[\frac{\partial}{\partial\xi}(\beta_{11}u) + \frac{\partial}{\partial\eta}(\beta_{12}u) + \frac{\partial}{\partial\xi}(\beta_{21}v) + \frac{\partial}{\partial\eta}(\beta_{22}v)\right] \tag{3.35}$$

$$\varepsilon_w = \frac{2\mu}{\rho}\left\{\frac{1}{J^2}\left[\frac{\partial}{\partial\xi}\left(\beta_{11}\sqrt{K}\right) + \frac{\partial}{\partial\eta}\left(\beta_{12}\sqrt{K}\right)\right]^2 + \frac{1}{J^2}\left[\frac{\partial}{\partial\xi}\left(\beta_{21}\sqrt{K}\right) + \right.\right.$$

$$\left.\left.\frac{\partial}{\partial\eta}\left(\beta_{22}\sqrt{K}\right)\right]^2\right\} \tag{3.36}$$

Turbulent kinetic energy dissipation equation:

$$\frac{1}{J}\left[\frac{\partial}{\partial\zeta}(\rho U^c\varepsilon)+\frac{\partial}{\partial\eta}(\rho V^c\varepsilon)\right]=\frac{1}{J}\frac{\partial}{\partial\xi}\left[\frac{\Gamma_\varepsilon}{J}\left(q_{11}\frac{\partial\varepsilon}{\partial\xi}-q_{12}\frac{\partial\varepsilon}{\partial\eta}\right)\right]$$

$$+\frac{1}{J}\frac{\partial}{\partial\eta}\left[\frac{\Gamma_\varepsilon}{J}\left(q_{22}\frac{\partial\varepsilon}{\partial\eta}-q_{12}\frac{\partial\varepsilon}{\partial\xi}\right)\right]+(C_1 f_1 P_K-\rho C_2 f_2\varepsilon)\frac{\varepsilon}{k}+\phi_\varepsilon \qquad (3.37)$$

Where:

$$\phi_\varepsilon=2\mu_t\frac{\mu}{\rho}\left\{\frac{1}{J^2}\left\{\frac{\partial}{\partial\xi}\left[\frac{1}{J}\left(\beta_{11}^2\frac{\partial u}{\partial\xi}+\beta_{11}\beta_{12}\frac{\partial u}{\partial\eta}\right)\right]+\frac{\partial}{\partial\eta}\left[\frac{1}{J}\left(\beta_{12}\beta_{11}\frac{\partial u}{\partial\xi}+\right.\right.\right.\right.$$

$$\left.\left.\left.\left.\beta_{12}^2\frac{\partial u}{\partial\eta}\right)\right]\right\}^2+\frac{1}{J^2}\left\{\frac{\partial}{\partial\xi}\left[\frac{1}{J}\left(\beta_{21}^2\frac{\partial u}{\partial\xi}+\beta_{21}\beta_{22}\frac{\partial u}{\partial\eta}\right)\right]+\frac{\partial}{\partial\eta}\left[\frac{1}{J}\left(\beta_{22}\beta_{21}\frac{\partial u}{\partial\xi}+\right.\right.\right.\right.$$

$$\left.\left.\left.\left.\beta_{22}^2\frac{\partial u}{\partial\eta}\right)\right]\right\}^2+\frac{2}{J^2}\left\{\frac{\partial}{\partial\xi}\left[\frac{1}{J}\left(\beta_{11}\beta_{21}\frac{\partial u}{\partial\xi}+\beta_{11}\beta_{22}\frac{\partial u}{\partial\eta}\right)\right]+\frac{\partial}{\partial\eta}\left[\frac{1}{J}\left(\beta_{12}\beta_{21}\frac{\partial u}{\partial\xi}+\right.\right.\right.\right.$$

$$\left.\left.\left.\left.\beta_{12}\beta_{21}\frac{\partial u}{\partial\eta}\right)\right]\right\}^2+\frac{1}{J^2}\left\{\frac{\partial}{\partial\xi}\left[\frac{1}{J}\left(\beta_{11}^2\frac{\partial v}{\partial\xi}+\beta_{11}\beta_{12}\frac{\partial v}{\partial\eta}\right)\right]+\frac{\partial}{\partial\eta}\left[\frac{1}{J}\left(\beta_{12}\beta_{11}\frac{\partial v}{\partial\xi}+\right.\right.\right.\right.$$

$$\left.\left.\left.\left.\beta_{12}^2\frac{\partial v}{\partial\eta}\right)\right]\right\}^2+\frac{1}{J^2}\left\{\frac{\partial}{\partial\xi}\left[\frac{1}{J}\left(\beta_{21}^2\frac{\partial v}{\partial\xi}+\beta_{21}\beta_{22}\frac{\partial v}{\partial\eta}\right)\right]+\frac{\partial}{\partial\eta}\left[\frac{1}{J}\left(\beta_{22}\beta_{21}\frac{\partial v}{\partial\xi}+\right.\right.\right.\right.$$

$$\left.\left.\left.\left.\beta_{22}^2\frac{\partial v}{\partial\eta}\right)\right]\right\}^2+\frac{2}{J^2}\left\{\frac{\partial}{\partial\xi}\left[\frac{1}{J}\left(\beta_{11}\beta_{21}\frac{\partial v}{\partial\xi}+\beta_{11}\beta_{22}\frac{\partial v}{\partial\eta}\right)\right]+\frac{\partial}{\partial\eta}\left[\frac{1}{J}\left(\beta_{12}\beta_{21}\frac{\partial v}{\partial\xi}+\right.\right.\right.\right.$$

$$\left.\left.\left.\left.\beta_{12}\beta_{22}\frac{\partial v}{\partial\eta}\right)\right]\right\}^2\right\} \qquad (3.38)$$

3.8 Discretization of Governing Equations

In the respect of body-fitted coordinate system, the general form of governing equations and turbulence model can be written as follows[51]:

$$\frac{1}{J}\left[\frac{\partial}{\partial\xi}(\rho\phi U^c)+\frac{\partial}{\partial\eta}(\rho\phi V^c)\right]=\frac{1}{J}\frac{\partial}{\partial\xi}\left[\frac{\Gamma_\phi}{J}\left(q_{11}\frac{\partial\phi}{\partial\xi}-q_{12}\frac{\partial\phi}{\partial\eta}\right)\right]$$

$$+\frac{1}{J}\frac{\partial}{\partial\eta}\left[\frac{\Gamma_\phi}{J}\left(q_{22}\frac{\partial\phi}{\partial\xi}-q_{12}\frac{\partial\phi}{\partial\eta}\right)\right]+b_\phi+b_p^\phi \qquad (3.39)$$

Equation 3.39 is discretized utilizing the Finite Volume Method (FVM) on the collocated grid as shown in Figure 3.5. The parameters of equation

3.39 are defined in Table 3.1. The central scheme is utilized to discretize the diffusion terms while the convection terms can be discretized by using the second-order upwind scheme.

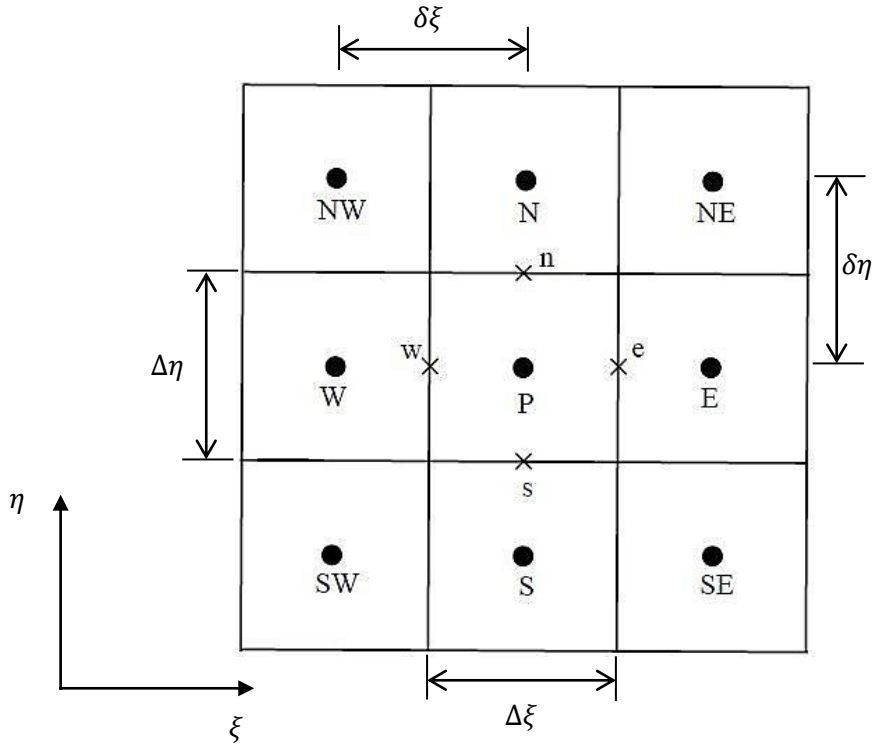

Figure 3.5: Control volume employed for the discretization of the governing equations.

Table 3.1: The parameters of general transport equation (Equation 3.39)

Equations	$\boldsymbol{\phi}$	$\boldsymbol{\Gamma_\phi}$	$\boldsymbol{b_\phi}$	$\boldsymbol{b_p^\phi}$
continuty	1	0	0	0
x-momentum	u	$\mu + \mu_t$	S_u	b_p^u
y-momentum	v		S_v	b_p^v
Energy	T	$k_f/C_p + \mu_t/Pr_t$	0	0
Turbulence kinatic energy	k	$\mu + \mu_t/\sigma_k$	$P_k - \rho\varepsilon$	0
Energy dissipation rate	ε	$\mu + \mu_t/\sigma_\varepsilon$	$(C_{\varepsilon1}f_{\varepsilon1}P_k - \rho C_{\varepsilon2}f_{\varepsilon2}\varepsilon)\varepsilon/k$	0

The integration of the convective, diffusion, and source terms on a control volume of around node P are given in Appendix A in detail. So, gathering all of the transport equation terms for convection, diffusion and source are as follows:

$$A_P\phi_P = A_E\phi_E + A_W\phi_W + A_N\phi_N + A_S\phi_S + S_\phi \tag{3.40}$$

In the above equation, it can also be written in the following form:

$$A_P\phi_P = \sum_{nb} A_{nb}\phi_{nb} + S_\phi \tag{3.41}$$

Here, *nb* refers for the adjacent nodes (E, W, N and S) of a control volume. In the above equation, the source term S_ϕ consisting of the non-orthogonal grid diffusion terms S_d^ϕ, non-pressure terms b_ϕ, and pressure terms b_P^ϕ is described as below:

$$S_\phi = S_d^\phi + b_\phi + b_P^\phi \tag{3.42}$$

The coefficients (A_E, A_W, A_N, A_S, and A_P) in equation 3.40 include the conductivity of diffusion (D_e, D_w, D_n, and D_s) and the flow rate (F_e, F_w, F_n, and F_s). So, these coefficients can be described as follows:

$$A_E = D_e + \max[-F_e, 0] \tag{3.43}$$

$$A_W = D_w + \max[F_w, 0] \tag{3.44}$$

$$A_N = D_n + \max[-F_n, 0] \tag{3.45}$$

$$A_S = D_s + \max[-F_s, 0] \tag{3.46}$$

$$A_P = A_E + A_W + A_N + A_S \tag{3.47}$$

All source terms of governing equations are given in Appendix A.

3.9 SIMPLE Algorithms

Generally, if the pressure field is recognized, the velocity field can be determined by solving discretized momentum equations. So, the produced velocity field must be achieved both the momentum and continuity equations. Furthermore, the continuity equation, which does not expressly include pressure, can be utilized to calculate the pressure field, along with momentum equations. The pressure field can thus be obtained employing the SIMPLE algorithm through a coupling of velocity and pressure equations over organized non-orthogonal grid [53]. To clarify the algorithm, discretized momentum equations are written as:

$$u_p = \left[\frac{1}{A_P}\sum_{nb} A_{nb}^{u}\, u_{nb} + S_d^u + b_u\right] + B_P^u(p_e - p_w) + C_P^u(p_n - p_s) \tag{3.48}$$

$$v_p = \left[\frac{1}{A_P}\sum_{nb} A_{nb}^{v}\, v_{nb} + S_d^v + b_v\right] + B_P^v(p_e - p_w) + C_P^v(p_n - p_s) \tag{3.49}$$

Here

$$B_p^u = -\frac{1}{A_P^u}(\Delta\eta\beta_{11})_p \tag{3.50}$$

$$C_p^u = -\frac{1}{A_P^u}(\Delta\xi\beta_{12})_p \tag{3.51}$$

$$B_p^v = -\frac{1}{A_P^v}(\Delta\eta\beta_{21})_p \tag{3.52}$$

$$C_p^v = -\frac{1}{A_P^v}(\Delta\xi\beta_{22})_p \tag{3.53}$$

Where nb indicates the adjacent nodes (E, W, N and S) of a control volume. The initial pressure value p^* is estimated in order to begin the SIMPLE algorithm calculation procedure. In Appendix A, the components of velocity u^* and v^* can be calculated through solving above

equations. The interpolation of velocity is achieved on a collocated non-orthogonal grid to determine the face velocities for a control volume as given in Appendix A. Moreover, the under- relaxation is employed to reduce the dependent variables updating for each iteration. The under-relaxation factor also can be inserted to the discretized equation as follows:

$$\frac{A_P^{\phi}}{\alpha_{\phi}}\phi_P = \sum_{nb} A_{nb}^{\phi}\phi_{nb} + S_{\phi} + \frac{1-\alpha_{\phi}}{\alpha_{\phi}} A_P^0 \phi_P^0 \tag{3.54}$$

Where, α_{ϕ} represents that the under-relaxation factor, and thus the equation 3.54 can be re-written as:

$$\frac{A_P^{\phi}}{\alpha_{\phi}}\phi_P = \sum_{nb} A_{nb}^{\phi}\phi_{nb} + S_{\phi}{}^{r} \tag{3.55}$$

where,

$$S_{\phi}^{r} = S_{\phi} + \frac{1-\alpha_{\phi}}{\alpha_{\phi}} A_P^0 \phi_P^0 \tag{3.56}$$

for the equation of pressure correction, the under-relaxation is explicitly applied as showns:

$$P^{new} = P^{*} + \alpha_P P^{'} \tag{3.57}$$

where, α_P refers to the under-relaxation factor for the pressure correction equation. So, 0.7 for energy and momentum equations, 0.3 for (k and ε) equations as well as 0.2 for pressure are the under-relaxation factors values employed in the present investigation.

3.10 Convergence Criteria

Since iteratively solved discretized transport equations, there is the residual through two sequential iterations. For all variables, if the residual is less than the specified value, the iteration is stopped. Then for all variables (except pressure), the relative convergence criteria can be formulated as follows [54]:

$$R_{\phi} = \frac{\sum_{node}\left|A_P^{\phi}\phi_P - \sum_{nb} A_{nb}^{\phi}\phi_{nb} - S_u^{\phi}\right|}{\sum_{node}\left|A_P^{\phi}\phi_P\right|} \tag{3.58}$$

Where S_u^{ϕ} indicates that the source term. Considering the continuity equation, the mass imbalance on the control volume should be checked. Therefore, the criterion of convergence for a continuity equation is specified by:

$$R = \sum_{node}|S_m| \tag{3.59}$$

So, S_m refers that the imbalance of mass which is previously expressed in equation A.140 in Appendix A. The computation is finished if the sum of absolute residual (i.e., R_{ϕ}) is less than (1×10^{-4}) for each parameter across the computational field [55]. Finally, the solution procedure of CFD code in the current investigation is shown in Figure 3.6.

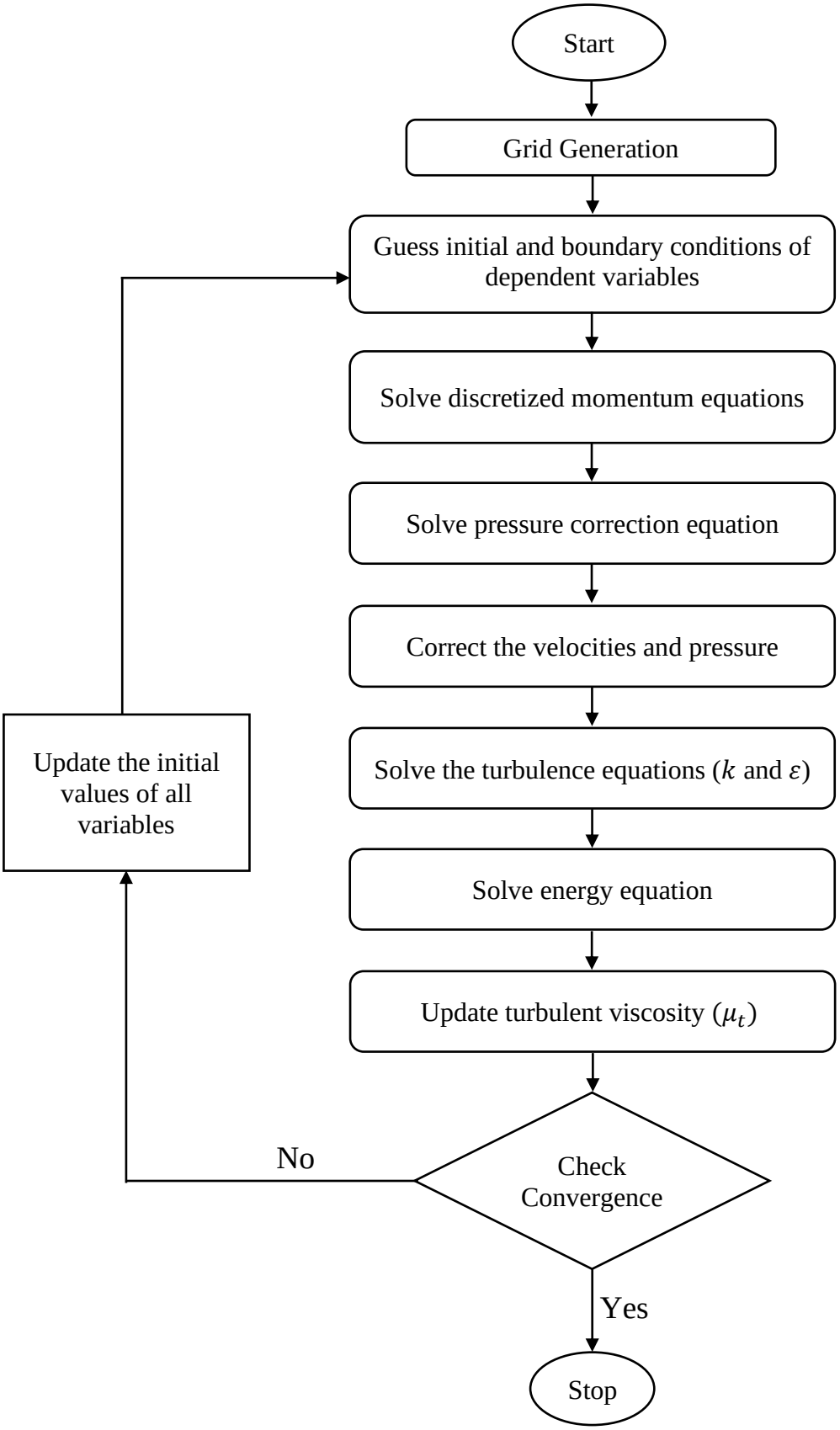

Figure 3.6: Solution procedure for CFD program in the present study.

3.11 Entropy Generation

Generally, entropy generation is one of the parameters directly associated with the second law of the thermodynamics that must be investigated in a process with fluid flow and heat transfer in order that the design efficient systems. The entropy generation rate is utilized to measure irreversibility attached to flow friction, heat transfer as well as other non-idealities inside the system due to modern thermodynamics. Furthermore, the entropy generation in processes can be classified into three main categories which the heat transfer and momentum are the occurring simultaneously:

- ✓ The entropy generation due to (conduction and convection) heat transfer,
- ✓ The entropy generation due to (flow friction) viscous dissipation, and
- ✓ The entropy generation due to (radiation) heat transfer.

The entropy generation is attached to heat transfer and viscous dissipation influences only. While the entropy generation caused by radiation heat transfer is conceded due to low fluid and system temperatures [56]. Thus, the average entropy generations due to the heat transfer (average thermal entropy generation) and the viscous dissipation (average viscous entropy generation) for two dimensional can be defined as follows [57]:

$$\dot{S}'''_{gen,th.} = \frac{k_f}{T^2}\left[\left(\frac{\partial T}{\partial x}\right)^2 + \left(\frac{\partial T}{\partial y}\right)^2\right] \tag{3.60}$$

$$\dot{S}'''_{gen,vi.} = \frac{\mu_f}{T}\left\{2\left[\left(\frac{\partial u}{\partial x}\right)^2 + \left(\frac{\partial v}{\partial y}\right)^2\right] + \left(\frac{\partial u}{\partial y} + \frac{\partial v}{\partial x}\right)^2\right\} \tag{3.61}$$

Where $\dot{S}'''_{gen,th.}$ and $\dot{S}'''_{gen,vi.}$ in the above equations represent the averages of thermal and viscous entropy generations, respectively. Therefore, the averages of the thermal and viscous entropy generations can be expressed as the dimensionless number by employing slot width and thermal conductivity as follows:

$$\left(\dot{S}'''_{gen,th}\right)_W = \dot{S}'''_{gen,th.} \times \frac{W^2}{k_f} \tag{3.62}$$

$$\left(\dot{S}'''_{gen,vi}\right)_W = \dot{S}'''_{gen,vi.} \times \frac{W^2}{k_f} \tag{3.63}$$

Here $\left(\dot{S}'''_{gen,th}\right)_W$ and $\left(\dot{S}'''_{gen,vi}\right)_W$ indicate that the dimensionless number of the averages of the thermal and viscous entropy generations, respectively. Thus, the average total entropy generation rate is the sum of the averages of the thermal and viscous entropy generations can be described as follows [56]:

$$\dot{S}'''_{gen,total} = \dot{S}'''_{gen,th.} + \dot{S}'''_{gen,vi.} \tag{3.64}$$

Substituting equations 3.60 and 3.61 in equation 3.64, gives:

$$\dot{S}'''_{gen,total} = \frac{k_f}{T^2}\left[\left(\frac{\partial T}{\partial x}\right)^2 + \left(\frac{\partial T}{\partial y}\right)^2\right] + \frac{\mu_f}{T}\left\{2\left[\left(\frac{\partial u}{\partial x}\right)^2 + \left(\frac{\partial v}{\partial y}\right)^2\right] + \left(\frac{\partial u}{\partial y} + \frac{\partial v}{\partial x}\right)^2\right\} \tag{3.65}$$

Furthermore, the dimensionless number of the average total entropy generation represents the sum of the dimensionless number of the averages of the thermal and viscous entropy generations can be given as follows:

$$\left(\dot{S}'''_{gen,total}\right)_W = \left(\dot{S}'''_{gen,th.}\right)_W + \left(\dot{S}'''_{gen,vi.}\right)_W \tag{3.66}$$

Substituting equations 3.62 and 3.63 in equation 3.66, gives:

$$\left(\dot{S}'''_{gen,total}\right)_W = \frac{k_f.W^2}{T^2}\left[\left(\frac{\partial T}{\partial x}\right)^2 + \left(\frac{\partial T}{\partial y}\right)^2\right] + \frac{\mu_f.W^2}{T}\left\{2\left[\left(\frac{\partial u}{\partial x}\right)^2 + \left(\frac{\partial v}{\partial y}\right)^2\right] + \left(\frac{\partial u}{\partial y} + \frac{\partial v}{\partial x}\right)^2\right\} \tag{3.67}$$

In addition, the previous relationships for equations A.10 and A.11 in Appendix A are utilized to transform equation 3.67 from the physical field into the computational field as shown below:

$$\left(\dot{S}'''_{gen,total}\right)_W = \frac{k_f.W^2}{T^2}\left[\left(\beta_{11}\frac{\partial T}{\partial \xi}+\beta_{12}\frac{\partial T}{\partial \eta}\right)^2+\left(\beta_{21}\frac{\partial T}{\partial \xi}+\beta_{22}\frac{\partial T}{\partial \eta}\right)^2\right] + \frac{\mu_f.W^2}{T}\left\{2\left[\left(\beta_{11}\frac{\partial u}{\partial \xi}+\beta_{12}\frac{\partial u}{\partial \eta}\right)^2+\left(\beta_{21}\frac{\partial v}{\partial \xi}+\beta_{22}\frac{\partial v}{\partial \eta}\right)^2\right] + \left(\left(\beta_{21}\frac{\partial u}{\partial \xi}+\beta_{22}\frac{\partial u}{\partial \eta}\right)+\left(\beta_{11}\frac{\partial v}{\partial \xi}+\beta_{12}\frac{\partial v}{\partial \eta}\right)\right)^2\right\} \quad (3.68)$$

3.12 Thermo-physical Properties of Working Fluid

The properties of water at the temperature of 25 ºC can be given in this investigation as follows [58].

Table 3.2: Thermo-physical Properties of water at 25 ºC.

$\rho_f\ (kg/m^3)$	$\mu_f\ (kg/m.s)$	$C_{p,f}\ (J/kg.K)$	$k_f\ (W/m.K)$
997.9	0.001	4144	0.6094

3.13 Boundary Conditions

Suitable boundary conditions of all relevant variables should be defined on each of the boundaries for the computational field in an attempt to solve the discretized governing equations. Although the final form for governing equations were obtained in term of the body-fitted coordinates system. In the same converted coordinate, the boundary conditions will be applied. The boundary conditions of the current investigation are the one inlet, two outlets, target surface (bottom wall), and the top wall. These boundary conditions are described in details as shown follows:

- Inlet boundary

  In this boundary (Inlet of slot jet region), the distributions of the uniform temperature and the uniform velocity are usually assumed as follows:

$$v = v_{in},\ u = w = 0, \text{and } T = T_{in} = 298\ K \tag{3.69}$$

  Furthermore, the turbulent kinetic energy (k_{in}) and its dissipation rate (ε_{in}) are determined from empirical correlation depending on the velocity at inlet and the turbulence intensity value (I_o) and hence the inlet condition can be given as [59]:

$$k = k_{in} = \frac{2}{3}(I_o \,.\, v_{in})^2 \tag{3.70}$$

$$\varepsilon = \varepsilon_{in} = \frac{C_\mu^{3/4} k_{in}^{3/2}}{(0.07 D_h)} \tag{3.71}$$

  Here ($C_\mu = 0.09$) is given in equation 3.15. In present investigation, the turbulence intensity value (I_o) at the inlet of slot jet region is 0.05 [60].

❖ Outlet boundary

Two outlets of the channel, the flow leaves the computational field in the left and right directions. The suitable location of the outlet boundary at the zone of fully developed occurs in the flow direction. Moreover, in a direction normal for the outlet boundary, the gradients for all variables are expressed by:

$$\frac{\partial u}{\partial \xi} = 0 \,, \frac{\partial v}{\partial \xi} = 0 \,, \frac{\partial T}{\partial \xi} = 0 \,, \frac{\partial k}{\partial \xi} = 0 \,, \text{and } \frac{\partial \varepsilon}{\partial \xi} = 0 \tag{3.72}$$

❖ Bottom wall and top walls boundaries

The condition of the uniform heat flux is applied only along the target surface (bottom wall) of the channel. The no-slip condition for velocities can be applied along the target surface (bottom wall) and top walls (on the left and right of the slot jet) of the channel. Also, the turbulent kinetic energy (k) and its dissipation rate (ε) equal to zero [47, 49], while the top walls are assumed to be adiabatic as follows:

$$u = 0 \,, v = 0 \,, k = 0 \,, \text{and } \varepsilon = 0 \tag{3.73}$$

$$\left.\frac{\partial T}{\partial \eta}\right|_w = \frac{q_w}{k_f} \,, \qquad \text{(along target surface)} \tag{3.74}$$

$$\left.\frac{\partial T}{\partial \eta}\right|_w = 0 \,, \qquad \text{(along top walls)} \tag{3.75}$$

Here, w indicates that the normal for the wall. Also, the heat flux (q_w) equal to $8000\ W/m^2$ that applied to target surface in the present investigation. The normal derivatives for temperature at wall in equations 3.74 and 3.75 can be obtained by:

$$\left.\frac{\partial T}{\partial \eta}\right|_w = \frac{1}{J\sqrt{q_{22}}}\left[q_{22}\frac{\partial T}{\partial \eta} - q_{12}\frac{\partial T}{\partial \xi}\right] \tag{3.76}$$

Where J, $q_{22,}$ and q_{12} are given in Appendix A in equations A.9, A.23, and A.24, respectively. In addition, the pressure value at the outlet boundary (left and right of the channel) equals zero, while the values of pressure at the inlet and walls can be found by linear extrapolation of the interior points for the pressure. Furthermore, the boundary conditions are shown in Figure 3.7 as follows:

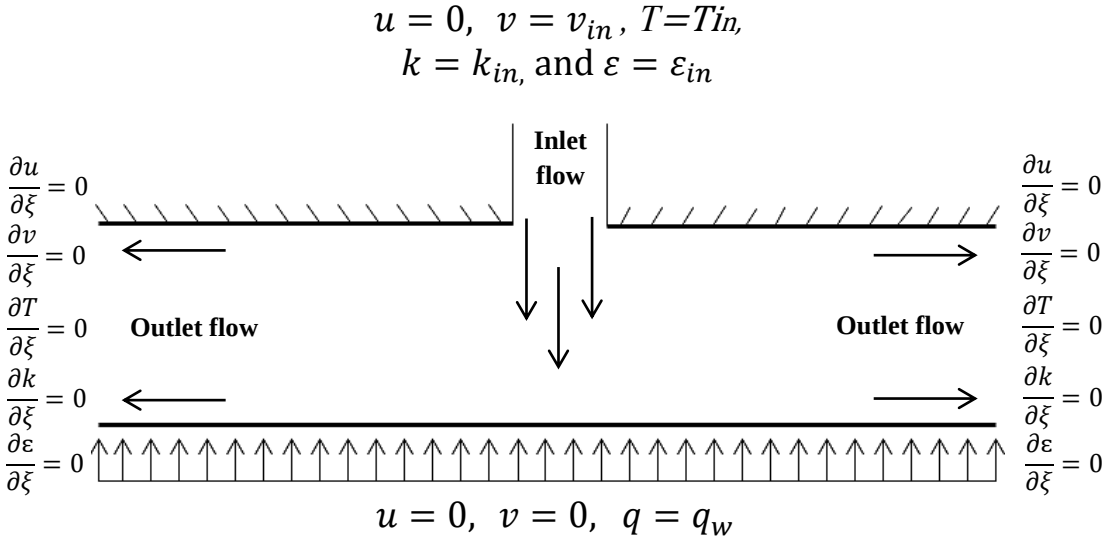

Figure 3.7: The boundary conditions of the present study.

3.14 Numerical Calculations

3.14.1 Local and Average Nusselt Numbers

After solving the discretized governing equations, the fields of the temperature and flow that are then utilized to compute the local and average Nusselt number are obtained. Thus, the local Nusselt number can be given as [61]:

$$Nu_{\xi} = \frac{D_h}{k_f} \frac{q_w}{(T(\xi)_w - T(\xi)_b)} \tag{3.77}$$

Here, $T(\xi)_w$ indicates that the temperature distribution only along the target surface (bottom wall) and $T(\xi)_b$ represents that the bulk fluid temperature that can be computed as follows [61]:

$$T(\xi)_b = \frac{\iint_A \rho_f u C_p T \, dA}{\iint_A \rho_f u C_p \, dA} \tag{3.78}$$

The average Nusselt number is obtained by:

$$Nu_{av} = \frac{1}{L}\int_0^L Nu_\xi \, d_\xi \tag{3.79}$$

Moreover, the percentage of average Nusselt number enhancement can be expressed as below:

$$Nu_{enh}(\%) = \left[\frac{Nu_{av,r} - Nu_{av,s}}{Nu_{av,s}}\right] \times 100 \tag{3.80}$$

3.14.2 Thermal-Hydraulic Performance Factor

It is necessary to show how the enhancement techniques will affect the thermal-hydraulic performance for jet impingement. Moreover, the performance evaluation criteria *PEC* is employed to assess the enhancement techniques which are utilized in the present investigation. It can be expressed as follows [59]:

$$PEC = \frac{(Nu_{av,r}/Nu_{av,s})}{(f_r/f_s)^{1/3}} \tag{3.81}$$

Where, (f) indicates that the Darcy friction factor in equation 3.81 which can be given as [62]:

$$f = \Delta p \frac{D_h}{L} \frac{2}{\rho_f u^2} \tag{3.82}$$

In above equation, Δp is the pressure drop and thus it can be defined as:

$$\Delta p = p_{in} - p_{out} \tag{3.83}$$

CHAPTER FOUR
EXPERIMENTAL SET-UP

4.1 Overview

In this chapter, the experimental set-up and the operational procedure utilized to perform the experimental work are presented. This chapter offers the description of the experimental instruments as well as the test sections utilized in the current investigation. The procedure of the data collection is described. This is also followed by uncertainties calculation in the experimental measurements.

4.2 Experimental Set-up

In order to validate the current numerical results, experiments are conducted to measure convective heat transfer and pressure drop in the jet impingement employing water, in according to those for a numerical investigation. The experimental set-up mainly consists of the water tank, pipes, water pump, control valves, water flow meter, test section, thermocouples type-K, electrical heater, AC power regulator, digital multimeter, thermostat, and digital data logger as depicted in Figure 4.1 and Appendix B. in addition, the schematic diagram of the experimental set-up as illustrated in Figure 4.2.

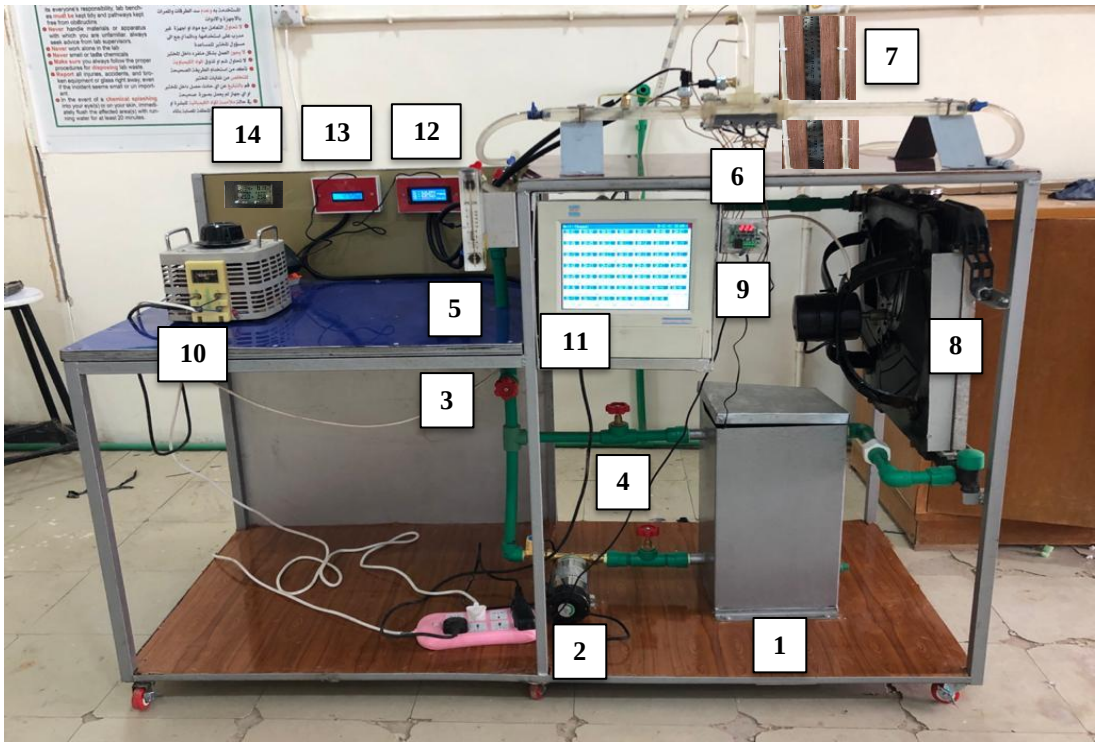

Figure 4.1: photograph of the experimental set-up.

1. Water tank
2. Water Pump
3. Control valve
4. Bypass
5. Flowmeter
6. Test section
7. Tube manometer
8. Radiator and Fan
9. Digital thermostat
10. Power regulator
11. Digital data logger
12. Pressure sensor
13. Water flow sensor
14. Digital multimeter

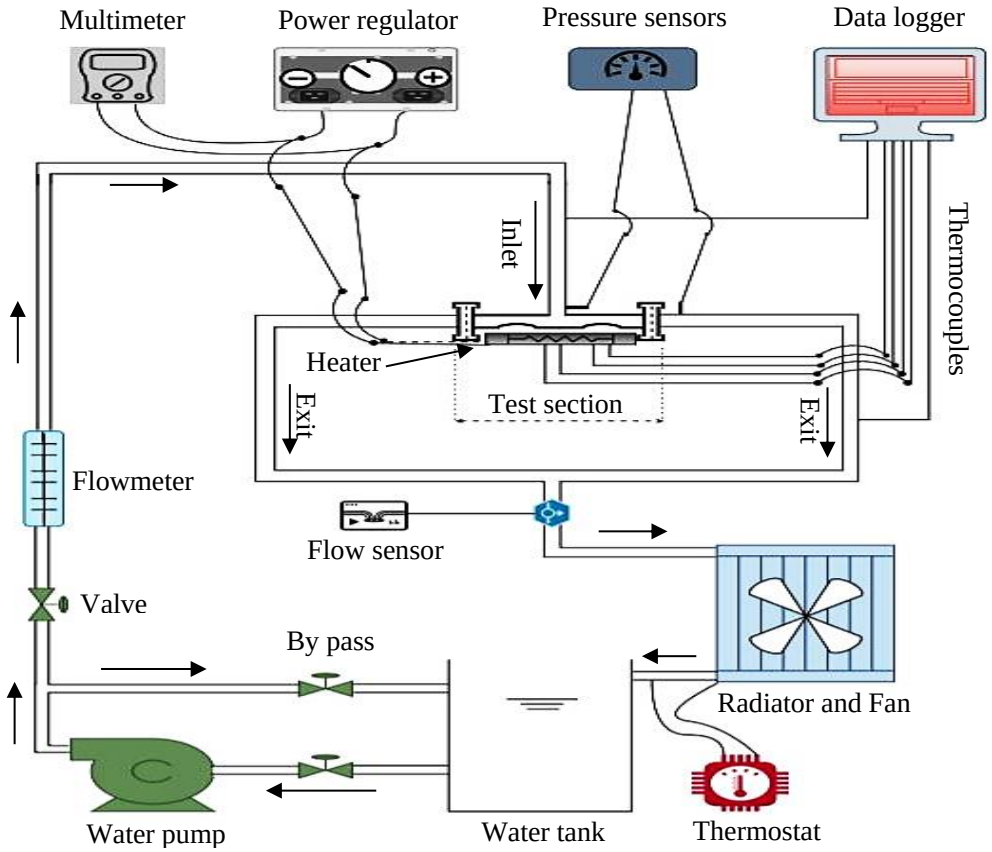

Figure 4.2: Schematic diagram of the experimental set-up.

4.2.1 Test Sections

In this part, the test section involves the lower and the upper surfaces and two side walls. The lower (smooth and ribbed) target surfaces for the test section were designed by using (Soildwork Program) and fabricated from an aluminum plate with dimensions of 122 mm long (110 mm heated part and 12 mm flanges thickness), 35 mm depth (30 mm heated part and 5 mm axial groove side walls), and 6 mm thick. Therefore, the ribs were created by using (CNC) machine as presented in Appendix B. Also, the dimensions of ribs of 10 mm length (L), 30 mm depth (Z), and 2 mm height (a). The upper surface and side walls of the test section were made of acrylic (sheet), 6 mm thick, to minimize the heat losses to the surrounding. The side walls have two axial grooves with deep of 2.5 mm

(over the length of the side wall) to avoid leakage of the working fluid (water) from the test section. The target surface and the upper surface of the test section were installed in the axial grooves formed in the side walls employing thermal epoxy. The lower surface was heated utilizing an electrical heater while the others were unheated (insulated) walls in the experiments. Three various shapes of ribs such as wing ribs, flat ribs, and oval ribs as well as the smooth surface were fabricated and tested in the present investigation, see Figure 4.3.

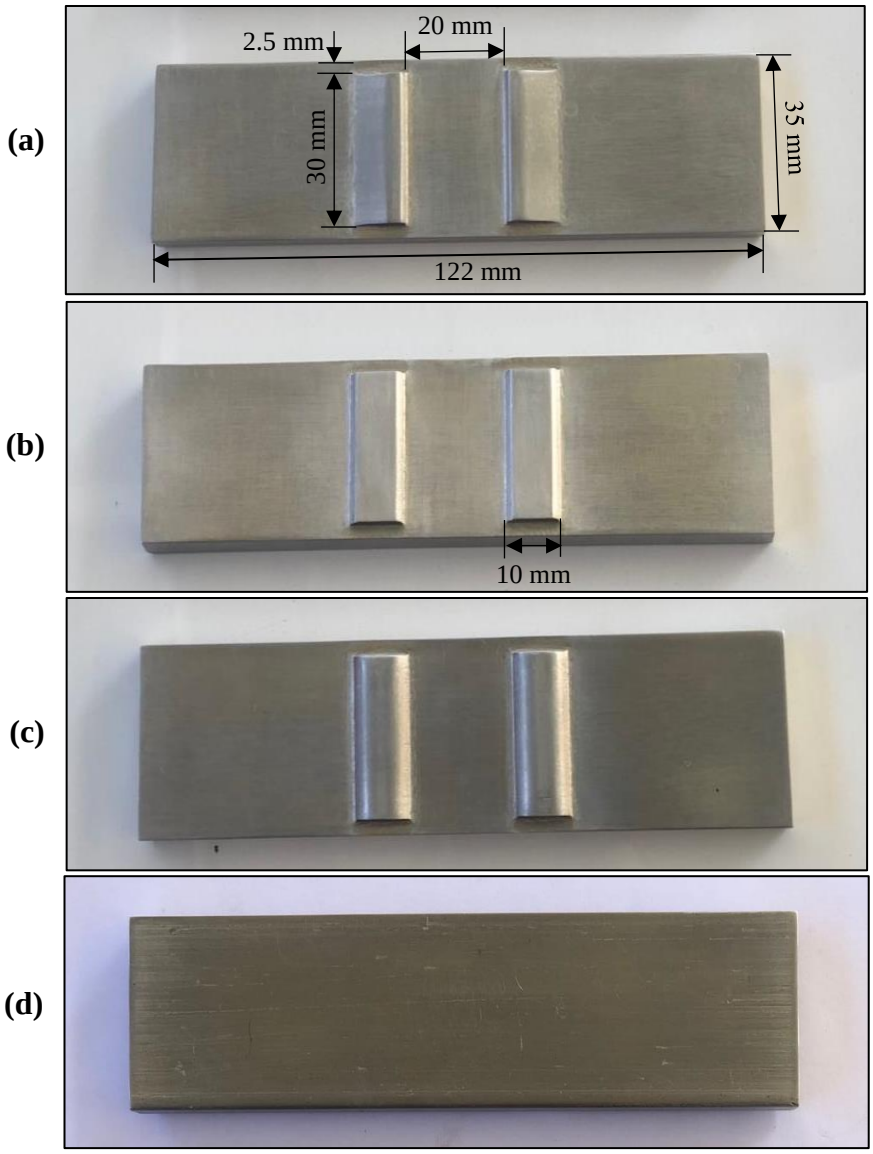

Figure 4.3: Different shapes of ribs for test section, (a) wing ribs (b) flat ribs, (c) oval ribs, and (d) smooth target surface.

On the other hand, the fixing method of the impinging target surface in the axial grooves for the acrylic sheets is shown in Figure 4.4.

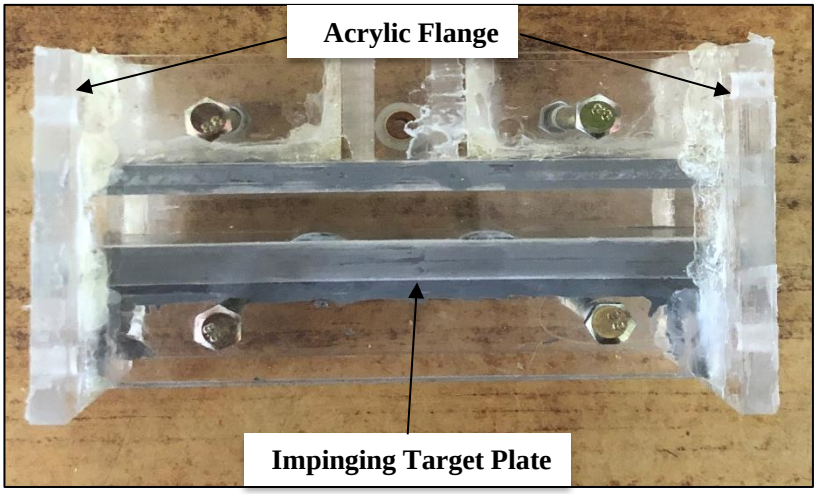

Figure 4.4: Front view of test section after installation.

4.2.2 Inlet Slot and Exit Sections

In order to create suitable conditions of the inlet flow and the outlet flows for the test section, three straight (inlet slot and two exits) sections have been used. The inlet slot section was located in the middle of the test section while the two exits were located at the right and left of the test section. These sections were made with a thickness of 6 mm from acrylic sheets. The inlet slot section has a vertical length of 250 mm and a cross-sectional area of (30 × 10 mm) (Z × W) while the axial length of two exits sections was 150 mm and the cross-sectional area of two exits was (30 × 10 mm) (Z × H). The two exit sections were fixed at the ends of the test section using the flanges, which were made of acrylic sheets of 6 mm thickness and it was installed on these sections utilizing thermal epoxy. However, exit sections were connected directly to the test section employing these flanges with fastening equipment; bolts and nuts, as shown in Figure 4.5 and Appendix B. Therefore, it is easy to change the

test section with other geometric shapes. Four different shapes including the smooth surface shape were tested.

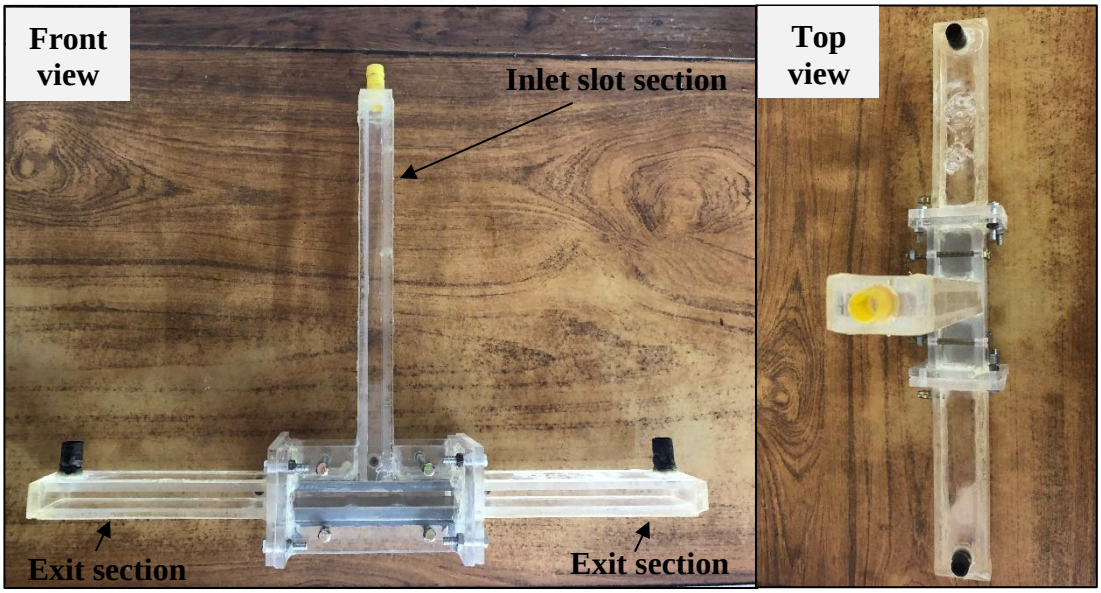

Figure 4.5: Front and top views for test section that connected with exit sections.

In order to avoid leakage of the working fluid from these junctions, a thin layer of clear (EASYSEAL EZ 1200) silicone sealant (gasket) was applied at the faces of the flanges. Also, all sections (test section, inlet, and exit sections) were fabricated by CNC machine as presented in Appendix B.

4.2.3 Thermocouples

The thermocouples (type-K) with 1 mm diameter of the probes were employed, which is considered the most common thermocouple type, in order to measure the temperatures of the bulk base fluid at the inlet slot and outlets of the test section and the surface temperatures of the target surface. Moreover, the temperature of the inlet bulk working fluid (water) was measured using two thermocouples inserted in the inlet slot-jet section at a distance of 100 and 200 mm, respectively. While, the other four thermocouples were that inserted into the two exit sections (two

thermocouples were inserted in the left exit section and the other two thermocouples were inserted in the right exit section) at distance between two thermocouples of 30 mm for two exit sections, to measure the working fluid outlet temperatures. On the other hand, the five thermocouples were installed on the back face of the impingement target surface (lower surface) of the test section to measure the temperature distribution on the target surface. The thermocouples were inserted into holes that drilled with a diameter of 2 mm and the depth of holes equal 4 mm on the back side of the lower surface (on the aluminum plate) and then installed utilizing an epoxy. The holes were distributed evenly and centered on the back face of the impingement target surface as depicted in Figure 4.6. These holes were located at a distance of 8, 30.5, 53, 75.5, and 98 mm. Furthermore, the points of temperature calibration for a single thermocouple were identified to be (0, 30, 60, and 90 ºC). The single thermocouple can be considered as the reference thermocouple while the other thermocouples are calibrated based on the reference thermocouple. The calibration results were displayed in Figure 4.7.

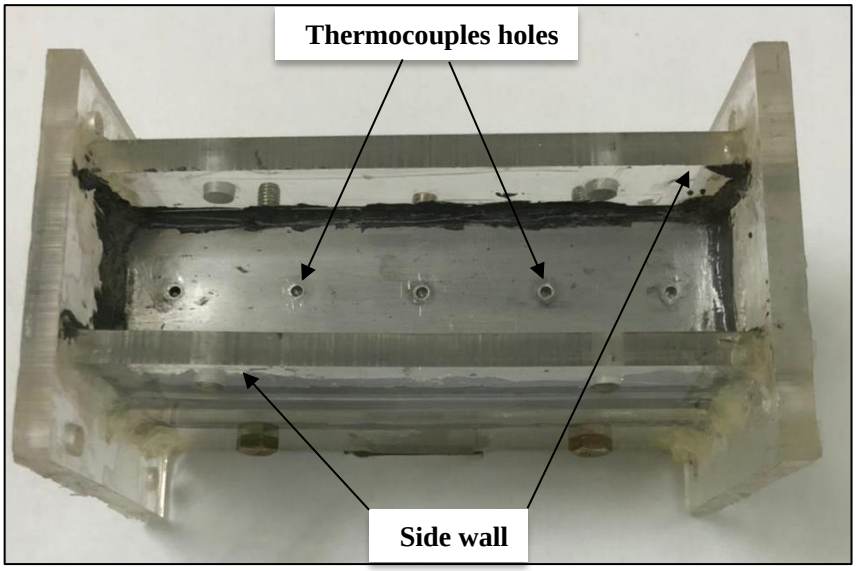

Figure 4.6: Bottom view for test section showing holes of thermocouples.

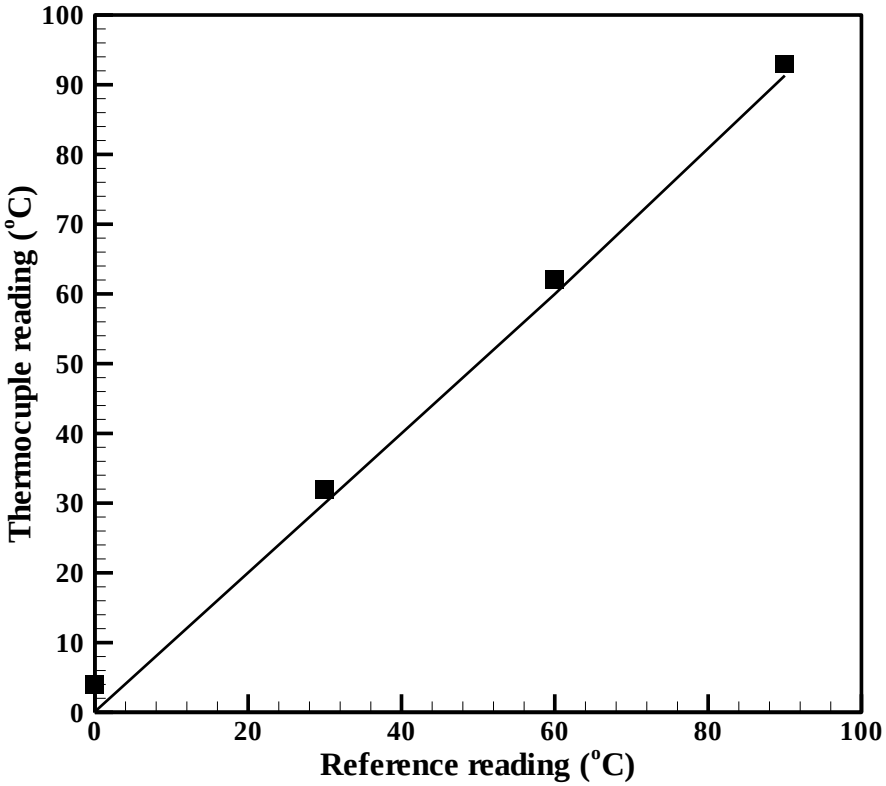

Figure 4.7: Calibration of thermocouple.

4.2.4 Electrical Heater and Power Regulator

To heat the impinging target surface of the test section, an electrical heater plate was attached to the back side of this surface. The electrical heater dimensions were 26 mm width, 106 mm length, and 4 mm thickness. The electrical heater was designed on the basis of the required power in the experimental work, load voltage (0-220 V), and the power (320 Watt). The electric heater has five holes with a diameter of 2 mm, which were employed to insert the thermocouples during holes as illustrated in Figure 4.8. However, the heater was jointed to the AC power regulator (Variac AC) unit which was utilized to control the current and input voltage to the heater. The Variac AC was connected with the stabilizer to maintain the constant voltage to be generated by the electrical heater. Also, the test section was surrounded by three layers of fiber glass insulation with a

thickness of 30 mm, in order to avoid the heat transfer from the test section to the outside environment, see Appendix B.

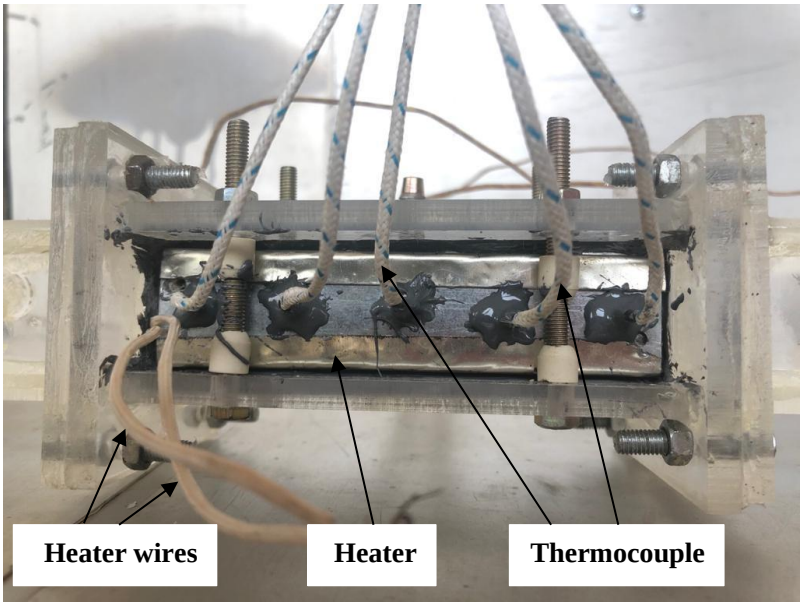

Figure 4.8: Installation of test section.

4.2.5 Water Pump, PPR Pipes, and Water Tank

In order to push the working fluid into the test section, a water pump (15WBX-15), the maximum flow rate of (26 LPM), a maximum head of 15m, and (0.15 PH, 0.6 A, 220-240 V, and 50 HZ) was used. The water pump was connected to the water tank and the test section by using plastic hollow pipes made of (Polypropylene Random Copolymer) that do not allow heat transfer into the environment. The water tank was designed with dimensions (250 × 250 × 400 mm) and a capacity of 25 liters. Moreover, three valves were used; after and before the water pump and on the bypass line, as shown in Figure 4.1. The amount of the water flow is controlled by the control valve after the pumped as well as the bypass valve. In experiments, the working fluid temperature was 25 ºC at the test section inlet, as illustrated in Appendix B.

4.2.6 Heat Exchanger

A heat exchanger with dimensions of (450 × 450 mm) was used to cool the working fluid. The upper part of the radiator contains an inlet through which the working fluid exits of the test section and passes to be cooled, and pushed from the outlet of the lower part connected to the water tank from the upper side. The fan consists of four blades that draw air from the surrounding and push it towards the radiator for the purpose of cooling the working fluid inside the radiator. It has been installed on the radiator using fastening equipment and separated by dampers to prevent vibration from the fan, as described in Appendix B.

4.3 Measurement Devices

To evaluate the performance of the jet impingement, various parameters such as the water flow rate, temperature of (inlet, outlet, and impinging target surface) for test sections, and pressure drop were measure.

4.3.1 Flowmeter and Flow Sensor

The water flow meter (LZM-15T) was fixed between the water pump and the inlet of the slot-jet section to determine the water flow rate. The water flow rate range of (2-18 LPM) with an accuracy of ±5.0% FS. To calibrate the water flow meter, the method of stopwatch and the laboratory glass beaker for determining the fluid flow rate was employed. In addition, a digital water flow sensor (YF-S201), the ranged (1-30 LPM), was placed between the final exit sections resulting from the combination of the two exit sections with the radiator. The flow meter and flow sensor of the water used in this study are presented in Appendix B.

4.3.2 Manometer and Pressure Sensor

The tube manometer was attached to two pressure taps installed on the inlet and outlet sections in order to measure the pressure drop. Also, the flow pressure sensor was created and connected to the (LCD) display screen using the Arduino to read the inlet and exit pressures. The pressure values resulting from the pressure sensor were not adopted due to the instability in the results and replaced by the tube manometer method. The pressure sensor and tube manometer have been displayed in Appendix B.

4.3.3 Data Logger

Generally, all thermocouples mounted on the impinging target surface, inlet slot section, and two exit sections for the test section were linked to 48-channels digital data logger (KH448G-U-NN Paperless Recorder) to measure the temperatures of bulk fluid and the target surface. The digital data logger is illustrated in Appendix B.

4.3.4 Thermostat

The temperature controller (thermostat) was connected with an accuracy of (0.1 ºC) to the fan, and the thermocouple in the thermostat was linked to the water tank for the purpose of controlling the inlet temperature to the test section. When the temperature reaches more than 25 ºC, the thermostat will connect the electrical circuit to run the fan. Also, the thermostat was calibrated with the reference thermocouple. The thermostat is illustrated in Appendix B.

4.3.5 Multimeter

A digital multimeter (PZEM-061) has been joined to the electrical heater circuit for measuring voltage and current that delivered to the electrical

heater. This device operates under a voltage range (AC 80 to 260 V), current (0 to 100 A), and frequency (50 to 60 Hz). It has been calibrated in the electrical engineering department. The digital multimeter is displayed in Appendix B.

4.4 Experimental Procedure

For the purpose of conducting practical experiments, the following steps were followed:

- ✓ The tank container was filled with the primary liquid (water), then it was pumped by the water pump attached at the bottom of the tank to the flowmeter.
- ✓ The required flow rate was controlled through the control valve installed under the flowmeter to the test section. Therefore, the working fluid was discharged through the two exit sections and then collected in one outlet.
- ✓ The working fluid coming out from the test section was discharged into the radiator for cooling by a fan connected to the thermostat when the temperature of the water tank reaches higher than (25 ºC) to obtain the required temperature.
- ✓ Also, the cold water was stored in the tank container and returned pumping to the test section.
- ✓ After the flow was stabilized, the electric heater is turned on, set it to the desired heat flux using a digital multimeter waited for a time period (one hour) for the temperature values displayed by the data logger to stabilize, which displays the temperatures of the impingement target surface, inlet jet and exit for the test section.

- ✓ Additionally, the pressure drop values were taken by measuring the difference between the inlet and exit pressures (head) in the tube manometer.
- ✓ This process was repeated periodically for a whole range of flow rates (i.e., jet Reynolds number of 3000, 4000, 5000, 6000, 7000, and 8000).
- ✓ In addition, the experimental work was used different shapes of test sections such as smooth target surface, wing, oval and flat ribs.

4.5 Data Reduction

The average Nusselt number, friction factor, and performance evaluation criteria of the ribs shapes can be measured based on collected experimental data such as the temperature of bulk fluid, target plate temperatures, flow rate, pressure drop, current, and voltage. On the other hand, the heat provided to the electrical heater is expressed by:

$$Q_{heater} = I \,.\, V \tag{4.1}$$

here, *(I)* and *(V)* indicate the current and voltage, respectively. Further, the heat received by the working fluid from the test section is expressed as follows [63]:

$$Q_f = \dot{m}_f \, C_{p,f} \left(T_{b,o} - T_{b,in}\right) \tag{4.2}$$

where $\dot{m}_f$ is the mass flow rate of working fluid, $C_{p,f}$ is the specific heat of working fluid and $T_{b,o}$ and $T_{b,in}$ represent the mean temperatures of bulk working fluid at outlet and inlet jet for test section, respectively. However, the average heat transfer coefficient is given as follows [63]:

$$h_{av} = \frac{Q_f}{A_s(T_{w,av} - T_{b,av})} \tag{4.3}$$

here, A_s is the area of the impingement target surface, $T_{w,av}$ is the mean wall temperature and $T_{b,av}$ the mean bulk working fluid temperature. Hence, the average Nusselt number can be determined as follows [63, 64]:

$$Nu_{av} = \frac{h_{av}\, D_h}{k_f} \tag{4.4}$$

where, k_f is the thermal conductivity of working fluid, D_h is the hydraulic diameter of the slot jet width which can be expressed as follows:

$$D_h = W \tag{4.5}$$

From equations (4.1) and (4.2), the heat loss out of thermal insulation can be given as follows:

$$Q_{loss} = Q_{heater} - Q_f \tag{4.6}$$

Hence, the error of heat balance, which is computed as:

$$\left(\frac{Q_{loss}}{Q_{heater}}\right) \times 100\% \tag{4.7}$$

The friction factor (f) can be calculated as follows [65]:

$$f = \frac{2D_h\, A_c^2\, \Delta p\, \rho_f}{L\, \dot{m}^2} \tag{4.8}$$

$$\dot{m} = \rho_f \,.\, v_{in} \,.\, A_c \tag{4.9}$$

Furthermore, the jet Reynolds number can be expressed as follows:

$$Re = \frac{\dot{m}\, D_h}{\mu_f\, A_c} \tag{4.10}$$

where, ρ_f is the density of working fluid, $\dot{m}$ is the mass flow rate which is obtained from the flowmeter, and μ_f is the viscosity of working fluid. A_c is the cross-section area of the slot jet which is given as:

$$A_c = W \,.\, Z \tag{4.11}$$

Here, W is the width of slot jet and Z is the depth of channel.

4.6 Uncertainty Analysis

In the present investigation, the experimental uncertainties of the key parameters such as jet Reynolds number, friction factor, and average Nusselt number were calculated according to the Kline and McClintock method [66]. For example, given the key parameters, *R*, as follows:

$$R = R(X_1,\ X_2,\ X_3, \cdots\cdots\cdots, X_n) \tag{4.12}$$

Here, $X_1,\ X_2,\ X_3$ and X_n are the independent measured parameters. Thus, the uncertainty of R is computed as below:

$$U_R = \pm\sqrt{\left(\frac{\partial R}{\partial X_1}\ U_{X_1}\right)^2 + \left(\frac{\partial R}{\partial X_2}\ U_{X_2}\right)^2 + \left(\frac{\partial R}{\partial X_3}\ U_{X_3}\right)^2 + \cdots\cdots + \left(\frac{\partial R}{\partial X_n}\ U_{X_n}\right)^2} \tag{4.13}$$

Where, $U_{X_1}, U_{X_2}, U_{X_3}, \cdots\cdots, U_{X_n}$ are the independent parameters uncertainties. Also, the partial derivatives $\frac{\partial R}{\partial X_1}$, $\frac{\partial R}{\partial X_1}$, $\frac{\partial R}{\partial X_1}$, $\cdots\cdots$, $\frac{\partial R}{\partial X_n}$ are computed from equation 4.12

Furthermore, the uncertainty in measurements was computed for the wing ribs with the highest jet Reynolds number of (Re=8000). The procedure of sample calculations for the key parameter's uncertainty is illustrated in Appendix C. It was also found that the uncertainties in jet Reynolds number (Re) and friction factor (f), as well as average Nusselt number (Nu_{av}), were within $\pm$ 5.20%, $\pm$ 10.808%, and $\pm$ 8.427%, respectively.

CHAPTER FIVE
RESULTS AND DISCUSSION

5.1 Overview

This chapter introduces the experimental and numerical results achieved in the current investigation. The first section in this chapter focuses on the grid independence test and then on the validation of the numerical solution given in chapter three. Furthermore, the comparison of the experimental data with the numerical results is displayed. Moreover, the influences of various parameters such as jet Reynolds number, ribs heights, ribs locations, and ribs shapes on heat transfer and flow characteristics have been displayed and studied in this chapter. Also, the results of the local Nusselt number and the contours are displayed in the right half domain because the physical domain is symmetric around the Y-axis.

5.2 Grid Independence Test

Generally, the grid resolution determines the accuracy of the numerical results. In order to test the mesh independence for the current investigation, five various mesh sizes which are 361×51, 461×61, 561×71, 661×81, and 761×101 have been selected. The average Nusselt number at the impinging target surface and the average friction factor for different jet Reynolds number at $a = 2$ mm and $d = 20$ mm using flat ribs are illustrated in Figure 5.1 and 5.2, respectively. It was found that the mesh size of 661×81 (i.e., 661 grid nodes in the X-direction and 81 grid nodes in the Y-direction) can give the grid independence results.

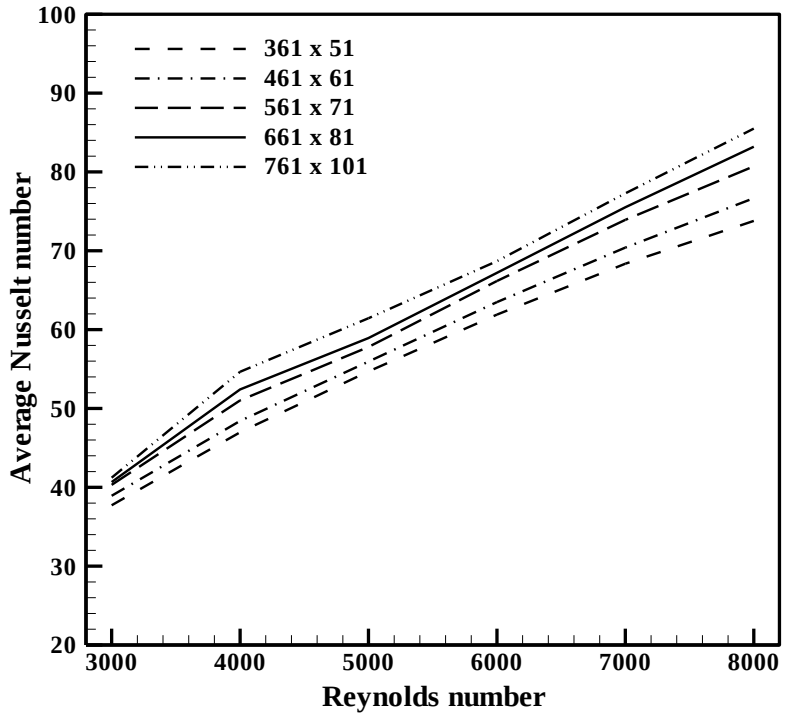

Figure 5.1: Average Nusselt number with jet Reynolds number for various mesh sizes at a=2 mm and d=20 mm.

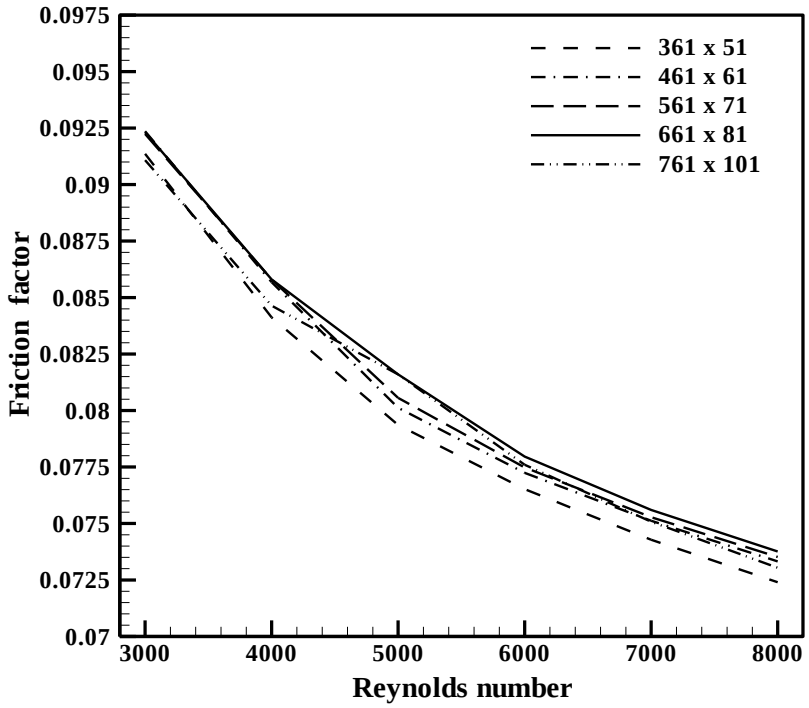

Figure 5.2: Friction factor with jet Reynolds number for various mesh sizes at a=2 mm and d=20 mm.

5.3 Code Validation

Generally, several comparisons with various previous investigations have been carried out in order to check the accuracy of the CFD code developed in the present investigation. In this section, a first comparison has been presented between the current study and the numerical study of Manca et al. [15]. Figure 5.3 shows the comparison of the average Nusselt number of a two-dimension confined impinging slot-jet for a previous numerical investigation with the present results. In their investigation, it has been assumed that the smooth impinging target surface kept at the jet Reynolds which; varied between 5000 and 9000 at a constant wall temperature of 343 K, inlet jet temperature of 293 K, slot width of 6.2 mm, channel height of 24.8 mm and the non-dimensional jet-to-target surface spacing of 4. The working fluid was water. It was noted that good results have been achieved. Also, the deviation between these results was 6.5%.

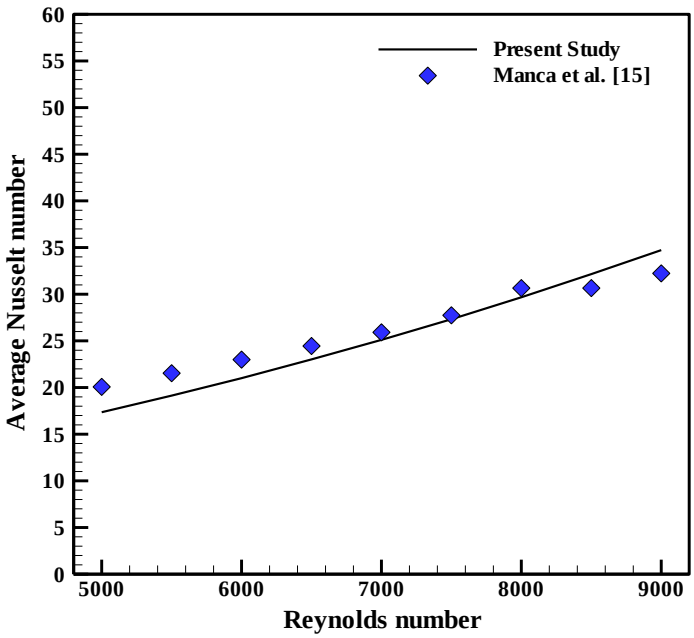

Figure 5.3: The comparison of the average Nusselt number for present study with numerical investigation of Manca et al. [15].

Furthermore, the local Nusselt number for the single-slot impinging nozzle from stagnation point to the channel exit has been presented and

compared with a numerical investigation of Sharif and Banerjee [20]. Figure 5.4 illustrates the variation of the local Nusselt number at jet Reynolds number of 5000, channel height of 24.8 mm, slot nozzle width of 6.2 mm, and nozzle to target spacing of 6. They assumed that the inlet temperature of nozzle was 373 K, impinging target plate under constant temperature of 338 K, and utilized air as the working fluid. It is found that the results are in a good agreement.

Moreover, the average friction factor and average Nusselt number at the stationary impinging target surface of the impinging confined slot jet have been calculated and compared with the numerical results of Buonomo et al. [23]. Figure 5.5 and 5.6 display the friction factor and the average Nusselt number, respectively at the jet-to-target plate spacing of 6 for jet Reynolds numbers between 5500 and 8500. They assumed that the target surface under constant temperature of 338 K and the water as a working fluid. It found that these results are in a good correspondence.

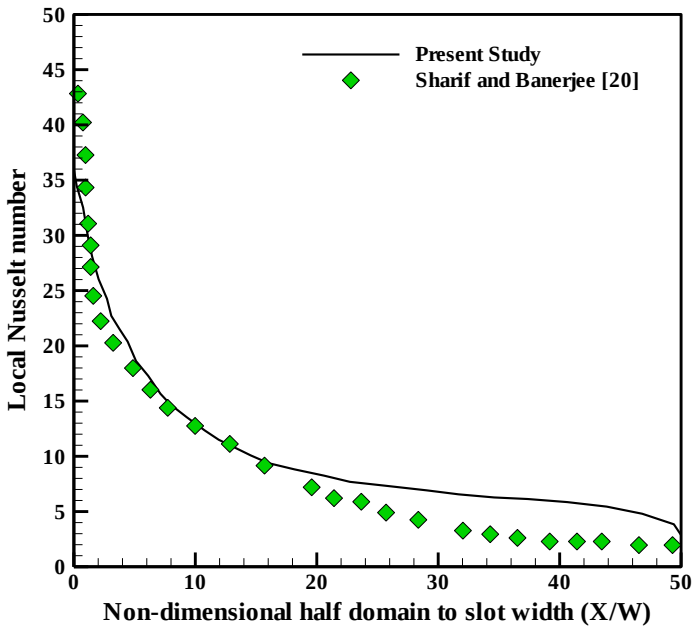

Figure 5.4: The comparison of the local Nusselt number for present study with the numerical investigation of Sharif and Banerjee [20].

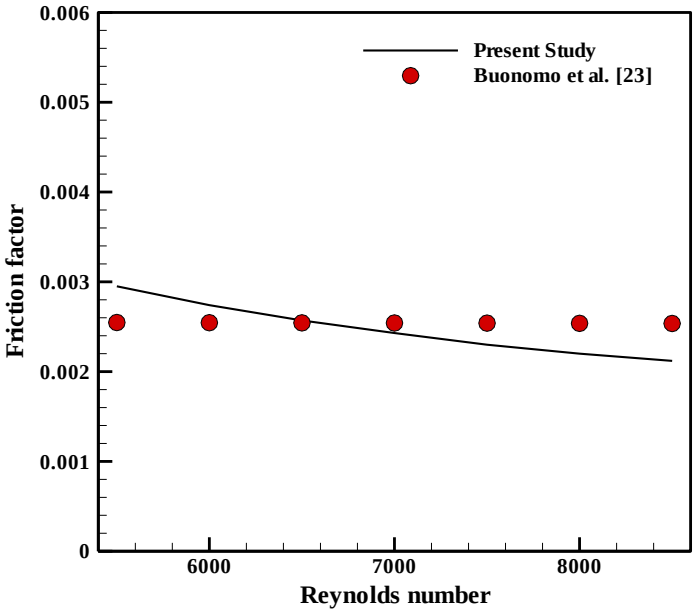

Figure 5.5: The comparison of the friction factor for present study with the numerical investigation of Buonomo et al. [23].

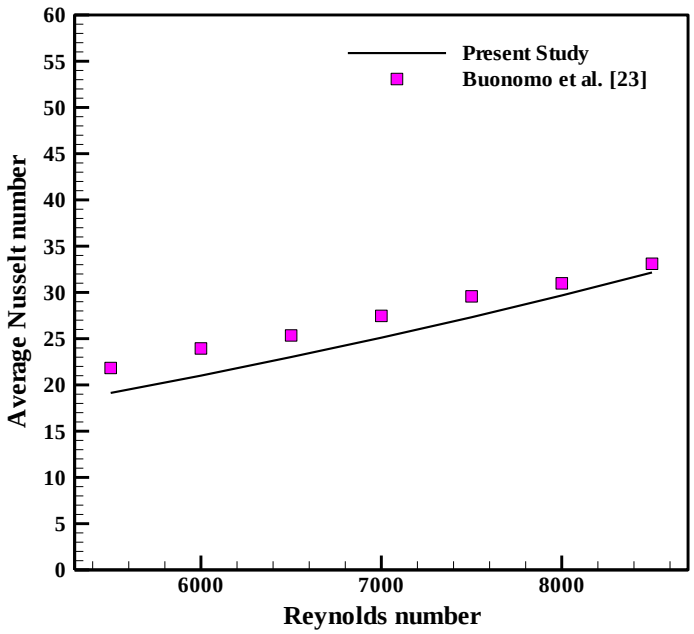

Figure 5.6: The comparison of the average Nusselt number for present study with the numerical investigation of Buonomo et al. [23].

In addition, the average total entropy generation is the two-dimensional corrugated channel has been displayed and compared with a numerical investigation of Rashidi et al. [57]. They assumed that the upper and lower surfaces of the corrugated channel were kept at a constant heat flux of

(8000 $^{W}/_{m^2}$), and the fluid inlet temperature of 298 K. The results were obtained at Reynolds number of 5500, non-dimensional wave amplitude of 0.3, and non-dimensional wavelength range of 1, 2, and 3 as well as the water was employed as a working fluid. It was found that the comparison between the present results and the previous results has good consistency as shown in Figure 5.7. Concerning the average total entropy generation, there was a good concord between these investigations.

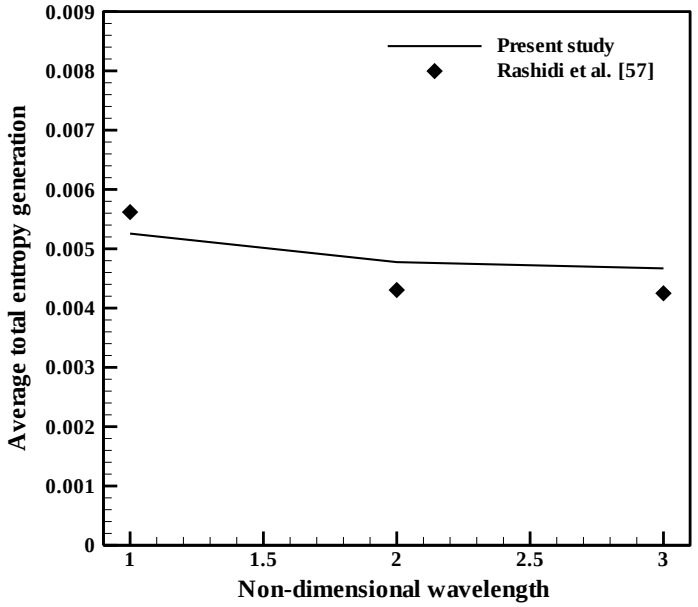

Figure 5.7: The comparison of the average total entropy generation for present study with the numerical investigation of Rashidi et al. [57].

Also, the local Nusselt number of the confined air slot-jet impinging from the impinging point into the end of the target surface was determined and compared with the experimental results of Cadek [67] as well as Gardon and Akfirat [68]. Figure 5.8 shows the local Nusselt number with non-dimensional half domain to slot width at jet Reynolds number of 11,000, jet-to-target surface spacing of 6, flat target plate temperature of 338 K, the air fluid inlet slot-jet temperature of 373 K, and jet width of 6.2 mm. Regarding those comparisons, it was reported that the results have a good consistency.

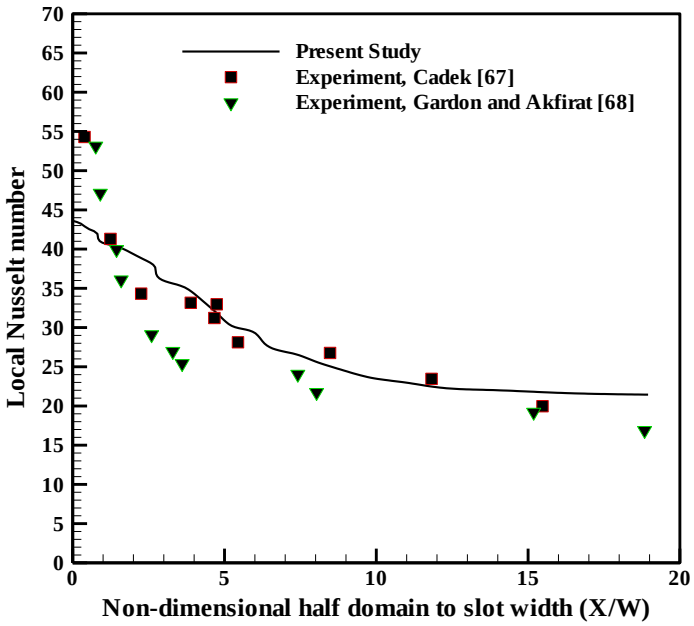

Figure 5.8: The comparison of the local Nusselt number for present study with the numerical investigation of Cadek [67], and Gardon and Akfirat [68].

5.4 Comparison Between Numerical and Experimental Results

The effect of several parameters such as; average Nusselt number, pressure drop, average Nusselt number enhancement, and performance evaluation criteria are investigated for the three different shapes of the ribs as well as the smooth target surface. The experiments were conducted at the height of the ribs ($a = 2$ mm) and the distance from the stagnation point to the rib ($d = 10$ mm) over the range of jet Reynolds number (3000 - 8000). Figure 5.9 compares the average Nusselt number obtained from the experimental results with that obtained from the numerical results. Three different geometries of the ribs have been investigated which are wing, oval, and flat ribs in addition to the smooth target surface. Generally, it can be noted that the average Nusselt number increases with jet Reynolds number for all shapes of ribs as well as the smooth target surface, as expected, for both the numerical and experimental results. This is because when jet Reynolds number increases, the temperature drop at

the target surface increase and hence increase the heat transfer rate. Furthermore, the wing ribs have the highest average Nusselt number for a given jet Reynolds number followed by the oval ribs and flat ribs due to the big size of re-circulation regions that grow in the vicinity between the upper wall and the lower target surface and hence improve the fluid mixing. Moreover, the smooth target surface (without ribs) has the lowest Nusselt number as compared to the using ribs due to the poor fluid mixing. It is also found that the average deviation between the current numerical and experimental result is around 9.12%

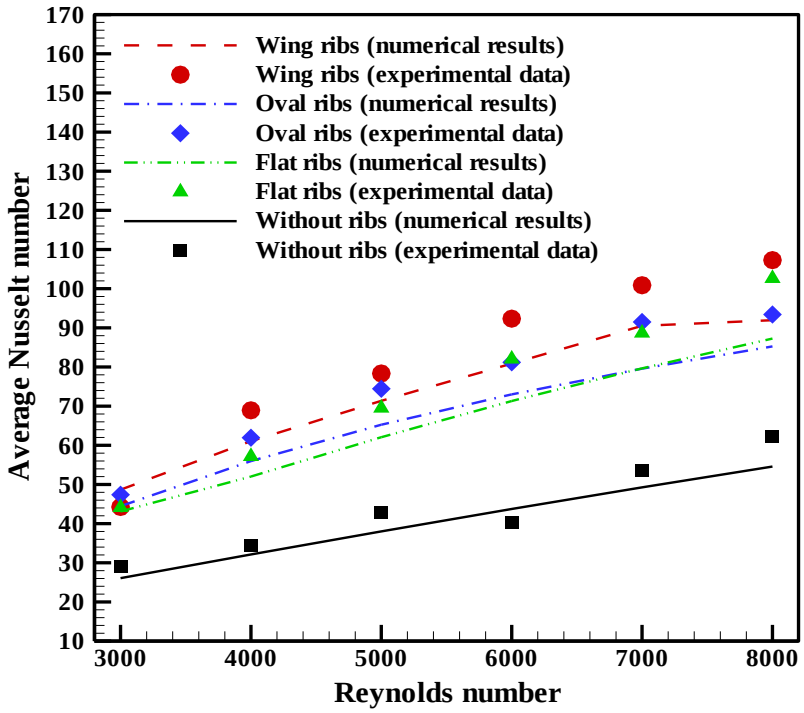

Figure 5.9: Average Nusselt number versus jet Reynolds number for various shapes of ribs at a=2 mm and d=10 mm.

Figure 5.10 shows the comparison between the pressure drop obtained from experimental data with the numerical results. As expected, the pressure drop obtained numerically and experimentally increases with jet Reynolds number for all shapes of ribs as well as the smooth target surface. It was found that the wing ribs have the highest pressure drop

followed by the oval ribs and flat ribs due to the high velocity gradient at the impinging target surface particularly in the ribs zones, as well as the influence of recirculation zones that created at the confined upper surface and the target surface. The smooth impinging target surface (without ribs) gives minimum pressure drop, as predicted. Furthermore, the average deviation between the experimental data and numerical results was about 11.14%.

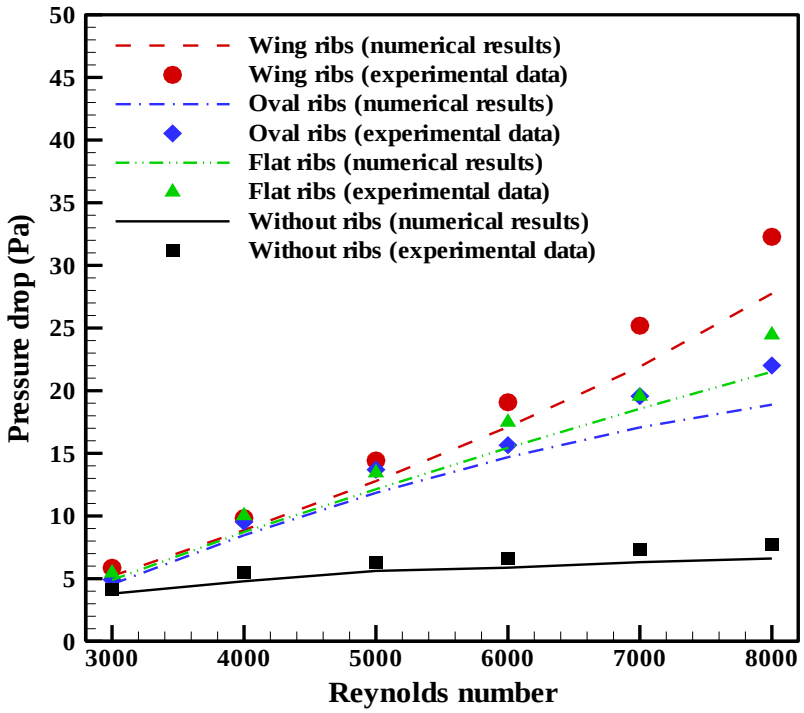

Figure 5.10: Pressure drop versus jet Reynolds number for various shapes of ribs at a=2 mm and d=10 mm.

On the other hand, the average Nusselt number enhancement was calculated and compared with the experimental results of the current study for different geometries of ribs as shown in Figure 5.11. It was found that the wing ribs have the highest average Nusselt number enhancement followed by the oval and the flat ribs. Also, the average deviation between numerical results and experimental data for all geometries of ribs was about 8.24%.

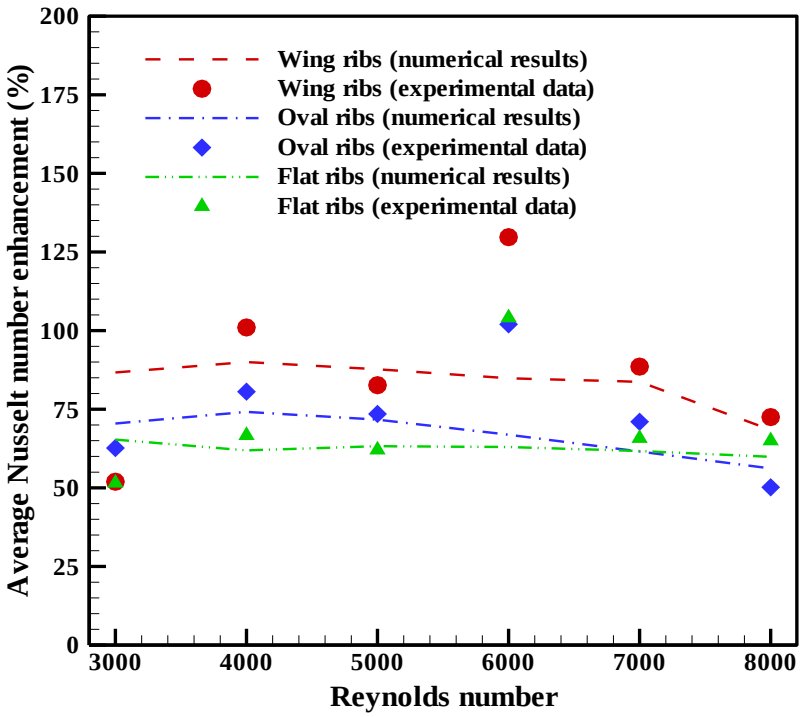

Figure 5.11: Average Nusselt number enhancement vs. jet Reynolds number for various shapes of ribs at a=2 mm and d=10 mm.

Figure 5.12 depicts the variation of the performance evaluation criteria versus jet Reynolds number with various ribs shapes. It is found that the wing ribs have the best of the performance evaluation criteria (*PEC*) followed by oval ribs and flat ribs at jet Reynolds number less than 7500. In addition, the mean deviation between the experimental data and numerical results for all shapes of ribs on the impinging target surface was 3.98 %.

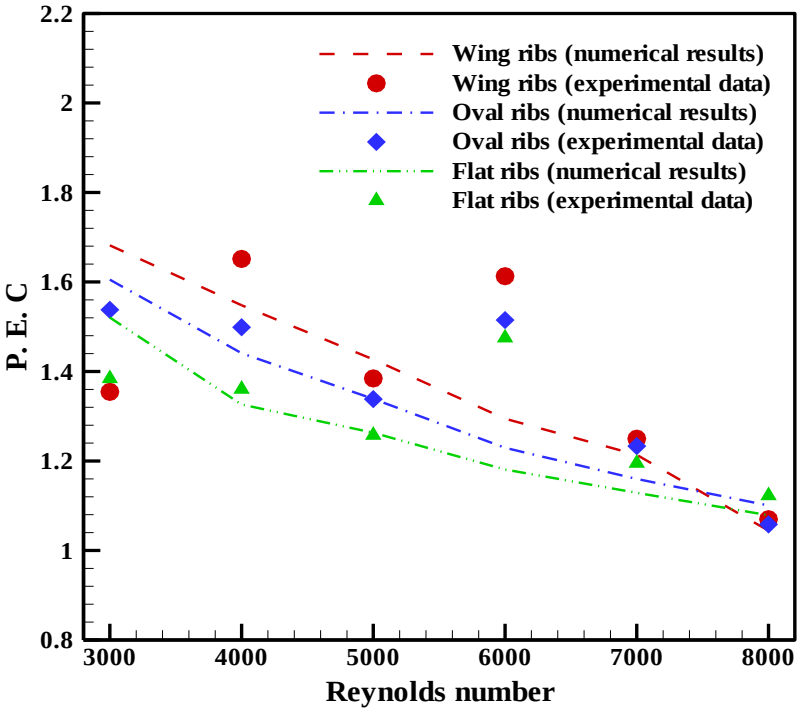

Figure 5.12: Performance evaluation criteria versus jet Reynolds number for various shapes of ribs at a=2 mm and d=10 mm.

5.5 Numerical Results

5.5.1 Effect of Jet Reynolds Number

In this section, the streamwise velocity, isotherms, and total entropy generation contours as well as velocity vector for the wing, oval, and flat ribs at a=2 mm and d=10 mm are displayed and discussed. Figures 5.13 and 5.14 depict the streamwise velocity contours and velocity vector, respectively, for various rib shapes and jet Reynolds numbers of (Re=3000, 5000, and 7000). In general, it is clear that the working fluid flow enters from the slot jet upon the left of the top confined plate and impinges on the impingement target surface and leaving from the right-hand side of the geometry field. As the flow of working fluid impinges on the impingement target plate, an initial counter-clockwise vortex generates on the top confined plate nearby the slot jet because of the shear force produced by the high velocity jet on the fluid flow. Moreover, a

secondary clockwise vortex grows downstream the rib with all shapes close to the impinging target surface. It is observed that as the jet Reynolds number rises from 3000 to 7000, the intensity and size of initial and secondary vortices rise. For different jet Reynolds numbers, the other counter-clockwise vortex occurs on the impingement target surface near the stagnation point. The development of these vortices leads to a decrease in the flow produced by the secondary re-circulation zone creating the gradient of reverse pressure in the flow domain.

Figure 5.15 illustrates the temperature contours for the slot jet impingement at various jet Reynolds numbers of (3000, 5000, and 7000) for the wing, oval, and flat ribs. Furthermore, it can be clearly observed that the minimum thermal boundary layer thickness occurred at the stagnation point, and it is also growing along with the impingement target plate. This is because of the high temperature drop that happened in the stagnation zone. The results indicated that all ribs have an important influence on the thermal boundary layer, disrupting these layers and thus improve heat transfer. Moreover, the appearance of a recirculation region downstream of all ribs can improve the hot fluid mixing close to the impingement target plate with the cold fluid in the channel core, resulting in raising the rates of heat transfer. Especially in the stagnation zone, the thickness of the thermal boundary layer decrease with increasing jet Reynolds number from 3000 to 7000.

Figure 5.16 presents the dimensionless total entropy generation contours (which includes the effect of thermal and viscous) for different jet Reynolds numbers and different rib shapes. It is found that the highest entropy generation happens at the stagnation point and progressively decreases along an impinging target surface because of the rise in the temperature gradients at a stagnation point. Whereas the total entropy

generation decreases along streamwise direction due to the thermal boundary layer thickness increases. Furthermore, all ribs have a significant effect on the total entropy generation. With increasing jet Reynolds number from 3000 to 7000, the viscous and heat transfer entropy generation rise owing to the irreversibility of thermal and viscous dissipation.

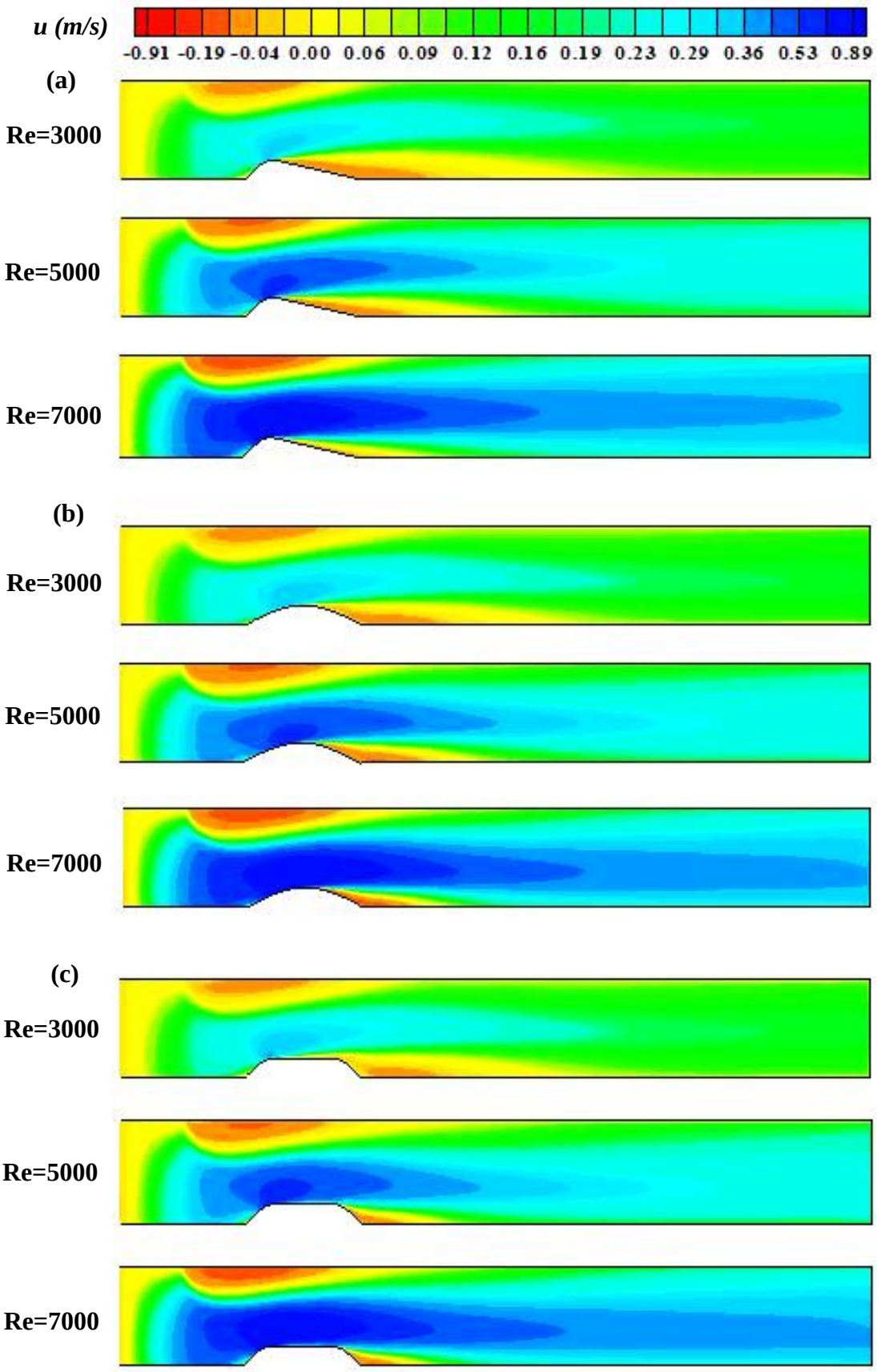

Figure 5.13: Streamwise velocity contours for various jet Reynolds number at a=2 mm and d=10 mm for (a) Wing rib, (b) Oval rib, (c) Flat rib.

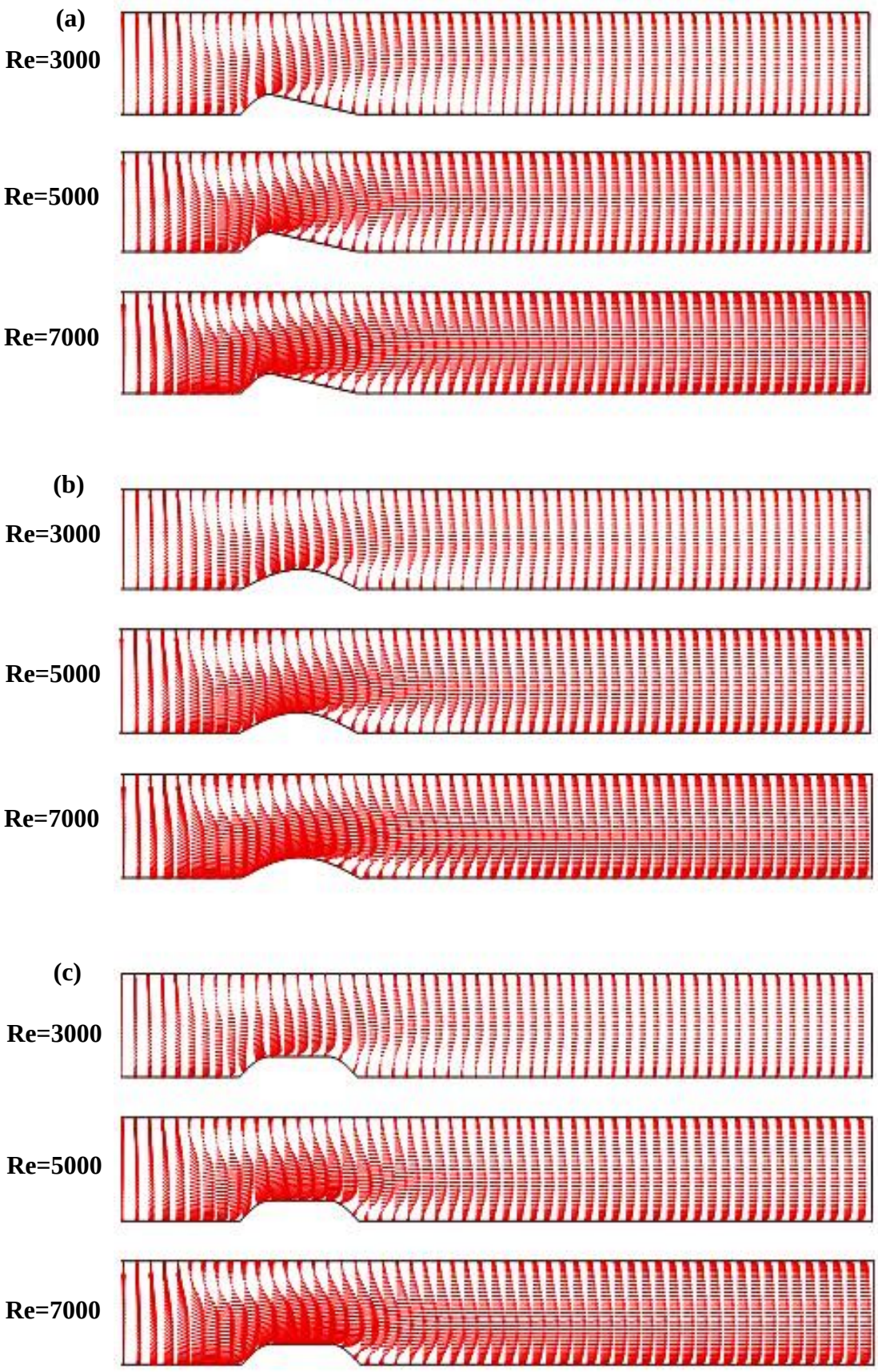

Figure 5.14: Velocity vector for various jet Reynolds number at a=2 mm and d=10 mm for (a) Wing rib, (b) Oval rib, (c) Flat rib.

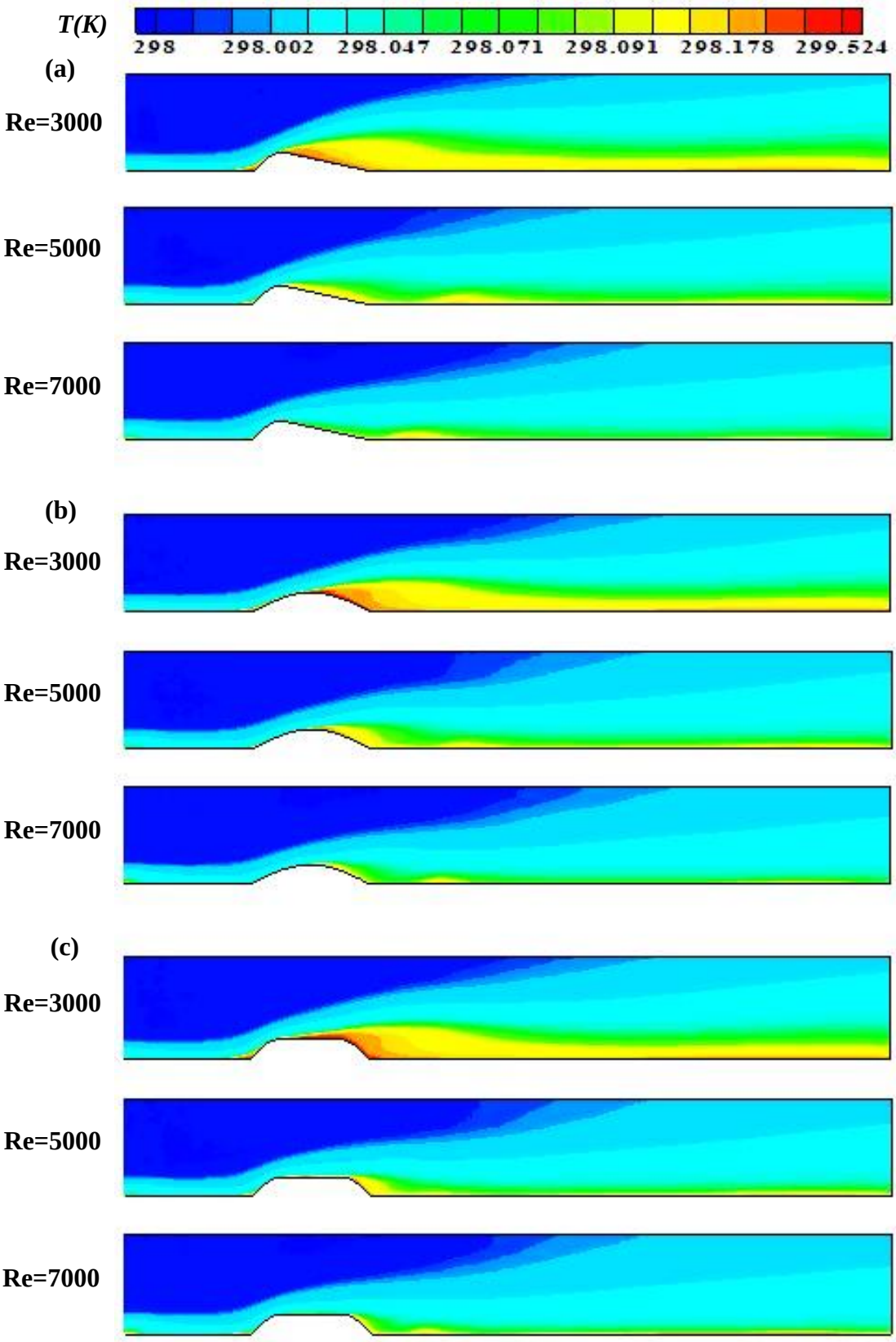

Figure 5.15: Temperature contours for various jet Reynolds number at a=2 mm and d=10 mm for (a) Wing rib, (b) Oval rib, (c) Flat rib.

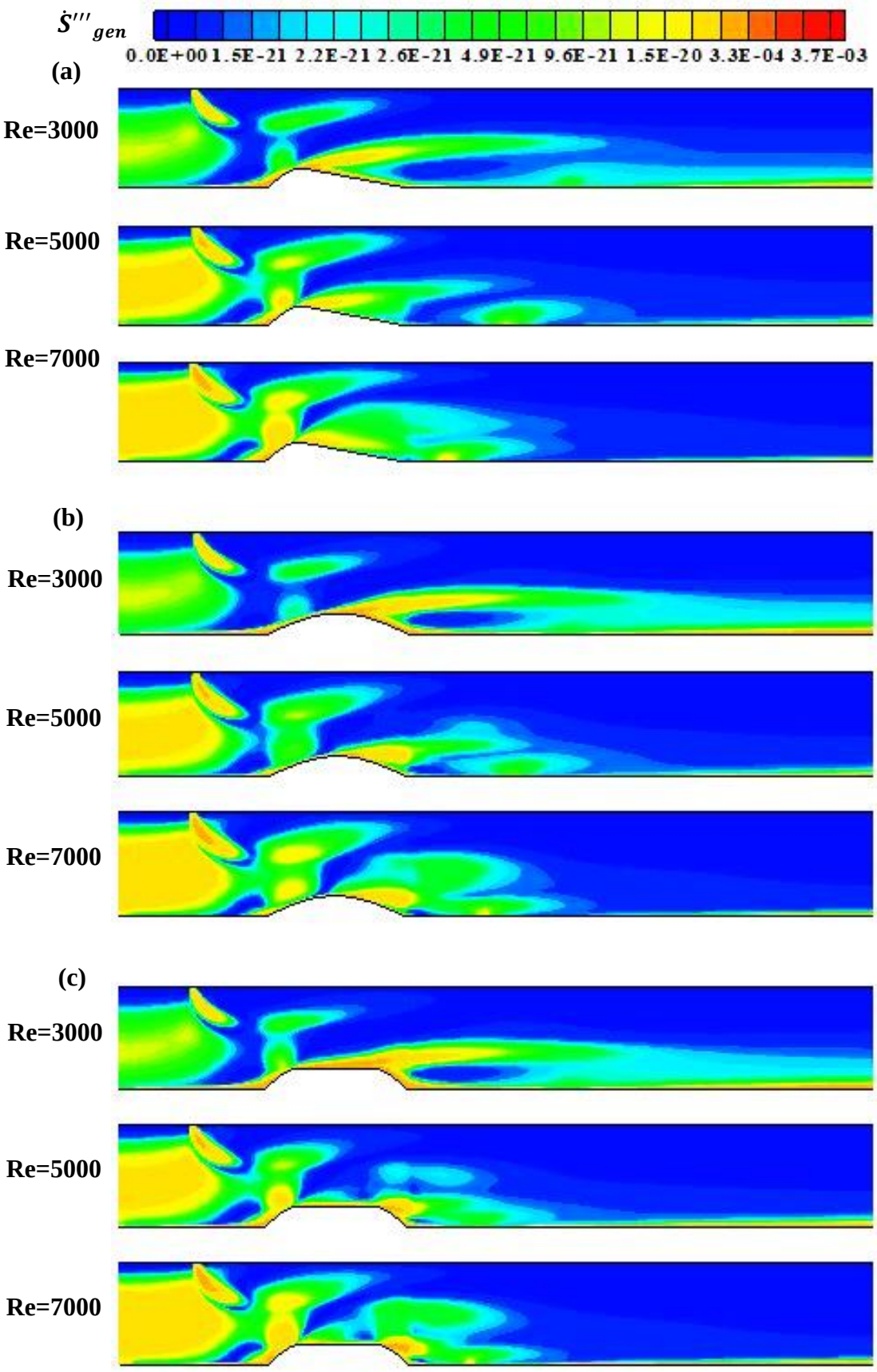

Figure 5.16: Total entropy generation contours for various jet Reynolds number at a=2 mm and d=10 mm for (a) Wing rib, (b) Oval rib, (c) Flat rib.

5.5.2 Effect of Ribs Heights

The effect of ribs height (a=0.0, 0.5, 1, 1.5, and 2 mm) on the flow and heat transfer characteristics for the wing, oval, and flat ribs of at d=10 mm has been displayed in this section.

The streamwise velocity contours for various rib heights at jet Re = 5000 with wing, oval, and flat ribs shapes and a smooth impinging target surface (without ribs) are depicted in Figure 5.17. Generally, the streamwise velocity has an identical behavior for all rib shapes. The addition of ribs on the target plate has a high influence on the initial vortex that grows near the top confined plate, resulting in the reduced intensity and size of the initial vortex. It should be noted that the initial vortex does not enhance heat transfer adiabatic (confined surface). But it increases the reverse flow of the working fluid and hence increases pressure drop. As a result, decreasing the intensity and size of the initial vortex leads to a reduction in the pressure drop. Moreover, at the impingement target surface, a secondary-clockwise vortex was created downstream of ribs with different shapes. The intensity and size of the secondary vortex increase with increasing the heights of the rib, resulting in enhanced mixing of working fluid flow and thus heat transfer improvement. Furthermore, the velocity of the fluid in the core of the channel increases with increasing the heights of the rib, due to the decrease in the spacing between the upper and lower surfaces. However, the rate of heat transfer improvement increases with an increase in the height of the rib. It has been observed that the highest intensity and size of the secondary vortex created with wing rib at a=2 mm, and hence can be enhanced the best enhancement in heat transfer.

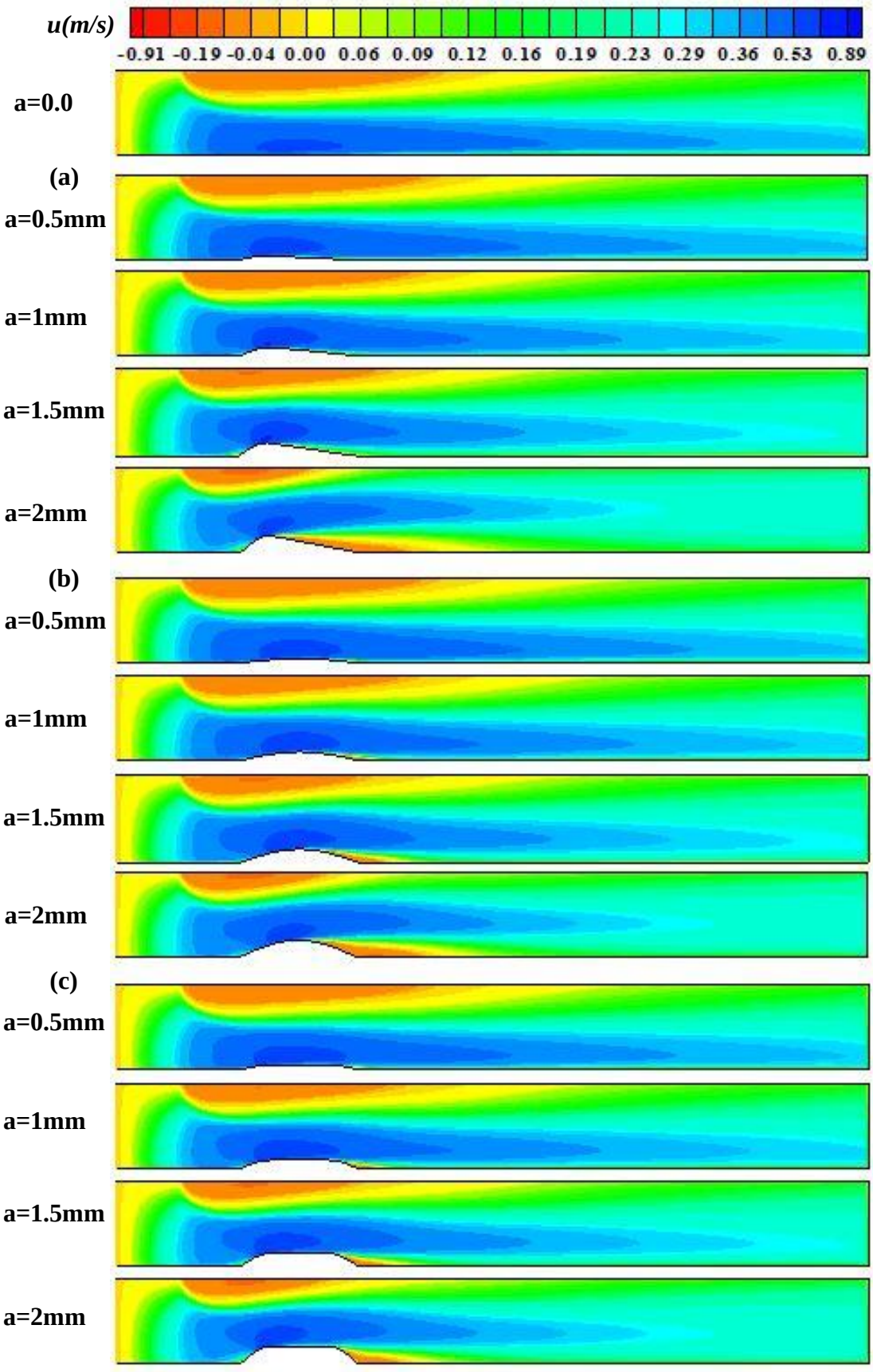

Figure 5.17: Streamwise velocity contours for various rib height at jet Re=5000 and d=10 mm for (a) Wing rib, (b) Oval rib, (c) Flat rib.

Figure 5.18 presents the temperature contours using wing, oval, and flat ribs with different heights at jet Re=5000. It can be observed that the smallest thermal boundary layer thickness occurs at the impingement point (stagnation point) for a=0.0 (without ribs) and the thickness of the thermal boundary layer increases along the target surface. As the rib heights increase, the size of recirculation regions increases and hence improve the mixing of the hot fluid near the target surface with the cold fluid in the core of the channel. It was also found that the similar trend has been seen for all shapes of ribs.

Figure 5.19 shows the total entropy generation contours of the wing, oval, and flat ribs for different rib heights at jet Re = 5000. For all shapes of ribs, it can be seen that the peak total entropy generation happens at the rib surface and a stagnation point and reduced progressively toward downstream. Therefore, the total entropy generation rises with increasing the heights of rib due to increasing the effects of irreversibility of viscous dissipation and heat transfer.

Figure 5.20 displays the local Nusselt number along target surface (from the stagnation point until the right outlet) with various rib heights (a=0.0, 0.5, 1, 1.5, and 2 mm) at d=10 mm and jet Re=5000. It can be seen that the influence of rib heights upon the local Nusselt number comparable behavior for all impingement target surfaces. It is also noted that at the stagnation point, the highest local Nusselt number will happen and reduce gradually along the impinging target surface owing to the high temperature gradient which is generated in that zone (stagnation zone). This result is consistent with the numerical study of Manca et al. [15]. When the rib height increases from 0.5 to 2 mm, the local Nusselt number rises notably at location (X=75 mm) and thereafter greatly increases at (X=90 mm) to the highest values for all rib shapes. In this zone, the rise in

the local Nusselt number is owing to the decrease cross sectional area in a convergence zone (at separation point), resulting grow the velocity of working fluid flow. Hence, the local Nusselt number increases in the convergence zone. On the other hand, the reduction in the local Nusselt number towards the downstream rib region is because of the increase in a cross-sectional area (at reattachment point) as well as the opposite fluid flow which generates at downstream rib that creates a poor flow zone. However, the location from (X=95 to 100 mm), the local Nusselt number increases owing to the enhancement in the mixing of fluid flow. It can be noted that the local Nusselt number rises as the rib height increases, thus, a=2 mm has the peak improvement of heat transfer, and the without ribs (a=0.0) has the lowest.

Figure 5.21 illustrates the average Nusselt number versus jet Reynolds number with various rib heights. According to this figure, it should be observed that the jet Reynolds number, as well as rib heights, have a strong effect on the average Nusselt number. At a given rib height, the average Nusselt number increase as the jet Reynolds number increases due to the increasing temperature gradient and at the lower target surface. It is also found that, at a given jet Reynolds number, the average Nusselt number increase with the rib height. This due to the fact, the size of re-circulation zones increases and hence improve fluid mixing and consequently increase the heat transfer rate. The results were similar to numerical investigation performed by Xu et al. [42]. In general, the average Nusselt number for all shapes of ribs has a similar trend.

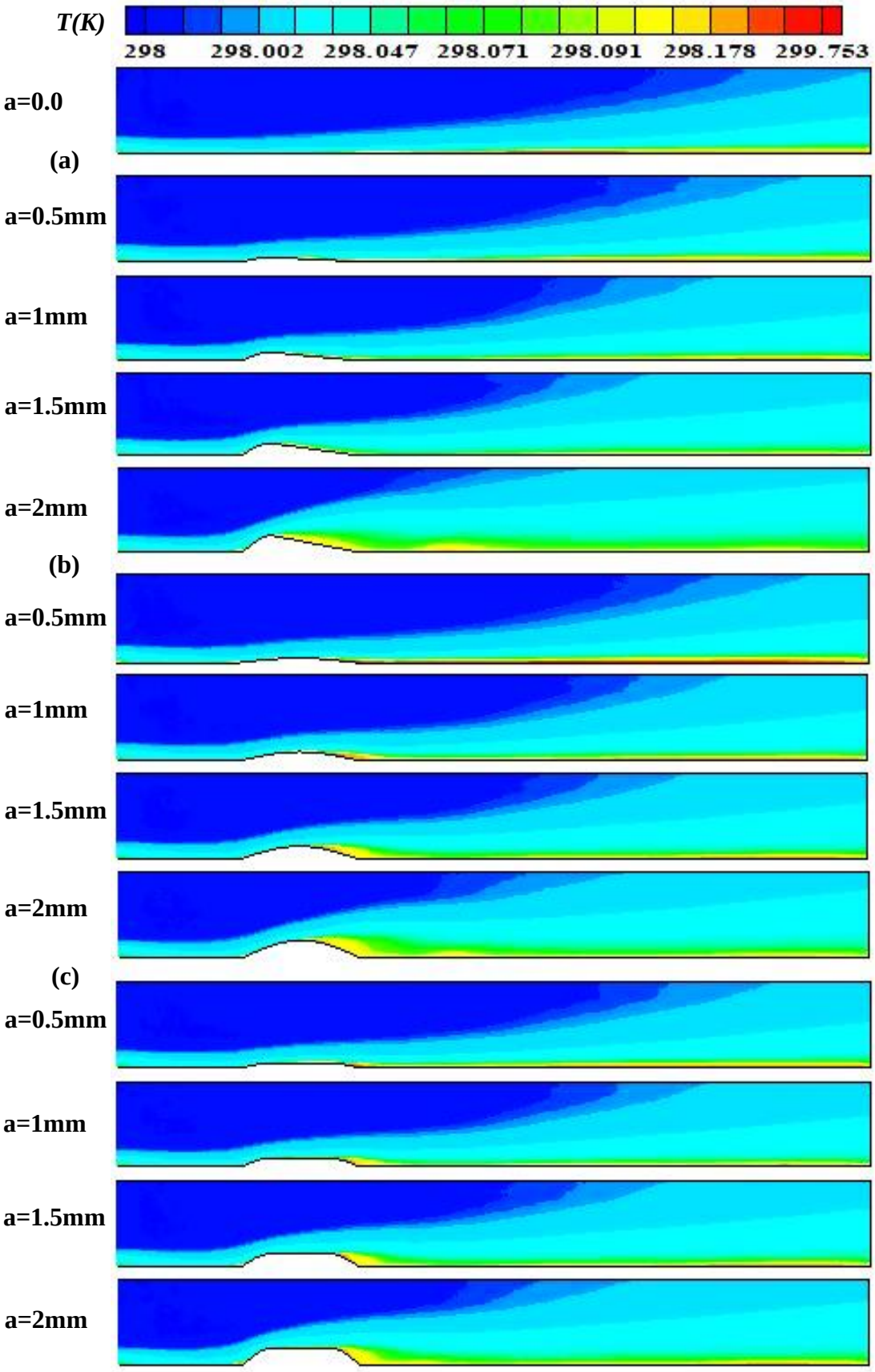

Figure 5.18: Temperature contours for various rib height at jet Re=5000 and d=10 mm for (a) Wing rib, (b) Oval rib, (c) Flat rib.

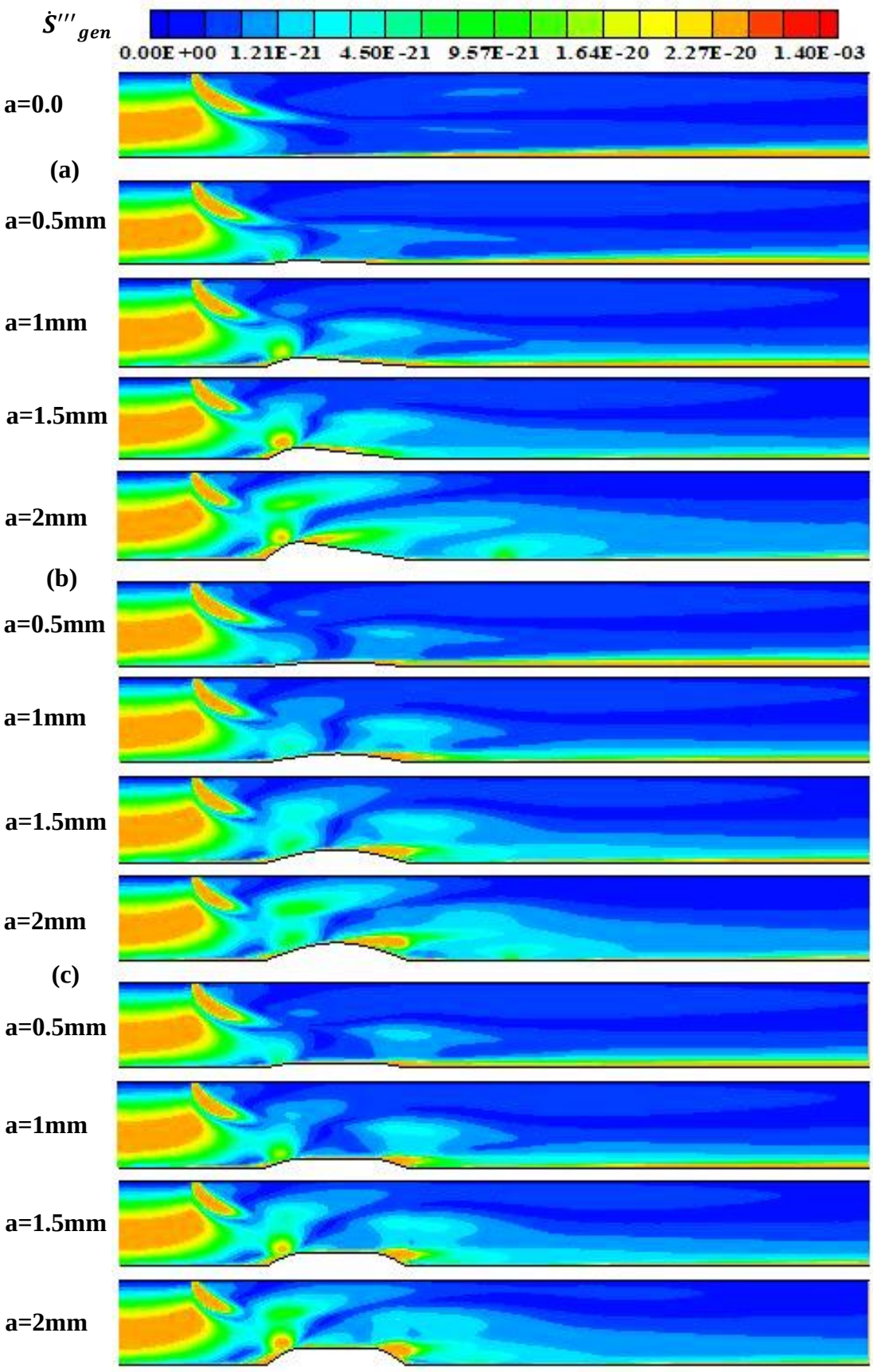

Figure 5.19: Total entropy generation contours for various rib heights at jet Re=5000 and d=10 mm for (a) Wing rib, (b) Oval rib, (c) Flat rib.

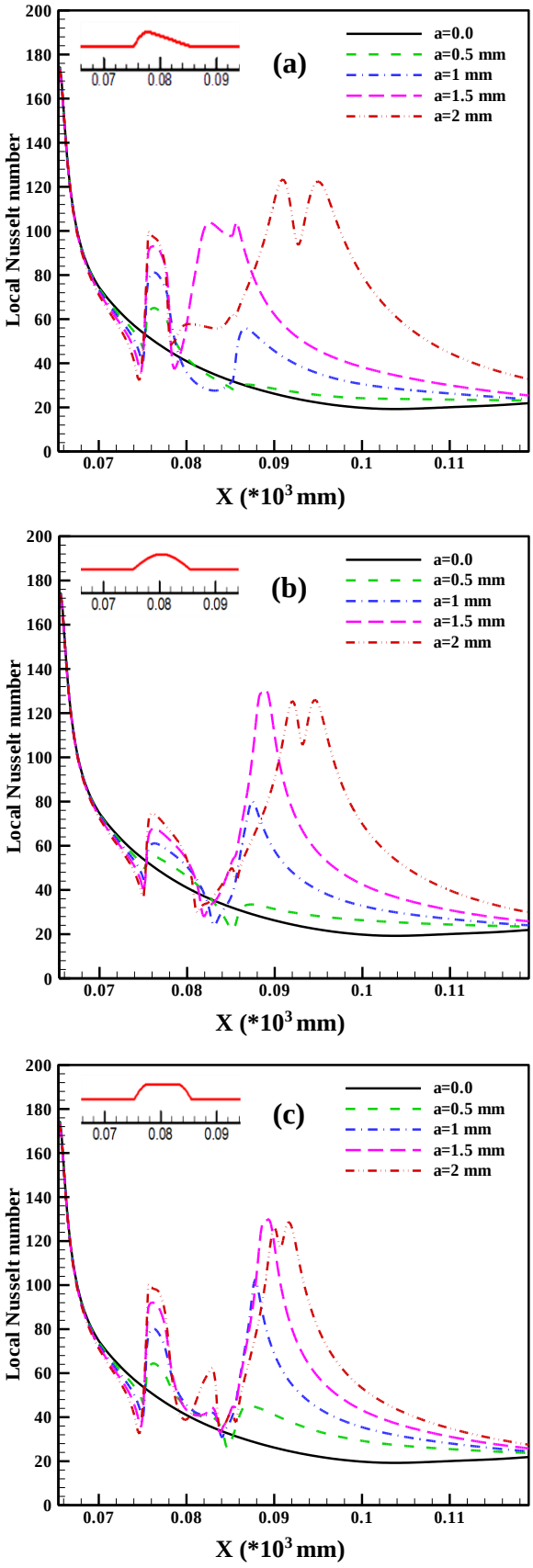

Figure 5.20: Local Nusselt number along the impinging target surface for various rib heights at jet Re=5000 and d=10 mm for (a) Wing rib, (b) Oval rib, (c) Flat rib.

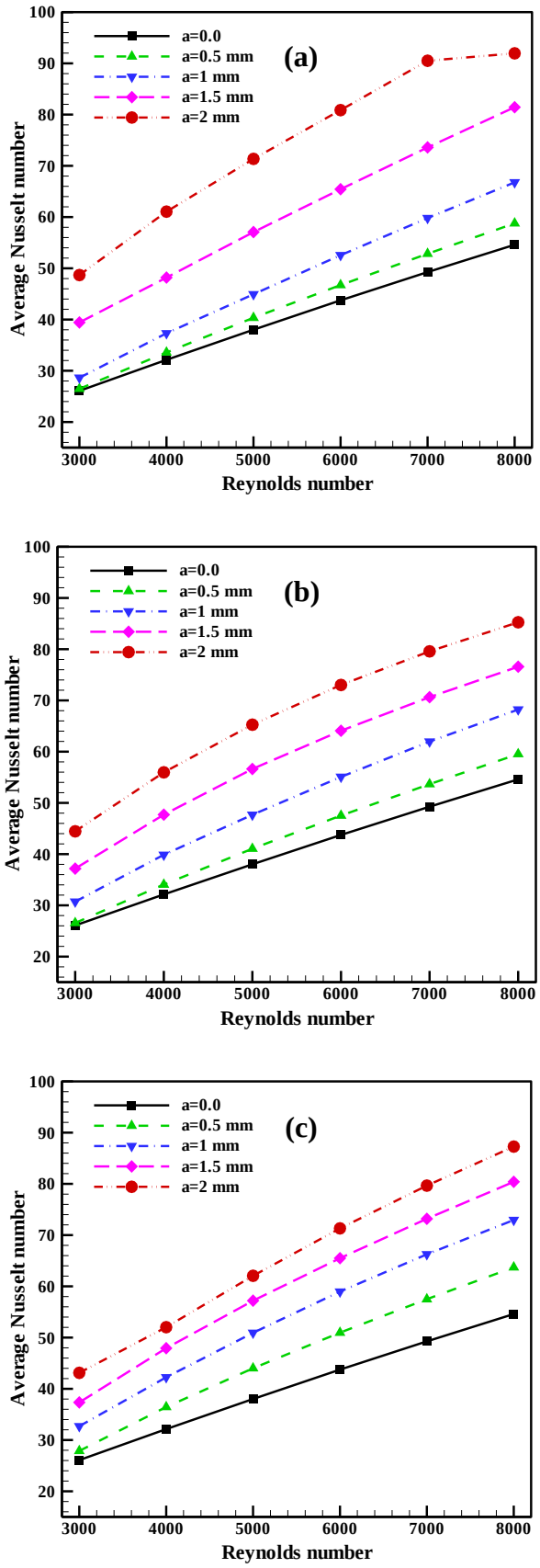

Figure 5.21: Average Nusselt number vs. jet Reynolds number for various rib heights at d=10 mm for (a) Wing rib, (b) Oval rib, (c) Flat rib.

The pressure drop versus jet Reynolds number with various rib heights at d=10 mm is depicted in Figure 5.22. For all heights rib, the pressure drop increases with increasing jet Reynolds number due to the velocity gradients. Moreover, it is noted that the minimum pressure drop occurred at a=0.0 (without ribs) compared with other rib heights. It is also found that the pressure drop increase as rib heights increases, due to the increase of the intensity and size recirculation region which led to increase the pressure drop.

The dimensionless mean total entropy generation versus jet Reynolds number with various rib heights utilizing wing, oval, and flat ribs at d=10 mm is illustrated in Figure 5.23. It may be observed that the average total entropy generation increases as the jet Reynolds number increase for all heights of rib. With increasing heights of rib, the mean total entropy generation increase, due to increasing the irreversibility. The result is consistent with the numerical investigation of Xu et al. [42]. A similar trend of entropy generation is observed for all shapes of ribs.

The average Nusselt number enhancement for jet impingement for different rib heights with various rib shapes is shown in Figure 5.24. It was found that the enhancement of the average Nusselt number increases with increasing rib height. This because the improve the fluid mixing in the spacing between the upper and lower surfaces. It is also observed that the highest enhancement in heat transfer was obtained at a=2 mm with different rib shapes over jet Reynolds number range.

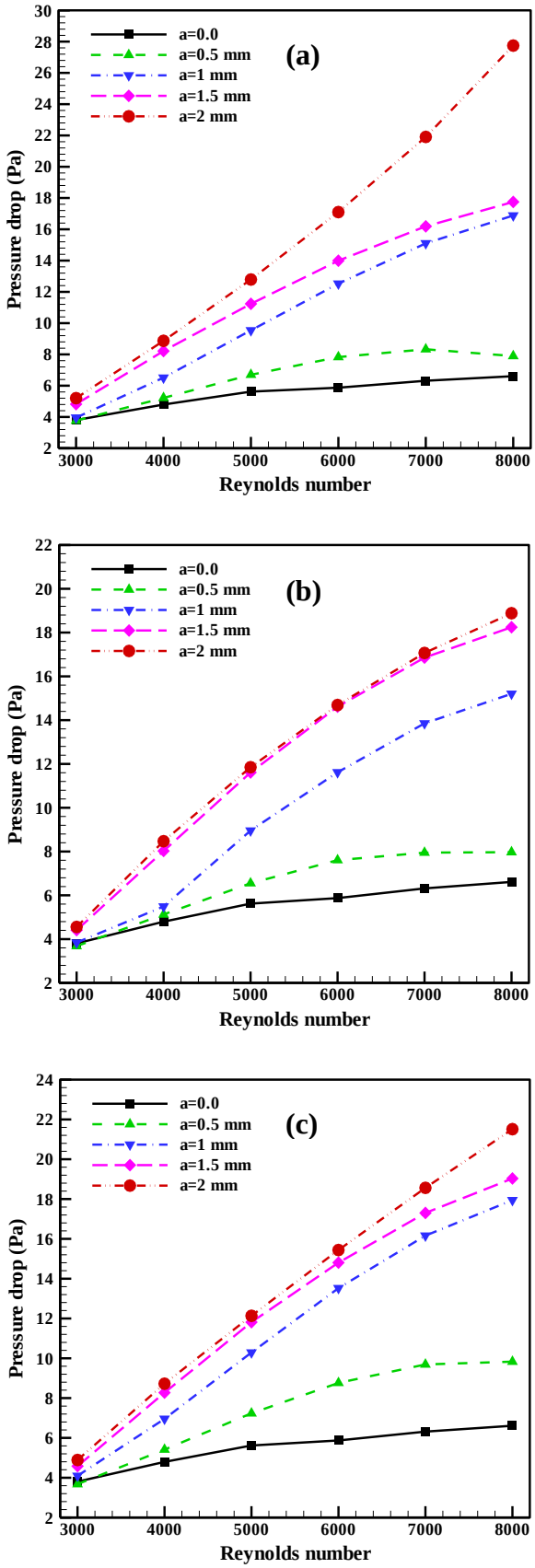

Figure 5.22: Pressure drop versus jet Reynolds number for various rib heights at d=10 mm for (a) Wing rib, (b) Oval rib, (c) Flat rib.

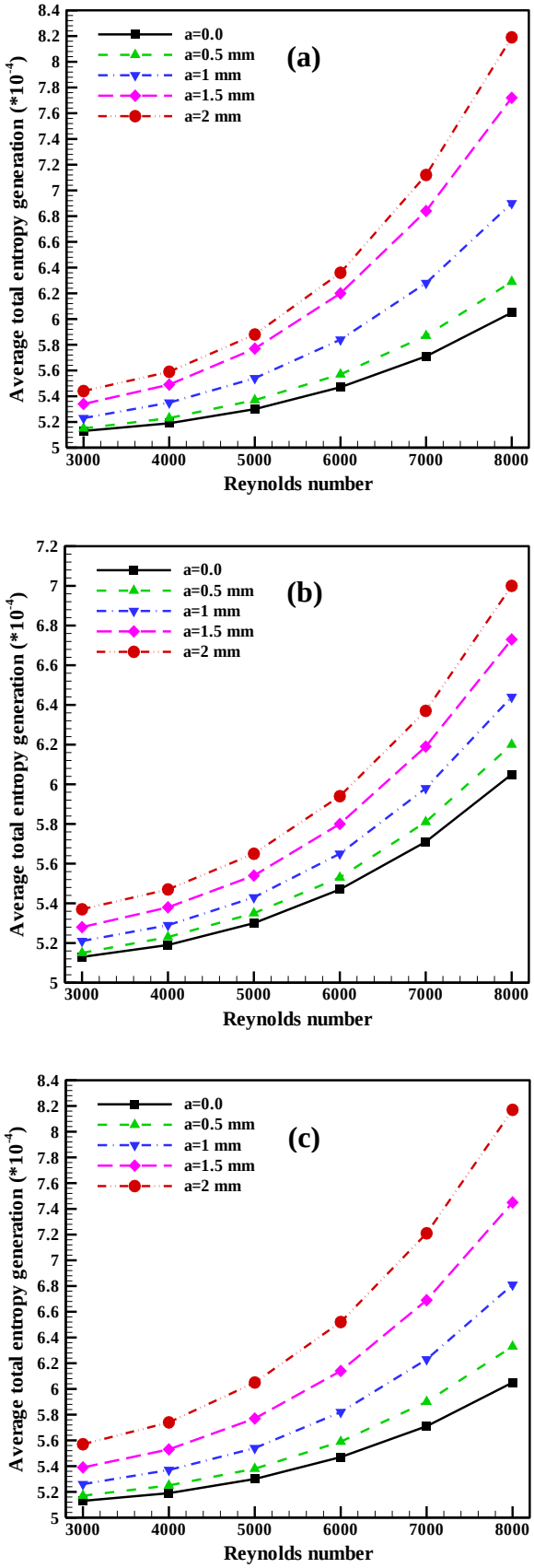

Figure 5.23: Average total entropy generation versus jet Reynolds number for various rib heights at d=10 mm for (a) Wing rib, (b) Oval rib, (c) Flat rib.

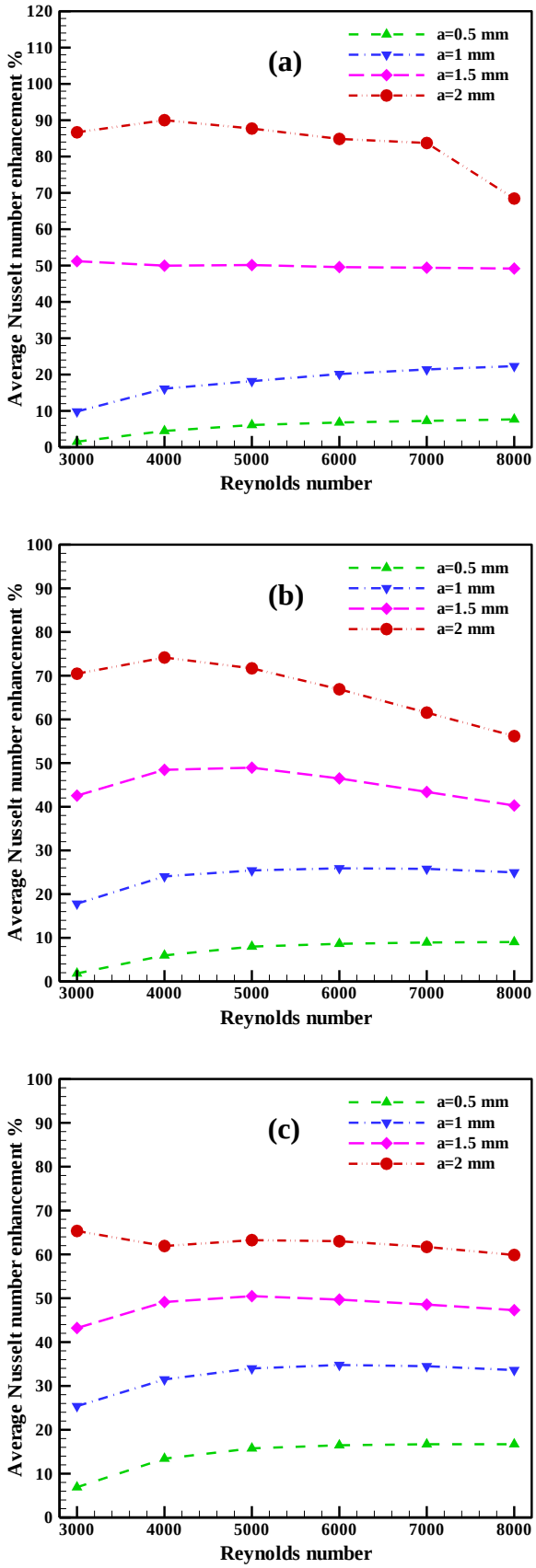

Figure 5.24: Average Nusselt number enhancement with jet Reynolds number for various rib heights at d=10 mm for (a) Wing rib, (b) Oval rib, (c) Flat rib.

Figure 5.25 displays the variation of the performance evaluation criteria (*PEC*) with jet Reynolds number for various rib shapes and different rib heights at d=10 mm. It may be noted that the rib heights have a clear influence on the *PEC*. Generally, the highest *PEC* can be obtained at a=2 mm with different rib shapes over jet Reynolds number range (except for wing ribs at Re=3000). This means that the positive effect of the heat transfer enhancement is higher than the negative effect of the pressure drop penalty. It was also found that the *PEC* at a=0.5 mm has the lowest value when jet Re < 6000 (except Re < 5000 for wing ribs). While the lowest value of *PEC* can be observed at a=1 mm when Re > 6000 for different rib shapes (except for wing ribs Re > 5000). Further, it was found that the maximum values of *PEC* for the wing, oval and flat ribs were 1.682, 1.61, and 1.52, respectively, at Re=3000 and a=2 mm.

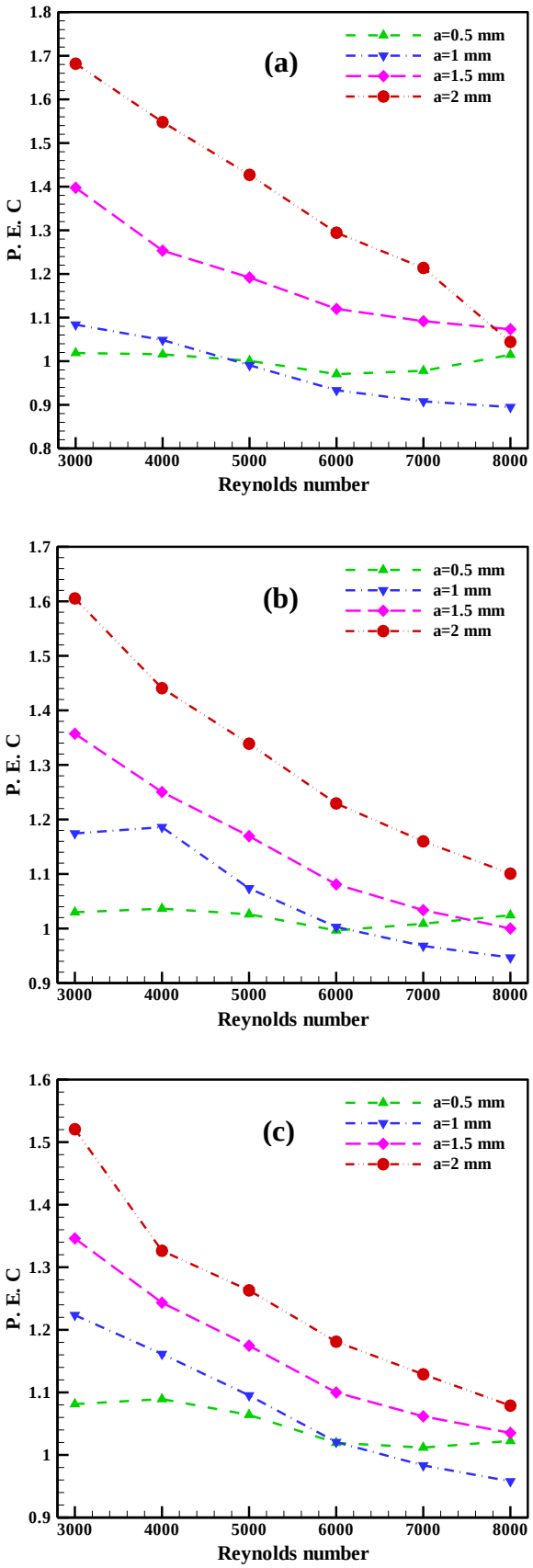

Figure 5.25: Performance evaluation criteria versus jet Reynolds number for various rib heights at d=10 mm for (a) Wing rib, (b) Oval rib, (c) Flat rib.

5.5.3 Effect of Ribs Locations

The effect of spacing between the stagnation point and the rib (d=10, 20, and 30 mm) for the wing, oval, and flat ribs at a=2 mm and jet Re=7000 on the velocity contours is depicted in Figure 5.26. For all rib shapes, it can be noted that the rib locations have a clear effect on the velocity. When d=10 mm, the reversal vortex fluid flow that creates downstream the ribs is very small as well as the ribs influence on the intensity and size of the initial recirculation at the top surface (confined wall) is higher than its effects on the secondary vortex. For d=20 mm, it may be observed that the secondary vortex zones begin increasing behind ribs, while the size of the initial recirculation significantly increases compared with the case of d=10 mm, which leads to reduce the enhancement of heat transfer. For d=30 mm, it was found that the size of the initial vortex largely increases compared with other cases. Therefore, the size of the initial vortex grows with increasing rib locations.

Figure 5.27 demonstrates the temperature contours at a=2 mm and jet Re=7000 with various rib locations for the wing, oval, and flat ribs. It can be clearly noted that the thermal boundary layer thickness in the region above ribs (upstream the rib) was less than that in the region after ribs (downstream the rib) due to the vortex zone effect that grows behind the ribs for all rib shapes. At the vortex zone which creates behind the ribs, the thermal boundary layer thickness increases as the spacing between the rib and stagnation point increases. Thus, the minimum thermal boundary layer thickness occurs at the stagnation point for all rib shapes because of the high-temperature gradient which occurred in this zone.

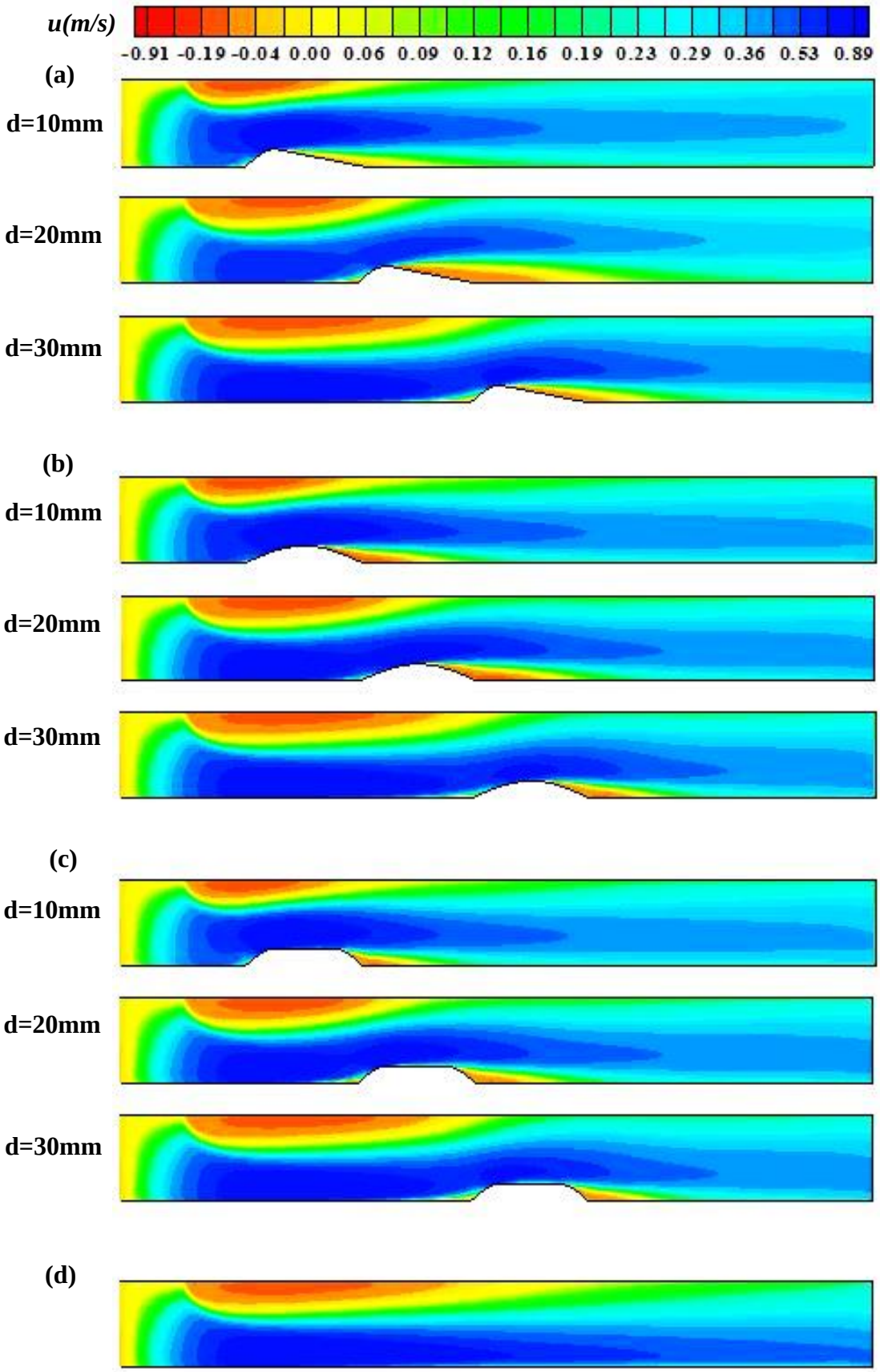

Figure 5.26: Velocity contours for various rib locations at jet Re=7000 and a=2 mm for (a) Wing rib, (b) Oval rib, (c) Flat rib, (d) smooth surface.

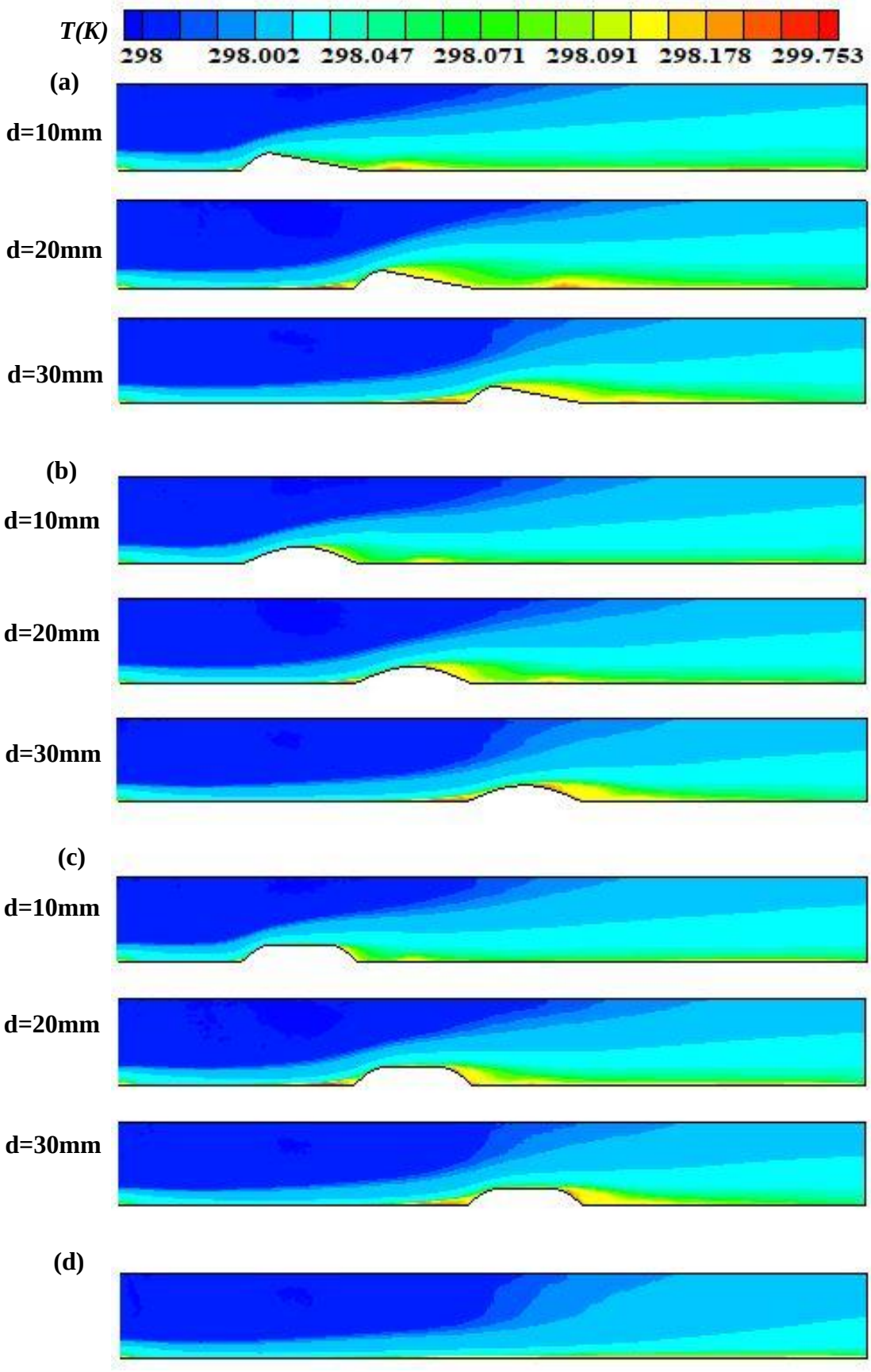

Figure 5.27: Temperature contours for various rib locations at jet Re=7000 and a=2 mm for (a) Wing rib, (b) Oval rib, (c) Flat rib, (d) smooth target.

The effect of various rib locations of (d=10, 20, and 30 mm) on the total entropy generation contours employing wing, oval and flat ribs at a=2 mm and jet Re=7000 is illustrated in Figure 5.28. It can be seen that the spacing between the stagnation point and the rib has a clear influence on the entropy generation. The total entropy generation close to the stagnation zone has the maximum values because of the high-temperature gradient in this zone. However, it can be observed that at the downstream rib, the total entropy generation is higher than that upstream the ribs due to the presence of vortex zones. Moreover, the highest total entropy generation occurs at the rib location of d=10 mm as well as it reduces when the spacing between the stagnation point and the rib increases.

Figure 5.29 shows the average Nusselt number with jet Reynolds number for using wing, oval and flat ribs at a=2 mm with various rib locations. It may be noted that the rib locations effect on the mean Nusselt number has a similar trend for all target shapes. With increasing jet Reynolds number, the average Nusselt number increases for all rib locations. Moreover, the average Nusselt number increases with decreasing distance (d) between the rib and the stagnation point. Regarding the velocity contours as depicted in Figure 5.26, the rib location of (d=10 mm) has the smallest size of the initial vortex zone at the adiabatic top wall close to slot jet, and also the intensity of this vortex will highest that leads to improve the mixing of working fluid and the augmentation in heat transfer compared to the other rib locations. Obviously, from the velocity contours, it was found that the weak mixing of working fluid occurred at d=30 mm which refers to the minimum heat transfer at that location. This due to increasing the size of the initial vortex compared to its intensity.

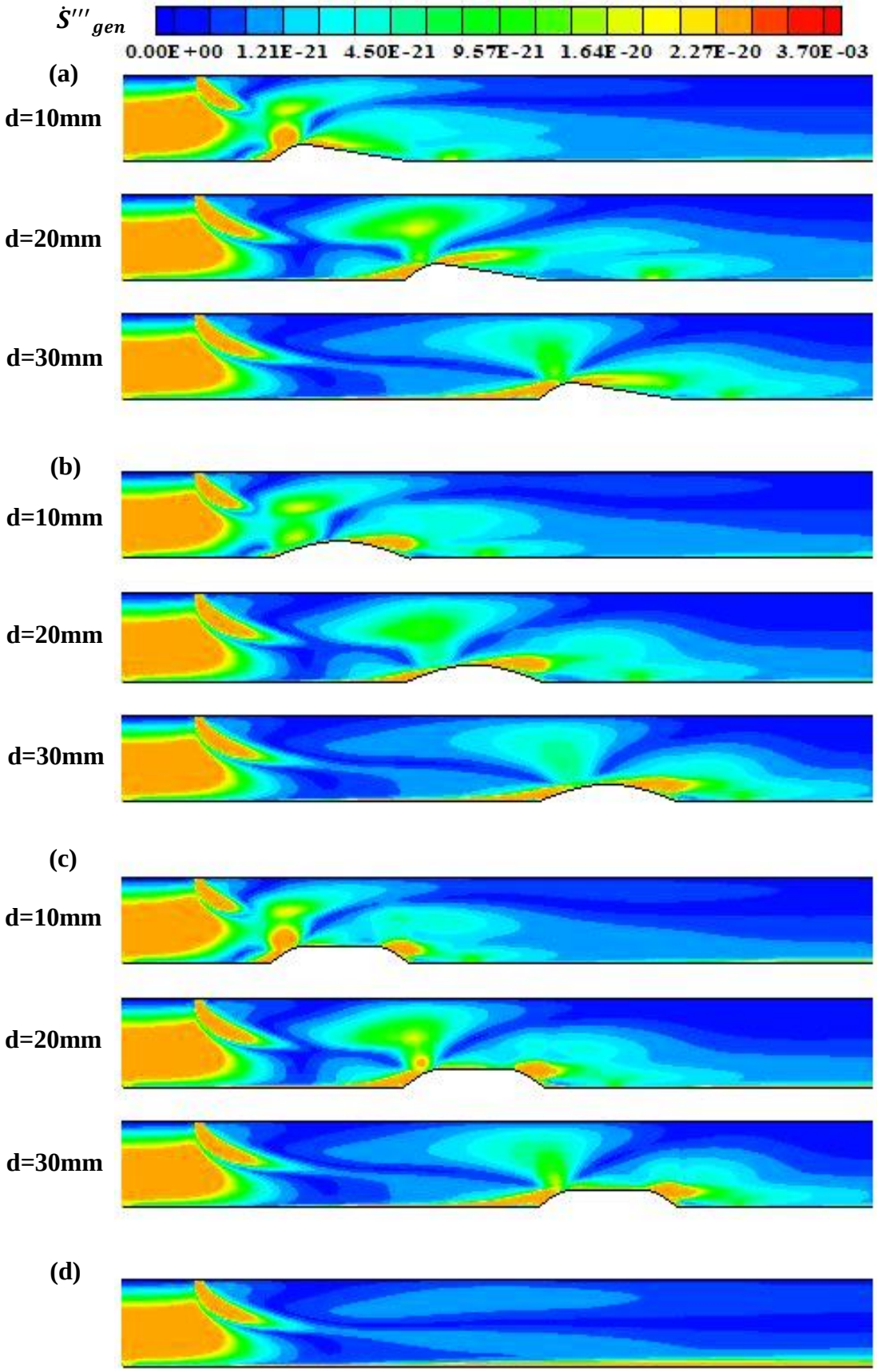

Figure 5.28: Total entropy generation contours for various rib locations at jet Re=7000 and a=2 mm for (a) Wing rib, (b) Oval rib, (c) Flat rib, (d) smooth target.

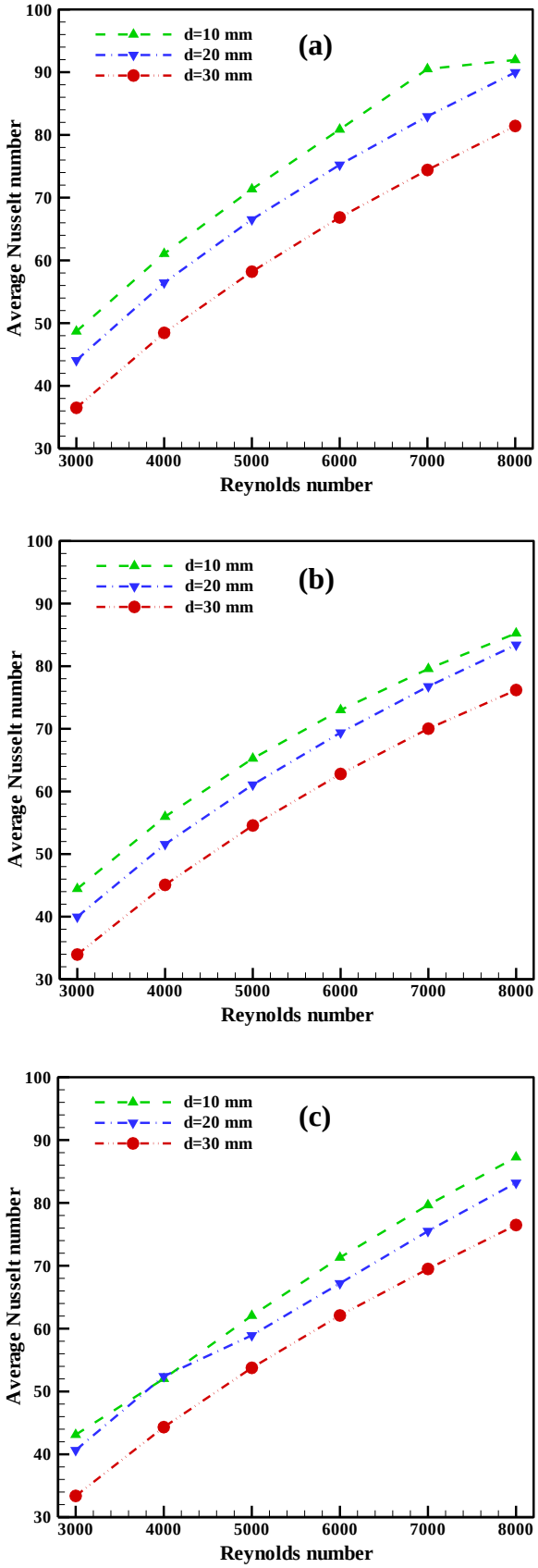

Figure 5.29: Average Nusselt number with jet Reynolds number for various rib locations at a=2 mm for (a) Wing rib, (b) Oval rib, (c) Flat rib.

Figure 5.30 gives the variation of the pressure drop versus jet Reynolds number for the wing, oval and flat ribs with various rib locations at a=2 mm. It can be indicated that the rib locations effect on the pressure drop has a similar trend for all shapes of ribs. As expected, it should be seen that the pressure drop increases as jet Reynolds number increases at presented rib locations. For all rib shapes, it was found that the pressure drop increases with decreasing the distance between the stagnation point and the ribs. This is due to the flow becomes more disturbed with decreasing the distance between the stagnation point and the ribs. Therefore, from the velocity contours as depicted in Figure 5.26, there is the influence of rib on the size and intensity of the initial vortex close to slot jet at the confined surface for d=10 mm which refers to the reverse working fluid flow in that location is the highest. Moreover, the intensity of the initial vortex zone at the top surface is the smallest for d=20 mm, this means that the pressure drop is lowest at this location. At d=30 mm, the reduce in the intensity of the initial vortex, which happens in this location, leads to a decrease in the reverse working fluid flow. However, the pressure drop of d=10 mm is higher than that of d=20 and 30 mm.

Figure 5.31 demonstrates the influence of the different spacing between the stagnation point and the rib on the average entropy generation using wing, oval, and flat ribs for various jet Reynolds numbers at a=2 mm. For all rib locations, with increasing jet Reynolds number, the mean of total entropy generation increases. It is seen that at jet Re < 4000, the rib locations influence on the mean of entropy generation has a small influence, and this influence increases with jet Reynolds number. It was also found that the total entropy generation increase with decreasing the spacing between stagnation point and rib. This is due to the effect of initial

and secondary regions that created near the upper and lower surfaces, respectively.

Figure 5.32 illustrates the variation of the performance evaluation criteria (*PEC*) with jet Reynolds number for various rib locations. It can be noted that the spacings between the rib and the stagnation point have a sharp influence on the *PEC*. With increasing jet Reynolds number, the performance factor decreases when d=10 and 20 mm. When d=30 mm, the performance factor increases when jet Re < 4000, and then it gradually decreases when jet Re > 4000 due to decrease the pressure losses compared to the heat transfer enhancement at that location. From Figure 5.32 (a), at the rib location of (d=10 mm), the peak value of the performance factor is around 1.68 at jet Re=3000, while, the minimum value of the *PEC* is approximately 1.044 at jet Re=8000 at this location. From Figure 5.32 (b), it may be noted that the highest performance factor happens at the rib location of (d=10 mm) and jet Re=3000, that equal to 1.61, whereas, the lowest value of the *PEC* equals 1.101 at d=20 mm and jet Re=8000. According to Figure 5.32 (c), it can be observed that the maximum thermal-hydraulic performance factor equals 1.562 which occurs at Re=3000 and the spacing between the stagnation point and the rib is (d=20 mm). At this location, the lowest performance factor value is 1.053, which occurs at the highest value of jet Reynolds number. Moreover, all values of the performance factor are higher than that unity for all rib shapes. This means that the increase in heat transfer enhancement is higher than the increase in pressure drop. Just when the jet Re < 5000, while jet Re > 5000 at d=30 mm is the optimum.

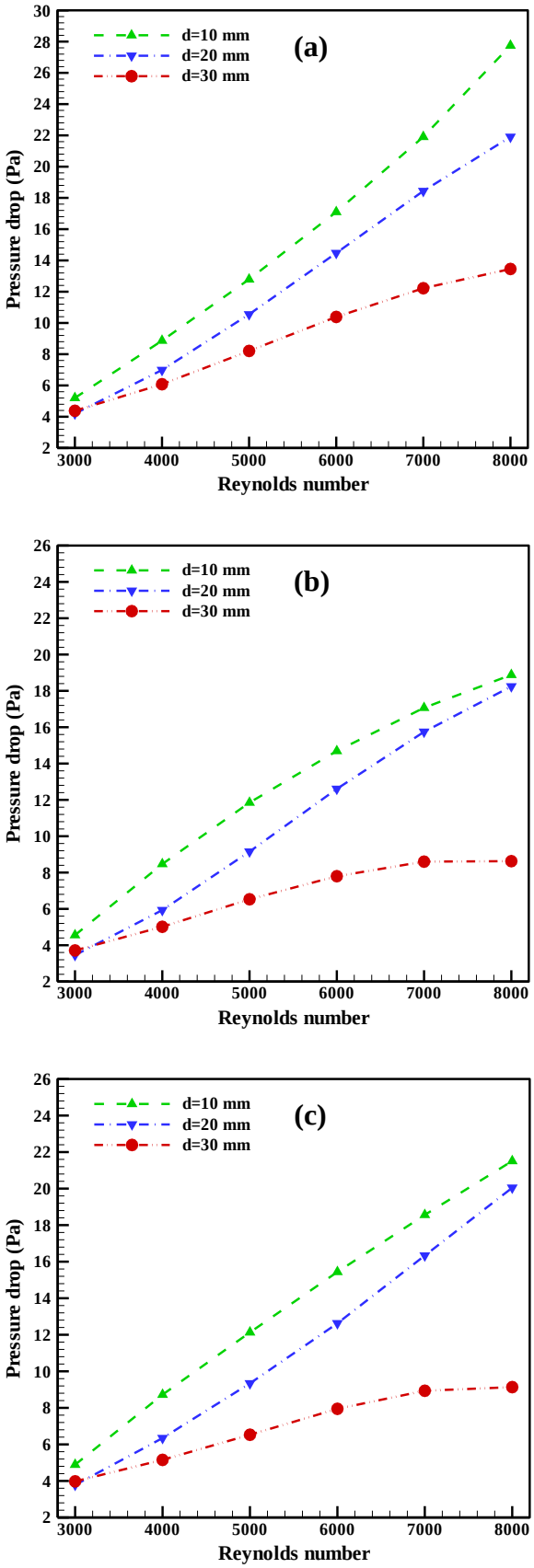

Figure 5.30: Pressure drop with jet Reynolds number for various rib locations at a=2 mm for (a) Wing rib, (b) Oval rib, (c) Flat rib.

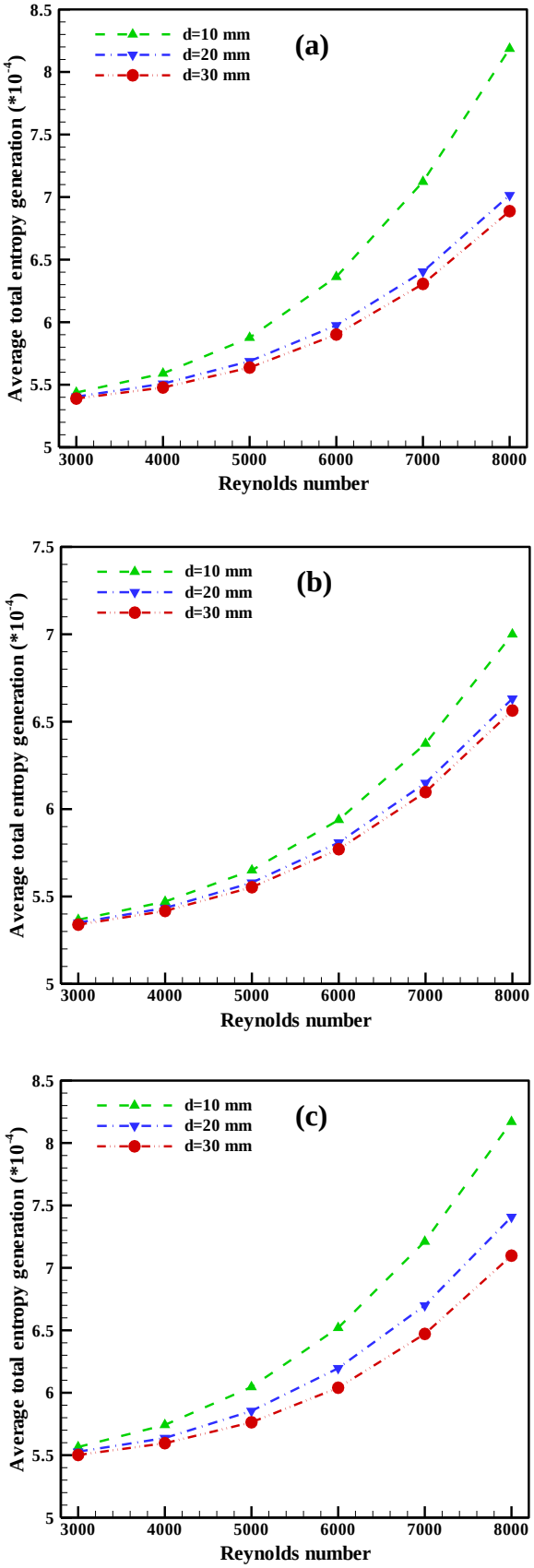

Figure 5.31: Average total entropy generation versus jet Reynolds number for various rib locations at a=2 mm for (a) Wing rib, (b) Oval rib, (c) Flat rib.

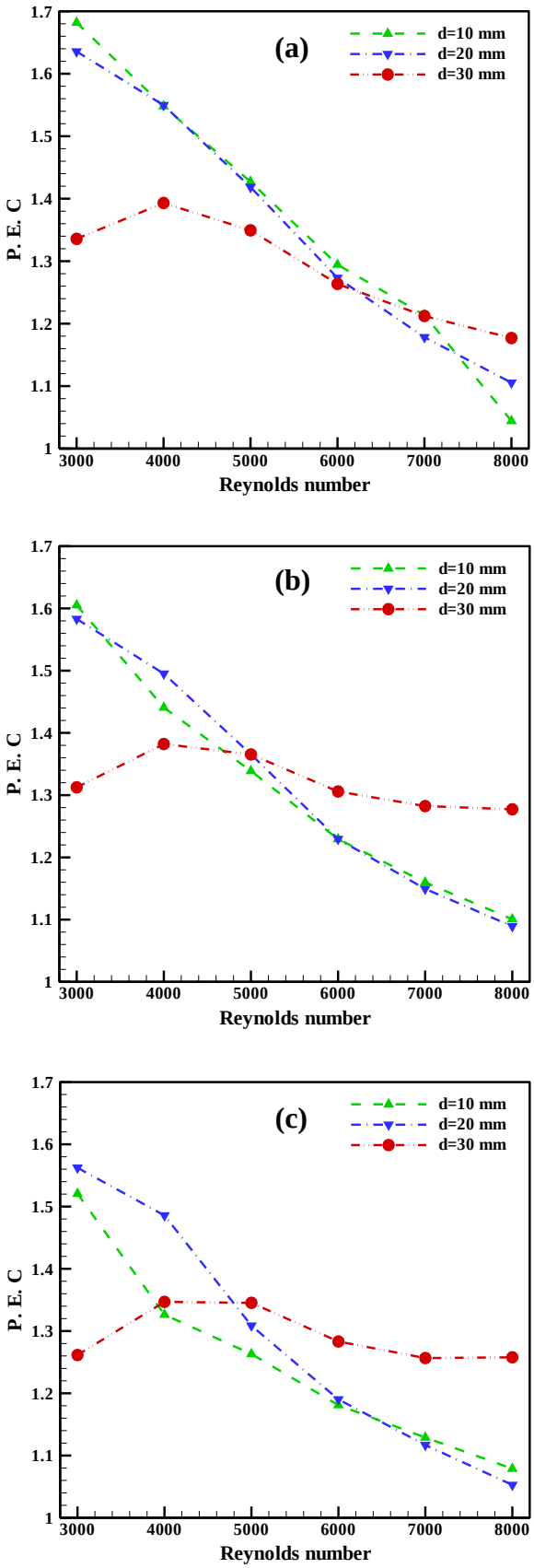

Figure 5.32: Performance evaluation criteria versus jet Reynolds number for various rib locations at a=2 mm for (a) Wing rib, (b) Oval rib, (c) Flat rib.

5.5.4 Effect of Ribs Shapes

In this section, the ribs shape effect on the average Nusselt number at rib location of (10 mm) for various rib height (a=0.5, 1, 1.5, and 2 mm) is depicted in Figure 5.33. It can be noted that with increasing jet Reynolds number, the average Nusselt number increases. It was also found that the average Nusselt number of various ribs shapes on the impinging target surface is higher than that of the smooth target surface (without ribs) due to the enhance mixing of working fluid flow. For (a=0.5 and 1 mm), the flat ribs have the highest Nusselt number compared with other shapes. For (a=1.5 mm), it can be observed that at jet Re < 6000, the rib shapes have a weak influence on the Nusselt number, and then it increases. At (a=2 mm), the shapes of ribs have a high influence on the mean Nusselt number. Moreover, the wing ribs give the maximum values of the mean Nusselt number followed by oval ribs and flat ribs at jet Reynolds number (Re < 7000). This is due to the wing ribs provide better mixing of working fluid flow compared to other shapes.

Figure 5.34 illustrates the variation of the pressure drop versus jet Reynolds number for rib height of a=0.5, 1, 1.5, and 2 mm with various shapes of ribs at d=10 mm. As expected, with increasing jet Reynolds number, the pressure drop increases due to increasing the velocity gradient with jet Reynolds number. For rib height of (d=0.5, 1, and 1.5 mm), it noted that the flat ribs have the highest pressure drop at jet Re > 4000. Whereas, the peak values of the pressure drop occur for wing ribs followed by flat ribs and oval ribs at rib height of (d=2 mm), due to the secondary vortex zone that generated downstream the ribs. In addition, using a smooth target surface (without ribs) provides the minimum pressure drop as compared to various shapes of ribs at d=1.5 and 2 mm.

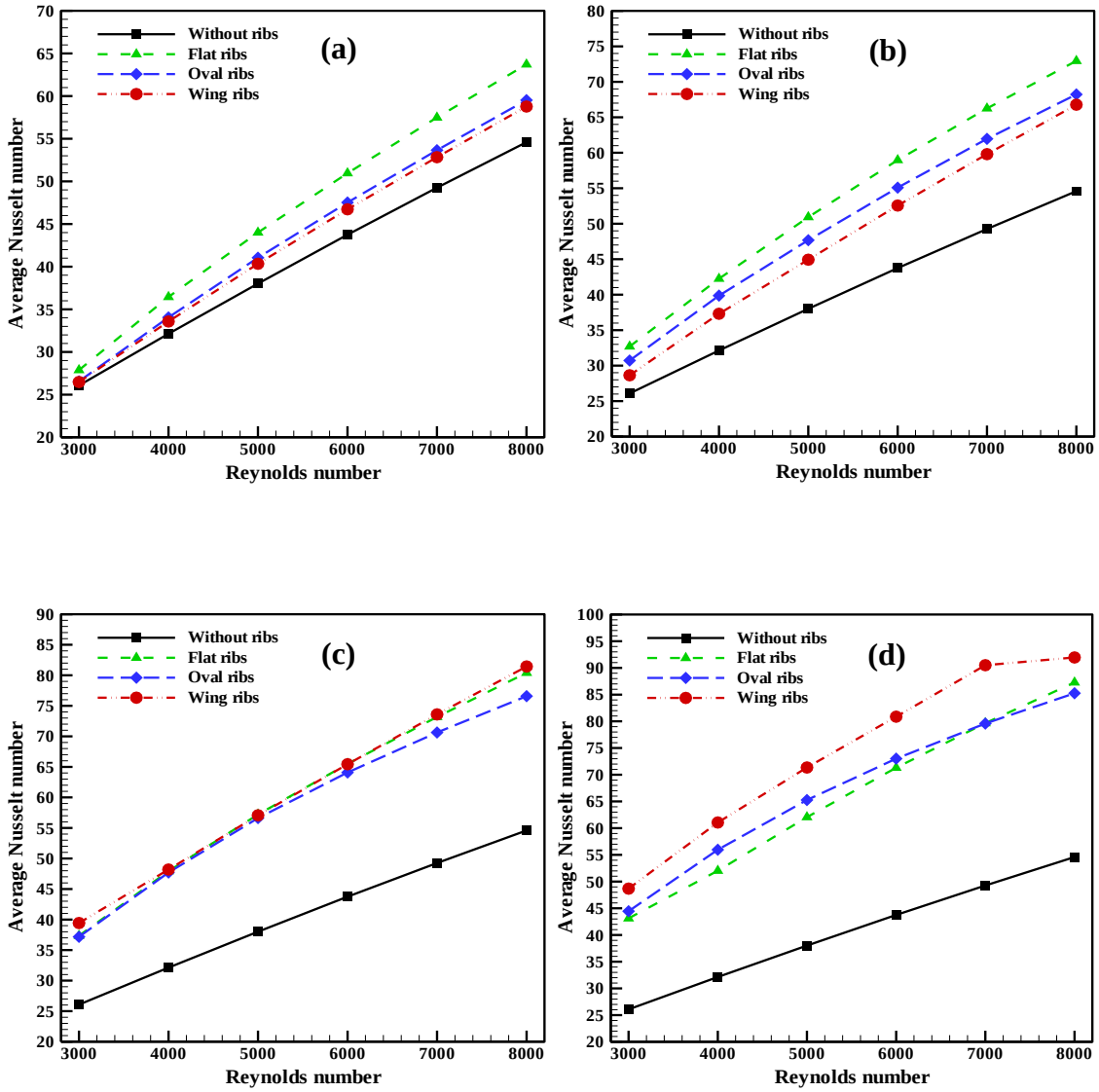

Figure 5.33: Average Nusselt number versus jet Reynolds number for various rib shapes at d=10 mm for (a) a=0.5 mm, (b) a=1 mm, (c) a=1.5 mm, (d) a=2 mm.

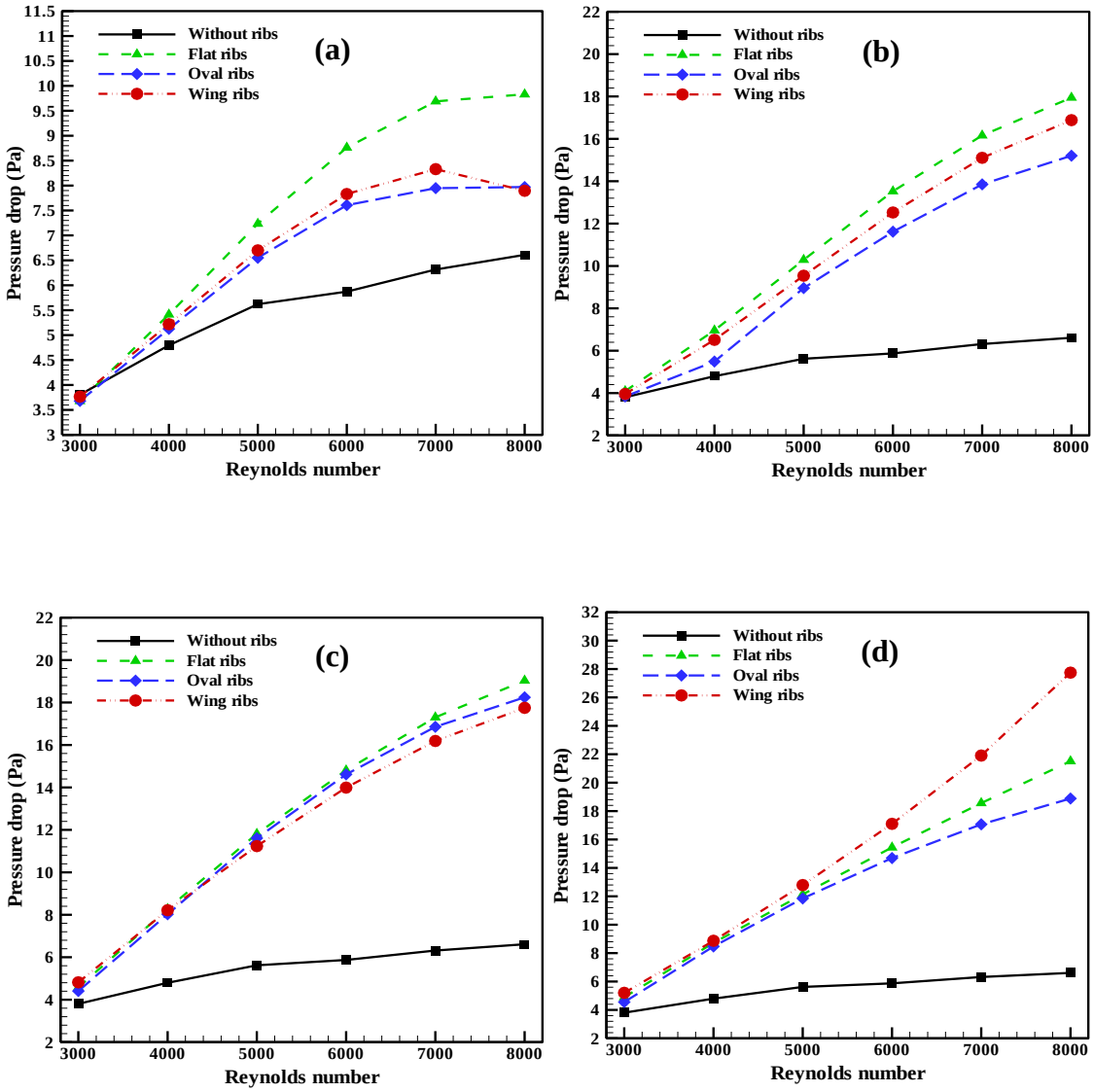

Figure 5.34: Pressure drop versus jet Reynolds number for various rib shapes at d=10 mm for (a) a=0.5 mm, (b) a=1 mm, (c) a=1.5 mm, (d) a=2 mm.

The average of the total entropy generation versus jet Reynolds number at rib location of (d=10 mm) for various ribs shapes and heights of the rib is displayed in Figure 5.35. It can be noted that the average entropy generation increase as jet Reynolds number increase for all target shapes. This is due to increase in the irreversibility of the thermal and viscous dissipation. As rib height increases, the shapes of ribs have a significant influence on the total entropy generation. It is found that without ribs give the lowest values of the mean total entropy generation compared with the

other shapes. When rib height of (a=2 mm), the average of the total entropy generation in flat ribs is higher than that of the wing ribs at jet Re < 7000, but the peak value of the total entropy generation happens at this height and the highest jet Reynolds number (Re=8000) for wing ribs compared with the other target shapes.

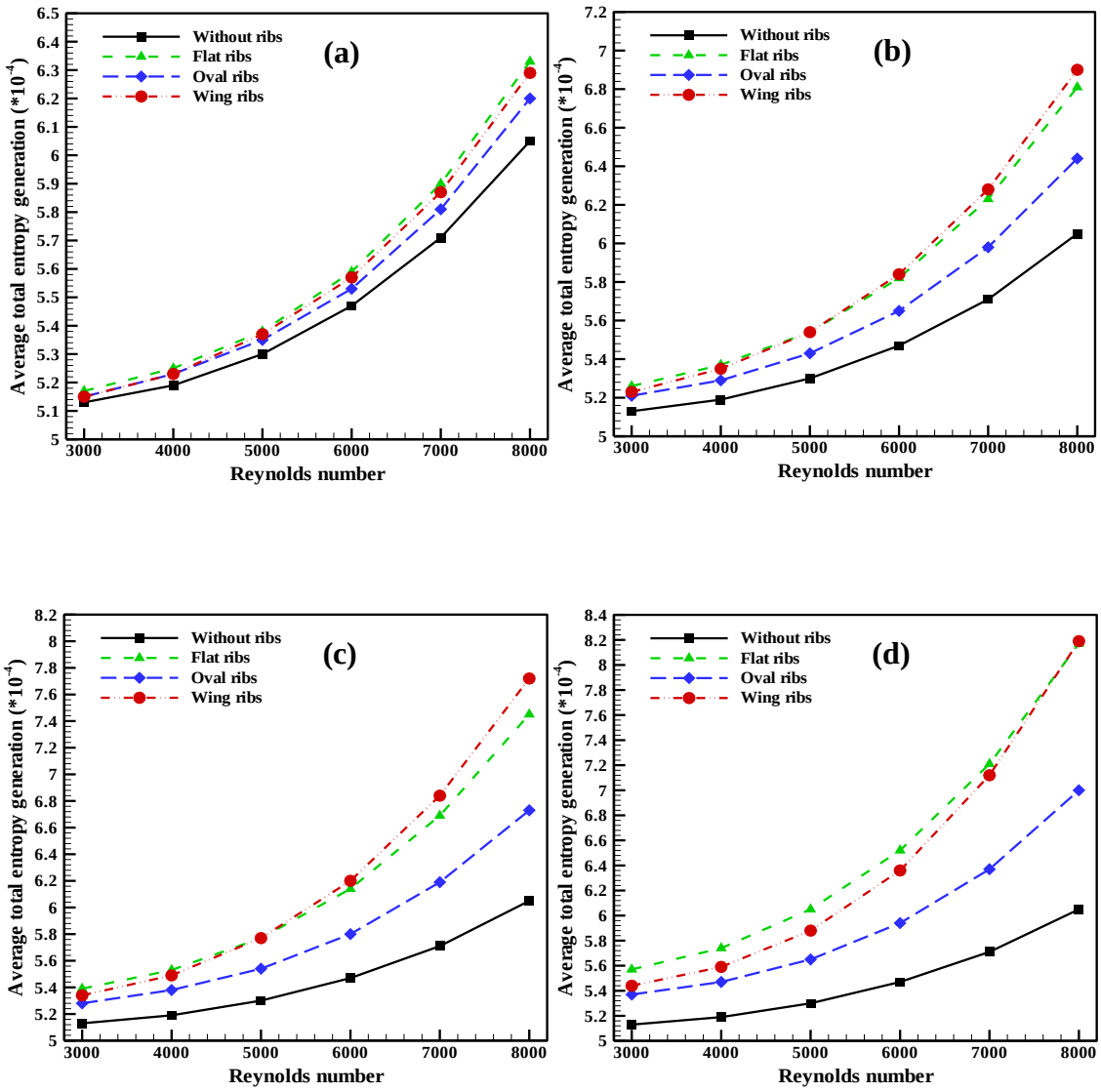

Figure 5.35: Average total entropy generation with jet Reynolds number for various rib shapes at d=10 mm for (a) a=0.5 mm, (b) a=1 mm, (c) a=1.5 mm, (d) a=2 mm.

Figure 5.36 shows the variation of the average Nusselt number enhancement with various rib height at d=10 mm for shapes of ribs. It can be observed that the flat ribs display the best heat transfer enhancement over jet Reynolds number range at a=0.5 and 1 mm. While the highest enhancement in heat transfer can be obtained by using wing ribs at a=1.5 and 2 mm over jet Reynolds number range (except Re between 5000 and 6500 at a=1.5 mm). It was also found that the maximum Nusselt number enhancement is around 90.01% which can be obtained using wing ribs at a=2 mm and jet Re=4000.

Figure 5.37 presents the performance evaluation criteria versus jet Reynolds number with various shapes of ribs and rib heights at d=10 mm. It can be seen that the performance evaluation criteria (*PEC*) sharply decrease as jet Reynolds number increases especially at rib height of (a=1, 1.5, and 2 mm), due to an increase in the pressure drop percentage. When a=0.5 mm, the wing ribs have a minimum value of the performance factor at jet Reynolds number of (Re=6000). Also, at a=1 mm, the lowest performance factor occurs at jet Re $\geq$ 5000 for wing ribs and it happens at jet Re $\geq$ 5000 for oval ribs and flat ribs. The reduced values of performance factor are due to the increase in pressure drop higher than that the augmentation in heat transfer. However, the wing ribs have the highest performance factor compared with other shapes. Moreover, it was found that at a=2 mm the maximum performance factor can occur for wing ribs followed by oval ribs and flat ribs at jet Re $\leq$ 7000 and then all values of performance factor are higher than unity for a whole range of jet Reynolds number at the same height. The peak values of the *PEC* are 1.68, 1.61, and 1.52 for wing ribs, oval ribs, and flat ribs, respectively, at jet Re=3000 and a=2 mm.

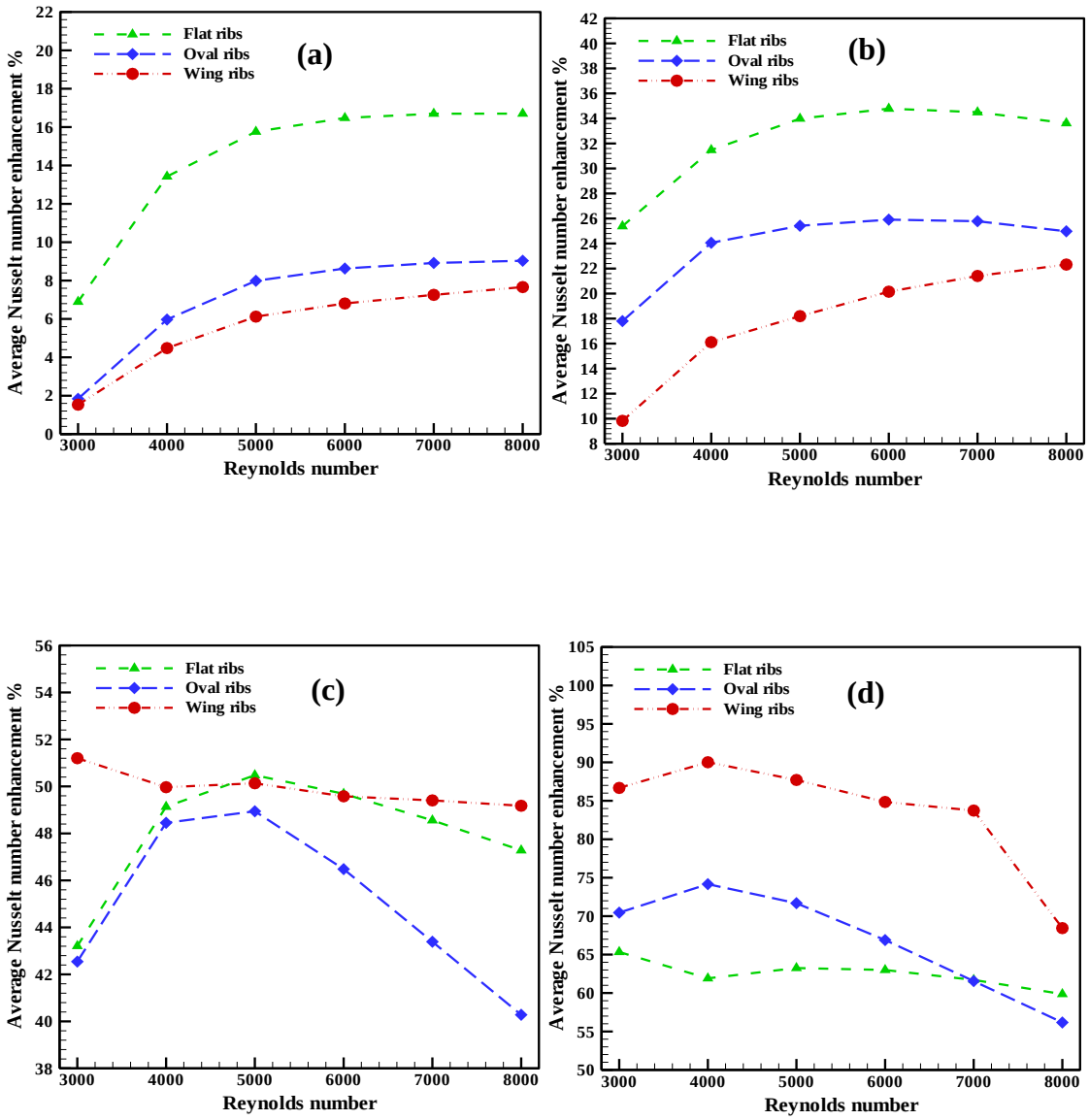

Figure 5.36: Average Nusselt number enhancement with jet Reynolds number for various rib shapes at d=10 mm for (a) a=0.5 mm, (b) a=1 mm, (c) a=1.5 mm, (d) a=2 mm.

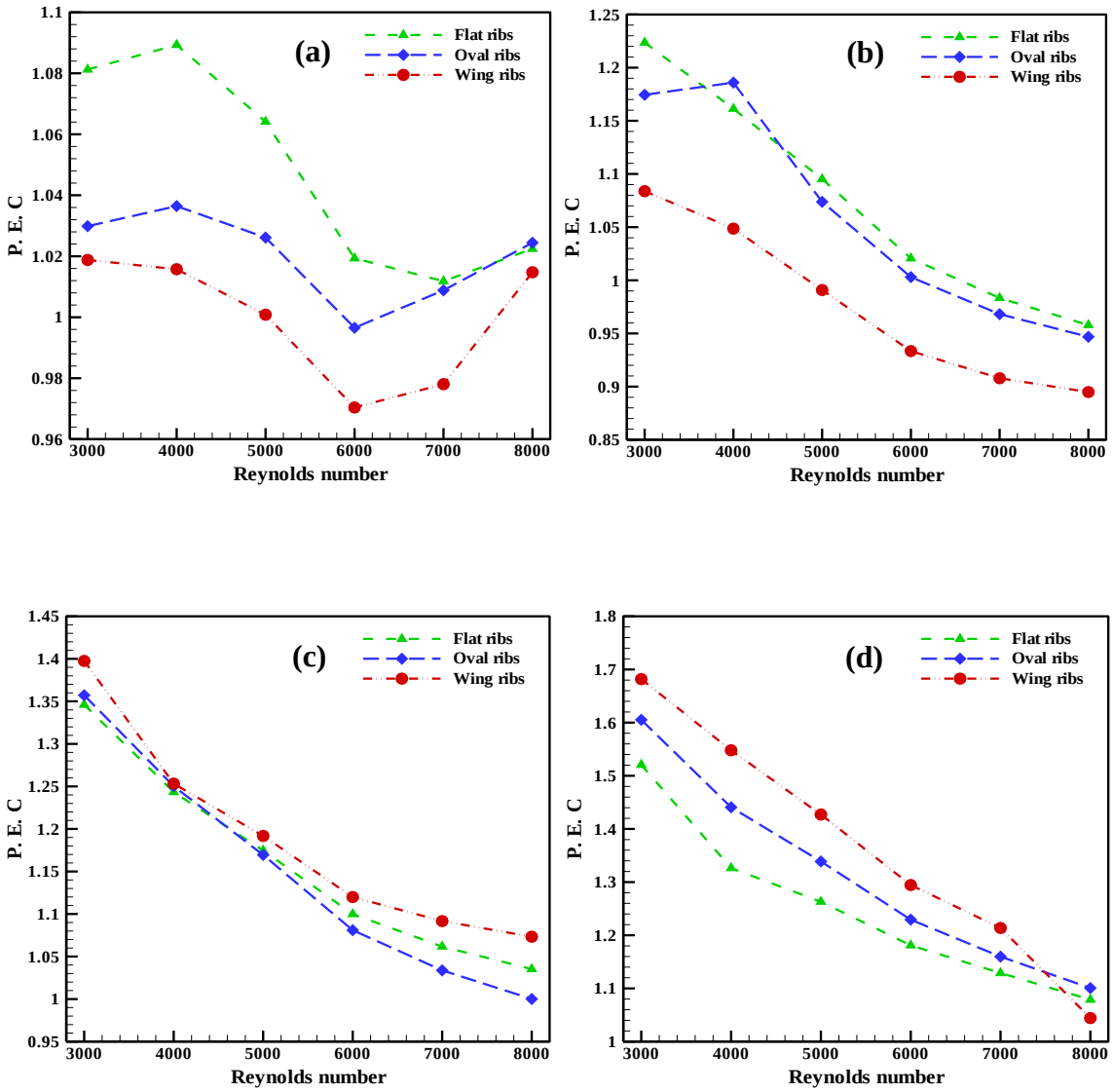

Figure 5.37: Performance evaluation criteria versus jet Reynolds number for various rib shapes at d=10 mm for (a) a=0.5 mm, (b) a=1 mm, (c) a=1.5 mm, (d) a=2 mm.

CHAPTER SIX
CONCLUSIONS AND RECOMMENDATIONS

6.1 Conclusions

Generally, experimental and numerical studies have been carried out to investigate the confined turbulent slot-jet impingement on heat transfer, fluid characteristics, and entropy generation in ribs shapes of target surfaces in this research. The numerical simulations have been conducted of three various ribs shapes; wing, oval, and flat ribs with rib heights of (a=0.5, 1, 1.5, and 2 mm) and rib locations of (d=10, 20, and 30 mm), as well as smooth target surface (a=0.0) have been considered in the present investigation. Also, the CFD code was developed using the FORTRAN programming language to simulate turbulent flows. The low Reynolds number (k-ε) turbulence model of Launder and Sharma was utilized to study the turbulent flow. Furthermore, the numerical results for the present investigation have been compared with some previous investigations to check the validity of the CFD code. The experiments have been carried out for various shapes of ribs; wing, oval, and flat ribs with rib location of (d=10 mm) and rib height of (a=2 mm) over jet Reynolds number range of 3000 to 8000. According to the experimental and numerical results presented in the previous chapter, the following conclusion can be summarized:

1. The average Nusselt number, pressure drop and average total entropy generation increase with increasing jet Reynolds number for all cases.

2. The performance evaluation criteria decreases as the jet Reynolds number increases.
3. The average Nusselt number, pressure drop, average total entropy generation, the enhancement of average Nusselt number, and performance evaluation criteria increase as height of rib increases.
4. The average Nusselt number and pressure drop as well as the total entropy generation decrease with increasing the spacing between the stagnation point and the rib.
5. The wing ribs have the highest values of average Nusselt number, pressure drop, entropy generation, average Nusselt number enhancement, and performance evaluation criteria at rib location of 10 mm and rib height of 2 mm compared with other ribs shapes.
6. The maximum values of the average Nusselt number enhancement are around 90.01, 74.16, and 65.34% for wing ribs, oval ribs and flat ribs at jet Reynolds number of 4000, 4000, and 3000, respectively, at rib location 10 mm and rib height of 2 mm.
7. The highest values of the performance factor are 1.68, 1.61, and 1.52 for the wing, oval and flat ribs, respectively, at jet Reynolds of 3000 and rib height of 2 mm.

In general, the flat ribs are recommended when jet Re > 5000, due to its highest *PEC*, while the wing ribs are the optimum design when jet Re < 5000.

6.2 Suggestions for Future Work

Based on the experimental and numerical results of the present investigation, the scope for further investigations can be presented as follows:

1. Numerical and experimental investigations to study the flow and heat transfer behavior employing multiple slot jets impinging on the isothermal target surface.
2. Numerical and experimental investigation to study the effect of a number of ribs on the heat transfer characteristics using the impinging slot jet.
3. Experimental study to investigate the effects of rib height and rib location on the flow and thermal field.
4. The effect of slot jet width on heat transfer improvement and entropy generation should be numerically and experimentally studied.

REFERENCES

[1] L. G. Hansen and B. W. Webb, “Air jet impingement heat transfer from modified surfaces,” *International Journal of Heat and Mass Transfer*, vol. 36, no. 4. pp. 989–997, 1993, doi: 10.1016/S0017-9310(05)80283-2.

[2] R. Viskanta, “Nusselt-Reynolds Prize Paper Heat Transfer to Impinging Isothermal Gas and Flame Jets,” *Exp. Therm. Fluid Sci.*, vol. 6, pp. 111–134, 1993.

[3] M. Tejas Sonawane, M. Prafulla Patil, M. A. Chavhan, B. M. Dusane, and N. Management, “a Review on Heat Transfer Enhancement By Passive Methodss,” *Int. Res. J. Eng. Technol.*, vol. 3, no. 9, pp. 1567–1574, 2016.

[4] J. Mahesh, A. R., B. Diksha, B. Amol, and M. Mayura, “Review on Enhancement of Heat Transfer by Active Method,” *Int. J. Curr. Eng. Technol.*, vol. 6, no. Special Issue-6 (Oct 2016), pp. 221–225, 2016.

[5] J. Jörg, S. Taraborrelli, E. Sabelberg, R. Kneer, R. De Doncker, and W. Rohlfs, “Hot spot removal in power electronics by means of direct liquid jet cooling,” in *2017 16th IEEE Intersociety Conference on Thermal and Thermomechanical Phenomena in Electronic Systems (ITherm)*, 2017, pp. 471–481.

[6] O. Al-aqal, “Heat transfer distributions on the walls of a narrow channel with jet impingement and cross flow.” University of Pittsburgh, 2003.

[7] C. Y. Li and S. V. Garimella, “Prandtl-number effects and generalized correlations for confined and submerged jet

impingement," *Int. J. Heat Mass Transf.*, vol. 44, no. 18, pp. 3471–3480, 2001, doi: 10.1016/S0017-9310(01)00003-5.

[8] A. M. Achari and M. K. Das, "Application of various RANS based models towards predicting turbulent slot jet impingement," *Int. J. Therm. Sci.*, vol. 98, pp. 332–351, 2015.

[9] T. H. Park, H. G. Choi, J. Y. Yoo, and S. J. Kim, "Streamline upwind numerical simulation of two-dimensional confined impinging slot jets," *Int. J. Heat Mass Transf.*, vol. 46, no. 2, pp. 251–262, 2003, doi: 10.1016/S0017-9310(02)00270-3.

[10] M. Nirmalkumar, V. Katti, and S. V. Prabhu, "Local heat transfer distribution on a smooth flat plate impinged by a slot jet," *Int. J. Heat Mass Transf.*, vol. 54, no. 1–3, pp. 727–738, 2011, doi: 10.1016/j.ijheatmasstransfer.2010.09.030.

[11] O. Caggese, G. Gnaegi, G. Hannema, A. Terzis, and P. Ott, "Experimental and numerical investigation of a fully confined impingement round jet," *Int. J. Heat Mass Transf.*, vol. 65, pp. 873–882, 2013, doi: 10.1016/j.ijheatmasstransfer.2013.06.043.

[12] P. Culun, N. Celik, and K. Pihtili, "Effects of design parameters on a multi jet impinging heat transfer," *Alexandria Eng. J.*, vol. 57, no. 4, pp. 4255–4266, 2018.

[13] W. Zhou, L. Yuan, Y. Liu, D. Peng, and X. Wen, "Heat transfer of a sweeping jet impinging at narrow spacings," *Exp. Therm. Fluid Sci.*, vol. 103, pp. 89–98, 2019.

[14] S. Fechter, A. Terzis, P. Ott, B. Weigand, J. Von Wolfersdorf, and M. Cochet, "Experimental and numerical investigation of narrow impingement cooling channels," *Int. J. Heat Mass Transf.*, vol. 67,

pp. 1208–1219, 2013.

[15] O. Manca, P. Mesolella, S. Nardini, and D. Ricci, “Numerical study of a confined slot impinging jet with nanofluids,” *Nanoscale Res. Lett.*, vol. 6, no. 1, pp. 1–16, 2011, doi: 10.1186/1556-276X-6-188.

[16] J. Lv, S. Chang, C. Hu, M. Bai, P. Wang, and K. Zeng, “Experimental investigation of free single jet impingement using Al2O3-water nanofluid,” *Int. Commun. Heat Mass Transf.*, vol. 88, pp. 126–135, 2017, doi: 10.1016/j.icheatmasstransfer.2017.08.017.

[17] N. K. Chougule, G. V. Parishwad, P. R. Gore, S. Pagnis, and S. N. Sapali, “CFD analysis of multi-jet air impingement on flat plate,” *Proc. World Congr. Eng. 2011, WCE 2011*, vol. 3, pp. 2431–2435, 2011.

[18] F. Afroz and M. A. R. Sharif, “Numerical study of heat transfer from an isothermally heated flat surface due to turbulent twin oblique confined slot-jet impingement,” *Int. J. Therm. Sci.*, vol. 74, pp. 1–13, 2013, doi: 10.1016/j.ijthermalsci.2013.07.004.

[19] D. Singh, B. Premachandran, and S. Kohli, “Experimental and numerical investigation of jet impingement cooling of a circular cylinder,” *Int. J. Heat Mass Transf.*, vol. 60, pp. 672–688, 2013.

[20] M. A. R. Sharif and A. Banerjee, “Numerical analysis of heat transfer due to confined slot-jet impingement on a moving plate,” *Appl. Therm. Eng.*, vol. 29, no. 2–3, pp. 532–540, 2009, doi: 10.1016/j.applthermaleng.2008.03.011.

[21] M. Amjadian, H. Safarzadeh, M. Bahiraei, S. Nazari, and B. Jaberi, “Heat transfer characteristics of impinging jet on a hot surface with constant heat flux using Cu2O–water nanofluid: An experimental

study," *Int. Commun. Heat Mass Transf.*, vol. 112, p. 104509, 2020.

[22] H. Huang, T. Sun, G. Zhang, D. Li, and H. Wei, "Evaluation of a developed SST k-*w* turbulence model for the prediction of turbulent slot jet impingement heat transfer," *Int. J. Heat Mass Transf.*, vol. 139, pp. 700–712, 2019, doi: 10.1016/j.ijheatmasstransfer.2019.05.058.

[23] B. Buonomo, O. Manca, N. S. Bondareva, and M. A. Sheremet, "Thermal and fluid dynamic behaviors of confined slot jets impinging on an isothermal moving surface with nanofluids," *Energies*, vol. 12, no. 11, 2019, doi: 10.3390/en12112074.

[24] M. Adimurthy and V. V. Katti, "Local distribution of wall static pressure and heat transfer on a smooth flat plate impinged by a slot air jet," *Heat Mass Transf. und Stoffuebertragung*, vol. 53, no. 2, pp. 611–623, 2017, doi: 10.1007/s00231-016-1847-9.

[25] J.-B. Huang, "Numerical Study of a Confined Axisymmetric Jet Impingement Heat Transfer with Nanofluids," *Engineering*, vol. 05, no. 01, pp. 69–74, 2013, doi: 10.4236/eng.2013.51b013.

[26] P. Xu, A. Sasmito, and A. Mujumdar, "A computational study of heat transfer under twin turbulent slot jets impinging on planar smooth and rough surfaces," *Therm. Sci.*, vol. 20, no. suppl. 1, pp. 47–57, 2016, doi: 10.2298/tsci151130016x.

[27] M. Attalla, A. A. Abdel Samee, and N. N. Salem, "Experimental investigation of heat transfer of impinging jet on a roughened plate by a micro cubic shape," *Exp. Heat Transf.*, vol. 33, no. 3, pp. 210–225, 2020, doi: 10.1080/08916152.2019.1614113.

[28] R. Mondal and D. Singh, "Numerical Study on Single Slot Jet

Impingement on Hemispherical Convex Dimple Surface," in *ICTEA: International Conference on Thermal Engineering*, 2019, vol. 2019.

[29] B. Sagot, G. Antonini, and F. Buron, "Enhancement of jet-to-wall heat transfer using axisymmetric grooved impinging plates," *Int. J. Therm. Sci.*, vol. 49, no. 6, pp. 1026–1030, 2010, doi: 10.1016/j.ijthermalsci.2009.12.011.

[30] C. Wan, Y. Rao, and P. Chen, "Numerical predictions of jet impingement heat transfer on square pin-fin roughened plates," *Appl. Therm. Eng.*, vol. 80, pp. 301–309, 2015, doi: 10.1016/j.applthermaleng.2015.01.053.

[31] H. Ahmadi, R. M. Moghari, K. Esmailpour, and A. S. Mujumdar, "Numerical investigation of semi-confined turbulent slot jet impingement on a concave surface using an Al2O3-water nanofluid," *Appl. Math. Model.*, vol. 40, no. 2, pp. 1110–1125, 2016, doi: 10.1016/j.apm.2015.06.021.

[32] A. H. Beitelmal, M. A. Saad, and C. D. Patel, "Effects of surface roughness on the average heat transfer of an impinging air jet," *Int. Commun. Heat Mass Transf.*, vol. 27, no. 1, pp. 1–12, 2000, doi: 10.1016/S0735-1933(00)00079-8.

[33] E. Öztekin, O. Aydin, and M. Avci, "Heat transfer in a turbulent slot jet flow impinging on concave surfaces," *Int. Commun. Heat Mass Transf.*, vol. 44, pp. 77–82, 2013.

[34] Y. Zhou, G. Lin, X. Bu, L. Bai, and D. Wen, "Experimental study of curvature effects on jet impingement heat transfer on concave surfaces," *Chinese J. Aeronaut.*, vol. 30, no. 2, pp. 586–594, 2017,

doi: 10.1016/j.cja.2016.12.032.

[35] Y. Xing, S. Spring, and B. Weigand, “Experimental and numerical investigation of impingement heat transfer on a flat and micro-rib roughened plate with different crossflow schemes,” *Int. J. Therm. Sci.*, vol. 50, no. 7, pp. 1293–1307, 2011.

[36] A. K. Shukla, A. Dewan, and B. Srinivasan, “Computational Study of Turbulent Slot Jet Impingement on a Ribbed Surface,” *Proceedings of the 6th International and 43rd National Conference on Fluid Mechanics and Fluid Power*, no. 08, pp. 8–10, 2016.

[37] L. A. El-Gabry and D. A. Kaminski, “Experimental investigation of local heat transfer distribution on smooth and roughened surfaces under an array of angled impinging jets,” *J. Turbomach.*, vol. 127, no. 3, pp. 532–544, 2005, doi: 10.1115/1.1861918.

[38] D. Zhang, H. Qu, J. Lan, J. Chen, and Y. Xie, “Flow and heat transfer characteristics of single jet impinging on protrusioned surface,” *Int. J. Heat Mass Transf.*, vol. 58, no. 1–2, pp. 18–28, 2013.

[39] N. Asghari Lafmajani, M. Ebrahimi Bidhendi, and M. Ashjaee, “SiO2 nanofluid planar jet impingement cooling on a convex heated plate,” *Heat Mass Transf. und Stoffuebertragung*, vol. 52, no. 12, pp. 2735–2746, 2016, doi: 10.1007/s00231-016-1778-5.

[40] L. Tan, J.-Z. Zhang, and H.-S. Xu, “Jet impingement on a rib-roughened wall inside semi-confined channel,” *Int. J. Therm. Sci.*, vol. 86, pp. 210–218, 2014.

[41] W. C. Buzzard, Z. Ren, P. M. Ligrani, C. Nakamata, and S. Ueguchi, “Influences of target surface small-scale rectangle roughness on impingement jet array heat transfer,” *Int. J. Heat Mass Transf.*, vol.

110, pp. 805–816, 2017.

[42] P. Xu, A. P. Sasmito, S. Qiu, A. S. Mujumdar, L. Xu, and L. Geng, “Heat transfer and entropy generation in air jet impingement on a model rough surface,” *Int. Commun. Heat Mass Transf.*, vol. 72, pp. 48–56, 2016, doi: 10.1016/j.icheatmasstransfer.2016.01.007.

[43] B. E. Launder and B. I. Sharma, “Application of the energy-dissipation model of turbulence to the calculation of flow near a spinning disc,” *Lett. heat mass Transf.*, vol. 1, no. 2, pp. 131–137, 1974.

[44] L. C. Yang, Y. Asako, Y. Yamaguchi, and M. Faghri, “Numerical prediction of transitional characteristics of flow and heat transfer in a corrugated duct,” *Journal of heat transfer*, vol. 119, no.1, pp. 62-69, 1997.

[45] J. Blazek, *Computational fluid dynamics: principles and applications*. Butterworth-Heinemann, 2015.

[46] C. J. Chen, *Fundamentals of turbulence modelling*. CRC Press, 1997.

[47] J. F. Wendt, *Computational fluid dynamics: An introduction*. 3rd edition. Springer Science, 2008.

[48] J. F. Thompson, F. C. Thames, and C. W. Mastin, “Automatic numerical generation of body-fitted curvilinear coordinate system for field containing any number of arbitrary two-dimensional bodies,” *J. Comput. Phys.*, vol. 15, no. 3, pp. 299–319, 1974, doi: 10.1016/0021-9991(74)90114-4.

[49] T. Cebeci, J. P. Shao, F. Kafyeke, and E. Laurendeau, *Computational fluid dynamics for engineers*. Springer Berlin

Heidelberg, 2005.

[50] H. Shokouhmand and S. Bigham, “Slip-flow and heat transfer of gaseous flows in the entrance of a wavy microchannel,” *Int. Commun. Heat Mass Transf.*, vol. 37, no. 6, pp. 695–702, 2010, doi: 10.1016/j.icheatmasstransfer.2010.03.008.

[51] J. H. Ferziger and M. Peric, “Computational Methods for Fluid Dynamics Springer Verlag.” Berlin, 1999.

[52] H. K. Versteeg and W. Malalasekera, *An introduction to computational fluid dynamics: the finite volume method*. Pearson education, 2007.

[53] S. V. PATANKAR and D. B. Spalding, *A calculation procedure for the transient and steady-state behaviour of shell-and-tube heat exchangers*. Imperial College of Science and Technology, Department of Mechanical Engineering, 1972.

[54] H. M. S. Bahaidarah, N. K. Anand, and H. C. Chen, “Numerical study of heat and momentum transfer in channels with wavy walls,” *Numer. Heat Transf. Part A*, vol. 47, no. 5, pp. 417–439, 2005.

[55] C. M. Rhie and W. L. Chow, “Numerical study of the turbulent flow past an airfoil with trailing edge separation,” *AIAA J.*, vol. 21, no. 11, pp. 1525–1532, 1983.

[56] K. Esmailpour, B. Bozorgmehr, S. M. Hosseinalipour, and A. S. Mujumdar, “Entropy generation and second law analysis of pulsed impinging jet,” *Int. J. Numer. Methods Heat Fluid Flow*, vol. 25, no. 5, pp. 1089–1106, 2015, doi: 10.1108/HFF-05-2014-0148.

[57] S. Rashidi, M. Akbarzadeh, R. Masoodi, and E. M. Languri, “Thermal-hydraulic and entropy generation analysis for turbulent

flow inside a corrugated channel," *Int. J. Heat Mass Transf.*, vol. 109, pp. 812–823, 2017.

[58] T. L. Bergman, F. P. Incropera, A. S. Lavine, and D. P. Dewitt, *Introduction to heat transfer*. John Wiley & Sons, 2011.

[59] L. Zhang and D. Che, "Influence of corrugation profile on the thermalhydraulic performance of cross-corrugated plates," *Numer. Heat Transf. Part A Appl.*, vol. 59, no. 4, pp. 267–296, 2011.

[60] A. Z. Dellil, A. Azzi, and B. A. Jubran, "Turbulent flow and convective heat transfer in a wavy wall channel," *Heat Mass Transf.*, vol. 40, no. 10, pp. 793–799, 2004.

[61] M. Kalteh, A. Abbassi, M. Saffar-Avval, and J. Harting, "Eulerian–Eulerian two-phase numerical simulation of nanofluid laminar forced convection in a microchannel," *Int. J. heat fluid flow*, vol. 32, no. 1, pp. 107–116, 2011.

[62] H. M. Maghrabie, M. Attalla, H. E. Fawaz, and M. Khalil, "Numerical investigation of heat transfer and pressure drop of in-line array of heated obstacles cooled by jet impingement in cross-flow," *Alexandria Eng. J.*, vol. 56, no. 3, pp. 285–296, 2017, doi: 10.1016/j.aej.2016.12.022.

[63] M. Khoshvaght-Aliabadi, F. Hormozi, and A. Zamzamian, "Experimental analysis of thermal–hydraulic performance of copper–water nanofluid flow in different plate-fin channels," *Exp. Therm. fluid Sci.*, vol. 52, pp. 248–258, 2014.

[64] X. Gao and B. Sundén, "Experimental investigation of the heat transfer characteristics of confined impinging slot jets," *Exp. Heat Transf.*, vol. 16, no. 1, pp. 1–18, 2003, doi: 10.1080/

08916150390126441.

[65] S. D. Pandey and V. K. Nema, “Experimental analysis of heat transfer and friction factor of nanofluid as a coolant in a corrugated plate heat exchanger,” *Exp. Therm. Fluid Sci.*, vol. 38, pp. 248–256, 2012.

[66] S. J. Kline, “Describing uncertainty in single sample experiments,” *Mech. Eng.*, vol. 75, pp. 3–8, 1953.

[67] F. F. Cadek, “A fundamental investigation of jet impingement heat transfer.,” University of Cincinnati, 1969.

[68] R. Gardon and J. C. Akfirat, “Heat Transfer Characteristics of Impinging Two-Dimensional Air Jets. J Heat Transfer. 1966;88:101. ensional Air Jets,” *J. Heat Transfer*, vol. 88, p. 101, 1966.

APPENDIX A
NUMERICAL SOLUTION

A.1 Body-Fitted Coordinates System

The governing equations are transformed from the Cartesian coordinate system (x, y) to a body-fitted coordinate system (ζ, η) presented as follows [47]:

$$\xi = \xi(x, y) \tag{A.1}$$

$$\eta = \eta(x, y) \tag{A.2}$$

In the above equations, the chain rule can be applied to express ξ and η derivatives in term of x and y as given below:

$$\frac{\partial \phi}{\partial \xi} = \frac{\partial \phi}{\partial x}\frac{\partial x}{\partial \xi} + \frac{\partial \phi}{\partial y}\frac{\partial y}{\partial \xi} \tag{A.3}$$

$$\frac{\partial \phi}{\partial \eta} = \frac{\partial \phi}{\partial x}\frac{\partial x}{\partial \eta} + \frac{\partial \phi}{\partial y}\frac{\partial y}{\partial \eta} \tag{A.4}$$

These equations can be given in a matrix form as below:

$$\begin{bmatrix} \frac{\partial \phi}{\partial \xi} \\ \frac{\partial \phi}{\partial \eta} \end{bmatrix} = \begin{bmatrix} \frac{\partial x}{\partial \xi} & \frac{\partial y}{\partial \xi} \\ \frac{\partial x}{\partial \eta} & \frac{\partial y}{\partial \eta} \end{bmatrix} \begin{bmatrix} \frac{\partial \phi}{\partial x} \\ \frac{\partial \phi}{\partial y} \end{bmatrix} \tag{A.5}$$

Using Cramer's rule to invert the above equation as below:

$$\frac{\partial \phi}{\partial x_i} = \frac{1}{J}\,\beta_{i,j}\frac{\partial \phi}{\partial \xi_j}\ , \text{where } i = 1, 2; j = 1, 2 \tag{A.6}$$

The system is become in matrix form as follow:

$$\begin{bmatrix} \frac{\partial \phi}{\partial x} \\ \frac{\partial \phi}{\partial y} \end{bmatrix} = \frac{1}{J}[\beta] \begin{bmatrix} \frac{\partial \phi}{\partial \xi} \\ \frac{\partial \phi}{\partial \eta} \end{bmatrix} \quad (A.7)$$

Where

$$[\beta] = \begin{bmatrix} \beta_{11} & \beta_{12} \\ \beta_{21} & \beta_{22} \end{bmatrix} = \begin{bmatrix} y_\eta & -y_\xi \\ -x_\eta & x_\xi \end{bmatrix} \quad (A.8)$$

Also, *J:* is the Jacobin of the transformation and is expressed as follows [51]:

$$J = \beta_{22}\beta_{11} - \beta_{21}\beta_{12} = x_\xi y_\eta - x_\eta y_\xi \quad (A.9)$$

Hence, in the terms of body-fitted coordinate, the transformation of the first partial derivatives can be described as follows [47]:

$$\frac{\partial \phi}{\partial x} = \frac{1}{J}\left[\beta_{11}\frac{\partial \phi}{\partial \xi} + \beta_{12}\frac{\partial \phi}{\partial \eta}\right] \quad (A.10)$$

$$\frac{\partial \phi}{\partial y} = \frac{1}{J}\left[\beta_{21}\frac{\partial \phi}{\partial \xi} + \beta_{22}\frac{\partial \phi}{\partial \eta}\right] \quad (A.11)$$

With respect to second derivatives, in a term of body-fitted coordinates, the general format of those derivatives is presented by:

$$\frac{\partial}{\partial x_j}\left(\frac{\partial \phi}{\partial x_l}\right) = \frac{1}{J}\frac{\partial}{\partial \xi_i}\left[\frac{1}{J}\beta_{ji}\beta_{lk}\frac{\partial \phi}{\partial \xi_k}\right], i = 1,2; j = 1,2; l = 1,2; k = 1,2 \quad (A.12)$$

Therefore, the second partial derivatives transformation for the respect of *x* is presented by:

$$\frac{\partial}{\partial x}\left(\frac{\partial \phi}{\partial x}\right) = \frac{1}{J}\frac{\partial}{\partial \xi}\left[\frac{1}{J}\left(\beta_{11}\beta_{11}\frac{\partial \phi}{\partial \xi} + \beta_{11}\beta_{12}\frac{\partial \phi}{\partial \eta}\right)\right]$$

$$+\frac{1}{J}\frac{\partial}{\partial\eta}\left[\frac{1}{J}\left(\left(\beta_{12}\,\beta_{11}\frac{\partial\phi}{\partial\xi}+\ \beta_{12}\,\beta_{12}\frac{\partial\phi}{\partial\eta}\right)\right]\right. \qquad (A.13)$$

Moreover, the second partial derivatives transformation for the respect of *y* is expressed as:

$$\frac{\partial}{\partial y}\left(\frac{\partial\phi}{\partial y}\right)=\frac{1}{J}\frac{\partial}{\partial\xi}\left[\frac{1}{J}\left(\beta_{21}\,\beta_{21}\frac{\partial\phi}{\partial\xi}+\ \beta_{21}\,\beta_{22}\frac{\partial\phi}{\partial\eta}\right)\right]$$

$$+\frac{1}{J}\frac{\partial}{\partial\eta}\left[\frac{1}{J}\left(\left(\beta_{22}\,\beta_{21}\frac{\partial\phi}{\partial\xi}+\ \beta_{22}\,\beta_{22}\frac{\partial\phi}{\partial\eta}\right)\right]\right. \qquad (A.14)$$

Furthermore, the second mixed partial derivative transformation for the respect of *x* and *y* is defined as:

$$\frac{\partial}{\partial x}\left(\frac{\partial\phi}{\partial y}\right)=\frac{1}{J}\frac{\partial}{\partial\xi}\left[\frac{1}{J}\left(\beta_{11}\,\beta_{21}\frac{\partial\phi}{\partial\xi}+\ \beta_{11}\,\beta_{22}\frac{\partial\phi}{\partial\eta}\right)\right]$$

$$+\frac{1}{J}\frac{\partial}{\partial\eta}\left[\frac{1}{J}\left(\left(\beta_{12}\,\beta_{21}\frac{\partial\phi}{\partial\xi}+\ \beta_{12}\,\beta_{22}\frac{\partial\phi}{\partial\eta}\right)\right]\right. \qquad (A.14)$$

In addition, the second mixed partial derivative transformation for the respect of *y* and *x* is given as:

$$\frac{\partial}{\partial x}\left(\frac{\partial\phi}{\partial x}\right)=\frac{1}{J}\frac{\partial}{\partial\xi}\left[\frac{1}{J}\left(\beta_{21}\,\beta_{11}\frac{\partial\phi}{\partial\xi}+\ \beta_{21}\,\beta_{12}\frac{\partial\phi}{\partial\eta}\right)\right]$$

$$+\frac{1}{J}\frac{\partial}{\partial\eta}\left[\frac{1}{J}\left(\left(\beta_{22}\,\beta_{11}\frac{\partial\phi}{\partial\xi}+\ \beta_{22}\,\beta_{12}\frac{\partial\phi}{\partial\eta}\right)\right]\right. \qquad (A.15)$$

Where,

ϕ : is the general dependent variable, such as $(u, v, T,$ and $P)$.

A.2 Computational Grid

Two-dimensional Poisson equations described in equation 3.21 and 3.22 in chapter three, can be defined as below:

$$q_{11}\frac{\partial^2 x}{\partial \xi^2} - 2q_{12}\frac{\partial^2 x}{\partial \xi \eta} + q_{22}\frac{\partial^2 x}{\partial \eta^2} + J^2\left(P\frac{\partial x}{\partial \xi} + Q\frac{\partial x}{\partial \eta}\right) = 0 \qquad (A.16)$$

$$q_{11}\frac{\partial^2 y}{\partial \xi^2} - 2q_{12}\frac{\partial^2 y}{\partial \xi \eta} + q_{22}\frac{\partial^2 y}{\partial \eta^2} + J^2\left(P\frac{\partial y}{\partial \xi} + Q\frac{\partial y}{\partial \eta}\right) = 0 \qquad (A.17)$$

Now, utilizing Finite Difference Method (FDM), equation A.16 and A.17 are discretized as below.

$$q_{11(i,j)}\left[\frac{x_{i+1,j}-2x_{i,j}+x_{i-1,j}}{\Delta\xi^2}\right] - 2q_{12(i,j)}\left[\frac{x_{i+1,j+1}-x_{i+1,j-1}-x_{i-1,j+1}+x_{i-1,j-1}}{4\Delta\xi\,\Delta\eta}\right] + q_{22(i,j)}\left[\frac{x_{i,j+1}-2x_{i,j}+x_{i,j-1}}{\Delta\eta^2}\right] + J^2{}_{(i,j)}\left[P_{(i,j)}\frac{x_{i+1,j}-x_{i-1,j}}{2\Delta\xi} + Q_{(i,j)}\frac{x_{i,j+1}-x_{i,j-1}}{2\Delta\eta}\right] = 0 \qquad (A.18)$$

$$q_{11(i,j)}\left[\frac{y_{i+1,j}-2y_{i,j}+y_{i-1,j}}{\Delta\xi^2}\right] - 2q_{12(i,j)}\left[\frac{y_{i+1,j+1}-y_{i+1,j-1}-y_{i-1,j+1}+y_{i-1,j-1}}{4\Delta\xi\,\Delta\eta}\right] + q_{22(i,j)}\left[\frac{y_{i,j+1}-2y_{i,j}+y_{i,j-1}}{\Delta\eta^2}\right] + J^2{}_{(i,j)}\left[P_{(i,j)}\frac{y_{i+1,j}-y_{i-1,j}}{2\Delta\xi} + Q_{(i,j)}\frac{y_{i,j+1}-y_{i,j-1}}{2\Delta\eta}\right] = 0 \qquad (A.19)$$

Re-arrangement equation A.18 and A.19 can be given as follow:

$$x_{i,j} = -\left(\frac{\Delta\xi^2+\Delta\eta^2}{\Delta\eta^2 q_{11(i,j)}+\Delta\xi^2 q_{22(i,j)}}\right)\left[q_{11(i,j)}\left(\frac{x_{i+1,j}+x_{i-1,j}}{\Delta\xi^2}\right) + q_{22(i,j)}\left(\frac{x_{i,j-1}+x_{i,j-1}}{\Delta\eta^2}\right) - 2q_{12(i,j)}\left(\frac{x_{i+1,j+1}-x_{i+1,j-1}-x_{i-1,j+1}+x_{i-1,j-1}}{4\Delta\xi\,\Delta\eta}\right) + J^2_{(i,j)}P_{(i,j)}\left(\frac{x_{i+1,j}-x_{i-1,j}}{2\Delta\xi}\right) + J^2_{(i,j)}Q_{(i,j)}\left(\frac{x_{i,j+1}-x_{i,j-1}}{2\Delta\eta}\right)\right] \qquad (A.20)$$

$$y_{i,j} = -\left(\frac{\Delta\xi^2+\Delta\eta^2}{\Delta\eta^2 q_{11(i,j)}+\Delta\xi^2 q_{22(i,j)}}\right)\left[q_{11(i,j)}\left(\frac{y_{i+1,j}+y_{i-1,j}}{\Delta\xi^2}\right) + q_{22(i,j)}\left(\frac{y_{i,j-1}+y_{i,j-1}}{\Delta\eta^2}\right) - 2q_{12(i,j)}\left(\frac{y_{i+1,j+1}-x_{i+1,j-1}-y_{i-1,j+1}+y_{i-1,j-1}}{4\Delta\xi\,\Delta\eta}\right) + J^2_{(i,j)}P_{(i,j)}\left(\frac{y_{i+1,j}-y_{i-1,j}}{2\Delta\xi}\right) + J^2_{(i,j)}Q_{(i,j)}\left(\frac{y_{i,j+1}-y_{i,j-1}}{2\Delta\eta}\right)\right] \qquad (A.21)$$

Where:

$$q_{11_{(i,j)}} = x_\eta^2 + y_\eta^2 = \left[\frac{x_{i,j+1}-2x_{i,j}+x_{i,j-1}}{\Delta\eta^2}\right]^2 + \left[\frac{y_{i,j+1}-2y_{i,j}+y_{i,j-1}}{\Delta\eta^2}\right]^2 \quad (A.22)$$

$$q_{22_{(i,j)}} = x_\xi^2 + y_\xi^2 = \left[\frac{x_{i,j+1}-2x_{i,j}+x_{i,j-1}}{\Delta\xi^2}\right]^2 + \left[\frac{y_{i,j+1}-2y_{i,j}+y_{i,j-1}}{\Delta\xi^2}\right]^2 \quad (A.23)$$

$$q_{12_{(i,j)}} = x_\xi x_\eta + y_\xi y_\eta$$

$$= \left[\frac{x_{i+1,j}-x_{i-1,j}}{2\Delta\xi}\right]\left[\frac{x_{i,j+1}-x_{i,j-1}}{2\Delta\eta}\right] + \left[\frac{y_{i+1,j}-y_{i-1,j}}{2\Delta\xi}\right]\left[\frac{y_{i,j+1}-y_{i,j-1}}{2\Delta\eta}\right] \quad (A.24)$$

Furthermore, equation A.20 and A.21 are resolved iteratively that use Successive Over-Relaxation algorithm. The control functions P(ξ,η), Q(ξ,η) in equation A.20 and A.21 for all an interior nodes of computational space can be expressed as below:

$$P(\xi,\eta) = p(\xi).e^{-a_1\eta} + r(\xi).e^{-a_2(\eta_{max}-\eta)} \quad (A.25)$$

$$Q(\xi,\eta) = q(\xi).e^{-a_1\eta} + s(\xi).e^{-a_2(\eta_{max}-\eta)} \quad (A.26)$$

In equation A.25 and A.26, the first terms for control the grid nodes at south (lower) boundary of computational space (η = 0), while the other terms for control the nodes at north (upper) boundary of computational space ($\eta_{max} = 0$), where a_1 and a_2 are called the positive constants. So, the functions *p(ξ)*, *r(ξ)*, *q(ξ)*, and *s(ξ)* can be given as below:

$$p(\xi) = P(\xi,0) \quad (A.27)$$

$$r(\xi) = P(\xi,\eta_{max}) \quad (A.28)$$

$$q(\xi) = Q(\xi,0) \quad (A.29)$$

$$s(\xi) = Q(\xi,\eta_{max}) \quad (A.30)$$

Two conditions are applied at the boundaries defined in the grid spacing and orthogonally to determine values of the functions *p(ξ), r(ξ), q(ξ),* and *s(ξ)*. Furthermore, if S_η is the required grid spacing along the boundaries, the condition can be displayed as below:

$$S_\eta^2 = \overrightarrow{r_\eta} . \overrightarrow{r_\eta} = x_\eta^2 + y_\eta^2 \qquad (A.31)$$

While, the other condition (orthogonally) can be expressed as below:

$$\overrightarrow{r_\xi} . \overrightarrow{r_\eta} = x_\xi x_\eta + y_\xi y_\eta = 0 \qquad (A.32)$$

Equation A.31 and A.32, the values of x_ξ and y_ξ at the lower boundary ($\eta = 0$), and the upper boundary ($\eta_{max} = 0$) are known. While, x_η and y_η in the above equations are unknown and it can be expressed as below:

$$x_\eta = \frac{-S_\eta y_\xi}{\sqrt{x_\xi^2 + y_\xi^2}} \qquad (A.33)$$

$$y_\eta = \frac{-S_\eta x_\xi}{\sqrt{x_\xi^2 + y_\xi^2}} \qquad (A.34)$$

$$\overrightarrow{r_\eta} = x_\eta \, \vec{i} + y_\eta \, \vec{j} = 0 \qquad (A.35)$$

In generalized form, two-dimensional Poisson equations, equation A.16 and A.17, it can be presented by as below:

$$\left(\overrightarrow{r_\eta} . \overrightarrow{r_\eta}\right)\left(\overrightarrow{r_{\xi\xi}} . P\overrightarrow{r_{\xi\xi}}\right) + \left(\overrightarrow{r_\xi} . \overrightarrow{r_\xi}\right)\left(\overrightarrow{r_{\eta\eta}} . Q\overrightarrow{r_\eta}\right) - 2\left(\overrightarrow{r_\xi} . \overrightarrow{r_\eta}\right)\overrightarrow{r_{\xi\eta}} = 0 \qquad (A.36)$$

Where,

$$q_{11} = \overrightarrow{r_\eta} . \overrightarrow{r_\eta} = x_\eta^2 + y_\eta^2 \qquad (A.37)$$

$$q_{22} = \overrightarrow{r_\xi} . \overrightarrow{r_\xi} = x_\xi^2 + y_\xi^2 \qquad (A.38)$$

$$q_{12} = \overrightarrow{r_\xi} . \overrightarrow{r_\eta} = x_\xi x_\eta + y_\xi y_\eta \qquad (A.39)$$

$$\vec{r} = x\vec{\imath} + y\vec{j} \tag{A.40}$$

$$\overrightarrow{r_\xi} = x_\xi \vec{\imath} + y_\xi \vec{j} \tag{A.41}$$

$$\overrightarrow{r_\eta} = x_\eta \vec{\imath} + y_\eta \vec{j} \tag{A.42}$$

$$\overrightarrow{r_{\xi\xi}} = x_{\xi\xi} \vec{\imath} + y_{\xi\xi} \vec{j} \tag{A.43}$$

$$\overrightarrow{r_{\eta\eta}} = x_{\eta\eta} \vec{\imath} + y_{\eta\eta} \vec{j} \tag{A.44}$$

$$\overrightarrow{r_{\xi\eta}} = x_{\xi\eta} \vec{\imath} + y_{\xi\eta} \vec{j} \tag{A.45}$$

Equation A.32 can be replaced by equation A.36, which gives:

$$\left(\overrightarrow{r_\eta}.\overrightarrow{r_\eta}\right)\left(\overrightarrow{r_{\xi\xi}}.P\overrightarrow{r_{\xi\xi}}\right) + \left(\overrightarrow{r_\xi}.\overrightarrow{r_\xi}\right)\left(\overrightarrow{r_{\eta\eta}}.Q\overrightarrow{r_\eta}\right)\Big|_{boundary} = 0 \tag{A.46}$$

The control functions at the boundaries are obtained as in below equations, multiplying equation A.40 by $\overrightarrow{r_\eta}$ or $\overrightarrow{r_\xi}$ and utilizing the orthogonally condition as defined in equation A.32.

$$P(\xi,\eta)\Big|_{boundary} = \frac{-\left(\overrightarrow{r_\xi}.\overrightarrow{r_{\xi\xi}}\right)}{\left(\overrightarrow{r_\xi}.\overrightarrow{r_\xi}\right)} - \frac{\left(\overrightarrow{r_\xi}.\overrightarrow{r_{\eta\eta}}\right)}{\left(\overrightarrow{r_\eta}.\overrightarrow{r_\eta}\right)} \tag{A.47}$$

$$Q(\xi,\eta)\Big|_{boundary} = \frac{-\left(\overrightarrow{r_\eta}.\overrightarrow{r_{\eta\eta}}\right)}{\left(\overrightarrow{r_\eta}.\overrightarrow{r_\eta}\right)} - \frac{\left(\overrightarrow{r_\eta}.\overrightarrow{r_{\xi\xi}}\right)}{\left(\overrightarrow{r_\xi}.\overrightarrow{r_\xi}\right)} \tag{A.48}$$

The functions *p(ξ)*, *r(ξ)*, *q(ξ)*, and *s(ξ)* can be obtained after calculating the values of control functions P and Q on the boundaries. Equation A.15 and A.26 are then used to determine the values of the control functions P and Q for the interior nodes. Also, in Figure A.1, the solution procedure for the computational grid of the present study is shown as below:

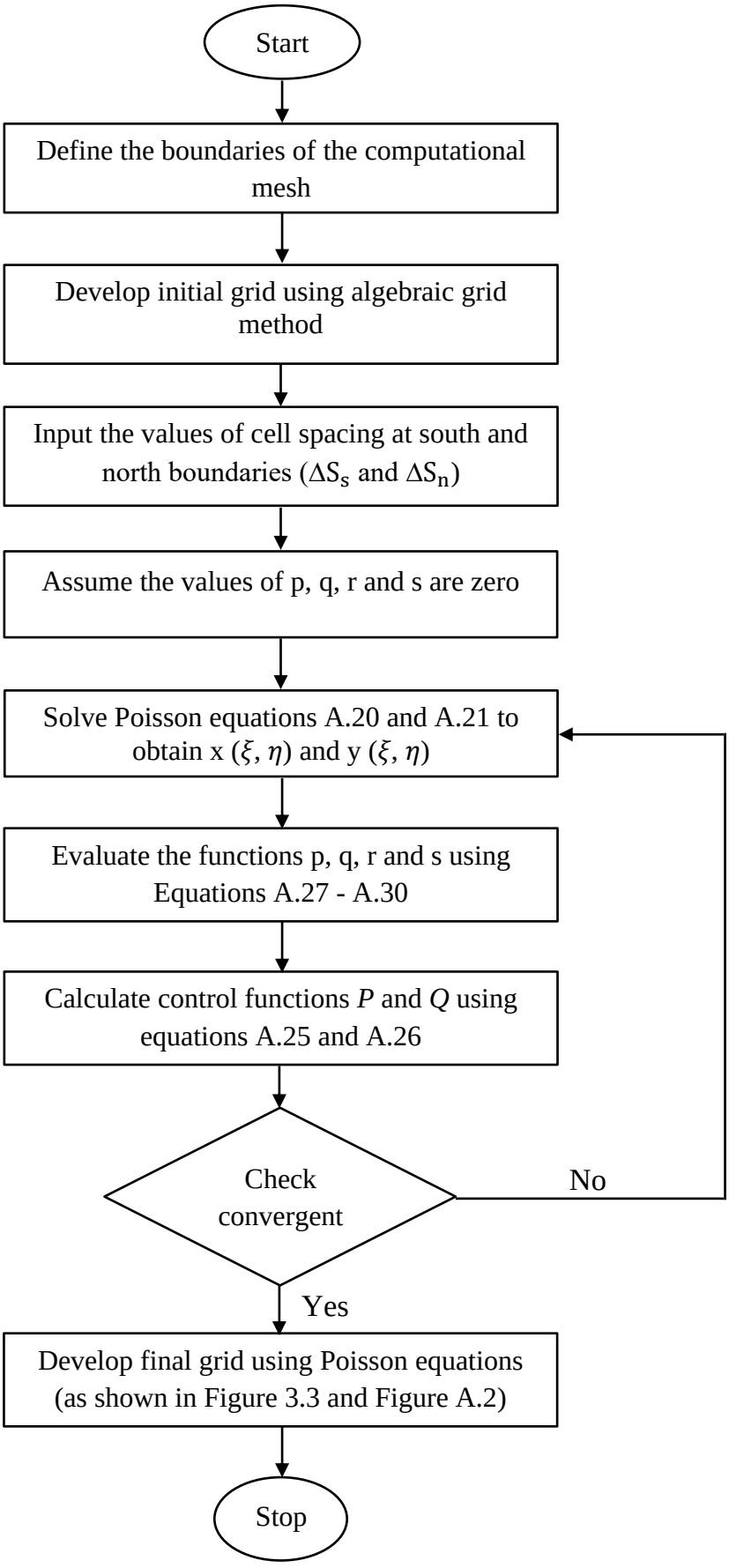

Figure A.1: Solution procedure for computational grid of present investigation.

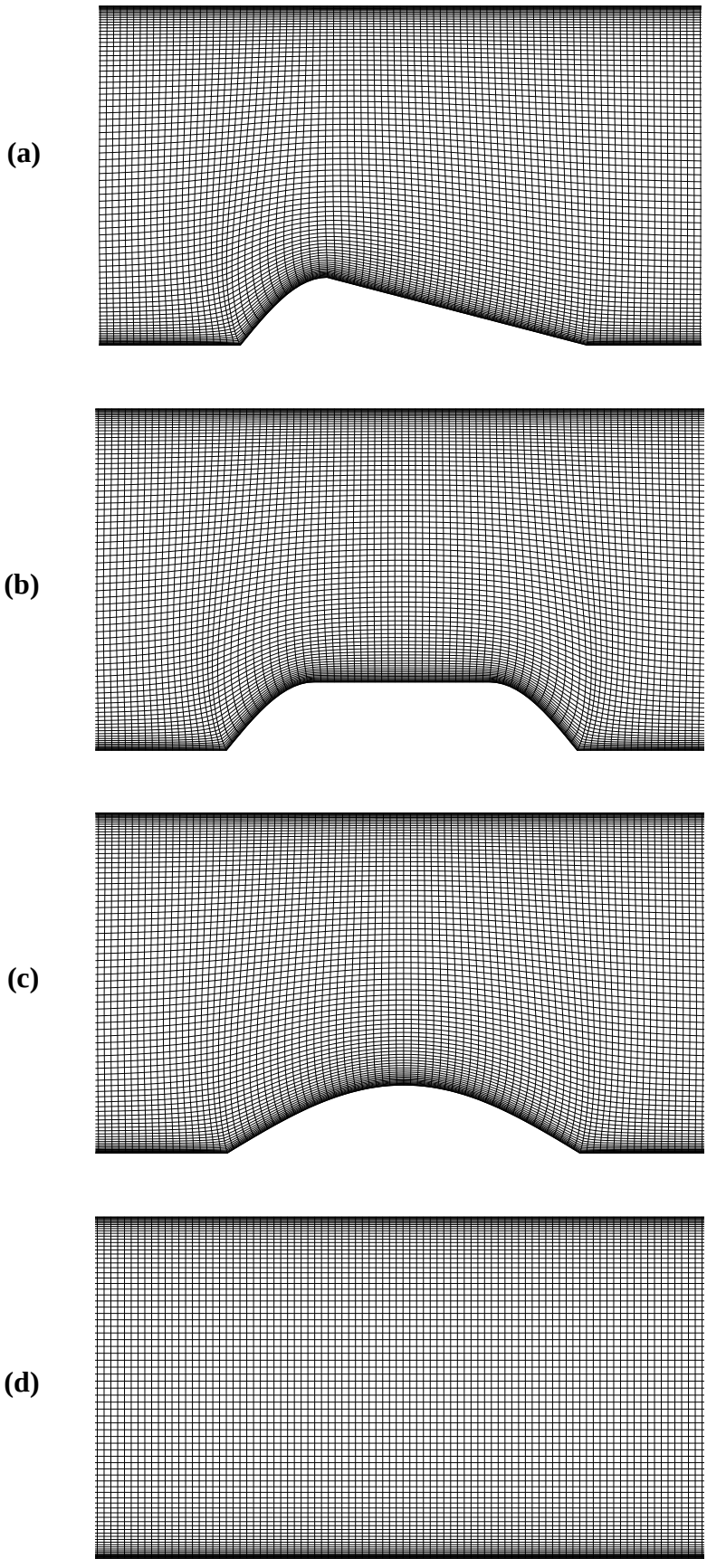

Figure A.2: Computational grid of current study; (a) Wing rib, (b) Flat rib, (c) Oval rib, (d) Smooth target.

A-3 Discretization of governing equations

In chapter three, the convective terms in equation 3.39 is integrated over a control volume around node P can be given as:

$$\iint_V \frac{1}{J}\left[\frac{\partial}{\partial\xi}(\rho\phi U^c)+\frac{\partial}{\partial\eta}(\rho\phi V^c)\right]Jd\xi d\eta$$

$$= \int[\rho\phi U^c d\eta]_w^e + [\rho\phi V^c d\xi]_s^n$$

$$= (\rho\phi U^c\Delta\eta)_e - (\rho\phi U^c\Delta\eta)_w + (\rho\phi V^c\Delta\xi)_n - (\rho\phi V^c\Delta\xi)_s$$

$$= F_e u_e - F_w u_w + F_n u_n - F_s u_s \qquad (A.48)$$

Here (F_e, F_w, F_n, and F_s) are the rates of mass flow for a cross cell faces that are expressed as follows:

$$F_e = (\rho U^c\Delta\eta)_e \qquad (A.49)$$

$$F_w = (\rho U^c\Delta\eta)_w \qquad (A.50)$$

$$F_n = (\rho V^c\Delta\xi)_n \qquad (A.51)$$

$$F_s = (\rho V^c\Delta\xi)_s \qquad (A.52)$$

Also, integrating the diffusion terms of equation 3.39 in chapter three, over control volume can be given as

$$\iint\left[\frac{\partial}{\partial\xi}\left[\frac{\Gamma_\phi}{J}\left(q_{11}\frac{\partial\phi}{\partial\xi}-q_{12}\frac{\partial\phi}{\partial\eta}\right)\right]+\frac{\partial}{\partial\eta}\left[\frac{\Gamma_\phi}{J}\left(q_{22}\frac{\partial\phi}{\partial\eta}-q_{12}\frac{\partial\phi}{\partial\xi}\right)\right]\right]d\xi d\eta$$

$$= \int\left[\frac{\Gamma_\phi}{J}\left(q_{11}\frac{\partial\phi}{\partial\xi}-q_{12}\frac{\partial\phi}{\partial\eta}\right)d\eta\right]_w^e + \int\left[\frac{\Gamma_\phi}{J}\left(q_{22}\frac{\partial\phi}{\partial\eta}-q_{12}\frac{\partial\phi}{\partial\xi}\right)d\xi\right]_s^n$$

$$= \left[\frac{\Gamma_\phi}{J}q_{11}\frac{\partial\phi}{\partial\xi}\Delta\eta\right]_w^e - \left[\frac{\Gamma_\phi}{J}q_{12}\frac{\partial\phi}{\partial\eta}\Delta\eta\right]_w^e + \left[\frac{\Gamma_\phi}{J}q_{22}\frac{\partial\phi}{\partial\eta}\Delta\xi\right]_s^n -$$

$$\left[\frac{\Gamma_\phi}{J}q_{12}\frac{\partial\phi}{\partial\xi}\Delta\xi\right]_s^n \qquad (A.53)$$

Re-arrangement the above equation affords:

$$= \left(\frac{\Gamma_\phi}{J}q_{11}\frac{\partial\phi}{\partial\xi}\Delta\eta\right)_e - \left(\frac{\Gamma_\phi}{J}q_{11}\frac{\partial\phi}{\partial\xi}\Delta\eta\right)_w + \left(\frac{\Gamma_\phi}{J}q_{22}\frac{\partial\phi}{\partial\eta}\Delta\xi\right)_n$$

$$-\left(\frac{\Gamma_\phi}{J} q_{22} \frac{\partial \phi}{\partial \eta} \Delta\xi\right)_s - S_d^\phi$$

$$= \left(\frac{\Gamma_\phi}{J} q_{11} \frac{\Delta\eta}{\Delta\xi}\right)_e (\phi_E - \phi_P) - \left(\frac{\Gamma_\phi}{J} q_{11} \frac{\Delta\eta}{\Delta\xi}\right)_w (\phi_P - \phi_W)$$

$$+ \left(\frac{\Gamma_\phi}{J} q_{22} \frac{\Delta\xi}{\Delta\eta}\right)_n (\phi_N - \phi_P) - \left(\frac{\Gamma_\phi}{J} q_{22} \frac{\Delta\xi}{\Delta\eta}\right)_s (\phi_P - \phi_S) - S_d^\phi$$

$$= D_e\phi_E + D_w\phi_W + D_n\phi_N + D_s\phi_S - (D_e + D_w + D_n + D_s)\phi_P - S_d^\phi \quad (A.54)$$

Here, (D_e, D_w, D_n, and D_s) are the diffusion conductance that can be awarded by:

$$D_e = \left(\frac{\Gamma_\phi}{J} q_{11} \frac{\Delta\eta}{\Delta\xi}\right)_e \quad (A.55)$$

$$D_w = \left(\frac{\Gamma_\phi}{J} q_{11} \frac{\Delta\eta}{\Delta\xi}\right)_w \quad (A.56)$$

$$D_n = \left(\frac{\Gamma_\phi}{J} q_{22} \frac{\Delta\xi}{\Delta\eta}\right)_n \quad (A.57)$$

$$D_s = \left(\frac{\Gamma_\phi}{J} q_{22} \frac{\Delta\xi}{\Delta\eta}\right)_s \quad (A.58)$$

In equation A.54, the linear interpolation can be used to evaluate the interface values of (ϕ_e, ϕ_w, ϕ_n, and ϕ_n) from nodal point's values as shown:

$$\phi_e = \frac{\phi_E + \phi_P}{2} \quad (A.59)$$

$$\phi_w = \frac{\phi_W + \phi_P}{2} \quad (A.60)$$

$$\phi_n = \frac{\phi_N + \phi_P}{2} \quad (A.61)$$

$$\phi_s = \frac{\phi_S + \phi_P}{2} \quad (A.62)$$

Also in equation A.54, the term S_d^ϕ is generated from converging the diffusion terms over a non-orthogonal grid. So, the term S_d^ϕ is added to a source term and thus can be discretized as below:

$$S_d^{\phi} = \left[\frac{\Gamma_\phi}{J} q_{12} \frac{\partial \phi}{\partial \eta} \Delta\eta\right]_w^e - \left[\frac{\Gamma_\phi}{J} q_{12} \frac{\partial \phi}{\partial \xi} \Delta\xi\right]_s^n$$

$$= \left(\frac{\Gamma_\phi}{J} q_{12} \frac{\partial \phi}{\partial \eta} \Delta\eta\right)_e - \left(\frac{\Gamma_\phi}{J} q_{12} \frac{\partial \phi}{\partial \eta} \Delta\eta\right)_w + \left(\frac{\Gamma_\phi}{J} q_{12} \frac{\partial \phi}{\partial \xi} \Delta\xi\right)_n$$

$$- \left(\frac{\Gamma_\phi}{J} q_{12} \frac{\partial \phi}{\partial \xi} \Delta\xi\right)_s$$

$$= \left(\frac{\Gamma_\phi}{J} q_{12} \frac{\Delta\eta}{\Delta\eta}\right)_e (\phi_{ne} - \phi_{se}) - \left(\frac{\Gamma_\phi}{J} q_{12} \frac{\Delta\eta}{\Delta\eta}\right)_w (\phi_{nw} - \phi_{sw})$$

$$+ \left(\frac{\Gamma_\phi}{J} q_{12} \frac{\Delta\xi}{\Delta\xi}\right)_n (\phi_{ne} - \phi_{nw}) - \left(\frac{\Gamma_\phi}{J} q_{12} \frac{\Delta\xi}{\Delta\xi}\right)_s (\phi_{se} - \phi_{sw}) \qquad (A.63)$$

In the above equation, the simple interpolation can be employed to determine the values of ($\phi_{ne,}$ $\phi_{se,}$ $\phi_{nw,}$ and ϕ_{sw}) as follows:

$$\phi_{ne} = \frac{1}{4}[\phi_{NE} + \phi_N + \phi_E + \phi_P] \qquad (A.64)$$

$$\phi_{se} = \frac{1}{4}[\phi_E + \phi_P + \phi_{SE} + \phi_S] \qquad (A.65)$$

$$\phi_{nw} = \frac{1}{4}[\phi_N + \phi_{NW} + \phi_P + \phi_W] \qquad (A.66)$$

$$\phi_{sw} = \frac{1}{4}[\phi_P + \phi_W + \phi_S + \phi_{SW}] \qquad (A.67)$$

Equation A.65 is subtracted from equation A.64 and thus gets:

$$\phi_{ne} - \phi_{se} = \frac{1}{4}[\phi_{NE} + \phi_N + \phi_E + \phi_P] - \frac{1}{4}[\phi_E + \phi_P + \phi_{SE} + \phi_S] \qquad (A.68)$$

Re-arrangement the above equation and thus provides:

$$\phi_{ne} - \phi_{se} = \frac{1}{4}[\phi_{NE} - \phi_{SE} + \phi_N - \phi_S] \qquad (A.69)$$

In the same above method, the following values can be calculated by

$$\phi_{nw} - \phi_{sw} = \frac{1}{4}[\phi_N + \phi_{NW} + \phi_P + \phi_W] - \frac{1}{4}[\phi_P + \phi_W + \phi_S + \phi_{SW}] \qquad (A.70)$$

$$= \frac{1}{4}[\phi_N - \phi_S + \phi_{NW} - \phi_{SW}] \quad (A.71)$$

$$\phi_{ne} - \phi_{nw} = \frac{1}{4}[\phi_{NE} + \phi_N + \phi_E + \phi_P] - \frac{1}{4}[\phi_N + \phi_{NW} + \phi_P + \phi_W] \quad (A.72)$$

$$= \frac{1}{4}[\phi_{NE} - \phi_{NW} + \phi_E - \phi_W] \quad (A.73)$$

$$\phi_{se} - \phi_{sw} = \frac{1}{4}[\phi_E + \phi_P + \phi_{SE} + \phi_S] - \frac{1}{4}[\phi_P + \phi_W + \phi_S + \phi_{SW}] \quad (A.74)$$

$$= \frac{1}{4}[\phi_E - \phi_W + \phi_{SE} - \phi_{SW}] \quad (A.75)$$

Thus, the term S_d^{ϕ} can be given in the final form:

$$S_d^{\phi} = B_E\phi_E + B_W\phi_W + B_N\phi_N + B_S\phi_S + B_{NE}\phi_{NE} + B_{SE}\phi_{SE} + B_{NW}\phi_{NW} + B_{SW}\phi_{SW} \quad (A.76)$$

Here,

$$B_E = \frac{1}{4}\left[\left(\frac{\Gamma_\phi}{J} q_{12} \frac{\Delta\xi}{\Delta\xi}\right)_n - \left(\frac{\Gamma_\phi}{J} q_{12} \frac{\Delta\xi}{\Delta\xi}\right)_s\right] \quad (A.77)$$

$$B_W = -\frac{1}{4}\left[\left(\frac{\Gamma_\phi}{J} q_{12} \frac{\Delta\xi}{\Delta\xi}\right)_n - \left(\frac{\Gamma_\phi}{J} q_{12} \frac{\Delta\xi}{\Delta\xi}\right)_s\right] \quad (A.78)$$

$$B_N = \frac{1}{4}\left[\left(\frac{\Gamma_\phi}{J} q_{12} \frac{\Delta\eta}{\Delta\eta}\right)_e - \left(\frac{\Gamma_\phi}{J} q_{12} \frac{\Delta\eta}{\Delta\eta}\right)_w\right] \quad (A.79)$$

$$B_S = -\frac{1}{4}\left[\left(\frac{\Gamma_\phi}{J} q_{12} \frac{\Delta\eta}{\Delta\eta}\right)_e - \left(\frac{\Gamma_\phi}{J} q_{12} \frac{\Delta\eta}{\Delta\eta}\right)_w\right] \quad (A.80)$$

$$B_{NE} = \frac{1}{4}\left[\left(\frac{\Gamma_\phi}{J} q_{12} \frac{\Delta\eta}{\Delta\eta}\right)_e + \left(\frac{\Gamma_\phi}{J} q_{12} \frac{\Delta\xi}{\Delta\xi}\right)_n\right] \quad (A.81)$$

$$B_{NW} = -\frac{1}{4}\left[\left(\frac{\Gamma_\phi}{J} q_{12} \frac{\Delta\eta}{\Delta\eta}\right)_w + \left(\frac{\Gamma_\phi}{J} q_{12} \frac{\Delta\xi}{\Delta\xi}\right)_n\right] \quad (A.82)$$

$$B_{SE} = -\frac{1}{4}\left[\left(\frac{\Gamma_\phi}{J} q_{12} \frac{\Delta\eta}{\Delta\eta}\right)_e + \left(\frac{\Gamma_\phi}{J} q_{12} \frac{\Delta\xi}{\Delta\xi}\right)_s\right] \quad (A.83)$$

$$B_{SW} = \frac{1}{4}\left[\left(\frac{\Gamma_\phi}{J} q_{12} \frac{\Delta\eta}{\Delta\eta}\right)_w + \left(\frac{\Gamma_\phi}{J} q_{12} \frac{\Delta\xi}{\Delta\xi}\right)_s\right] \quad (A.84)$$

Furthermore, the source term of the u-momentum equation is known as follows:

$$S_u = S_d^u + b_u + b_P^u \quad (A.85)$$

The coefficients b_u and S_d^u in above equation can be written as follows:

$$b_u = \iint \left[\frac{\partial}{\partial\xi}\left[\frac{\Gamma_u}{J}\left(\beta_{11}^2 \frac{\partial u}{\partial\xi} + \beta_{11}\beta_{12} \frac{\partial u}{\partial\eta}\right)\right] + \frac{\partial}{\partial\eta}\left[\frac{\Gamma_u}{J}\left(\beta_{12}\beta_{11} \frac{\partial u}{\partial\xi} + \beta_{12}^2 \frac{\partial u}{\partial\eta}\right)\right] + \frac{\partial}{\partial\xi}\left[\frac{\Gamma_u}{J}\left(\beta_{21}\beta_{11} \frac{\partial v}{\partial\xi} + \beta_{21}\beta_{12} \frac{\partial v}{\partial\eta}\right)\right] + \frac{\partial}{\partial\eta}\left[\frac{\Gamma_u}{J}\left(\beta_{22}\beta_{11} \frac{\partial v}{\partial\xi} + \beta_{22}\beta_{12} \frac{\partial v}{\partial\eta}\right)\right] - \frac{2}{3}\rho\left(\frac{\partial}{\partial\xi}(\beta_{11}k) + \frac{\partial}{\partial\eta}(\beta_{12}k)\right)\right] d\xi d\eta \quad (A.86)$$

$$b_u = \left[\frac{\Gamma_u \Delta\eta}{J}\left(\beta_{11}^2 \frac{\partial u}{\partial\xi} + \beta_{11}\beta_{12} \frac{\partial u}{\partial\eta}\right)\right]_w^e + \left[\frac{\Gamma_u \Delta\xi}{J}\left(\beta_{12}\beta_{11} \frac{\partial u}{\partial\xi} + \beta_{12}^2 \frac{\partial u}{\partial\eta}\right)\right]_s^n + \left[\frac{\Gamma_u \Delta\eta}{J}\left(\beta_{21}\beta_{11} \frac{\partial v}{\partial\xi} + \beta_{21}\beta_{11} \frac{\partial v}{\partial\eta}\right)\right]_w^e + \left[\frac{\Gamma_u \Delta\xi}{J}\left(\beta_{22}\beta_{11} \frac{\partial v}{\partial\xi} + \beta_{22}\beta_{12} \frac{\partial v}{\partial\eta}\right)\right]_s^n - \frac{2}{3}\rho[\Delta\eta\beta_{11}k]_w^e - \frac{2}{3}\rho[\Delta\xi\beta_{12}k]_s^n \quad (A.87)$$

$$b_u = \left[\frac{\Gamma_u}{J}\frac{\Delta\eta}{\Delta\xi}\beta_{11}^2\right]_e (u_E - u_P) - \left[\frac{\Gamma_u}{J}\frac{\Delta\eta}{\Delta\xi}\beta_{11}^2\right]_w (u_P - u_W) + \left[\frac{\Gamma_u}{J}\frac{\Delta\eta}{\Delta\eta}\beta_{11}\beta_{12}\right]_e (u_{ne} - u_{se}) + \left[\frac{\Gamma_u}{J}\frac{\Delta\xi}{\Delta\eta}\beta_{12}^2\right]_n (u_N - u_P) - \left[\frac{\Gamma_u}{J}\frac{\Delta\xi}{\Delta\eta}\beta_{12}^2\right]_s (u_P - u_S) + \left[\frac{\Gamma_u}{J}\frac{\Delta\eta}{\Delta\xi}\beta_{21}\beta_{11}\right]_e (v_E - v_P) - \left[\frac{\Gamma_u}{J}\frac{\Delta\eta}{\Delta\xi}\beta_{21}\beta_{11}\right]_w (v_P - v_W) + \left[\frac{\Gamma_u}{J}\frac{\Delta\eta}{\Delta\eta}\beta_{21}\beta_{11}\right]_e (v_{ne} - v_{se}) - \left[\frac{\Gamma_u}{J}\frac{\Delta\eta}{\Delta\eta}\beta_{21}\beta_{11}\right]_w (v_{nw} - v_{sw})$$

$$+\left[\frac{\Gamma_u}{J}\frac{\Delta\xi}{\Delta\xi}\beta_{22}\beta_{11}\right]_n(v_{ne}-v_{nw})-\left[\frac{\Gamma_u}{J}\frac{\Delta\xi}{\Delta\xi}\beta_{22}\beta_{11}\right]_s(v_{se}-v_{sw})+$$

$$\left[\frac{\Gamma_u}{J}\frac{\Delta\xi}{\Delta\eta}\beta_{22}\beta_{12}\right]_n(v_N-v_P)-\left[\frac{\Gamma_u}{J}\frac{\Delta\xi}{\Delta\eta}\beta_{22}\beta_{12}\right]_s(v_P-v_S)-\frac{2}{3}\rho[\Delta\eta\beta_{11}]_P(k_e-k_w)-$$

$$\frac{2}{3}\rho[\Delta\xi\beta_{12}]_P(k_n-k_s) \quad (A.88)$$

Also, in the u-momentum equation, the pressure terms b_P^u can be assessed as follows:

$$b_P^u=-\iint\left[\left(\frac{\partial}{\partial\xi}(\beta_{11}p)+\frac{\partial}{\partial\eta}(\beta_{12}p)\right)\right]d\xi d\eta$$

$$=-[\Delta\eta\ \beta_{11}\ p]_w^e-[\Delta\xi\ \beta_{12}\ p]_s^n$$

$$=-(\Delta\eta\ \beta_{11})(p_e-p_w)-(\Delta\xi\ \beta_{12})(p_n-p_s) \quad (A.89)$$

Here, $S_d^u=S_d^\phi$ (Equation A.85). In addition, the pressure at cell faces (p_e, p_w, p_n, and p_s) in above equation can be defined as shown:

$$p_e=\frac{p_E+p_P}{2} \quad (A.90)$$

$$p_w=\frac{p_W+p_P}{2} \quad (A.91)$$

$$p_n=\frac{p_N+p_P}{2} \quad (A.92)$$

$$p_s=\frac{p_S+p_P}{2} \quad (A.93)$$

Substituting the values of above equations in equation (A.89) gives:

$$b_P^u=-\frac{1}{2}(\Delta\eta\ \beta_{11})(p_e-p_w)-\frac{1}{2}(\Delta\xi\ \beta_{12})(p_n-p_s)$$

$$=-\frac{1}{2}[(\Delta\eta\ \beta_{11})_P(p_E-p_W)+(\Delta\xi\ \beta_{12})_P(p_N-p_S)] \quad (A.94)$$

Identically, the source term of the v-momentum equation is expressed as follows:

$$S_v = S_d^v + b_v + b_P^v \tag{A.95}$$

In above equation, $S_d^v = S_d^\phi$ and hence the coefficient b_v can be expressed as follows:

$$b_v = \iint \left[\frac{\partial}{\partial\xi}\left[\frac{\Gamma_v}{J}\left(\beta_{21}^2\frac{\partial v}{\partial\xi} + \beta_{21}\beta_{22}\frac{\partial v}{\partial\eta}\right)\right] + \frac{\partial}{\partial\eta}\left[\frac{\Gamma_v}{J}\left(\beta_{22}\beta_{21}\frac{\partial v}{\partial\xi} + \beta_{21}^2\frac{\partial v}{\partial\eta}\right)\right] + \frac{\partial}{\partial\xi}\left[\frac{\Gamma_v}{J}\left(\beta_{11}\beta_{21}\frac{\partial u}{\partial\xi} + \beta_{11}\beta_{22}\frac{\partial u}{\partial\eta}\right)\right] + \frac{\partial}{\partial\eta}\left[\frac{\Gamma_v}{J}\left(\beta_{12}\beta_{21}\frac{\partial u}{\partial\xi} + \beta_{12}\beta_{22}\frac{\partial u}{\partial\eta}\right)\right] - \frac{2}{3}\rho\left(\frac{\partial}{\partial\xi}(\beta_{21}k) + \frac{\partial}{\partial\eta}(\beta_{22}k)\right)\right] d\xi d\eta \tag{A.96}$$

$$b_v = \left[\frac{\Gamma_v\Delta\eta}{J}\left(\beta_{21}^2\frac{\partial v}{\partial\xi} + \beta_{21}\beta_{22}\frac{\partial v}{\partial\eta}\right)\right]_w^e + \left[\frac{\Gamma_v\Delta\xi}{J}\left(\beta_{22}\beta_{21}\frac{\partial v}{\partial\xi} + \beta_{22}^2\frac{\partial v}{\partial\eta}\right)\right]_s^n + \left[\frac{\Gamma_v\Delta\eta}{J}\left(\beta_{11}\beta_{21}\frac{\partial u}{\partial\xi} + \beta_{11}\beta_{22}\frac{\partial u}{\partial\eta}\right)\right]_w^e + \left[\frac{\Gamma_v\Delta\xi}{J}\left(\beta_{12}\beta_{21}\frac{\partial u}{\partial\xi} + \beta_{12}\beta_{22}\frac{\partial u}{\partial\eta}\right)\right]_s^n - \frac{2}{3}\rho[\Delta\eta\beta_{21}k]_w^e - \frac{2}{3}\rho[\Delta\xi\beta_{22}k]_s^n \tag{A.97}$$

$$\begin{aligned} b_v = {} & \left[\frac{\Gamma_v}{J}\frac{\Delta\eta}{\Delta\xi}\beta_{21}^2\right]_e (v_E - v_P) - \left[\frac{\Gamma_v}{J}\frac{\Delta\eta}{\Delta\xi}\beta_{21}^2\right]_w (v_P - v_W) + \\ & \left[\frac{\Gamma_v}{J}\frac{\Delta\eta}{\Delta\eta}\beta_{21}\beta_{22}\right]_e (v_{ne} - v_{se}) + \left[\frac{\Gamma_v}{J}\frac{\Delta\xi}{\Delta\eta}\beta_{22}^2\right]_n (v_N - v_P) - \\ & \left[\frac{\Gamma_v}{J}\frac{\Delta\xi}{\Delta\eta}\beta_{22}^2\right]_s (v_P - v_S) + \left[\frac{\Gamma_v}{J}\frac{\Delta\eta}{\Delta\xi}\beta_{11}\beta_{21}\right]_e (u_E - u_P) \\ & - \left[\frac{\Gamma_v}{J}\frac{\Delta\eta}{\Delta\xi}\beta_{11}\beta_{21}\right]_w (u_P - u_W) + \left[\frac{\Gamma_v}{J}\frac{\Delta\eta}{\Delta\eta}\beta_{11}\beta_{22}\right]_e (u_{ne} - u_{se}) - \\ & \left[\frac{\Gamma_v}{J}\frac{\Delta\eta}{\Delta\eta}\beta_{11}\beta_{22}\right]_w (u_{nw} - u_{sw}) + \left[\frac{\Gamma_v}{J}\frac{\Delta\xi}{\Delta\xi}\beta_{12}\beta_{21}\right]_n (u_{ne} - u_{nw}) - \\ & \left[\frac{\Gamma_v}{J}\frac{\Delta\xi}{\Delta\xi}\beta_{12}\beta_{21}\right]_s (u_{se} - u_{sw}) + \left[\frac{\Gamma_v}{J}\frac{\Delta\xi}{\Delta\eta}\beta_{12}\beta_{22}\right]_n (u_N - u_P) \\ & - \left[\frac{\Gamma_v}{J}\frac{\Delta\xi}{\Delta\eta}\beta_{12}\beta_{22}\right]_s (u_P - u_S) - \frac{2}{3}\rho[\Delta\eta\beta_{21}]_P (k_e - k_w) - \\ & \frac{2}{3}\rho[\Delta\xi\beta_{22}]_P (k_n - k_s) \end{aligned} \tag{A.98}$$

Moreover, in the v-momentum equation, the pressure terms b_P^v can be assessed as follows:

$$b_P^v = -\iint \left[\left(\frac{\partial}{\partial \xi}(\beta_{21} p) + \frac{\partial}{\partial \eta}(\beta_{22} p)\right)\right] d\xi d\eta$$

$$= -[\Delta\eta\ \beta_{21}\ p]_w^e - [\Delta\xi\ \beta_{22}\ p]_s^n$$

$$= -(\Delta\eta\ \beta_{21})(p_e - p_w) - (\Delta\xi\ \beta_{22})(p_n - p_s) \qquad (A.99)$$

Substituting the values in equations (A.90 to A.93) in above equation gives:

$$b_P^v = -\frac{1}{2}(\Delta\eta\ \beta_{21})(p_e - p_w) - \frac{1}{2}(\Delta\xi\ \beta_{22})(p_n - p_s)$$

$$= -\frac{1}{2}[(\Delta\eta\ \beta_{21})_P(p_E - p_W) + (\Delta\xi\ \beta_{22})_P(p_N - p_S)] \qquad (A.100)$$

In the energy equation, the coefficients value of (b_T and b_P^T) equal to zero and therefore, the source terms can be written as follows:

$$S_T = S_d^T \qquad (A.101)$$

In the k-equation, the source term is given by:

$$S_k = S_d^k + b_k + b_P^k \qquad (A.102)$$

Here,

$$b_P^k = 0 \qquad (A.103)$$

$$b_k = \iint [P_k(\xi,\eta) - \rho(\varepsilon_w(\xi,\eta) + \varepsilon)]\, J\, d\xi d\eta \qquad (A.104)$$

In the ε-equation, the source term is expressed as:

$$S_\varepsilon = S_d^\varepsilon + b_\varepsilon + b_P^\varepsilon \qquad (A.105)$$

Here,

$$b_P^{\varepsilon} = 0 \tag{A.106}$$

$$b_{\varepsilon} = \iint \left[c_1 f_1 P_k(\xi,\eta)\frac{\varepsilon}{k} - \rho c_2 f_2 \frac{\varepsilon^2}{k} + \phi_{\varepsilon} \right] J\, d\xi d\eta \tag{A.107}$$

The integrating (b_k) and (b_{ε}) in equations A.104 and A.107, respectively, over the control volume are given by:

$$\begin{aligned}
b_k = {} & 2\mu_t \left(\frac{\Delta\xi\Delta\eta}{J}\right)_P \left[\left(\frac{\beta_{11}}{\Delta\xi}\right)_e u_e - \left(\frac{\beta_{11}}{\Delta\xi}\right)_w u_w + \left(\frac{\beta_{12}}{\Delta\eta}\right)_n u_n - \left(\frac{\beta_{12}}{\Delta\eta}\right)_s u_s\right]^2 \\
& + 2\mu_t \left(\frac{\Delta\xi\Delta\eta}{J}\right)_P \left[\left(\frac{\beta_{21}}{\Delta\xi}\right)_e v_e - \left(\frac{\beta_{21}}{\Delta\xi}\right)_w v_w + \left(\frac{\beta_{22}}{\Delta\eta}\right)_n v_n - \left(\frac{\beta_{22}}{\Delta\eta}\right)_s v_s\right]^2 \\
& + 2\mu_t \left(\frac{\Delta\xi\Delta\eta}{J}\right)_P \left[\left(\frac{\beta_{21}}{\Delta\xi}\right)_e u_e - \left(\frac{\beta_{21}}{\Delta\xi}\right)_w u_w + \left(\frac{\beta_{22}}{\Delta\eta}\right)_n u_n - \left(\frac{\beta_{22}}{\Delta\eta}\right)_s u_s\right]^2 \\
& + 2\mu_t \left(\frac{\Delta\xi\Delta\eta}{J}\right)_P \left[\left(\frac{\beta_{11}}{\Delta\xi}\right)_e v_e - \left(\frac{\beta_{11}}{\Delta\xi}\right)_w v_w + \left(\frac{\beta_{12}}{\Delta\eta}\right)_n v_n - \left(\frac{\beta_{12}}{\Delta\eta}\right)_s v_s\right]^2 \\
& - \frac{2}{3}\rho(\Delta\xi\Delta\eta)_P k_P \left[\left(\frac{\beta_{11}}{\Delta\xi}\right)_e u_e - \left(\frac{\beta_{11}}{\Delta\xi}\right)_w u_w + \left(\frac{\beta_{12}}{\Delta\eta}\right)_n u_n - \left(\frac{\beta_{12}}{\Delta\eta}\right)_s u_s\right] \\
& - \frac{2}{3}\rho(\Delta\xi\Delta\eta)_P k_P \left[\left(\frac{\beta_{21}}{\Delta\xi}\right)_e v_e - \left(\frac{\beta_{21}}{\Delta\xi}\right)_w v_w + \left(\frac{\beta_{22}}{\Delta\eta}\right)_n v_n - \left(\frac{\beta_{22}}{\Delta\eta}\right)_s v_s\right] \\
& - 2\mu \left(\frac{\Delta\xi\Delta\eta}{J}\right)_P \left[\left(\frac{\beta_{11}}{\Delta\xi}\right)_e \sqrt{k_e} - \left(\frac{\beta_{11}}{\Delta\xi}\right)_w \sqrt{k_w} + \left(\frac{\beta_{12}}{\Delta\eta}\right)_n \sqrt{k_n} - \right. \\
& \left. \left(\frac{\beta_{12}}{\Delta\eta}\right)_s \sqrt{k_s}\right]^2 - 2\mu \left(\frac{\Delta\xi\Delta\eta}{J}\right)_P \left[\left(\frac{\beta_{21}}{\Delta\xi}\right)_e \sqrt{k_e} - \left(\frac{\beta_{21}}{\Delta\xi}\right)_w \sqrt{k_w} + \right. \\
& \left. \left(\frac{\beta_{22}}{\Delta\eta}\right)_n \sqrt{k_n} - \left(\frac{\beta_{22}}{\Delta\eta}\right)_s \sqrt{k_s}\right]^2 - \rho\varepsilon_P (J\Delta\xi\Delta\eta)_P
\end{aligned} \tag{A.108}$$

$$\begin{aligned}
b_{\varepsilon} = {} & c_1 f_1 \left(2\mu_t \frac{\Delta\xi\Delta\eta}{J}\right)_P \left\{\left[\left(\frac{\beta_{11}}{\Delta\xi}\right)_e u_e - \left(\frac{\beta_{11}}{\Delta\xi}\right)_w u_w + \left(\frac{\beta_{12}}{\Delta\eta}\right)_n u_n - \right.\right. \\
& \left.\left. \left(\frac{\beta_{12}}{\Delta\eta}\right)_s u_s\right]^2 + \left[\left(\frac{\beta_{21}}{\Delta\xi}\right)_e v_e - \left(\frac{\beta_{21}}{\Delta\xi}\right)_w v_w + \left(\frac{\beta_{22}}{\Delta\eta}\right)_n v_n - \left(\frac{\beta_{22}}{\Delta\eta}\right)_s v_s\right]^2
\end{aligned}$$

$$+\left[\left(\frac{\beta_{21}}{\Delta\xi}\right)_e u_e - \left(\frac{\beta_{21}}{\Delta\xi}\right)_w u_w + \left(\frac{\beta_{22}}{\Delta\eta}\right)_n u_n - \left(\frac{\beta_{22}}{\Delta\eta}\right)_s u_s\right]^2$$

$$+\left[\left(\frac{\beta_{11}}{\Delta\xi}\right)_e v_e - \left(\frac{\beta_{11}}{\Delta\xi}\right)_w v_w + \left(\frac{\beta_{12}}{\Delta\eta}\right)_n v_n - \left(\frac{\beta_{12}}{\Delta\eta}\right)_s v_s\right]^2\Bigg\}\left(\frac{\varepsilon_P}{k_P}\right)$$

$$-\rho c_2 f_2 (\Delta\xi\Delta\eta)_P \left(\frac{{\varepsilon_P}^2}{k_P}\right) + 2(\mu_t)_P \left(\frac{\mu}{\rho}\right)(G_{u11} + G_{u12} + G_{u22} + G_{v11} +$$

$$G_{v12} + G_{v22}) \qquad \text{(A. 109)}$$

So, the terms (G_{u11}, G_{u12}, G_{u22}, G_{v11}, G_{v12}, and G_{v22}) can be evaluated as follows:

$$G_{\phi 11} = \left(\frac{\Delta\xi\Delta\eta}{J}\right)_P \left[\left(\frac{1}{J}\frac{\beta_{11}\beta_{11}}{\Delta\xi\Delta\xi}\right)_e (\phi_E - \phi_P) - \left(\frac{1}{J}\frac{\beta_{11}\beta_{11}}{\Delta\xi\Delta\xi}\right)_w (\phi_P - \phi_w)\right.$$
$$+\left(\frac{1}{J}\frac{\beta_{11}\beta_{12}}{\Delta\xi\Delta\eta}\right)_e (\phi_{ne} - \phi_{se}) - \left(\frac{1}{J}\frac{\beta_{11}\beta_{12}}{\Delta\xi\Delta\eta}\right)_w (\phi_{nw} - \phi_{sw})$$
$$+\left(\frac{1}{J}\frac{\beta_{12}\beta_{11}}{\Delta\xi\Delta\eta}\right)_n (\phi_{ne} - \phi_{nw}) - \left(\frac{1}{J}\frac{\beta_{12}\beta_{11}}{\Delta\xi\Delta\eta}\right)_s (\phi_{se} - \phi_{sw})$$
$$\left.+\left(\frac{1}{J}\frac{\beta_{12}\beta_{12}}{\Delta\eta\Delta\eta}\right)_n (\phi_N - \phi_P) - \left(\frac{1}{J}\frac{\beta_{12}\beta_{12}}{\Delta\eta\Delta\eta}\right)_s (\phi_P - \phi_S)\right]^2 \qquad \text{(A. 110)}$$

$$G_{\phi 12} = \left(\frac{\Delta\xi\Delta\eta}{J}\right)_P \left[\left(\frac{1}{J}\frac{\beta_{11}\beta_{21}}{\Delta\xi\Delta\xi}\right)_e (\phi_E - \phi_P) - \left(\frac{1}{J}\frac{\beta_{11}\beta_{21}}{\Delta\xi\Delta\xi}\right)_w (\phi_P - \phi_w)\right.$$
$$+\left(\frac{1}{J}\frac{\beta_{11}\beta_{22}}{\Delta\xi\Delta\eta}\right)_e (\phi_{ne} - \phi_{se}) - \left(\frac{1}{J}\frac{\beta_{11}\beta_{22}}{\Delta\xi\Delta\eta}\right)_w (\phi_{nw} - \phi_{sw})$$
$$+\left(\frac{1}{J}\frac{\beta_{12}\beta_{21}}{\Delta\xi\Delta\eta}\right)_n (\phi_{ne} - \phi_{nw}) - \left(\frac{1}{J}\frac{\beta_{12}\beta_{21}}{\Delta\xi\Delta\eta}\right)_s (\phi_{se} - \phi_{sw})$$
$$\left.+\left(\frac{1}{J}\frac{\beta_{12}\beta_{22}}{\Delta\eta\Delta\eta}\right)_n (\phi_N - \phi_P) - \left(\frac{1}{J}\frac{\beta_{12}\beta_{22}}{\Delta\eta\Delta\eta}\right)_s (\phi_P - \phi_S)\right]^2 \qquad \text{(A. 111)}$$

$$G_{\phi 22} = \left(\frac{\Delta\xi\Delta\eta}{J}\right)_P \left[\left(\frac{1}{J}\frac{\beta_{21}\beta_{21}}{\Delta\xi\Delta\xi}\right)_e (\phi_E - \phi_P) - \left(\frac{1}{J}\frac{\beta_{21}\beta_{21}}{\Delta\xi\Delta\xi}\right)_w (\phi_P - \phi_w)\right.$$
$$+\left(\frac{1}{J}\frac{\beta_{21}\beta_{22}}{\Delta\xi\Delta\eta}\right)_e (\phi_{ne} - \phi_{se}) - \left(\frac{1}{J}\frac{\beta_{21}\beta_{22}}{\Delta\xi\Delta\eta}\right)_w (\phi_{nw} - \phi_{sw})$$

$$+\left(\frac{1}{J}\frac{\beta_{21}\beta_{22}}{\Delta\xi\Delta\eta}\right)_n(\phi_{ne}-\phi_{nw})-\left(\frac{1}{J}\frac{\beta_{21}\beta_{22}}{\Delta\xi\Delta\eta}\right)_s(\phi_{se}-\phi_{sw})$$

$$+\left(\frac{1}{J}\frac{\beta_{22}\beta_{22}}{\Delta\eta\Delta\eta}\right)_n(\phi_N-\phi_P)-\left(\frac{1}{J}\frac{\beta_{22}\beta_{22}}{\Delta\eta\Delta\eta}\right)_s(\phi_P-\phi_S)\Big]^2 \qquad (A.112)$$

Where, (ϕ) represents that the (u or v). Finally, the discretized equations (equation 3.49 in chapter three) are recursively solved employing Tri-Diagonal Matrix Algorithm (TDMA). So, the specifics of the (TDMA) steps are not offered here, but it is given in specifics in [52]. The CFD code based on FORTRAN 90 has also been developed to carry out the current investigation numerical solution. In addition to, through solving the equations 3.48 and 3.49 (in chapter three) can be calculated the components of velocity u^* and v^* as follows:

$$u_p^* = \frac{1}{A_P^u}\sum_{nb} A_{nb}^u\, u_{nb}^* + S_d^u + b_u + B_P^u(p_e^* - p_w^*) + C_P^u(p_n^* - p_s^*) \qquad (A.113)$$

$$v_p^* = \frac{1}{A_P^v}\sum_{nb} A_{nb}^v\, v_{nb}^* + S_d^v + b_v + B_P^v(p_e^* - p_w^*) + C_P^v(p_n^* - p_s^*) \qquad (A.114)$$

In above equations, can be obtained the velocities u^* and v^* that will not content the continuity equation. So, the velocities corrections u' and v' and the pressure correction p' is attached to u^*, v^* and p^* respectively, are issued as follows:

$$u = u^* + u' \qquad (A.115)$$

$$v = v^* + v' \qquad (A.116)$$

$$p = p^* + p' \qquad (A.117)$$

Both the continuity and momentum equations are satisfied by the components of correct velocity u and v. By deducting equations A.113 and A.114 from equations 3.48 and 3.49 (in chapter three), respectively, the velocity corrections $u^{'}$ and $v^{'}$ are coupled with pressure corrections $p^{'}$ as given by:

$$u_p - u_p^* = \underbrace{\frac{1}{A_P}\left[\sum_{nb} A_{nb}^u u_{nb} + S_d^u + b_u\right]} + B_P^u(p_e - p_w) + C_P^u(p_n - p_s)$$

$$\underbrace{-\frac{1}{A_P}\left[\sum_{nb} A_{nb}^u u_{nb}^* + S_d^u + b_u\right]} - B_P^u(p_e^* - p_w^*) - C_P^u(p_n^* - p_s^*) \quad (A.118)$$

$$v_p - v_p^* = \underbrace{\frac{1}{A_P}\left[\sum_{nb} A_{nb}^v v_{nb} + S_d^v + b_v\right]} + B_P^v(p_e - p_w) + C_P^v(p_n - p_s)$$

$$\underbrace{-\frac{1}{A_P}\left[\sum_{nb} A_{nb}^v v_{nb}^* + S_d^v + b_v\right]} - B_P^v(p_e^* - p_w^*) - C_P^v(p_n^* - p_s^*) \quad (A.119)$$

Depended on the approximation of the SIMPLE algorithm, the underlined terms on a right side from above equations are neglected. It is also possible to re-write the above equations as follows:

$$u_p - u_p^* = B_P^u(p_e - p_e^*) - B_P^u(p_w - p_w^*) + C_P^u(p_n - p_n^*) - C_P^u(p_s - p_s^*) \quad (A.120)$$

$$v_p - v_p^* = B_P^v(p_e - p_e^*) - B_P^v(p_w - p_w^*) + C_P^v(p_n - p_n^*) - C_P^v(p_s - p_s^*) \quad (A.121)$$

Substituting equations A.115 to A.117 into equations A.120 and A.121 gives as:

$$u_P^{'} = B_P^u p_e^{'} - B_P^u p_w^{'} + C_P^u p_n^{'} - C_P^u p_s^{'} \quad (A.122)$$

$$v_P^{'} = B_P^v p_e^{'} - B_P^v p_w^{'} + C_P^v p_n^{'} - C_P^v p_s^{'} \quad (A.123)$$

The components of correct velocity u and v can be calculated by substituting equations A.122 and A.123 into equations A.115 and A.116 as follows:

$$u_P = u_P^* + B_P^u (p_e^{'} - p_w^{'}) + C_P^u (p_n^{'} - p_s^{'}) \quad (A.124)$$

$$v_P = v_P^* + B_P^v (p_e^{'} - p_w^{'}) + C_P^v (p_n^{'} - p_s^{'}) \quad (A.125)$$

The correction of contra-variant velocity components U^c and V^c can be determined by substituting equations A.124 and A.125 into equations 3.32 and 3.33 (in chapter three) as follows:

$$U^c = \left[u_P^* + B_P^u (p_e^{'} - p_w^{'}) + C_P^u (p_n^{'} - p_s^{'})\right] y_\eta - \left[v_P^* + B_P^v (p_e^{'} - p_w^{'}) + C_P^v (p_n^{'} - p_s^{'})\right] x_\eta \quad (A.126)$$

$$V^c = \left[u_P^* + B_P^v (p_e^{'} - p_w^{'}) + C_P^v (p_n^{'} - p_s^{'})\right] y_\xi - \left[u_P^* + B_P^u (p_e^{'} - p_w^{'}) + C_P^u (p_n^{'} - p_s^{'})\right] y_\xi \quad (A.127)$$

Rearranging above equations obtains:

$$U^c = U^{c*} + \left(B_P^u y_\eta - B_P^v x_\eta\right)\left(p_e^{'} - p_w^{'}\right) + \underbrace{\left(C_P^u y_\eta - C_P^v x_\eta\right)\left(p_n^{'} - p_s^{'}\right)} \quad (A.128)$$

$$V^c = V^{c*} + \left(C_P^v x_\xi - C_P^u y_\xi\right)\left(p_n^{'} - p_s^{'}\right) + \underbrace{\left(B_P^v x_\xi - B_P^u y_\xi\right)\left(p_n^{'} - p_s^{'}\right)} \quad (A.129)$$

It must be observed that, depended on the approximation of the SIMPLE algorithm [55]. The last two terms of Equations A.128 and A.129 are

neglected if the computational grid is almost orthogonal. These equations can thus be updated as:

$$U^c = U^{c*} + B\left(p_e^{'} - p_w^{'}\right) \quad (A.130)$$

$$V^c = V^{c*} + C\left(p_n^{'} - p_S^{'}\right) \quad (A.131)$$

Here;

$$B = B_P^u\, y_\eta - B_P^v\, x_\eta \quad (A.132)$$

$$C = C_P^v x_\xi - C_P^u\, y_\xi \quad (A.133)$$

The discretized of continuity equation can be expressed as:

$$(\rho\, \Delta\eta\, U^c)_e - (\rho\, \Delta\eta\, U^c)_w + (\rho\, \Delta\xi\, V^c)_n - (\rho\, \Delta\xi\, V^c)_s = 0 \quad (A.134)$$

Replacing the velocities of the correct face contra-variants over to the above equations affords:

$$A_P P_P^{'} = A_E P_E^{'} + A_W P_W^{'} + A_N P_N^{'} + A_S P_S^{'} + S_m \quad (A.135)$$

Here;

$$A_E = (\rho\, \Delta\eta\, B)_e \quad (A.136)$$

$$A_W = (\rho\, \Delta\eta\, B)_w \quad (A.137)$$

$$A_N = (\rho\, \Delta\xi\, C)_n \quad (A.138)$$

$$A_S = (\rho\, \Delta\xi\, C)_s \quad (A.139)$$

Where S_m represents the mass imbalance on a control volume and thus it can be expressed by:

$$S_m = (\rho\, \Delta\eta\, U^{c*})_e - (\rho\, \Delta\eta\, U^{c*})_w + (\rho\, \Delta\xi\, V^{c*})_n - (\rho\, \Delta\xi\, V^{c*})_s \quad (A.140)$$

The momentum interpolation method (proposed by Rhie and Chow [55]) is introduced in the present investigation for this purpose and to prevent unreal pressure oscillation. Therefore, at the nodes P and E, the discretized u-momentum equation can be updated as.

$$u_p = \frac{1}{(A_P^u)_P}[\sum_{nb} A_{nb}^u u_{nb} + S_d^u + b_u]_P - \frac{1}{(A_P^u)_P}\big[(\Delta\eta\beta_{11})_p(p_e - p_w) + (\Delta\xi\beta_{12})_p(p_n - p_s)\big]_P \quad (A.141)$$

$$u_E = \frac{1}{(A_P^u)_E}[\sum_{nb} A_{nb}^u u_{nb} + S_d^u + b_u]_E - \frac{1}{(A_P^u)_E}\big[(\Delta\eta\beta_{11})_p(p_e - p_w) + (\Delta\xi\beta_{12})_p(p_n - p_s)\big]_E \quad (A.142)$$

The velocity on the east face can in a similar way be expressed as:

$$u_e = \underline{\frac{1}{(A_P^u)_e}[\sum_{nb} A_{nb}^u u_{nb} + S_d^u + b_u]_e} - \underline{\frac{1}{(A_P^u)_e}}[(\Delta\eta\beta_{11})_e(p_E - p_P) + (\Delta\xi\beta_{12})_e(p_{ne} - p_{se})\big]_e \quad (A.143)$$

The underline-terms in the above equation are interpolated linearly as shown below:

$$\frac{1}{(A_P^u)_e}(\sum_{nb} A_{nb}^u u_{nb} + S_d^u + b_u)_e = f_e^+ \frac{1}{(A_P^u)_E}(\sum_{nb} A_{nb}^u u_{nb} + S_d^u + b_u)_E + (1 - f_e^+)\frac{1}{(A_P^u)_P}(\sum_{nb} A_{nb}^u u_{nb} + S_d^u + b_u)_P \quad (A.144)$$

$$\frac{1}{(A_P^u)_e} = f_e^+ \frac{1}{(A_P^u)_E} + (1 - f_e^+)\frac{1}{(A_P^u)_P} \quad (A.145)$$

Here, f_e^+ indicates that the linear interpolation factor and it is recognized as:

$$f_e^+ = \frac{\Delta\xi_P}{2\,\delta\xi_e} \tag{A.146}$$

After all of the above, it is possible to re-arrange the equations A.141 and A.142 and thus can be obtained as:

$$\frac{1}{(A_P^u)_P}[\sum_{nb} A_{nb}^u\, u_{nb} + S_d^u + b_u]_P = u_p + \frac{1}{(A_P^u)_P}\Big[(\Delta\eta\beta_{11})_p(p_e - p_w) + (\Delta\xi\beta_{12})_p(p_n - p_s)\Big]_P \tag{A.147}$$

$$\frac{1}{(A_P^u)_E}[\sum_{nb} A_{nb}^u\, u_{nb} + S_d^u + b_u]_E = u_E + \frac{1}{(A_P^u)_E}\Big[(\Delta\eta\beta_{11})_p(p_e - p_w) + (\Delta\xi\beta_{12})_p(p_n - p_s)\Big]_E \tag{A.148}$$

Replacing equations A.148 and A.147 into equation A.144, affords as:

$$\frac{1}{(A_P^u)_e}(\sum_{nb} A_{nb}^u\, u_{nb} + b_u)_e = f_e^+\left[u_E + \frac{1}{(A_P^u)_E}\Big[(\Delta\eta\beta_{11})_p(p_e - p_w) + (\Delta\xi\beta_{12})_p(p_n - p_s)\Big]_E\right] + (1 - f_e^+)\left[u_p + \frac{1}{(A_P^u)_P}\Big[(\Delta\eta\beta_{11})_p(p_e - p_w) + (\Delta\xi\beta_{12})_p(p_n - p_s)\Big]_P\right] \tag{A.149}$$

Replacing equations A.149 in equation A.143, affords as:

$$u_e = f_e^+\left[u_E + \frac{1}{(A_P^u)_E}[(\Delta\eta\beta_{11})(p_e - p_w) + (\Delta\xi\beta_{12})(p_n - p_s)]_E\right] + (1 - f_e^+)\left[u_p + \frac{1}{(A_P^u)_P}[(\Delta\eta\beta_{11})(p_e - p_w) + (\Delta\xi\beta_{12})(p_n - p_s)]_P\right] - \frac{1}{(A_P^u)_e}[(\Delta\eta\beta_{11})(p_E - p_P) + (\Delta\xi\beta_{12})(p_n - p_s)]_e \tag{A.150}$$

Re-arrangement of the above equation, affords:

$$u_e = \left[f_e^+ u_E + (1 - f_e^+)u_p\right]\left[\frac{1}{(A_P^u)_e}[(\Delta\eta\beta_{11})(p_E - p_P)+(\Delta\xi\beta_{12})(p_n - p_s)]_e\right] + f_e^+\left[\frac{1}{(A_P^u)_E}[(\Delta\eta\beta_{11})(p_e - p_w)+(\Delta\xi\beta_{12})(p_n - p_s)]_E\right]$$

$$+(1 - f_e^+)\left[\frac{1}{(A_P^u)_P}[(\Delta\eta\beta_{11})(p_e - p_w) + (\Delta\xi\beta_{12})(p_n - p_s)]_P\right] \quad (A.151)$$

The same procedure is employed to determine u_w , u_n and u_s at w, n, and s faces, respectively.

APPENDIX B

EXPERIMENTAL SET-UP

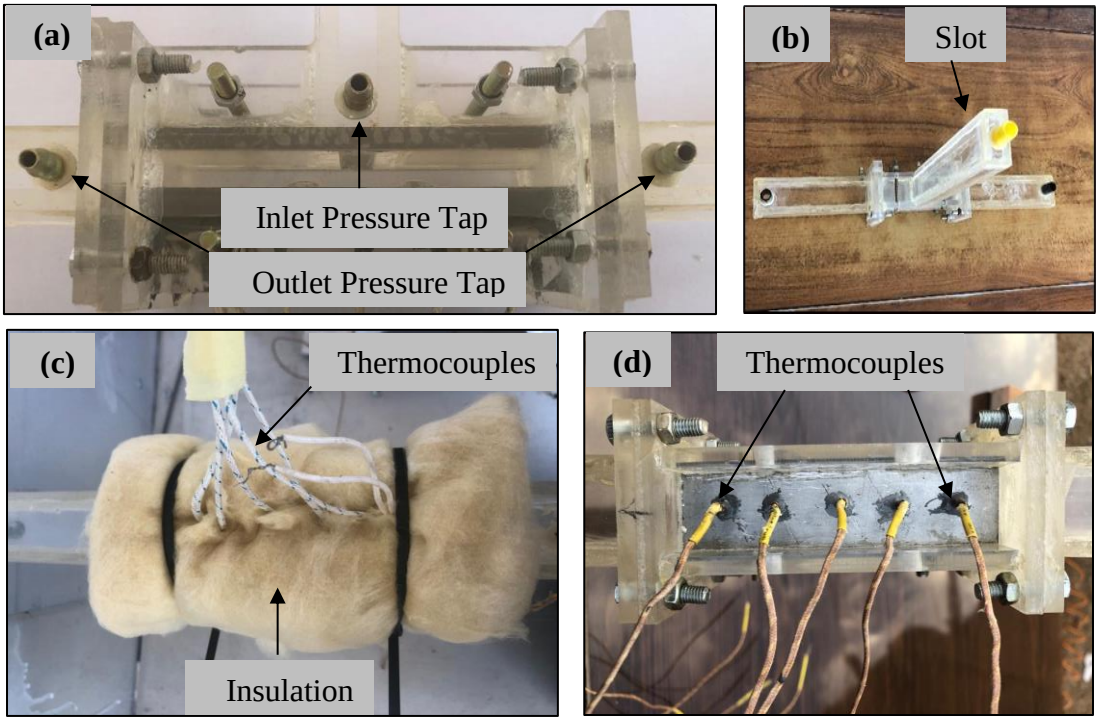

Figure B.1: (a) Pressure taps, (b) Side view of test section, (c) Insulation of test section, (d) installation of thermocouples on target surface.

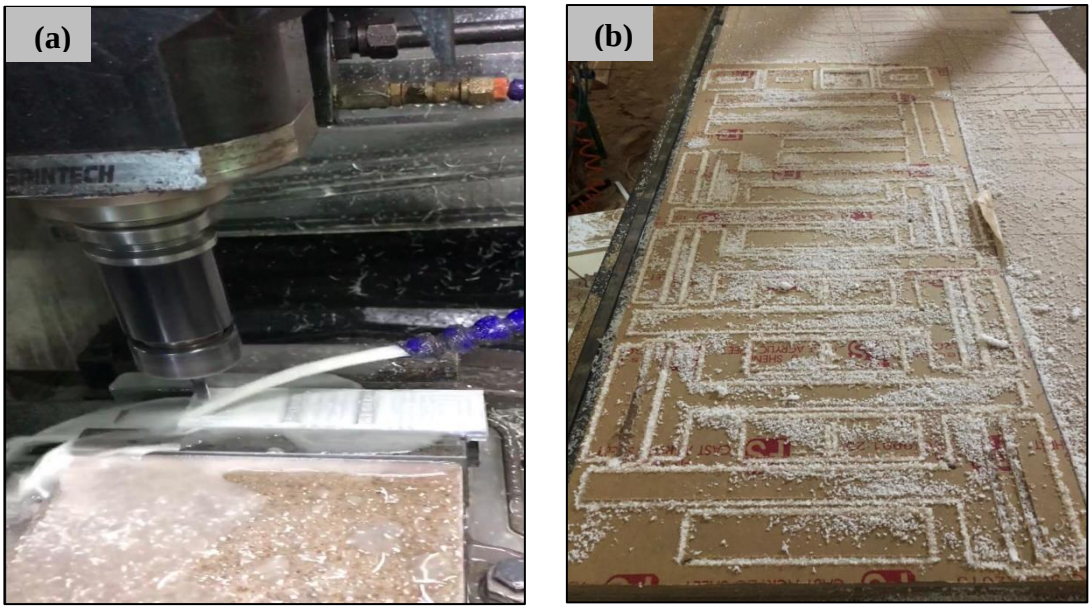

Figure B.2: CNC machine used to fabricate (a) target shapes, (b) acrylic surfaces.

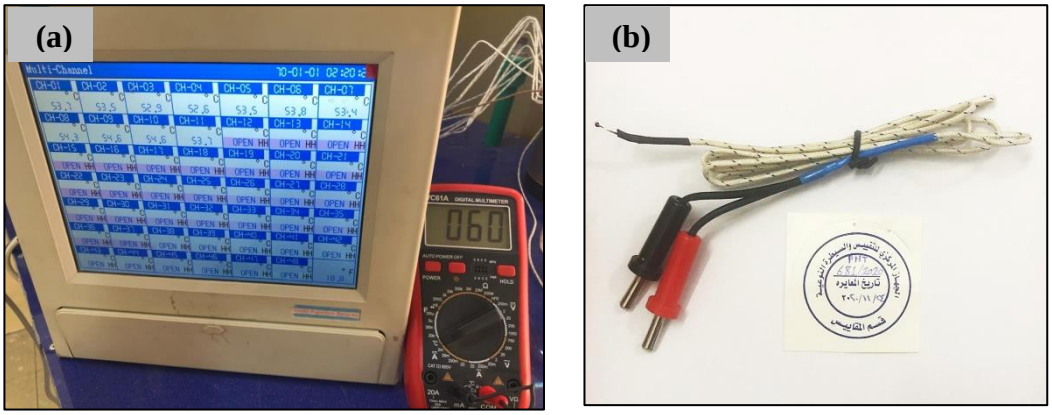

Figure B.3: (a) Calibration device, (b) Reference thermocouple, (c) Electrical heater.

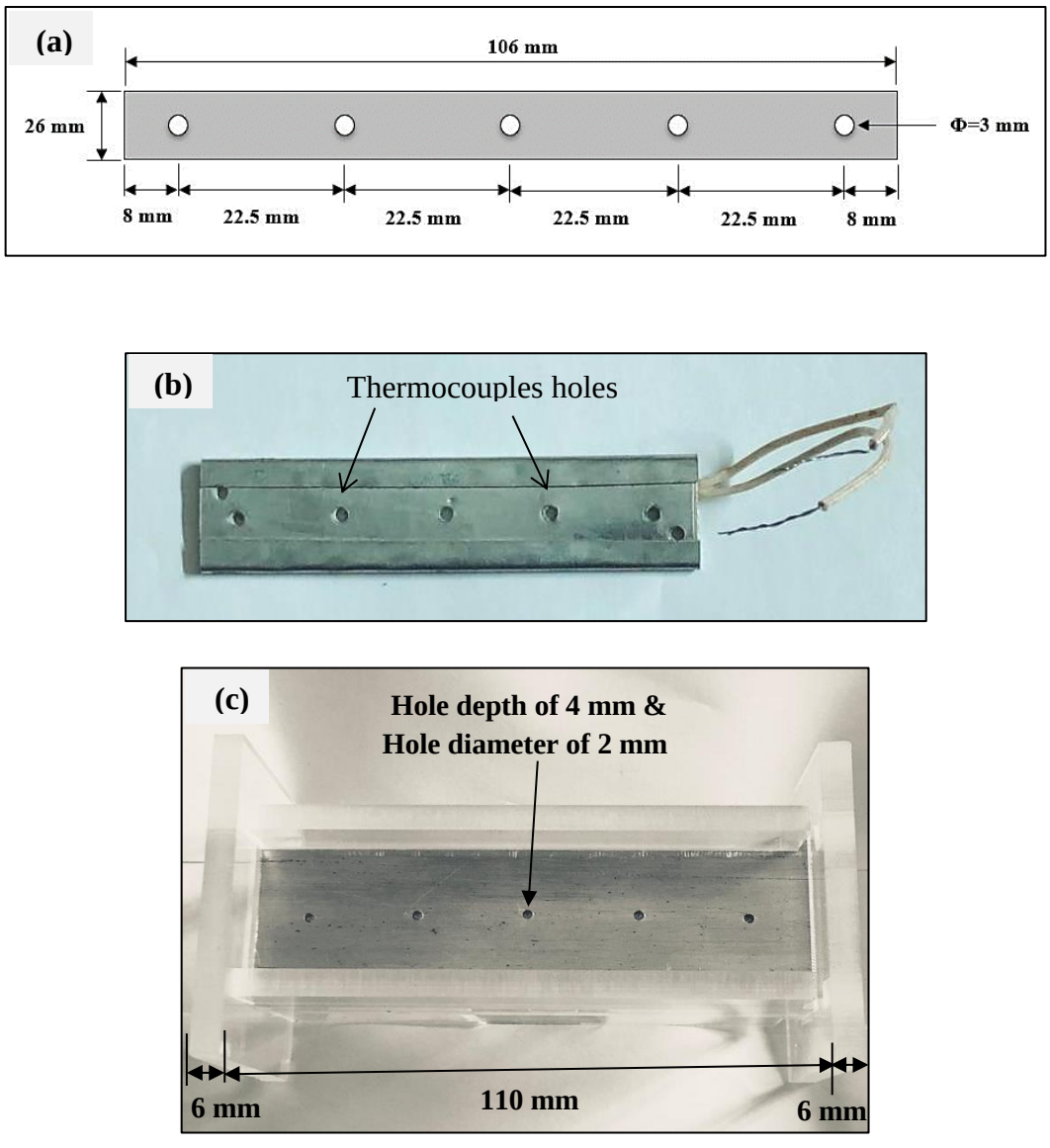

Figure B.4: (a) Schematic diagram of heater, (b) Electrical heater, (c) Hole depth of bottom view for target surface.

Figure B.5: (a) AC power regulator (Variac AC), (b) Voltage stabilizer.

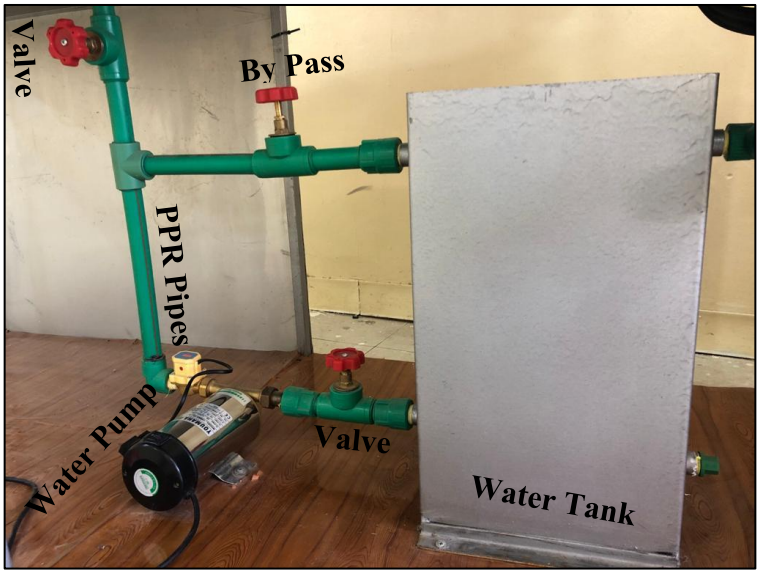

Figure B.6: The parts of the storage and control system.

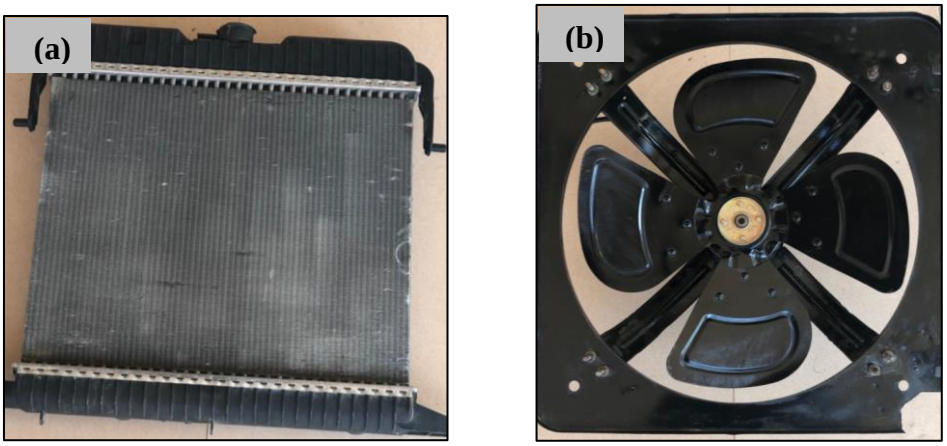

Figure B.7: The parts of the cooling system (a) Radiator, (b) Fan.

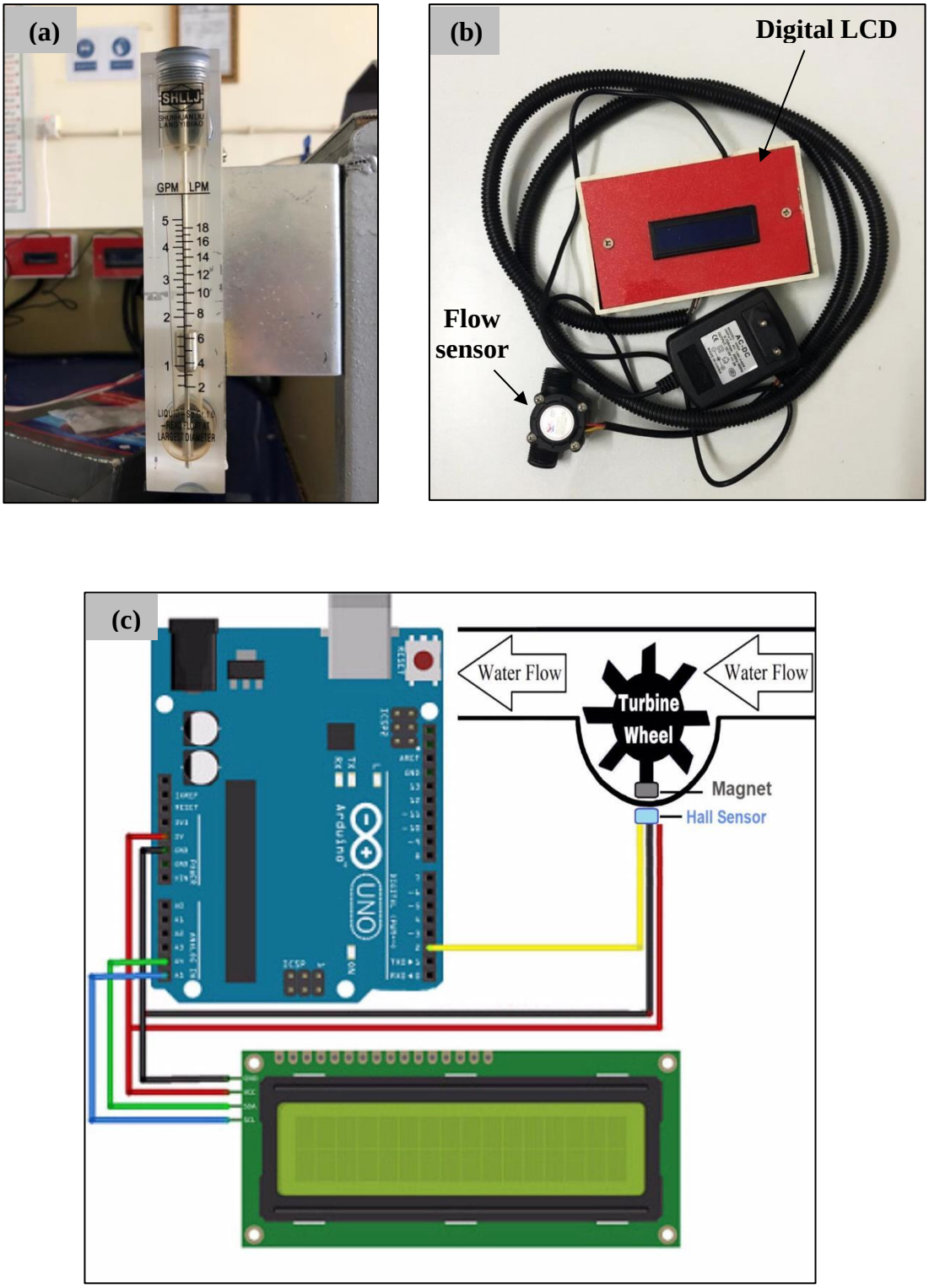

Figure B.8: (a) Flowmeter, (b) Flow sensor, (c) Method of connecting the flow sensor to the Arduino and digital LCD screen.

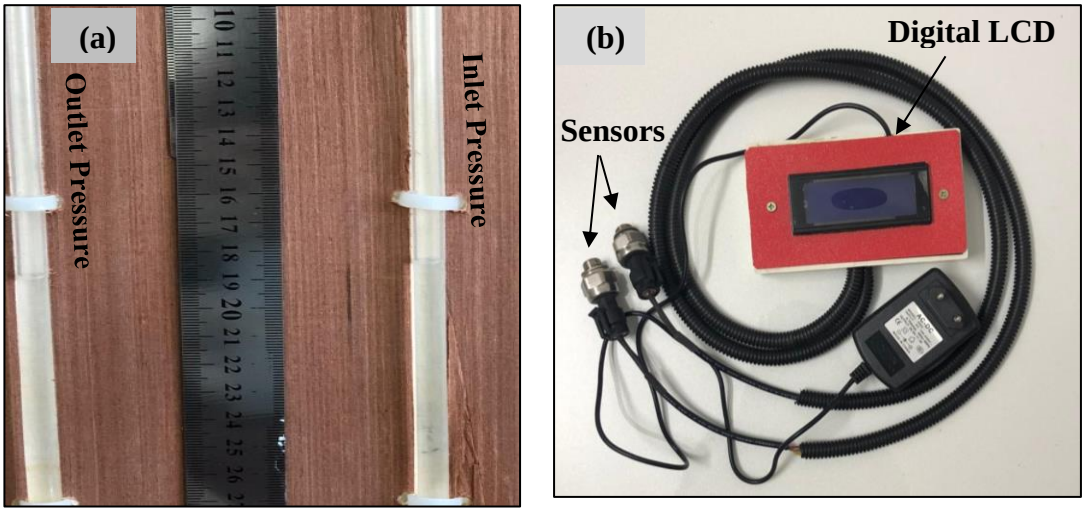

Figure B.9: (a) Tube Manometer, (b) Pressure sensor with LCD

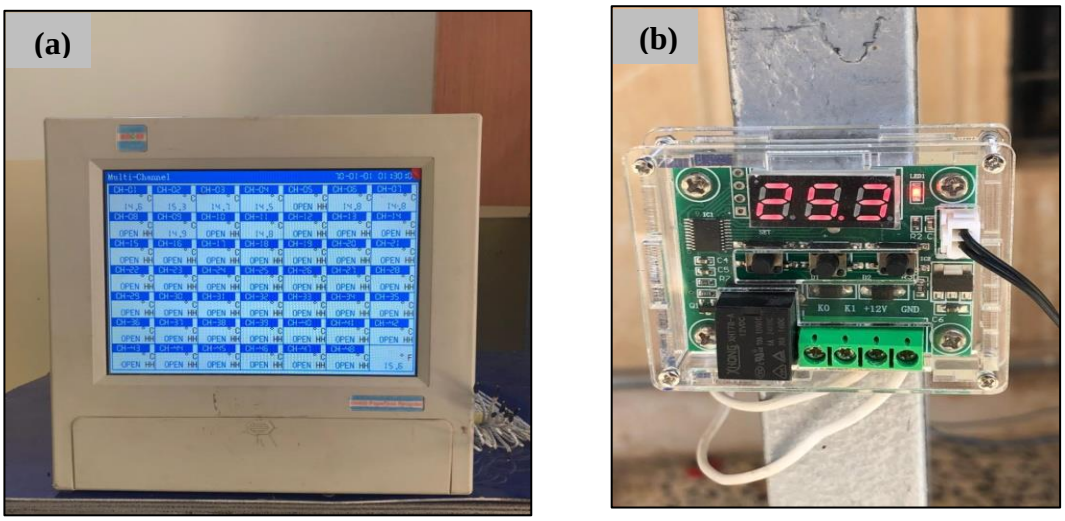

Figure B.10: (a) Data Logger, (b) Thermostat.

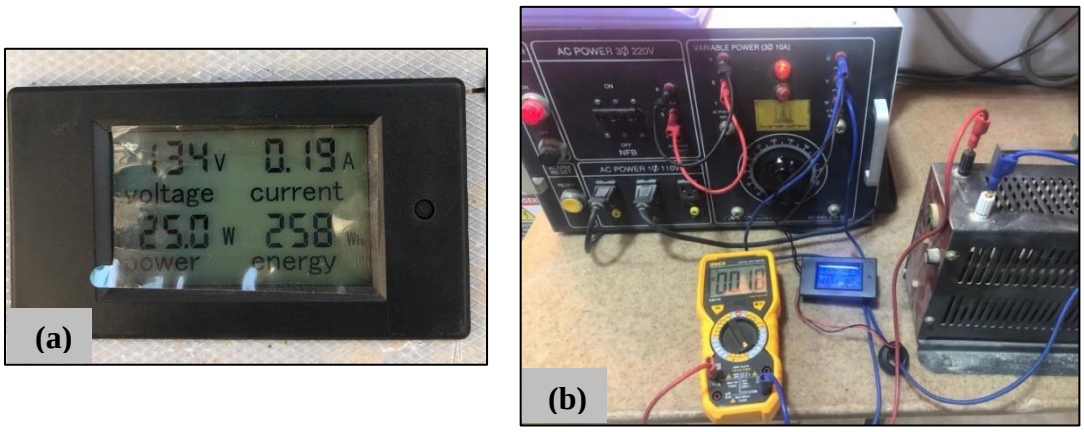

Figure B.11: (a) Digital Multimeter, (b) Multimeter Calibration with reference multimeter.

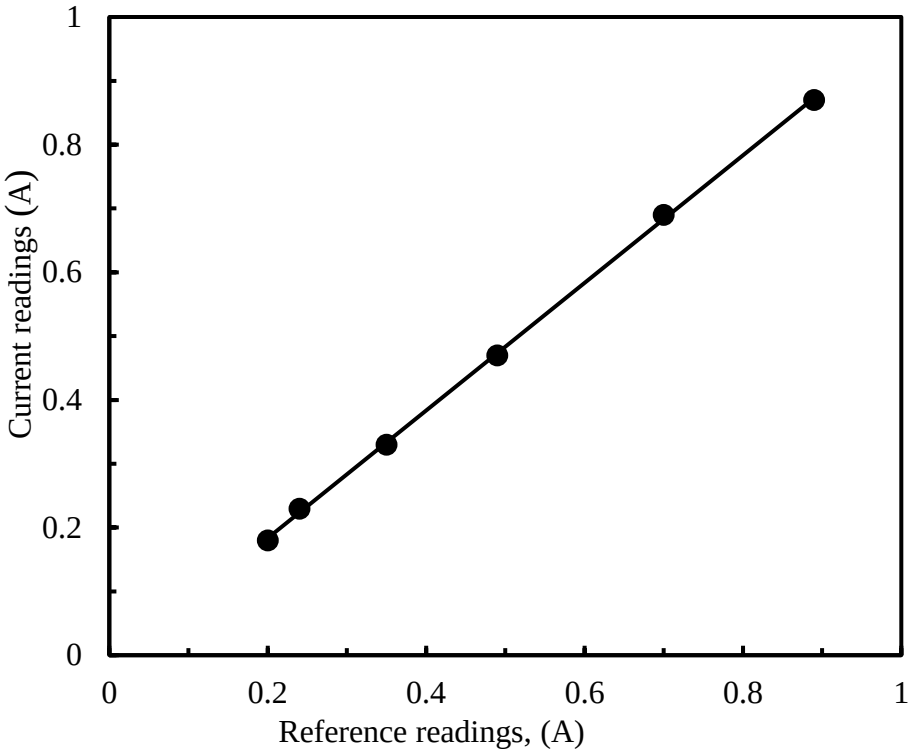

Figure B.12: Calibration of current multimeter.

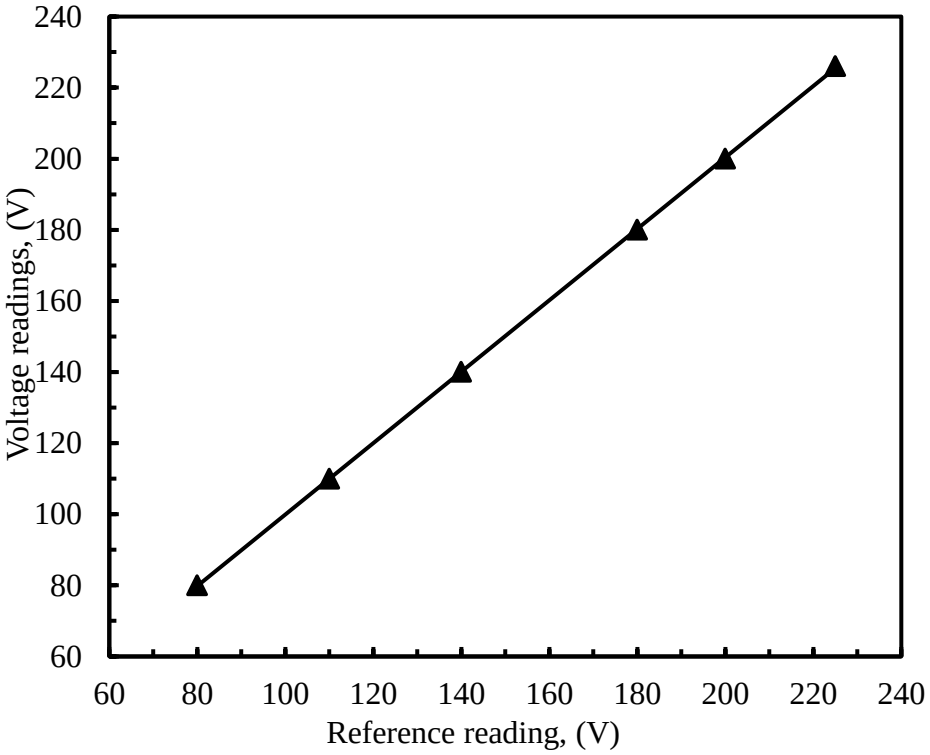

Figure B.13: Calibration of voltage multimeter.

APPENDIX C

CALCULATION OF MEASUREMENTS UNCERTAINTY

C.1 Experimental Results for Wing Ribs

The experimental results for different parameters (such as; the averages of inlet, outlet, and bulk fluid temperatures, heat received, heat transfer coefficient, Nusselt number, head, and pressure drop) for the case of the wing ribs shape at d=10 mm and a=2 mm for whole jet Reynolds number range. These results presented that in the Table C.1.

Table C.1: The experimental results for different parameters.

Average							
Re	***T_{in} (K)***	***T_o (K)***	***T_b (K)***	***T_w (K)***	***Q_f***	***h***	***Nu***
3000	298	298.355	298.178	309.545	120.021	3199.47	52.4933
4000	298.125	298.471	298.298	309.545	155.961	4202.09	68.9432
5000	298.25	298.589	298.419	310.22	190.831	4900.34	80.3994
6000	298.1	298.385	298.243	309.545	192.793	5168.95	84.8064
7000	298.325	298.61	298.468	309.55	224.867	6148.58	100.879
8000	298.5	298.745	298.623	308.645	220.849	6677.37	109.555

Average		$(\Delta p = \rho_f \, . g \, . H)$
Re	***Head (m)***	$\Delta p \; (pa)$
3000	0.0006	5.8691
4000	0.001005	9.831
5000	0.001475	14.4282
6000	0.00195	19.0745
7000	0.002575	25.1882
8000	0.0033	32.28

C.2 Uncertainty of Key Parameters

The uncertainties of key various parameters are presented in follow table.

Table C.2: The primary uncertainties for various parameters.

NO.	Variable	Accuracy
1	The length of channel, L	± 1.0 mm
2	The width of channel, Z	± 0.1 mm
3	The height of channel, H	± 0.1 mm
4	The width of slot jet, W	± 0.1 mm
5	Inlet bulk temperature, $T_{b,in}$	$\pm 1\%$
6	outlet bulk temperature, $T_{b,o}$	$\pm 1\%$
7	Wall temperature, T_w	$\pm 1\%$
8	Mass flow rate, $\dot{m}$	$\pm 5.0\%$
9	Pressure drop, Δp	3.25%

C.3 Uncertainty of Hydraulic Diameter

The hydraulic diameter was displayed in equation 4.5 (in chapter four) as follows:

$$D_h = W \tag{C.1}$$

The uncertainty of hydraulic diameter is expressed by:

$$U_{D_h} = \pm\sqrt{\left(\frac{\partial D_h}{\partial W} U_W\right)^2} \tag{C.2}$$

Where,

$$\frac{\partial D_h}{\partial W} = 1 \tag{C.3}$$

Substitute this value in equation C.2 as follows:

$$U_{D_h} = \pm\sqrt{(U_W)^2} \quad (C.4)$$

Substitute the value of W from Table C.2 in above equation expresses:

$$U_{D_h} = \pm\sqrt{(0.1)^2} = \pm 0.1\ mm \quad (C.5)$$

Furthermore, the relative uncertainty is determined as follows:

$$\frac{U_{D_h}}{D_h} = \pm\frac{0.1}{10} = \pm 1\ \% \quad (C.6)$$

C.4 Uncertainty of Cross - Sectional Area

The cross-sectional area was computed in equation 4.11 (in chapter four) as follows:

$$A_c = W\ .\ Z \quad (C.7)$$

Also, the cross-sectional area uncertainty (A_c) is computed as follows:

$$U_{A_c} = \pm\sqrt{\left(\frac{\partial A_c}{\partial W}U_W\right)^2 + \left(\frac{\partial A_c}{\partial Z}U_Z\right)^2} \quad (C.8)$$

Where,

$$\frac{\partial A_c}{\partial W} = Z \quad (C.9)$$

$$\frac{\partial A_c}{\partial Z} = W \quad (C.10)$$

Substitute the above terms in equation C.8 as follows:

$$U_{A_c} = \pm\sqrt{(ZU_W)^2 + (WU_Z)^2} \quad (C.11)$$

$$= \pm\sqrt{(30 * 0.1)^2 + (10 * 0.1)^2} = \pm 3.1623\ mm^2 \quad (C.12)$$

The relative uncertainty of A_c is obtained as follows:

$$\frac{U_{A_C}}{A_C} = \pm\frac{3.1623}{10*30} = \pm 1.0541\ \% \qquad (C.13)$$

C.5 Uncertainty of Surface Area

The surface area of the impinging target surfaces is given as:

$$A_S = L\ .\ Z \qquad (C.14)$$

The relative uncertainty of A_S is evaluated as follows:

$$\frac{U_{A_S}}{A_S} = \pm\frac{1}{A_S}\sqrt{\left(\frac{\partial A_S}{\partial L}U_L\right)^2 + \left(\frac{\partial A_S}{\partial Z}U_Z\right)^2} \qquad (C.15)$$

Here,

$$\frac{\partial A_S}{\partial L} = \frac{A_S}{L} \qquad (C.16)$$

$$\frac{\partial A_S}{\partial Z} = \frac{A_S}{Z} \qquad (C.17)$$

Substituting the above terms in equation C.15 gives:

$$\frac{U_{A_S}}{A_S} = \pm\sqrt{\left(\frac{U_L}{L}\right)^2 + \left(\frac{U_Z}{Z}\right)^2} \qquad (C.18)$$

$$= \pm\sqrt{\left(\frac{1.0}{110}\right)^2 + \left(\frac{0.1}{30}\right)^2} = \pm 0.9683\% \qquad (C.19)$$

C.6 Uncertainty of Jet Reynolds Number

Jet Reynolds number can be expressed as follows:

$$Re = \frac{\dot{m} D_h}{\mu_f A_c} \tag{C.20}$$

The jet Reynolds number uncertainty is presented as follows:

$$U_{Re} = \pm \sqrt{\left(\frac{\partial Re}{\partial \dot{m}} U_{\dot{m}}\right)^2 + \left(\frac{\partial Re}{\partial D_h} U_{D_h}\right)^2 + \left(\frac{\partial Re}{\partial A_c} U_{A_c}\right)^2} \tag{C.21}$$

Where,

$$\frac{\partial Re}{\partial \dot{m}} = \frac{D_h}{\mu_f A_c} = \frac{Re}{\dot{m}} \tag{C.22}$$

$$\frac{\partial Re}{\partial D_h} = \frac{\dot{m}}{\mu_f A_c} = \frac{Re}{D_h} \tag{C.23}$$

$$\frac{\partial Re}{\partial A_c} = -\frac{\dot{m} D_h}{\mu_f {A_c}^2} = -\frac{Re}{A_c} \tag{C.24}$$

Substituting these terms in equation C.21, thus, the relative uncertainty of jet Reynolds number is presented as:

$$\frac{U_{Re}}{Re} = \pm \sqrt{\left(\frac{U_{\dot{m}}}{\dot{m}}\right)^2 + \left(\frac{U_{D_h}}{D_h}\right)^2 + \left(\frac{-U_{A_c}}{A_c}\right)^2} \tag{C.25}$$

$$= \pm \sqrt{\left(\frac{0.010785}{0.2157}\right)^2 + \left(\frac{0.1}{10}\right)^2 + \left(\frac{-3.1623}{300}\right)^2} = \pm 5.207\% \tag{C.26}$$

C.7 Uncertainty of Friction Factor

The friction factor was expressed in equation 4.8 (in chapter four) as follows:

$$f = \frac{2\Delta p \, \rho_f \, A_c^2}{\dot{m}^2} \frac{D_h}{L} \tag{C.27}$$

The friction factor uncertainty is as shown by:

$$U_f = \pm \sqrt{\begin{matrix}\left(\frac{\partial f}{\partial \Delta p} U_{\Delta p}\right)^2 + \left(\frac{\partial f}{\partial \dot{m}} U_{\dot{m}}\right)^2 + \left(\frac{\partial f}{\partial A_c} U_{A_c}\right)^2 \\ + \left(\frac{\partial f}{\partial D_h} U_{D_h}\right)^2 + \left(\frac{\partial f}{\partial L} U_L\right)^2\end{matrix}} \quad (C.28)$$

Where,

$$\frac{\partial f}{\partial \Delta p} = \frac{2\rho_f A_c^2}{\dot{m}^2} \frac{D_h}{L} = \frac{f}{\Delta p} \quad (C.29)$$

$$\frac{\partial f}{\partial \dot{m}} = \frac{-4}{\dot{m}} \frac{\Delta p\, \rho_f A_c^2}{\dot{m}^2} \frac{D_h}{L} = \frac{-2}{\dot{m}} f \quad (C.30)$$

$$\frac{\partial f}{\partial A_c} = \frac{4\Delta p\, \rho_f A_c}{\dot{m}^2} \frac{D_h}{L} = \frac{f}{A_c} \quad (C.31)$$

$$\frac{\partial f}{\partial\, D_h} = \frac{2\Delta p\, \rho_f A_c^2}{\dot{m}^2} \frac{1}{L} = \frac{f}{D_h} \quad (C.32)$$

$$\frac{\partial f}{\partial L} = \frac{-2\Delta p\, \rho_f A_c^2}{\dot{m}^2} \frac{D_h}{L} = \frac{-f}{L} \quad (C.33)$$

Substituting above terms in equation C.28, thus, the relative uncertainty of friction factor is expressed by:

$$\frac{U_f}{f} = \pm \sqrt{\left(\frac{U_{\Delta p}}{\Delta p}\right)^2 + \left(\frac{-2U_{\dot{m}}}{\dot{m}}\right)^2 + \left(\frac{2U_{A_c}}{A_c}\right)^2 + \left(\frac{U_{D_h}}{D_h}\right)^2 + \left(\frac{-U_L}{L}\right)^2} \quad (C.34)$$

$$\frac{U_f}{f} = \pm \sqrt{\begin{matrix}\left(\frac{1.0491}{32.28}\right)^2 + \left(\frac{-2*0.010785}{0.2157}\right)^2 + \left(\frac{2*3.1623}{300}\right)^2 \\ + \left(\frac{0.1}{10}\right)^2 + \left(\frac{1.0}{110}\right)^2\end{matrix}}$$

$$= \pm 10.80895\% \quad (C.35)$$

C.8 Uncertainty of Heat Received (Q_f)

The heat received by working fluid was displayed in equation 4.2 (in chapter four) can be given by:

$$Q_f = \dot{m}\, C_{p,f} \left(T_{b,o} - T_{b,in}\right) \quad (C.36)$$

The uncertainty of Q_f is achieved by:

$$U_{Q_f} = \pm\sqrt{\left(\frac{\partial Q_f}{\partial \dot{m}} U_{\dot{m}}\right)^2 + \left(\frac{\partial Q_f}{\partial \Delta T_b} U_{\Delta T_b}\right)^2} \quad (C.37)$$

Where,

$$\frac{\partial Q_f}{\partial \dot{m}} = C_{p,f}\, \Delta T_b = \frac{Q_f}{\dot{m}} \quad (C.38)$$

$$\frac{\partial Q_f}{\partial \Delta T_b} = \dot{m}\, C_{p,f} = \frac{Q_f}{\Delta T_b} \quad (C.39)$$

From equations C.38 and C.39 and re-arranging equation C.37, hence the relative uncertainty of Q_f is determined as:

$$\frac{U_{Q_f}}{Q_f} = \pm\sqrt{\left(\frac{U_{\dot{m}}}{\dot{m}}\right)^2 + \left(\frac{U_{\Delta T_b}}{\Delta T_b}\right)^2} \quad (C.40)$$

Here,

$$\frac{U_{\Delta T_b}}{\Delta T_b} = \pm\sqrt{\left(\frac{U_{T_{b,in}}}{T_{b,in}}\right)^2 + \left(\frac{U_{T_{b,o}}}{T_{b,o}}\right)^2} \quad (C.41)$$

$$= \pm\sqrt{\left(\frac{0.252}{25.2}\right)^2 + \left(\frac{0.25445}{25.445}\right)^2} = \pm 1.4142\% \quad (C.42)$$

Substitute the above equation in equation C.40 gives:

$$\frac{U_{Q_f}}{Q_f} = \pm\sqrt{\left(\frac{0.010785}{0.2157}\right)^2 + \left(\frac{0.003465}{0.245}\right)^2} = \pm 5.1962\% \quad (C.43)$$

C.9 Uncertainty of Nusselt Number

The average Nusselt number can be expressed as:

$$Nu_{av} = \frac{Q_f D_h}{k_f A_s (T_{w,av} - T_{b,av})} \tag{C.44}$$

The uncertainty in Nusselt number is determined as:

$$U_{Nu_{av}} = \pm \sqrt{\begin{matrix}\left(\frac{\partial Nu_{av}}{\partial Q_f} U_{Q_f}\right)^2 + \left(\frac{\partial Nu_{av}}{\partial D_h} U_{D_h}\right)^2 + \left(\frac{\partial Nu_{av}}{\partial A_c} U_{A_s}\right)^2 \\ + \left(\frac{\partial Nu_{av}}{\partial T_w} U_{T_w}\right)^2 + \left(\frac{\partial Nu_{av}}{\partial T_{b,av}} U_{T_{b,av}}\right)^2\end{matrix}} \tag{C.45}$$

Where,

$$\frac{\partial Nu_{av}}{\partial Q_f} = \frac{D_h}{k_f A_s (T_w - T_{b,av})} = \frac{Nu_{av}}{Q_f} \tag{C.46}$$

$$\frac{\partial Nu_{av}}{\partial D_h} = \frac{Q_f}{k_f A_s (T_w - T_{b,av})} = \frac{Nu_{av}}{D_h} \tag{C.47}$$

$$\frac{\partial Nu_{av}}{\partial A_s} = \frac{-Q_f D_h}{k_f {A_s}^2 (T_w - T_{b,av})} = \frac{-Nu_{av}}{A_s} \tag{C.48}$$

$$\frac{\partial Nu_{av}}{\partial T_w} = \frac{-Q_f D_h}{k_f A_s (T_w - T_{b,av})^2} = \frac{-Nu_{av}}{(T_w - T_{b,av})} \tag{C.49}$$

$$\frac{\partial Nu_{av}}{\partial T_{b,in}} = \frac{Q_f D_h}{k_f A_s (T_w - T_{b,av})^2} = \frac{Nu_{av}}{(T_w - T_{b,av})} \tag{C.50}$$

Re-arranging equation C.45, the relative uncertainty of Nusselt number is given as:

$$\frac{U_{Nu_{av}}}{Nu_{av}} = \pm \sqrt{\begin{matrix}\left(\frac{U_{Q_f}}{Q_f}\right)^2 + \left(\frac{U_{D_h}}{D_h}\right)^2 + \left(\frac{-U_{A_s}}{A_s}\right)^2 \\ + \left(\frac{-U_{T_w}}{T_w - T_{b,av}}\right)^2 + \left(\frac{-U_{T_{b,av}}}{T_w - T_{b,av}}\right)^2\end{matrix}} \tag{C.51}$$

Where,

$$\frac{U_{T_{b,av}}}{T_{b,av}} = \pm\sqrt{\left(\frac{U_{T_{b,in}}}{T_{b,in}}\right)^2 + \left(\frac{U_{T_{b,o}}}{T_{b,o}}\right)^2}$$

$$= \pm\sqrt{\left(\frac{0.252}{25.2}\right)^2 + \left(\frac{0.25445}{25.445}\right)^2} = \pm 1.4142\% \qquad (C.52)$$

Equation C.51 becomes as follows:

$$\frac{U_{Nu_{av}}}{Nu_{av}} = \pm\sqrt{\begin{matrix}\left(\frac{5.1962}{72}\right)^2 + \left(\frac{0.1}{10}\right)^2 + \left(\frac{-0.9683}{3300}\right)^2 \\ + \left(\frac{-0.35645}{35.645-25.3225}\right)^2 + \left(\frac{-0.253225}{35.645-25.3225}\right)^2\end{matrix}}$$

$$= \pm 8.42776\% \qquad (C.53)$$

الخلاصة

يعتبر تبريد التصادم النفاث أحد أفضل التقنيات لتحقيق تحسين نقل الحرارة العالي بشكل خاص، وبالتالي يتم إستخدامه في العديد من التطبيقات الهندسية. يمكن إستخدام أشكال الأضلاع المختلفة المثبته على الأسطح المستهدفة لتحقيق أداء حراري عالي.

في الدراسة المقدمه، تم إجراء دراسة عددية وتجريبية لتدفق السائل و إنتقال الحرارة و توليد الإنتروبي لتصادم النفاث ذي الفتحة المحصورة تم إستخدام ثلاث أشكال مختلفة من الأضلاع مثل أضلاع الجناح والبيضوية والمسطحة وتثبيتها على لوحة هدف الإصطدام. تم عرض ومناقشة تأثيرات المعاملات المختلفة مثل إرتفاع الضلع (النتوء) والتباعد بين نقطة الركود والضلع و رقم رينولدز النفاث على مجالات إنتقال الحرارة والجريان. تم إجراء عمليات التحقق من صحة النتائج العددية مع الدراسات السابقة المتوفرة في المراجعات ولوحظ وجود توافق جيد بين النتائج. من ناحية أخرى، تمت مقارنة النتائج العددية مع البيانات التجريبية وتم تحقيق التوافق الجيد.

أشارت النتائج إلى أن متوسط رقم نسلت وإنخفاض الضغط ومتوسط توليد الإنتروبي الكلي يزداد عند زيادة رقم رينولدز النفاث وزيادة إرتفاع الضلع, ونقصان التباعد بين نقطة الركود وموقع الضلع. بينما معايير تقييم الأداء تزداد مع زيادة إرتفاع الضلع. وجد أن قيم الذروة لمتوسط تحسين رقم نسلت هي حوالي 90.01 ,74.16 , 65.34 ٪ لأضلاع الجناح والبيضوية والمسطحة عند إرتفاع الضلع 2 ملم وموقع الضلع 10 ملم ورقم رينولدز النفاث 4000 , 4000 , 3000, على التوالي. في حين أن أفضل معايير تقييم الأداء تصل إلى 1.682 والتي توفرها أضلاع الجناح عند موقع الضلع 10 ملم وإرتفاع الضلع 2 ملم ورقم رينولدز النفاث 3000.

جمهوريـــــــــــة العـــــــــراق
وزارة التعليم العـالي والبحث العلمي
جامـعـة الأنبـار – كـلـيـة الهـنـدسة
قســـــم الهندســـــة الميكانيكيـــــة

UNIVERSITY OF ANBAR

دراسة خصائص إنتقال الحرارة والجريان للتصادم النفاث على سطح ساخن مع نتوءات

رسالة مقدمة إلى مجلس
كـلـيـة الهـنـدسة - جامـعـة الأنبـار
وهي جزء من متطلبات نيل درجة الماجستير
في علوم الهندسة الميكانيكية

من قِبل

سعد مطلك حاتم

(بكـالـوريـوس هـنـدسة مـيـكـانـيـكـية – 2017)

بإشراف

أ.م.د. محمد عبد أحمد

1442 2021